

Copyright is owned by the Author of the thesis. Permission is given for a copy to be downloaded by an individual for the purpose of research and private study only. The thesis may not be reproduced elsewhere without the permission of the Author.

**The unusual structure of the
mercury chalcogenides:
relativistic effects
in the solid state**



A thesis presented in partial fulfillment of the
requirements for the degree of
Doctor of Philosophy
at
Massey University, Albany
New Zealand

Susan Biering

September 10, 2010

"While I'm still confused and uncertain, it's on a much higher plane, d'you see, and at least I know I'm bewildered about the really fundamental and important facts of the universe."

Terry Pratchett, *Equal Rites*

Abstract

Mercury oxide in its solid state crystallizes in a rather unusual structure and at ambient pressure two equally intriguing yet different polymorphs are distinguished. Both the low-temperature so-called montroydite form and the high-temperature cinnabar modification consist of planar O-Hg-O zigzag or spiral chains. These sophisticated structures significantly differ from those found for the lighter group 12 chalcogenides zinc oxide and cadmium oxide, which under ambient conditions are known to crystallize in rather simple hexagonal wurtzite and cubic rocksalt or zinc blende structures. Descending the chalcogenide group in the periodic table, the cinnabar structure disappears as an equilibrium modification for mercury selenide and telluride but is still present as a high-pressure modification. However, the deviations in the crystal arrangement between the mercury chalcogenides as opposed to the corresponding zinc and cadmium congeners are still obvious in terms of a different coordination.

Considering this curious behaviour of the mercury chalcogenides the question arises: What causes the occurrence of the unusual structures in the mercury chalcogenides? To this end relativistic as well as nonrelativistic density functional calculations have been carried out to investigate this question with respect to the influence of relativistic effects. Even though relativistic effects in atoms and molecules are well-known and understood, little attention has been given to their influence on the electronic structure and properties of the solid state yet.

The study at hand for the first time demonstrates that the structural differences between the mercury chalcogenides and their lighter zinc and cadmium congeners are a result of relativistic effects. The montroydite and cinnabar modifications of HgO and HgS disappear if relativity is neglected due to a substantial decrease of the cohesive energies by up to 2.2 eV. This deviation becomes smaller for HgSe and HgTe, yet a slight change in the coordination can be attributed to the influence of relativity. Furthermore, the electronic structure and density of states of the mercury chalcogenides are discussed with respect to relativistic effects including the consideration of spin-orbit effects. It was found that relativistic effects have a major impact on the electronic structure. In mercury selenide and telluride the neglect of relativity goes as far as changing the experimentally observed semimetallic behaviour to the restoration of semiconducting properties.

Acknowledgements

I owe my deepest gratitude to Prof. Peter Schwerdtfeger, who has been a wonderful supervisor to me in sharing his knowledge and experience as well as showing plenty of patience over the last five years. His guidance, generous support, unique sense of humour and encouragement throughout good times and bad has made my Ph.D. study an invaluable and pleasant experience. The financial support of Massey University, the Marsden Fund and the New Zealand Study Abroad Award is greatly acknowledged.

I would like to thank my colleagues and co-workers, Vesna, Behnam, Matthias, Brian, Robert, Tilo, Elke, Joachim, Patrick, Detlev, Ralf, Beata, Renyuan, David, Julie, Andrew, Jake, Kyle, Anastasia and Michael, for always making their advice and assistance available, for the pleasant atmosphere and the coffeeholics anonymous meetings throughout all stages of my journey. Many of you became wonderful friends. Special thanks go to Andreas Hermann and Christian Thierfelder for their support in many ways, the countless helpful discussions as well as for the good old times aside from university.

I am grateful to New Zealand and its people for the hospitality and for giving me a new home, where I could truly find myself. Most importantly, I wish to thank Prof. Gero Schmidt for luring me here in the first place.

I am indebted to my family. Most importantly to my parents, Heide-Marie and Roland Biering, for their love, trust and for their bravery to let me go. Thank you for your unconditional support in all my choices throughout my whole life. And to my grandmother for the spirit! To her I dedicate this thesis.

My deepest gratitude goes to Thomas, for his infinite love, the wholehearted support, his endless believe in me and his ability to put a smile on my face when least expected - and for always having tissues :)

It is a pleasure to thank all of my wonderful friends who made this thesis possible in being there for me in countless ways, even though it is not possible to name everybody here. You all rock!

Table of Contents

1	Introduction	1
1.1	Motivation	1
1.2	Outline	6
2	Theoretical background	7
2.1	The many-electron problem	7
2.1.1	The Hamiltonian for the n -electron system	8
2.1.2	The Born-Oppenheimer approximation	9
2.2	The electronic Problem	11
2.2.1	The Hartree-Fock approximation	12
2.2.2	Electron correlation	13
2.2.3	Density functional theory	15
2.2.4	Relativistic effects in quantum chemistry	21
2.3	Periodic systems	25
2.3.1	Crystal symmetries and Bravais lattices	25
2.4	Numerical implementation	29
2.4.1	Plane-wave basis and Bloch's Theorem	30
2.4.2	The frozen-core approximation and pseudopotentials	32
2.5	Optimization and solid-state properties	34
2.5.1	Optimization	35
2.5.2	Equilibrium properties of crystals	36
2.5.3	Determination of the crystal structure and phase transitions	39
3	Structural and computational details	41
3.1	Structures	41
3.1.1	Cubic lattices	42
3.1.2	Hexagonal structures	46

3.1.3	Trigonal structures	48
3.1.4	Orthorhombic structures	49
3.1.5	Tetragonal structures	52
3.2	Computational details	52
3.2.1	Cutoff energy and k -point mesh	53
3.2.2	Ground-state properties and transition pressures	54
3.2.3	Determination of the electronic structure	55
4	The group 12 oxides	59
4.1	Occurring crystal structures	59
4.1.1	Zinc oxide	59
4.1.2	Cadmium oxide	60
4.1.3	Mercury oxide	60
4.2	Equilibrium structures	61
4.2.1	Zinc oxide	61
4.2.2	Cadmium oxide	64
4.2.3	Mercury oxide	65
4.3	High-pressure phases	68
4.3.1	Zinc oxide	68
4.3.2	Cadmium oxide	69
4.3.3	Mercury oxide	70
4.4	Electronic structure	71
4.4.1	Zinc oxide	71
4.4.2	Cadmium oxide	73
4.4.3	Mercury oxide	73
4.5	Relativistic influences	77
4.5.1	Equilibrium structure	77
4.5.2	High-pressure structure	81
4.5.3	Electronic structure	82
4.6	Summary	83
5	The group 12 sulfides	85
5.1	Occurring crystal structures	85
5.1.1	Zinc sulfide	85
5.1.2	Cadmium sulfide	86

5.1.3	Mercury sulfide	87
5.2	Equilibrium structures	89
5.2.1	Zinc sulfide	89
5.2.2	Cadmium sulfide	90
5.2.3	Mercury sulfide	92
5.3	High-pressure phases	94
5.3.1	Zinc sulfide	94
5.3.2	Cadmium sulfide	98
5.3.3	Mercury sulfide	102
5.4	Electronic structure	106
5.4.1	Zinc sulfide	106
5.4.2	Cadmium sulfide	106
5.4.3	Mercury sulfide	109
5.5	Relativistic influences	115
5.5.1	Equilibrium structure	115
5.5.2	High-pressure structure	118
5.5.3	Electronic structure	119
5.6	Summary	122
6	The group 12 selenides	125
6.1	Occurring crystal structures	125
6.1.1	Zinc selenide	125
6.1.2	Cadmium selenide	126
6.1.3	Mercury selenide	127
6.2	Equilibrium structures	128
6.2.1	Zinc selenide	128
6.2.2	Cadmium selenide	130
6.2.3	Mercury selenide	132
6.3	High-pressure phases	133
6.3.1	Zinc selenide	133
6.3.2	Cadmium selenide	137
6.3.3	Mercury selenide	140
6.4	Electronic structure	144
6.4.1	Zinc selenide	144

6.4.2	Cadmium selenide	146
6.4.3	Mercury selenide	150
6.5	Relativistic influences	151
6.5.1	Equilibrium structure	151
6.5.2	High-pressure structure	153
6.5.3	Electronic properties	157
6.6	Summary	157
7	The group 12 tellurides	159
7.1	Occurring crystal structures	159
7.1.1	Zinc tellurides	159
7.1.2	Cadmium tellurides	160
7.1.3	Mercury tellurides	162
7.2	Equilibrium structures	163
7.2.1	Zinc telluride	163
7.2.2	Cadmium telluride	165
7.2.3	Mercury telluride	167
7.3	High-pressure phases	168
7.3.1	Zinc telluride	168
7.3.2	Cadmium telluride	172
7.3.3	Mercury telluride	175
7.4	Electronic structure	179
7.4.1	Zinc telluride	179
7.4.2	Cadmium telluride	179
7.4.3	Mercury telluride	181
7.5	Relativistic influences	184
7.5.1	Equilibrium structure	184
7.5.2	High-pressure structure	186
7.5.3	Electronic properties	187
7.6	Summary	188
8	Conclusion and outlook	191
	Bibliography	195

List of Figures

1.1	Crystals of mercury oxide	2
1.2	Two views of the montroydite structure	2
1.3	Two views of the cinnabar structure	3
2.1	Sketch of the pair distribution function for the homogeneous electron gas	14
2.2	Ratio of relativistic and non-relativistic Bohr radius	23
2.3	Primitive vectors of a unit cell	26
2.4	Comparison of the all-electron and the pseudopotential wavefunction	33
3.1	Unit vectors and angles of a unit cell	42
3.2	Unit cells of the cesium chloride and the rocksalt structure	44
3.3	The units cells of the zinc blende and the wurtzite structure	45
3.4	The unit cell of the cinnabar structure	49
3.5	Structural change from the cinnabar to the rocksalt structure	50
3.6	The unit cell of the montroydite structure	51
3.7	Brillouin zone of the fcc lattice	55
3.8	Brillouin zone of the hexagonal primitive lattice	56
3.9	Brillouin zone of the orthorhombic side-face centred lattice	56
4.1	Lattice energies for the ZnO and CdO crystal structures	63
4.2	Relativistic and nonrelativistic lattice energies for the HgO crystal structures	66

4.3	Band structures and DOS for the ZnO and CdO equilibrium polymorphs	72
4.4	Band structures and DOS for the HgO polymorph montroydite	74
4.5	Site-projected DOS for the HgO polymorph montroydite	75
4.6	Band structures and DOS for the HgO polymorph cinnabar	78
4.7	Site-projected DOS for the HgO polymorph cinnabar	79
4.8	Band structures and DOS for the nonrelativistic equilibrium HgO polymorph	82
4.9	Site-projected DOS for the nonrelativistic equilibrium HgO polymorph	83
5.1	Lattice energies for the ZnS and CdS crystal structures	88
5.2	Lattice parameter of Pmmn-CdS	102
5.3	Lattice parameter of Pmmn-HgS	105
5.4	Band structures and DOS for the ZnS polymorphs wurtzite and zinc blende	107
5.5	Band structures and DOS for the CdS polymorphs wurtzite and zinc blende	108
5.6	Band structures and DOS for the HgS polymorph cinnabar	110
5.7	Site-projected DOS for the HgS polymorph cinnabar	111
5.8	Band structures and DOS for the HgS polymorph zinc blende	113
5.9	Site-projected DOS for the HgS polymorph zinc blende	114
5.10	Relativistic and nonrelativistic lattice energies for the HgS crystal structures	116
5.11	Lattice parameters of nonrelativistic Pmmn-HgS	118
5.12	Band structures and DOS for the nonrelativistic equilibrium HgS polymorphs	120
5.13	Site-projected DOS for the nonrelativistic equilibrium HgS polymorphs	121
6.1	Lattice energies for the ZnSe and CdSe crystal structures	129

6.2	Band structures and DOS for the ZnSe polymorphs zinc blende and wurtzite	145
6.3	Band structures and DOS for the CdSe polymorphs zinc blende and wurtzite	147
6.4	Band structures and DOS for the HgSe polymorph zinc blende	148
6.5	Site-projected DOS for the HgSe polymorph zinc blende	149
6.6	Relativistic and nonrelativistic lattice energies for the HgSe crystal structures	152
6.7	Band structures and DOS for the nonrelativistic equilibrium HgSe polymorphs	155
6.8	Site-projected DOS for the nonrelativistic equilibrium HgSe polymorphs	156
7.1	Lattice energies for the ZnTe and CdTe crystal structures	164
7.2	Band structures and DOS for the ZnTe and CdTe equilibrium polymorph zinc blende	180
7.3	Band structures and DOS for the HgTe polymorph zinc blende	182
7.4	Site-projected DOS for the HgTe polymorph zinc blende	183
7.5	Relativistic and nonrelativistic lattice energies for the HgTe crystal structures	185
7.6	Band structures and DOS for the nonrelativistic equilibrium HgTe polymorph	188
7.7	Site-projected DOS for the nonrelativistic equilibrium HgTe polymorph	189

List of Tables

1.1	Structures of the HgO equilibrium phases	3
2.1	Bravais lattices of a three-dimensional crystal	28
3.1	Adopted and investigated structures of the group 12 chalcogenides	43
3.2	Atomic total energies	54
4.1	Ground-state properties of the ZnO equilibrium phases	62
4.2	Ground-state properties of the CdO equilibrium phases	64
4.3	Ground-state properties of the HgO equilibrium phases	67
4.4	Ground-state properties of the ZnO high-pressure phases	68
4.5	Ground-state properties of the CdO high-pressure phases	69
4.6	Ground-state properties of the HgO high-pressure phases	70
4.7	Bond distances of the equilibrium group 12 oxides	80
4.8	Ground-state properties of the nonrelativistic HgO equilibrium and high-pressure phases	81
5.1	Ground-state properties of the ZnS equilibrium phases	89
5.2	Ground-state properties of the CdS equilibrium phases	91
5.3	Ground-state properties of the HgS equilibrium phases	92
5.4	Ground-state properties of the ZnS high-pressure phases I	95
5.5	Ground-state properties of the ZnS high-pressure phases II	96
5.6	Ground-state properties of the CdS high-pressure phases I	99
5.7	Ground-state properties of the CdS high-pressure phases II	100

5.8	Ground-state properties of the HgS high-pressure phases	103
5.9	Ground-state properties of the nonrelativistic HgS equilibrium and high-pressure phases	115
5.10	Bond distances of the equilibrium group 12 sulfides	118
6.1	Ground-state properties of the ZnSe equilibrium phases	130
6.2	Ground-state properties of the CdSe equilibrium phases	131
6.3	Ground-state properties of the HgSe equilibrium phases	133
6.4	Ground-state properties of the ZnSe high-pressure phases I	134
6.5	Ground-state properties of the ZnSe high-pressure phases II	135
6.6	Ground-state properties of the CdSe high-pressure phases I	138
6.7	Ground-state properties of the CdSe high-pressure phases II	139
6.8	Ground-state properties of the HgSe high-pressure phases I	141
6.9	Ground-state properties of the HgSe high-pressure phases II	142
6.10	Ground-state properties of the nonrelativistic HgSe equilibrium and high-pressure phases	151
6.11	Bond distances of the equilibrium group 12 selenides	153
7.1	Ground-state properties of the ZnTe equilibrium phases	165
7.2	Ground-state properties of the CdTe equilibrium phases	166
7.3	Ground-state properties of the HgTe equilibrium phases	167
7.4	Ground-state properties of the ZnTe high-pressure phases I	169
7.5	Ground-state properties of the ZnTe high-pressure phases II	170
7.6	Ground-state properties of the CdTe high-pressure phases I	173
7.7	Ground-state properties of the CdTe high-pressure phases II	174
7.8	Ground-state properties of the HgTe high-pressure phases I	176
7.9	Ground-state properties of the HgTe high-pressure phases II	177
7.10	Ground-state properties of the nonrelativistic HgTe equilibrium and high-pressure phases	184
7.11	Bond distances of the equilibrium group 12 tellurides	186

Nomenclature

ADA	Averaged Density Approximation
ADX	Angle Dispersive Xray
AIMD	Ab-Initio Molecular Dynamics
APW+lo	Augmented Plane-Wave method plus Local Orbitals
CBM	Conduction-Band Minimum
CC	Coupled Cluster
CI	Configuration Interaction
DFT	Density Functional Theory
DOS	Density Of States
EDX	Energy Dispersive Xray
EOS	Equation Of State
EXAFS	Extended X-ray Absorption Fine Structure
FFT	Fast-Fourier Transform
FP	Full Potential
GDSP	Gaussian Dual Space Pseudopotentials
GGA	Generalized Gradient Approximation
GTO	Gaussian Type Orbital
HF	Hartree-Fock
IBZ	Irreducible Brillouin Zone

LAPW	Linearised Augmented-Plane Wave
LCAO	Linear Combination of Atomic Orbitals
LDA	Local Density Approximation
LMTO	Linear Muffin-Tin Orbital
LSDA	Local Spin-Density Approximation
MBPT	Many-Body Perturbation Theory
MD	Molecular Dynamics
MP2	2nd order Møller-Plesset perturbation theory
MR	Multi Reference
NAO+GC	Natural Atomic Orbital plus Gradient Corrections
PBE	Perdew-Burke-Ernzerhof functional
PP	PseudoPotential
PW	Plane Wave
PW91	PerdewWang 1991 functional
SCF	Self-Consistent Field
SCR	Self-Consistent Relativistic
TB	Tight Binding
US	UltraSoft pseudopotential
VASP	Vienna Ab-initio Simulation Package
VBM	Valence-Band Maximum

Chapter 1

Introduction

1.1 Motivation

Mercury oxide, HgO, is a crystalline solid with a melting point of 773 K (500°C). Already in 1774 Joseph Priestley observed that by heating, mercury oxide easily decomposes into mercury and oxygen, which led to the important discovery of oxygen. This decomposition reaction is still used in the production of mercury. It implies that the mercury-oxygen bond for HgO in the gas phase is quite weak, which was confirmed by a recent analysis of Shepler and Peterson [1]. They obtained a rather small dissociation energy of only 0.17 eV and compared their result to various previous estimates [2]. More recent critical discussions can be found in the articles by Filatov and Cremer [3] and Peterson *et al.* [4]. Having this unusually low dissociation energy, mercury oxide in the gas phase is rather unique compared to its group 12 congeners.

In the solid state, however, HgO is even more intriguing, as it crystallizes in a rather unique structure. Two different polymorphs of HgO exist under ambient pressure, both equally unusual and interesting. At low temperatures HgO crystallizes in an orthorhombic structure with the spacegroup $Pnma$ [5]. This is, even though scarcely found, in fact the naturally occurring mineral form of mercury oxide, called montroydite (see fig. 1.1), and adapts a yellow or reddish-brown colour depending on the grain size. Another polymorph exists and crystallizes in a cinnabar-like structure (belonging to the trigonal crystal system) [6], which derives its name from the naturally occurring mercury sulfide mineral. This hexagonal phase is stable above 220°C and has a yellow colour [7].

Both structures were thought to be unique to the mercury chalcogenides, and



Figure 1.1: Crystals of mercury oxide in its mineral montroydite form [8].

it was not until 1993 that Nelmes *et al.* reported the cinnabar structure as an intermediate high pressure phase in CdTe [9]. The only other compound apart from the group 12 chalcogenides, that exists in this structure as well, even though only under high pressure, is GaAs.

The crystal structure of the montroydite phase is built from planar O-Hg-O zigzag chains, which are formed parallel to the x -axis in the a - c -plane, whereas in the high-temperature form spiral chains are formed running parallel to the z -axis [5, 6, 10]. This leads to the rather unique crystal structures shown in figs. 1.2 and 1.3. In both cases the O-Hg-O group building the chains is linear, having a Hg-O bond distance of 2.028 and 2.030 Å for the montroydite and cinnabar form, respectively. The Hg-O-Hg group, however, is bent with an angle of 108.8° in the case of the low-temperature phase and 107.9° in the cinnabar structure (see table 1.1). More information regarding the structure including pictures of the respective unit cells can be found in chapters 3.1 and 4.

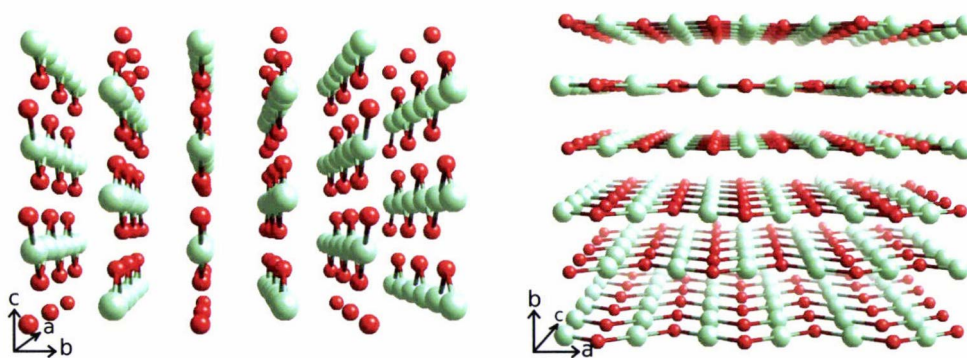


Figure 1.2: Two views of the montroydite structure (red: oxygen, cyan: mercury).

The equilibrium phases of mercury oxide are, however, in stark contrast to the lighter group 12 oxides, namely zinc (ZnO) and cadmium oxide (CdO). At room temperature and low pressure they are known to crystallize in a rather simple

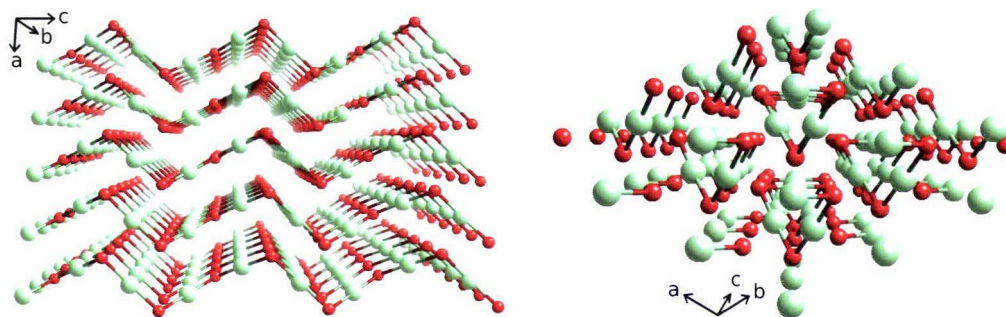


Figure 1.3: Two views of the cinnabar structure (red: oxygen, cyan: mercury).

	Montroydite	Cinnabar
spacegroup:	62 ($Pnma$) orthorhombic	152 ($P3_121$) / 154 ($P3_221$) hexagonal
structure:		
O-Hg-O chains	in ac -plane, parallel to a -axis	spiral, parallel to c -axis
O-Hg-O group	linear	linear
Hg-O bond	2.028 Å	2.030 Å
$\angle(\text{Hg-O-Hg})$	108.8°	107.9°

Table 1.1: A comparison of the structures of the montroydite and cinnabar phases of HgO.

hexagonal wurtzite and a cubic rocksalt structure, respectively. For HgO those less complicated structures are only accessible at higher pressures, where mercury oxide undergoes a phase transition into a tetragonal distortion of the rocksalt structure with the spacegroup $I4/mmm$ first, and then finally into the common rocksalt structure (NaCl) [11, 12].

Following the periodic table down to the group 12 sulfides, selenides and tellurides, HgS crystallizes in the cinnabar structure, being the prototype for this unusual structure. However, the cinnabar form is replaced as the equilibrium phase for HgSe and HgTe, where the zinc blende structure is found to be the preferred form. Even more interestingly, the transition to the cinnabar phase occurs in a rather low pressure range of 0.74-1.5 GPa for HgSe and at 1.3 GPa for HgTe [12]. Moreover, for ZnTe and CdTe the cinnabar phase also exists, even though only as a high pressure phase and with a coordination strongly varying from the one found in HgO and HgS. Considering this unusual behaviour within the mercury chalcogenide series of compounds, the unique montroydite form of HgO and the very rare appearance of the cinnabar structure in general,

the question naturally arises as to "what causes the occurrence of these unusual structures in the mercury chalcogenides?".

However, the understanding of bulk structures and their influence on the solid state properties,¹ also in the context of the ongoing challenge of the design of new materials for various applications, is a difficult task. The prediction of crystal structures from simple bonding models is currently hard, if not impossible, as discussed by Maddox and Cohen [13, 14]. Very often polymorphs are separated only by a small energy, which makes this task even more complicated. In contrast, simple bonding models are rather successful for the prediction of molecular structures [15]. The mercury chalcogenides with their extraordinary low pressure modifications are prime examples of this plight. Investigating those structures contributes to bringing us one step closer to the answer of one of the major problems we currently face in solid-state chemistry.

Mercury has 80 electrons surrounding a heavy nucleus of 80 protons and 121 neutrons for its most stable isotope, hence making it one of the heavier elements (atomic weight: $200.59 \text{ g}\cdot\text{mol}^{-1}$). Due to its large nuclear charge the electrons close to the core reach velocities that demand for a relativistic treatment. In fact, together with gold, mercury is one of the elements that proved to be influenced exceptionally strong by relativistic effects, known as the relativistic maximum within a period of elements [16, 17]. This raises the question, whether the highly unorthodox structures found for the mercury chalcogenides are due to the relativistic influence on the electronic structure? Therefore and because of its size, mercury and its compounds are complex systems that ask for a very accurate (relativistic) treatment and hence grand computational effort. However, even though relativistic effects are known to play an important role in the molecular structure of compounds containing mercury [16, 18–25], it has not been investigated in detail yet for the structure of the solid state [26, 27].

In addition, the thesis at hand deals not only with the crystal structures of the mercury chalcogenides at equilibrium conditions, but under high pressure as well. High pressure physics and chemistry are fields of increasing interest. This has not always been like this due to the fact that life on earth is limited to a rather small range of temperatures and pressures. In a for humans commonly accessible world, more extreme conditions are only known of the interior of planets and stars, and detonations of explosives. However, on a much smaller scale high

¹The atomic arrangement in a crystal is essential to understand the chemical and physical properties of a solid, which are dependent on its crystal structure.

pressure science leads to interesting effects and new properties of materials. Already in 1888 Henry Le Chatelier made an observation that if administrating a constraint on a chemical system in its equilibrium state by changing external conditions, as a consequence, the system will adjust by descending into a new equilibrium state, which will minimize the impact of the given constraint [28]. This is now known as Le Chatelier's principle or principle of least constraint. Applied to high pressure chemistry this means increasing pressure will induce a shift of the equilibrium state towards a negative change in volume.

The energy transferred through this pressure-induced volume contraction can easily range into the for chemical bonds typical regions/magnitudes leading to breaking and reforming of those bonds, hence changing the structure of condensed matter. This is usually accompanied by a change of electronic and magnetic properties. Therefore, materials chemistry under high pressure is a research field, crucial for the development of new materials or peculiar structures of renowned compounds.

Furthermore, it should be mentioned that the group 12 chalcogenides are not only interesting from a fundamental point of view, but from a practical one as well. Mercury oxide for instance is used as an anode material in mercury batteries as well as in the synthesis of high-temperature mercury based superconductors [29] to name but a few applications. Cinnabar-HgS is well-known as a red pigment (vermilion) and is involved in the production of mercury metal [30]. Mercury selenide on the other hand is formed as a product, when filtering mercury from exhaust gases using selenium and is used as an ohmic contact when connecting II-VI semiconductors, e.g. zinc oxide or zinc selenide. Last but not least, HgTe finds application in combination with other elements as doped semiconductors. Theoretical studies can always shed light on and give new impulses for the experimental development of those applications. It should be mentioned that the toxicity of most of the compounds often makes it hard to investigate them experimentally and therefore it is often difficult to find experimental data to compare with.

The objective of this study is to show that indeed the unusual structures of the mercury chalcogenides are a result of relativistic effects and to study their electronic structure in detail. Therefore, comparative relativistic and nonrelativistic density functional studies of equilibrium and high pressure phases of ZnX , CdX and HgX ($X=O, S, Se, Te$) are carried out to investigate these compounds.

1.2 Outline

The thesis at hand is structured as follows. Chapter 2 gives an introduction to the theoretical background that forms the basis of this study. This includes the approximations necessary to carry out the calculations and the formalism to obtain the actual solid-state properties.

This is followed by an overview of the group 12 chalcogenides in chapter 3. Here the crystal structures commonly occurring in the group 12 chalcogenides are described in detail. The computational parameters needed, as well as the preliminary calculations for their optimization for the subsequent simulations, are demonstrated.

The results for the group 12 oxides, sulfides, selenides and tellurides are presented and discussed in chapters 4, 5, 6 and 7, respectively. Each chapter is organized in the following manner: first a brief description of the crystal structures known to exist in the respective group 12 chalcogenide by experimental as well as theoretical means is given, followed by the presentation of the results obtained. The latter will be partitioned into a discussion of the equilibrium structures, the high pressure phases and electronic structure. The influence of relativistic effects on each of those matters will be emphasized. The short summary of the findings is given at the end of each chapter.

Finally, conclusions will be drawn in chapter 8.

Chapter 2

Theoretical background and numerical implementation

In the following chapter a short description of the theoretical quantum mechanical methods that form the basis of this thesis will be given. For further information on the applied methodology the reader is referred to standard quantum chemistry, e.g. refs. [31, 32], electronic structure theory (ref. [33]) and solid-state theory textbooks, e.g. refs. [34–36].

2.1 The many-electron problem

The thesis at hand is a computational study of several bulk systems consisting of an infinite yet periodic amount of atoms. In general, electronic systems ranging from just single atoms and molecules to small clusters consist of nuclei and electrons and therefore exhibit typical length scales of a few Ångströms. This means the theory by which to describe the interactions between those particles in a correct manner, even for the solid-state, is quantum mechanics. At this level, all mutual interactions like para- and ferromagnetic effects and transversal electromagnetic interactions including electron correlation, as well as relativistic corrections including spin-orbit-coupling have to be considered. As a fully relativistic treatment including electron correlation is not feasible for the solid state, even for the simplest atoms and crystals, approximations need to be made which are outlined in the following.

2.1.1 The Hamiltonian for the n -electron system

The basis for performing ab-initio calculations for those real systems is supplied by the non-relativistic time-independent Schrödinger equation

$$H|\Psi\rangle = E|\Psi\rangle. \quad (2.1)$$

This is a differential equation for the Hamilton operator H with the eigenvalue $E = \langle\Psi|H|\Psi\rangle$ describing the total energy of the system and the (normalized) eigenfunction Ψ is referred to as the n -particle wavefunction of the physical system. Here $|\Psi|^2$ characterizes the probability density. The full Hamiltonian is of the form

$$H = T_e + T_N + V_{eN} + V_{ee} + V_{NN}, \quad (2.2)$$

where the separate terms of the sum indicate the operator for the kinetic energy of the electrons T_e , the kinetic energy of the nuclei T_N , the term for the Coulomb attraction between electrons and nuclei V_{eN} , the terms for the repulsion between the electrons V_{ee} and the repulsion between the nuclei V_{NN} , respectively.

More precisely, for a system with N nuclei and n electrons this can be reformulated as

$$H = -\sum_{i=1}^n \frac{1}{2} \nabla_i^2 - \sum_{A=1}^N \frac{1}{2M_A} \nabla_A^2 - \sum_{i=1}^n \sum_{A=1}^N \frac{Z_A}{r_{iA}} + \sum_{i=1}^n \sum_{j>i}^n \frac{1}{r_{ij}} + \sum_{A=1}^N \sum_{B>A}^N \frac{Z_A Z_B}{r_{AB}} \quad (2.3)$$

using atomic units ($e = m_e = \hbar = 1$) for the following. Here M_A denotes the mass of nucleus A , Z_A the corresponding nuclear charge, and r the distance between two considered objects, e.g. $r_{iA} = |\mathbf{r}_{iA}| = |\mathbf{r}_i - \mathbf{R}_A|$. Lower case letters indicate electrons and capital letters the nuclei, respectively.

The starting point for all investigations in electronic structure theory is always to solve the above equation as accurately as possible. Indeed, an exact analytical solution is not feasible for problems other than one-electron systems. Therefore several approximations need to be exploited and numerous formalisms have been developed in theoretical chemistry and physics to simplify the problem, of which some will be introduced below.

2.1.2 The Born-Oppenheimer approximation

The first approximation required and, with very few exceptions, always applied in solid-state physics is the Born-Oppenheimer approximation [37, 38], which is based on the fact that the nuclei in a system are by orders of magnitude heavier than the electrons and as a consequence move considerably slower. Hence, we can assume that the electrons will reach their equilibrium state to any configuration of the nuclei in an instant. This means relatively speaking that the nuclei can be considered at rest (clamped nucleus approximation),

$$T_N = 0 \quad (2.4)$$

$$V_{N,N} = \text{constant}. \quad (2.5)$$

and the electrons move in an effective field of fixed nuclear point charges.

This adiabatic approach is crucial to electronic structure theory and allows for the separate treatment of the nuclei and electrons, meaning that in first order the wave function of the system can be factorized

$$\Psi(\mathbf{r}_i, \mathbf{R}_A) = \Psi_e(\mathbf{r}_i, \mathbf{R}_A)\Psi_N(\mathbf{R}_A), \quad (2.6)$$

where $\Psi_e(\mathbf{r}_i, \mathbf{R}_A)$ is only depending parametrically on the position of the nuclei. It leads to a decoupling of the Schrödinger equation through an expansion of the Hamiltonian in terms of $(\frac{m}{M})^{\frac{1}{4}}$.

This reduces the problem a priori to the motion of the electron, i.e. to solving the electronic Schrödinger equation

$$H_e|\Psi_e\rangle = E_e|\Psi_e\rangle \quad (2.7)$$

involving only the electronic Hamiltonian

$$H_e = T_e + V_{ee} + V_{Ne}. \quad (2.8)$$

Note again that the electronic wavefunction as well as the electronic energy only depend parametrically on the nuclear coordinates.

If we add the nuclear repulsion as an effective potential, we get the total energy

of the electronic problem for fixed nuclei

$$E_{tot} = E_e + \sum_{A=1}^N \sum_{B>A}^N \frac{Z_A Z_B}{r_{AB}}. \quad (2.9)$$

Solving those equations and averaging over the electronic wavefunction and coordinates (due to their fast motion compared to the nuclei) then determines the Hamiltonian for the motion of the nucleus

$$H_n = - \sum_{A=1}^N \frac{1}{2M_A} \nabla_A^2 + \left\langle - \sum_{i=1}^n \frac{1}{2} \nabla_i^2 - \sum_{i=1}^n \sum_{A=1}^N \frac{Z_A}{r_{iA}} + \sum_{i=1}^n \sum_{j>i}^n \frac{1}{r_{ij}} \right\rangle + \sum_{A=1}^N \sum_{B>A}^N \frac{Z_A Z_B}{r_{AB}} \quad (2.10)$$

$$= - \sum_{A=1}^N \frac{1}{2M_A} \nabla_A^2 + E_{tot}(\{\mathbf{R}_A\}) \quad (2.11)$$

where $E_{tot}(\{\mathbf{R}_A\})$ generates the Born-Oppenheimer potential energy surface according to the ground-state energy of the electronic system for the nuclei being fixed in the configuration $\{\mathbf{R}_A\}$. The brackets indicate the averaging.

Solving the nuclear Schrödinger equation

$$H_N |\Psi_N\rangle = E |\Psi_N\rangle \quad (2.12)$$

gives the full wavefunction $\Psi_N = \Psi_N(\{\mathbf{R}_A\})$ and energy (including electronic, vibrational, rotational and translational) leading to the Born-Oppenheimer approximation of the total wavefunction

$$\Psi(\{\mathbf{r}_i\}, \{\mathbf{R}_A\}) = \Psi_e(\{\mathbf{r}_i\}, \{\mathbf{R}_A\}) \Psi_N \{\mathbf{R}_A\} \quad (2.13)$$

as already stated in the factorization earlier on.

Furthermore Ψ will also depend on the spin of the electron, which is not written down explicitly here.

Note that, whereas the nuclei can be treated with a classical approach as well, solving the electronic equations is a many body problem. Since the electrons interact with each other, no decoupling is possible and further approximations are needed, some of which will be elaborated in the following.

2.2 Approximations to solve the electronic problem

In order to solve the electronic Schrödinger equation (2.7) the Hamiltonian H_e can be further separated into one- and two-particle components h_i and $g_{i,j}$

$$H_e = \sum_{i=1}^n h_i + \sum_{i=1}^n \sum_{i<j}^n g_{i,j}. \quad (2.14)$$

Here the one-particle term is simply the sum of the kinetic energy of an electron and its potential energy in the field of the nuclei

$$h_i = -\frac{1}{2}\nabla_i^2 - \sum_{A=1}^N \frac{Z_A}{r_{iA}} \quad (2.15)$$

and the two-particle term is given by

$$g_{i,j} = \frac{1}{r_{ij}}, \quad (2.16)$$

which is equivalent to the potential energy of two moving electrons.

In order to solve the problem another approximation is needed which concerns the chosen wavefunction. A successful approach is to express Ψ from a function using a set of single electron wavefunctions Φ_i (see also chapter 2.4.1), called orbitals

$$\bar{\Psi} = \sum_{l=1}^n a_l f_l(\Phi_1 \dots \Phi_n). \quad (2.17)$$

Those approximate wavefunctions can then be trialed employing the Rayleigh-Ritz variational principle, which optimizes the energy of the system giving an upper limit by

$$\bar{E} = \frac{\langle \bar{\Psi} | H | \bar{\Psi} \rangle}{\langle \bar{\Psi} | \bar{\Psi} \rangle} \geq \frac{\langle \Psi | H | \Psi \rangle}{\langle \Psi | \Psi \rangle} = E \quad (2.18)$$

to find the one closest resembling the exact wavefunction.

2.2.1 The Hartree-Fock approximation

The Hartree-Fock method is the simplest approach to solve the many body electron problem. The fundamental concept is to describe the Coulomb interaction between the electrons by an adequate effective potential leaving behind a system of non-interacting particles (mean-field approach).

This means that the wave function Ψ can be embodied by a set of single electron orbitals Φ_i , more precisely the antisymmetric sum of a product of wavefunctions

$$\Psi = \frac{1}{\sqrt{n!}} \begin{vmatrix} \Phi_1(\mathbf{r}_1, \sigma_1) & \Phi_2(\mathbf{r}_1, \sigma_1) & \dots & \Phi_n(\mathbf{r}_1, \sigma_1) \\ \Phi_1(\mathbf{r}_2, \sigma_2) & \Phi_2(\mathbf{r}_2, \sigma_2) & \dots & \Phi_n(\mathbf{r}_2, \sigma_2) \\ \dots & \dots & \dots & \dots \\ \Phi_1(\mathbf{r}_n, \sigma_n) & \Phi_2(\mathbf{r}_n, \sigma_n) & \dots & \Phi_n(\mathbf{r}_n, \sigma_n) \end{vmatrix}. \quad (2.19)$$

This configuration was introduced by Fock and Slater [39, 40] and is known as the Slater determinant and already accounts for Pauli's exclusion principle, where σ_i represents the spin coordinate. However, it does not specify which electron occupies which orbital, as electrons are indistinguishable. In fact, the Pauli principle follows directly from Fermi-Dirac statistics.

Applying the Rayleigh-Ritz variational principle to this trial function generates the so-called Hartree-Fock equations

$$f_i |\Phi_i\rangle = \varepsilon_i |\Phi_i\rangle, \quad (2.20)$$

This is an eigenvalue equation for the Fock-Operator

$$f_i = h_i + \sum_{j=1}^n (J_j - K_j), \quad (2.21)$$

where the eigenfunctions are given by the orbitals $|\Phi_i\rangle$ and the eigenvalues by the orbital energies ε_i . The operator h_i is characterized by (2.15). The sum describes the electron-electron interaction at which J_j is the Coulomb repulsion operator (Hartree term) between two individual electrons and K_j is the exchange operator (Fock term), which is necessary to describe the effect of interchanging the coordinates of two respective electrons (antisymmetry):

$$J_j|\Phi_i(2)\rangle = \langle\Phi_j(1)|r_{12}^{-1}|\Phi_j(1)\rangle|\Phi_i(2)\rangle \quad (2.22)$$

$$K_j|\Phi_i(2)\rangle = \langle\Phi_j(1)|r_{12}^{-1}|\Phi_i(1)\rangle|\Phi_j(2)\rangle. \quad (2.23)$$

Note that the orbitals Φ_i , with respect to which the energy is optimized in order to obtain the Hartree-Fock wavefunction of the system, are in turn depending on the Fock operator of the system. Since f_i again is correlated to the orbitals, solving the Hartree-Fock equations demands for an iterative procedure. Therefore, this approach introduced here is a self-consistent field (SCF) method.

Finally, the total energy of the electronic system is characterized by

$$E = \sum_{i=1}^n \langle\Phi_i|f_i|\Phi_i\rangle - \frac{1}{2} \sum_{i,j=1}^n \langle\Phi_i|J_j - K_j|\Phi_i\rangle \quad (2.24)$$

$$= \sum_{i=1}^n \varepsilon_i - \frac{1}{2} \sum_{i,j=1}^n (\langle\Phi_i|J_j|\Phi_i\rangle - \langle\Phi_i|K_j|\Phi_i\rangle). \quad (2.25)$$

2.2.2 Electron correlation

Within the Hartree-Fock approach electrons are regarded as independent particles (as far as the Pauli exclusion principle allows for), expressed in the description of the electronic wavefunction with a single Slater determinant (2.19). By means of this theory the electronic repulsion is only accounted for (in terms of the exchange term) between electrons of the same spin, preventing them from co-existing at the exact same point in space. However, this neglects the Coulomb correlation between electrons of different spin, meaning that more than a single determinant would be necessary to treat the system accurately.

This increases the repulsive interaction between electrons creating a so-called exchange-correlation hole around an arbitrary electron at any position in space and leads to an intrinsic total electronic energy difference between the so-called Hartree-Fock limit and the exact solution of the electronic problem. This is reflected in the so-called pair distribution function $g(\mathbf{r}, \mathbf{r}')$, which indicates the probability of an electron to be found at the position \mathbf{r}' in space, if another one is assumed to occupy position \mathbf{r} . For a homogeneous electron gas $g(\mathbf{r}, \mathbf{r}') = g(|\mathbf{r} - \mathbf{r}'|)$, which is illustrated in fig. 2.1 for several numerical approaches. Despite

yielding similar results for large inter-electron distances, the Hartree approximation does not account for the exchange operator K_j leading to $g(\mathbf{r}, \mathbf{r}') = 1$. Hartree-Fock however, improves this result, since it already prevents electrons of the same spin from occupying the same region in space in terms of the Pauli principle ($g(\mathbf{r}, \mathbf{r}') = 0.5$ for $\mathbf{r} = \mathbf{r}'$). Ideally, however, correlation needs to be accounted for as well, creating a more localized and deeper 'exchange-correlation hole'.

Generally speaking this energy loss relative to the Hartree-Fock results is referred to as the correlation energy

$$E_{corr} = E_{exact} - E_{HF} \quad (2.26)$$

according to P. O. Löwdin [41]. Yet, one has to be careful how to use the term, as exchange is a part of electron correlation already and arguably already considered in the Hartree-Fock energy of an electronic system.

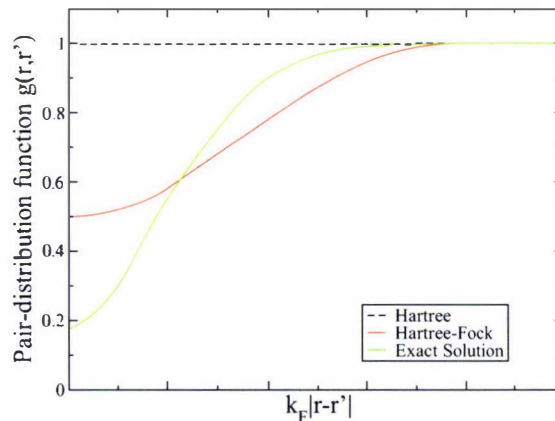


Figure 2.1: Sketch of the pair distribution function $g(\mathbf{r}, \mathbf{r}') = g(|\mathbf{r} - \mathbf{r}'|)$ for the homogeneous electron gas. The variable $k_F|\mathbf{r} - \mathbf{r}'|$ is given in arbitrary units, k_F being the Fermi wave vector.

Induced by this inconsistency numerous wavefunction-based advanced methods have been developed, treating electron correlation on top of Hartree-Fock. Some of those are many-body perturbation theory (MBPT) [42], configuration interaction (CI) [43, 44], multi-reference (MR) methods and coupled-cluster (CC) theory [45, 46]. However, they shall not be discussed here as in the solid-state studies carried out for this thesis solely density-functional theory was used. It is only mentioned that Hartree-Fock theory, as well as the many advancements based upon, have proven very valuable in theoretical quantum chemistry, but are

mainly used in atomic and molecular electronic structure calculations, although more recently a localized version of second-order MBPT has been developed for solids with large band-gaps (local MP2 approach) [47].

2.2.3 Density functional theory

Most wavefunction-based theories have one major drawback. For their application in solid-state physics, even if enhanced to include systems with periodic boundary conditions, they turn out to be less feasible. This is primarily to be blamed on the non-local character of the exchange operator K_j (2.23), making calculations for periodic systems rather inefficient and therefore computer-time expensive. Nevertheless, one program system called CRYSTAL has been developed which is based on the Hartree-Fock model using Gaussian type orbitals (e.g. [48], [49]). A more cost-effective alternative method is density functional theory (DFT), which approaches the problem from a completely different direction using a functional of the one-particle density to describe the properties of a system. DFT has two main advantages. First of all, the electron density is an actual observable and secondly, it is only depending on three coordinates independent of the size of the n -electron system, thus reducing the complexity of the problem dramatically.

The Hohenberg-Kohn theorem and the Kohn-Sham equations

That this concept is indeed valid, was proven by the so-called Hohenberg-Kohn theorem [50]. Here Hohenberg and Kohn state that the ground state of an electronic system is completely and uniquely defined as a functional of the electron density of the ground state.

This is indeed plausible as the relation for the particle density of the ground state of the n -electron system

$$n(\mathbf{r}) = n \int d^3r_2 \int d^3r_3 \dots \int d^3r_n \Psi^*(\mathbf{r}, \mathbf{r}_2, \dots, \mathbf{r}_n) \Psi(\mathbf{r}, \mathbf{r}_2, \dots, \mathbf{r}_n) \quad (2.27)$$

can be reversed to determine the wavefunction as a functional of the electron density, more precisely the ground-state wavefunction is then given by

$$\Psi_0 = \Psi[n_0] \quad (2.28)$$

Hence, the ground-state expectation value of an observable is a functional of the density, too. In particular, it is

$$E_0 = E[n_0] = \langle \Psi_0 | T_e + V_{ee} + V_{eN} | \Psi_0 \rangle \quad (2.29)$$

$$= T_e[n_0] + V_{ee}[n_0] + \int d^3r V_{eN}(\mathbf{r}) n_0(\mathbf{r}) \quad (2.30)$$

the ground-state energy of the system. $T_e[n_0]$ and $V_{ee}[n_0]$ are called universal functionals, since they do not depend on the external potential defining the problem.

Minimizing this functional of the energy by applying the variational principle with respect to $n(\mathbf{r})$ will yield the ground-state density n_0 and therefore all further ground-state properties. This can be done using the method introduced by Kohn and Sham [51], where a fictitious system of non-interacting electrons, having the same ground-state particle density as the real system of interacting electrons, is introduced. The universal functionals $T_e[n_0]$ and $V_{ee}[n_0]$ of the interacting system can then be expressed as the sum of the kinetic energy of the "non-interacting system" and additional terms accounting for inter-particle contributions. Using Kohn-Sham orbitals as an ansatz for the one-particle density, the density and ground-state energy of the interacting system are then given by

$$n(\mathbf{r}) = \sum_{i=1}^n |\langle \mathbf{r} | \Phi_i \rangle|^2 \quad (2.31)$$

$$E = -\frac{1}{2} \sum_{i=1}^n \langle \Phi_i | \nabla^2 | \Phi_i \rangle + E_H[n] + E_{xc}[n] + \sum_{i=1}^n \langle \Phi_i | V_{eN} | \Phi_i \rangle. \quad (2.32)$$

Hence, with the help of the variational principle under the constraint of the conservation of the total particle number the so-called Kohn-Sham equations

$$H_{KS} |\Phi_i\rangle = \left(-\frac{1}{2} \nabla^2 + V_H[n] + V_{xc}[n] + V_{eN} \right) |\Phi_i\rangle = \varepsilon_i |\Phi_i\rangle \quad (2.33)$$

are obtained, where the Coulomb inter-electron interaction in terms of their density is described by the Hartree term V_H and the so-called exchange-correlation functional V_{xc} summarizes all electron-electron interaction that is not accounted

for yet¹,

$$V_H(\mathbf{r}) = \frac{\delta E_H}{\delta n(\mathbf{r})} = \int d^3\mathbf{r}' n(\mathbf{r}') |\mathbf{r} - \mathbf{r}'|^{-1} \quad (2.34)$$

$$V_{xc}(\mathbf{r}) = \frac{\delta E_{xc}}{\delta n(\mathbf{r})}. \quad (2.35)$$

This is again an eigenvalue equation for the Kohn-Sham operator H_{KS} , which can be regarded as an effective Hamiltonian for the non-interacting system with the effective Kohn-Sham potential $V_{KS} = V_{xc} + V_{eV}$ including interparticle interactions of the real system. Equation (2.33) has to be solved iteratively in a self-consistency loop, since the obtained Kohn-Sham orbitals $|\Phi_i\rangle$ in turn determine the operator H_{KS} . Finally the total energy of the system is determined as

$$E = \sum_{i=1}^n \varepsilon_i - E_H[n] + E_{xc}[n] - \int d^3\mathbf{r} V_{xc}(\mathbf{r}) n(\mathbf{r}). \quad (2.36)$$

It is worth mentioning that the obtained orbitals have no physical meaning due to the fact that they are actually electronic orbitals of the non-interacting system and therefore merely the eigenstates of the used density matrix.

The major advantage of density functional theory is that solving those equations gives in principle the exact ground-state energy. Be that as it may, unfortunately the exchange-correlation functional E_{xc} is unknown, which means sensible approximations have to be introduced to describe the interaction of the electrons, some of which will be presented in the following section. The types of functionals available are generally categorized into local (LDA), semilocal or gradient dependent (GGA), nonlocal (hybrids) and integral-dependent (ADA) functionals.

Functionals for the approximation of exchange-correlation energy

A very widely used approximation for the exchange correlation energy is the local density approximation (LDA). Here the density of an ensemble of electrons

¹This obviously includes all deviations between the fictitious non-interacting and the interacting ensemble, e.g. corrections for the Coulomb and kinetic terms as well.

in a system is locally compensated for with a density of the free homogeneous electron gas. This is the most obvious approach and rather convenient, since the exchange-correlation functional for the free electron gas is numerically known exactly.

This means E_{xc} depends on the density only at the coordinate where the functional is evaluated, assuming that the density is a slowly varying function,

$$E_{xc}^{LDA}[n] = \int d^3\mathbf{r} n(\mathbf{r}) \epsilon_{xc}^{hom}(n)|_{n(\mathbf{r})} \quad (2.37)$$

with the according exchange correlation potential

$$V_{xc}^{LDA}[n](\mathbf{r}) = \epsilon_{xc}^{hom}(n)|_{n(\mathbf{r})} + n(\mathbf{r}) \frac{\delta}{\delta n} \epsilon_{xc}^{hom}(n)|_{n(\mathbf{r})}. \quad (2.38)$$

Here $\epsilon_{xc}^{hom}(n)$ is the exchange-correlation energy density of the homogeneous electron gas, which consists of an exchange part $\epsilon_x^{hom}(n)$ and a correlation part $\epsilon_c^{hom}(n)$. The exchange part of the density can be easily derived analytically [52] and is given by

$$\epsilon_x^{hom}(n) = -\frac{3}{4} \left(\frac{3}{\pi} \right)^{1/3} n^{1/3} \quad (2.39)$$

leading to the exchange energy as obtained within LDA²

$$E_x^{LDA}[n] = -\frac{3}{4} \left(\frac{3}{\pi} \right)^{1/3} \int d^3\mathbf{r} n(\mathbf{r})^{4/3}. \quad (2.40)$$

The above equation assumes a closed shell problem, meaning the number of spin up and down electrons is equal. Where this is not the case, a straightforward generalization of LDA is possible, the local spin-density approximation (LSDA), to include spin-polarization as well.

More effort has to be made, however, to derive the correlation energy density of the uniform electron gas. In that case rather complex many body techniques have to be employed [53] or its calculation is limited to specific densities carrying

²Combining the term for the exchange energy obtained using this model with the expressions for T_e and V_{ee} in the renowned Thomas-Fermi model leads to the so-called Thomas-Fermi-Dirac approximation of the total energy of the system. Multiplication with an adjustable parameter α on the other hand is known as the so-called $X\alpha$ approximation. However, these approximations are rarely applied nowadays.

out quantum Monte-Carlo simulations [54]. Further work was done by Vosko, Wilk and Nusair [55] as well as Perdew and Zunger [56] again using quantum Monte Carlo methods for different densities n , hence obtaining a suitable fit for $\epsilon_c^{hom}(n)$.

In general, LDA has proven to be a very useful tool in quantum chemistry and solid-state physics, even though it uses a rather simple approach. Surprisingly so, this is not only true for systems with a slowly varying density (such as metals and intrinsic semiconductors), which can be partially explained by systematic³ error cancellation due to the combination of generally underestimated correlation energies and overestimated exchange energies. For nonhomogeneous bulk systems (e.g. transition metals) and even for molecules one obtains very good results for structure, total energy and bulk moduli or force constants, with deviations of only few percents, especially for the ground state. However, this approximation tends to underestimate bond lengths (in particular in molecules with a clearly strong varying particle density), leading consequently to an overestimation of dissociation energies of often more than 10%. However, the major shortcoming of LDA is the severe underestimation of the band gap in semiconductors and insulators of up to 100%.

To improve the performance of LDA, the self-evident measure is to not only rely on the local density but further take into account the gradient of the spatially varying density at the point of evaluation. The so-called 'gradient-expansion approximation' aims at a systematic calculation of those gradient-corrections, an example being the Weizsäcker term for the description of $T_e[n]$. However, low-order corrections usually lead to worse results than LDA, whereas higher-order corrections are extremely difficult to calculate.

Later it was discovered that this systematic expansion is not necessary and a semi-empirical approach known as the so-called generalized gradient approximations (GGA) gives a far better value for the exchange-correlation energy, expressed as

$$E_{xc}^{GGA}[n] = \int d^3\mathbf{r} n(\mathbf{r}) \epsilon_{xc}(n, \nabla n)|_{n(\mathbf{r})}. \quad (2.41)$$

The most commonly used GGA functionals nowadays are the ones developed by Perdew and Wang (PW91) [57, 58] and Perdew, Burke and Ernzerhof (PBE) [59].

³Systematic, since LDA satisfies the sum rule for the charge of the exchange correlation hole to equal -1.

Especially in quantum chemistry BLYP is very popular as well, combining Becke's exchange functional [60] with the correlation functional of Lee, Yang and Parr [61].

With this approach generally speaking structural properties are calculated with improved accuracy and even bonding energies are significantly improved. This is even true for most cases where LDA fails, e.g. some transition metals and other inhomogeneous systems.⁴ However, it cannot account for interactions like van der Waals forces and other many-body effects and still the band gaps are severely underestimated. In addition, DFT has one major drawback. No systematic improvement of the theory is currently possible in order to obtain better results, as it is the case for wavefunction-based methods.

Further improvements therefore include the incorporation of exact exchange (hybrid-functionals) and corrections for dispersive type of interactions (long-range corrected functionals). For further reading on density functional theory the reader is referred to [62].

However, DFT GGA, as chosen for this thesis, is a good compromise between a realistic treatment and keeping the computational cost low. Explicitly, the parametrization according to Perdew and Wang (PW91) [57, 58] is used in this study, where the exchange and correlation contributions to the energy for equal numbers of spin up and down electrons are given by

$$E_x^{PW91}[n] = - \int d\mathbf{r} n(\mathbf{r}) \frac{3k_F}{4\pi} \frac{1 + 0.1965s \sinh^{-1}(7.796s) + (0.274 - 0.151e^{-100s^2})s^2}{1 + 0.1964s \sinh^{-1}(7.796s) + 0.004s^4} \quad (2.42)$$

$$E_c^{PW91}[n] = \int d\mathbf{r} n(\mathbf{r}) (\epsilon_c(\mathbf{r}_s) + H(t, \mathbf{r}_s)). \quad (2.43)$$

Here k_F is the local Fermi vector, s the scaled density gradient and k_s the local screening wave vector as defined by

$$k_F = (3\pi^2 n)^{1/3} = 1.9196/r_s \quad (2.44)$$

$$s = |\nabla n|/2k_F n \quad (2.45)$$

$$t = |\nabla n|/2k_s n \quad (2.46)$$

$$k_s = (4k_F/\pi)^{1/2}, \quad (2.47)$$

⁴GGA correctly predicts the ferromagnetic ground state of bulk iron.

For a generalization to an open-shell problem and a definition of the function H the reader is referred to ref. [58].

2.2.4 Relativistic effects in quantum chemistry

In general, the term relativistic effect in quantum chemistry accounts for all deviations of results obtained using methods either considering relativity or not. This is mainly for historical reasons, since the theory of relativity, although developed already in 1905 by Einstein, was not regarded to have a substantial influence in quantum chemistry. In 1929 Dirac commented on the topic:

"The general theory of quantum mechanics is now almost complete, the imperfection that still remains being in connection with the exact fitting in the theory with relativity ideas. These give rise to difficulties only when high-speed particles are involved, and are therefore of no importance in the consideration of atomic and molecular structure and ordinary chemical reactions, in which it is, indeed, usually sufficiently accurate if one neglects relativity variation of mass with velocity and assumes only Coulomb forces between the various electrons and atomic nuclei. The underlying physical laws necessary for the mathematical theory of a large part of physics and the whole of chemistry are thus completely known, and the difficulty is only that the exact application of these laws leads to equations much too complicated to be solvable. Therefore, it becomes desirable that approximate practical methods of applying quantum mechanics should be developed, which can lead to an explanation of the main features of complex atomic systems without too much computation." [63]

However, Dirac (unknowingly at that time) was incorrect with this statement, since especially close to the nucleus core electrons travel at a significant speed compared to the velocity of light. For the inner 1s-orbital of heavy elements velocities of $0.5c$ and more can be reached [64]. Therefore, for the heavier atoms with large nuclear charge a relativistic treatment is required, especially for s-electrons which have considerable density close to the nucleus. Moreover, relativistic effects are important for higher angular momentum electrons as well despite the fact that the density goes to zero close to the nucleus. It was not until the seventies that attention was paid to relativistic effects in electronic structure theory [16]. Even worse, in the solid-state community relativistic effects were basically ignored for a long time with the exception of spin-orbit effects in band structure calculations. However, Christiansen and Seraphin showed in 1976 that

relativistic effects change the band structure in solid gold [65] considerably and Takeuchi *et al.* showed in 1989 that the lattice constant, cohesive energy, and bulk modulus for fcc gold is greatly influenced by relativistic effects [66].

Basically, relativistic effects originate from the fact that light can only travel at a finite speed c . For objects, moving with a velocity close to this, corrections have to be made to physical variables such as mass, time and length being the most prominent. On this note, a qualitative estimate of the impact of relativity in quantum chemistry can be made, when including the relativistic mass increase

$$m = \frac{m_0}{\sqrt{1 - v_e^2/c^2}} \quad (2.48)$$

on the effective Bohr radius

$$a_0 = \frac{\hbar}{m\alpha} \quad (2.49)$$

Here m_0 describes the electron mass at rest and v_e the electron velocity. Furthermore, \hbar and α denote the reduced Planck's constant and the fine structure constant, respectively. Hence, if considering the velocity of an electron in atomic units $v_e = Z/n$, a ratio of

$$\frac{a}{a_0} = \sqrt{1 - v_e^2/c^2} = \sqrt{1 - (Z/nc)^2} \quad (2.50)$$

is obtained for the relativistic and non-relativistic Bohr radius (see fig. 2.2), where n is the principal quantum number. Therefore, it is obvious that this effect, being most pronounced for electrons with a low quantum number and a nucleus with a high charge, would lead to a contraction of all orbitals. Quantifying this effect for e.g. mercury with a nuclear charge of $Z = 80$, means that the radius for an 1s-electron would be 0.81 times its nonrelativistic value and therefore decreased by 19%. The speed of light in atomic units amounts to $c = \alpha^{-1} = 137$.

From this rather simple approach it is already apparent that relativistic perturbation operators will affect primarily the region close to the nucleus, which exhibits a major part of the valence s electron density. Hence, major energy contributions stem from the K-shell region in stark contrast to the nonrelativistic case, where the valence shell region is responsible for 90% of the total orbital energy [64].

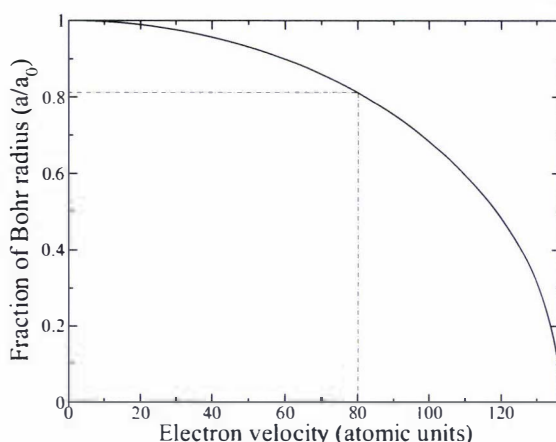


Figure 2.2: Ratio of relativistic and non-relativistic Bohr radius as a function of the electron velocity. The dash-dotted line indicates the position of mercury.

One could now argue that this at least has little effect on the d - and f -electrons. However, it turns out that the contraction of the s -electrons due to the above discussed *direct relativistic effect* leads in turn to a more efficient shielding of the core, resulting in a reduced effective nuclear charge Z_{eff} (*relativistic shielding*). This on the other hand induces an expansion and energetic destabilization of all orbitals as an *indirect relativistic effect* [67]. Hence, whereas direct relativistic effects are predominant for s -orbitals and almost cancel out the indirect effects for p -electrons, these indirect effects are of utmost importance for electrons with higher angular momentum. In addition, the destabilization and expansion of the d and f -orbitals again triggers an *indirect stabilization* for all other orbitals due to a relativistic deshielding going along with an increased effective charge of the nucleus. This however brief summary shows the sophisticated yet very subtle interplay caused by direct and indirect relativistic influences on the orbitals of heavy atoms.

Equation (2.50) explains why this subtle interplay was first discovered for the heavier elements of the periodic table. Most certainly this is not the only achievement of relativistic quantum chemistry. Prime examples are the explanation of the inert pair effect, the liquid state of mercury at room temperature and the unusual reflectivity of gold explaining its golden colour [16].

Especially in gold and mercury relativistic effects are exceptionally strong, known as the relativistic maximum. This can partly be explained with the filled d -shells, causing the increased indirect stabilization to overcompensate for the indirect destabilization, which results in a significantly larger stabilization and contrac-

tion than for other elements. From group 13 onwards with the filling of the next p -orbitals this indirect stabilization starts to decrease again. For further reading on relativistic effects see refs. [16, 17, 64, 68].

For a comprehensive treatment of relativity in quantum chemistry the one-particle Hamiltonian (2.15) has to be substituted by the Dirac operator

$$h_i^D = -i c \boldsymbol{\alpha} \nabla_i + m \beta c^2 + V_{nucl}(r_{iA}), \quad (2.51)$$

where $V_{nucl}(r_{iA})$ describes the electrostatic potential between the nucleus and the i th electron. The components of the vector $\boldsymbol{\alpha} = (\alpha_x, \alpha_y, \alpha_z)$ and β are 4×4 matrices

$$\beta = \begin{pmatrix} I_2 & 0_2 \\ 0_2 & -I_2 \end{pmatrix}, \alpha_x = \begin{pmatrix} 0_2 & \sigma_x \\ \sigma_x & 0_2 \end{pmatrix}, \alpha_y = \begin{pmatrix} 0_2 & \sigma_y \\ \sigma_y & 0_2 \end{pmatrix}, \alpha_z = \begin{pmatrix} 0_2 & \sigma_z \\ \sigma_z & 0_2 \end{pmatrix}, \quad (2.52)$$

referred to as the Dirac matrices. I_2 stands for the 2×2 unit matrix and the matrices σ_x , σ_y and σ_z are known as the 2×2 Pauli spin matrices

$$\sigma_x = \begin{pmatrix} 0 & 1 \\ 1 & 0 \end{pmatrix}, \sigma_y = \begin{pmatrix} 0 & -i \\ i & 0 \end{pmatrix}, \sigma_z = \begin{pmatrix} 1 & 0 \\ 0 & -1 \end{pmatrix}. \quad (2.53)$$

Similar to the one-particle term, the two-particle term (2.16) can be extended by a relativistic correction leading to the Coulomb-Breit operator

$$g_{i,j}^{CB} = \frac{1}{r_{ij}} - \frac{1}{2r_{ij}} \left(\boldsymbol{\alpha}_i \boldsymbol{\alpha}_j + \frac{(\boldsymbol{\alpha}_i \mathbf{r}_{ij})(\boldsymbol{\alpha}_j \mathbf{r}_{ij})}{r_{ij}^2} \right), \quad (2.54)$$

although this only includes corrections of $\sim c^{-1}$ up to second order. Terms of higher order can be derived using quantum electrodynamical considerations.

Ultimately, the Dirac equation can be written as

$$\begin{pmatrix} mc^2 + V_{nucl}(r_{iA}) & -i c \boldsymbol{\alpha} \nabla_i \\ -i c \boldsymbol{\alpha} \nabla_i & -mc^2 + V_{nucl}(r_{iA}) \end{pmatrix} \begin{pmatrix} \Psi_L \\ \Psi_S \end{pmatrix} = E \begin{pmatrix} \Psi_L \\ \Psi_S \end{pmatrix}. \quad (2.55)$$

This is a system of four differential equations being split into two systems of equations. In this case the wavefunction consists of four components, which can be

separated into a so-called small Ψ_S and large Ψ_L component. In general, positive as well as negative energies are allowed, giving rise to 'positronic' solutions.

Analogously to the nonrelativistic case the so-called Dirac-Hartree equations can be set up, where operators and wavefunctions need to be four component spinors.

Exploiting this formalism is rather sophisticated. However, by applying various sophisticated approximations to those four component equations, it is possible to create a so-called pseudopotential, which already accounts for all those relativistic effects and simplifying further calculations drastically. The concept of the relativistic pseudopotential is introduced and explained in chapter 2.4.2.

2.3 Periodic systems

In fact, every physical or chemical system inherits a certain symmetry that if not determines at least crucially influences their properties. This is especially true for the systems treated in this thesis, i.e. solids or more specifically crystals, which due to their periodicity by definition possess a certain symmetry. Hence, in the following chapter a brief summary of the basics and definitions of periodic systems and their symmetries in the context of crystallography will be given. The mathematical background to describe and quantify symmetries is provided by the theory of finite groups, by systematically classifying periodic systems according to the irreducible representation of their point and space groups.

2.3.1 Crystal symmetries and Bravais lattices

Ideal crystals are solids which are defined by a periodic arrangement of the atoms or molecules they consist of. This means they inherit a long-range order, where the positions of the component atoms are pinpointed by an underlying infinite array of discrete points, called Bravais lattice⁵. This lattice spans over the whole crystal and is identical from whichever point in the array it is viewed. Hence, it could be defined as a set of translations defined through all vectors

$$\mathbf{R} = n_1\mathbf{a}_1 + n_2\mathbf{a}_2 + n_3\mathbf{a}_3, \quad (2.56)$$

where the \mathbf{a}_i are linearly independent and n_i is an integer. Although those so-

⁵Named after the French physicist Auguste Bravais (1811-1863), who listed all possible Bravais lattices for the first time correctly.

called primitive vectors \mathbf{a}_i are not unique, they generate the whole lattice as indicated by fig. 2.3.1, meaning one can reach each point $\sum n_i \mathbf{a}_i$ in the lattice by translating a length a_i in steps of n_i .

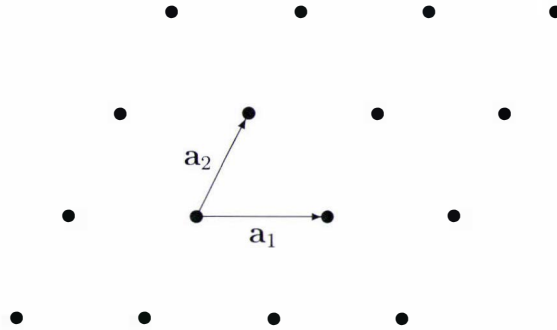


Figure 2.3: The primitive vectors of a unit cell in two dimensions.

The parallelepiped of the volume $\Omega_0 = (\mathbf{a}_1 \times \mathbf{a}_2) \cdot \mathbf{a}_3$ spanned by the lattice vectors \mathbf{a}_i is called unit cell of the crystal. In the special case where this volume of space, when translated through all vectors, fills the whole Bravais lattice space without any overlapping or leaving gaps the term primitive unit cell is used. This special unit cell contains exactly one lattice point (smallest volume), but again, like for the primitive vectors this choice is not unique. Therefore, usually a special primitive cell, the so-called Wigner-Seitz cell is used, which displays the full symmetry of the Bravais lattice. It is confined by the median lines between a lattice point and all its neighbours, meaning that no lattice point in this region of space is closer to the lattice point contained in this unit cell than to any other lattice point. The absolute values of the \mathbf{a}_i including the angles between them are characteristic for each crystal and known as lattice parameters.

As mentioned earlier the Bravais lattice is only the underlying structure of a crystal. It describes purely the translational symmetry of the crystal. In order to describe a real crystal structure a physical unit of atoms, like a motif, needs to be centred at each point of the Bravais lattice within a particular unit cell. By doing this a point lattice is created as the set of all points in space where the atomic basis atoms are placed. The position of the atoms within the basis are then specified by placing the centre of reference, meaning a lattice point in the centre of one particular basis atom, giving the coordinates of the other atoms as fractions of the lattice constants.

Using this definition of a crystal a whole range of different crystal structure is

possible. The purpose of crystallography is to achieve a full classification of all possible structures by identifying their inherent symmetry. This means all operations that leave the properties of the crystal unchanged. Looking just at the Bravais lattices they can be characterized by a set of rigid operations under which the lattice remains the same, known as the space or symmetry group. Possible symmetry operations are translation through the lattice vectors, inversion at the origin⁶, rotation around symmetry axes and reflection in a plane.

All of those operations can be separated into a pure translation and one that leaves at least one point of the lattice unchanged, a so-called point group, which is a subset of the full symmetry group (without translation). Just considering those point groups the Bravais lattices can be categorized into seven different crystal systems with specific ratios of their lattice vectors and different angles α , β and γ between those vectors. Those are with increasing symmetry the triclinic, monoclinic, orthorhombic, hexagonal, rhombohedral or trigonal, tetragonal and cubic system.

Of course there are not only primitive lattices, but also nonprimitive ones with more than one atom per unit cell, which adds up to a total of 14 different Bravais lattices. Most of the time it is possible to describe the non-primitive lattices using a primitive cell, which might in turn not have the full symmetry of the Bravais lattice anymore.

Applying the same considerations to the crystal structure, the complete crystal system will not have the maximum symmetry of the Bravais lattice anymore, since the basis is not required to be symmetric. Therefore, one obtains 32 crystallographic point groups (crystal class) analogous to the 7 crystal systems of the Bravais lattice, which are summarized in table 2.1.

The corresponding point groups in Schönflies notation are characterized by rotational operations and symmetry planes and defined as follows. C_n describes an n -fold rotation axis and S_{2n} the mirror-rotation, where n is the order of rotation. Both of them directly name the according point group. In the special case, where no symmetry axis or planes can be found at all, leaving only a centre of inversion, the class is denoted C_i . Furthermore, a point group which possesses n two-fold axes perpendicular to the principal C_n axis is called D_n . However, in addition to a rotation axis, a group might contain mirror (reflection) planes σ , which can either be vertical (σ_v) or horizontal (σ_h) to the rotation axis or none of the two

⁶Inversion replaces all points with their coordinates \mathbf{r} by their inverse $-\mathbf{r}$ with respect to the origin.

Crystal system	Unit cell	Class	Point group	
			HM	SF
Triclinic	$a \neq b \neq c$	1	1	C_1
	$\alpha \neq \beta \neq \gamma$	2	-1	$S_2(C_i)$
Monoclinic	$a \neq b \neq c$	3	m	$C_s(C_{1h})$
	$\alpha = \gamma = 90^\circ \neq \beta$	4	2	C_2
		5	$2/m$	C_{2h}
Orthorhombic	$a \neq b \neq c$	6	mm	C_{2v}
	$\alpha = \beta = \gamma = 90^\circ$	7	222	D_2
		8	mmm	D_{2h}
Tetragonal	$a = b \neq c$	9	4	C_4
	$\alpha = \beta = \gamma = 90^\circ$	10	-4	S_4
		11	$4/m$	C_{4h}
		12	$4mm$	C_{4v}
		13	$-42m$	D_{2d}
		14	422	D_4
		15	$4/mmm$	D_{4h}
Rhombohedral (trigonal)	$a = b = c$	16	3	C_3
	$\alpha = \beta = \gamma < 120^\circ \neq 90^\circ$	17	-3	$S_6(C_{3i})$
		18	$3m$	C_{3v}
		19	32	D_3
		20	$-3m$	D_{3d}
Hexagonal	$a = b \neq c$	21	6	C_6
	$\alpha = \beta = 90^\circ, \gamma = 120^\circ$	22	-6	C_{3h}
		23	$6/m$	C_{6h}
		24	$-6m2$	D_{3h}
		25	$6mm$	C_{6v}
		26	622	D_6
		27	$6/mmm$	D_{6h}
Cubic	$a = b = c$	28	23	T
	$\alpha = \beta = \gamma = 90^\circ$	29	$m-3$	T_h
		30	$43m$	T_d
		31	432	O
		32	$m-3m$	\bullet_h

Table 2.1: The seven Bravais lattices of a three-dimensional crystal with their according classification into 32 point groups. It is $\alpha = \sphericalangle(b, c)$, $\beta = \sphericalangle(a, c)$ and $\gamma = \sphericalangle(a, b)$, respectively. The point group is given according to the international Hermann-Mauguin (HM) and the historical Schönflies (SF) notation.

(σ_d). Those point groups are indicated as C_{nv} , C_{nh} , D_{nh} and D_{nd} , respectively. They include C_s or C_{1h} standing for the point groups, in which only a single symmetry plane can be found. The cubic point groups T , T_d , T_h , O and O_h have more than one rotation axis of highest symmetry that is at least threefold. Using Hermann-Mauguin notation 1 denotes the identity, -1 inversion, n the n -fold rotation axis, $-n$ the n -fold mirror-rotation axis and m the mirror plane. If the reflection plane is perpendicular to the n -fold rotation axis this is indicated by n/m .

Compared to the 14 space groups of the Bravais lattices, there are 230 different symmetry groups a lattice with a basis can have, when the basis is required to be completely symmetric. Those include more sophisticated symmetry operations induced by screw axes and glide planes as well.

Furthermore, it should be noted that sometimes a different notation is used to categorize different crystal lattice structures. The Pearson symbol designates a structure by symmetry class, lattice type and the number of atoms per unit cell (e.g. oP4, cF4). For instance, cinnabar has a hexagonal (h) primitive (P) unit cell, which consists of 6 atoms and is therefore labelled as hP6. It should be mentioned that the Pearson symbol does not always specify a unique structure (e.g. cF8, see chapter 3.1.1).

It is worth mentioning that in the real world a crystal of course is not ideal. This means the periodic arrangement can be disrupted by localized defects, that can arise during crystal growth, and by the fact that real crystals are finite objects.

2.4 Numerical implementation

Almost all calculations forming the basis of this thesis were carried out using the Vienna ab-initio simulation package (VASP) [69, 70]. This program uses two basic concepts to reduce the computational cost considerably. First of all plane waves are used as a basis set for the one-electron wavefunctions. This is particularly advantageous for the treatment of periodic systems due to Bloch's theorem [71]. Secondly, the core electrons are accounted for by a pseudopotential, hence only including the valence electrons explicitly in the computations.

2.4.1 Plane-wave basis and Bloch's Theorem

Since the Kohn-Sham equations (2.33) cannot be solved exactly an expansion of the Kohn-Sham orbitals $|\Phi_i\rangle$ into a linear combination of basis functions is necessary in order to solve them numerically:

$$|\Phi_i\rangle = \sum_l^m C_{li} |\chi_l\rangle, \quad (2.57)$$

where $C_{li} = \langle \chi_l | \Phi_i \rangle$.

Technically, those can be any suitable kind of function. However, the most intuitive ansatz for atomic and molecular calculations is to use a linear combination of atomic orbitals (LCAO, see also equations (2.17) and (2.19)), which are of the form of a single electron wavefunction derived from solving the Schrödinger equation for the hydrogen atom. A popular approximation of those atomic orbitals are Slater type orbitals which were initially used and consist of a set of functions, exponentially decaying with the distance r from the nucleus. Those have the advantage of correctly describing the cusp of the electronic wavefunction at the nucleus and the long-range decay, but can be further simplified by an expansion into Gaussian type orbitals (GTOs), thus substantially reducing the computational cost to solve overlap and exchange integrals.

For the investigation of the solid state and periodic systems in general, however, the decomposition of the Kohn-Sham orbitals into plane waves is beneficial. One of the reasons for this lies in the nature of plane waves, being of the form $\chi(\mathbf{r}) \propto e^{i\mathbf{k}\mathbf{r}}$ with the wave vector \mathbf{k} , to automatically fulfil Bloch's Theorem [71]

$$\psi_{\mathbf{k}}(\mathbf{r} + \mathbf{R}) = e^{i\mathbf{k}\mathbf{R}} \psi_{\mathbf{k}}(\mathbf{r}) \quad (2.58)$$

for every lattice vector \mathbf{R} . This means, if in addition one exploits the periodicity of the translational invariant system, it is sufficient to describe the investigated system by just a unit cell and a respective atomic basis, which reduces the computational cost tremendously.

Taking those considerations into account it is possible to expand the Kohn-Sham orbitals into a Fourier-Series

$$\langle \mathbf{r} | \Phi_i \rangle = \langle \mathbf{r} | \Phi_{\lambda, k} \rangle = \frac{1}{\sqrt{\Omega_0}} \sum_{\mathbf{G}} c_{\lambda}(\mathbf{k} + \mathbf{G}) e^{i(\mathbf{k} + \mathbf{G})\mathbf{r}} \quad (2.59)$$

with \mathbf{G} and Ω_0 being the reciprocal lattice vector and unit cell volume respectively. Here, the wavefunction is determined by just a band index i and a continuous wavevector \mathbf{k} , which is limited to the first Brillouin zone. In general, this means by taking advantage of the periodicity (Bloch's theorem), an initially infinite spectrum with the continuous wavevector \mathbf{k} is transformed into a discrete basis set, which is numerically manageable. This means the basis will be infinite, even though for a given \mathbf{k} it is technically discrete. The transition from the real space description $|\Phi_i\rangle$ to the k -space of plane waves $|q\rangle = |\mathbf{k} + \mathbf{G}\rangle$ is facilitated by a Fourier transformation.

In contrast to many other basis set choices, plane-wave basis sets will due to their completeness always converge very quickly to the exact wavefunction with respect to the number of basis functions involved. This means, in practice, the basis set can be truncated to a sphere in reciprocal space defined by the so-called cutoff energy E_{cut}

$$E_{cut} \geq \frac{\hbar^2 |\mathbf{G}_{max}|^2}{2m_e}, \quad (2.60)$$

determining a maximum \mathbf{G} vector in the expansion and possibly truncating the high spacial frequency parts as much as possible, since the number of basis functions is $\propto E_{cut}^{3/2}$. A typical number of a few hundred plane waves per atom is usually needed.

Another advantage of plane-wave basis sets over atomic orbitals is the fact that due to their orthogonality they do not inherit the so-called basis set superposition error generated by the overlap of basis functions contributed by different atoms. By utilization of plane waves the Kohn-Sham equations turn into a system of linear equations for the coefficient $c_{\lambda,k}$ that need to be solved in momentum space, hereby determining the matrix elements for the effective potential. It appears that through this ansatz integrals, such as for the kinetic energy, which need to be calculated, as well as derivatives, e.g. forces (due to the non-local character) can be computed with far more efficiency in reciprocal space. However, since the exchange-correlation potential is mostly calculated in real space, the transformation of the matrix elements is carried out by a Fast-Fourier transform (FFT).

In practise, the numerical integrations in the Brillouin zone are substituted by a summation over a discrete mesh of k -points according to equation (2.59). Several

schemes are available to generate this mesh in a systematic way. The approach by Monkhorst and Pack [72] for instance respects the space group symmetry of the investigated system. Especially for hexagonal systems it is recommended to include the Γ -point as well for faster convergence of the energy.

To keep computational costs as low as possible it is desirable to reduce the number of k -points as much as possible. Here the symmetry of the crystal is of further assistance, decreasing the number of non-equivalent k -points to the irreducible part of the Brillouin zone (IBZ).

In general, for the interatomic part of the wave function, where fluctuations are small and hence the wavefunction at neighbouring k -points are usually very similar, high accuracy can be reached using just a relatively small number of k -points. However, the plane-wave approximation demands for a huge number of basis functions (high cutoff energy) when it comes to the description of localized states and the atomic core region, where the wavefunction inherits nodes and strong fluctuations (high spacial frequencies) in order to maintain orthogonality to the core state wavefunctions. Therefore, as a further approximation pseudopotentials are utilized (see chapter 2.4.2).

Based on the information given above it is sensible to preliminarily test calculations with respect to their convergence depending on the chosen energy cutoff and k -mesh. For comparable computations it is important to keep the basis as similar as possible, since e.g. with relaxation of the unit cell (varying the lattice constant), G_{max} changes, influencing the total energy even with a fixed energy cutoff.

2.4.2 The frozen-core approximation and pseudopotentials

As mentioned earlier, it is a challenge to describe the in the core region strongly oscillating valence states using a sensible number of basis functions. However, since fortunately most chemical and physical properties as well as chemical bonding characteristics are mainly determined by the wavefunction of the valence electrons outside the core region, it is rendered obvious to either just account for those in an actual calculation or to modify both the wavefunction of the valence electrons and ionic core potential in the core region accordingly to make those strong fluctuations disappear.

The first step to achieve this is the separation of the system into a core and valence region known as the frozen-core approximation. In this concept, the wavefunctions of the core electrons are assumed to be independent from the chemical environment of the atom and therefore independent from the valence particle density n_v . The Kohn Sham equation can hereupon be solved for the valence electrons only, where the kept fixed (frozen) wavefunction for the core electrons is derived from an all-electron atomic calculation.

Even though this means a further reduction of the basis set size, it turns out that this approach is only suitable for atoms with well separated (spatially and energetically) electronic states, deeming it unsuitable especially for elements with partially filled d orbitals, e.g. transition metals. Here, the concept of pseudopotentials has proven to be a valuable tool. At this, in addition to the frozen-core approximation, it is assumed that the valence electron density of the core region as well have little influence on the chemical bonding.

Therefore, a pseudopotential is created which aims to embody a pseudo-atom substituting the actual atom by an effective core plus inner valence shell and is supposed to lead to reasonably smooth pseudo-wavefunctions in the core region (fig. 2.4 gives an idea). It is desirable that this pseudopotential describes not only the core atoms but also their influence on the valence electrons. As mentioned in chapter 2.2.4 this should include all interactions and therefore account for relativistic effects also.

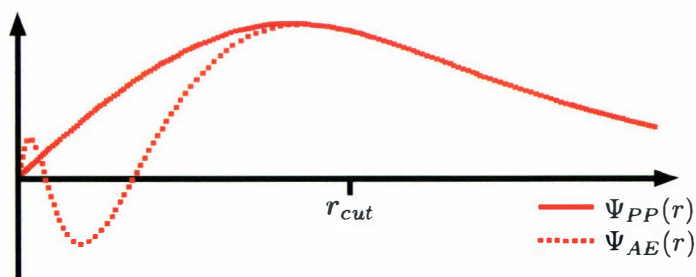


Figure 2.4: The real (all-electron) wavefunction (dotted) compared to the pseudopotential wavefunction (straight) as a function of the radius. Both only match above a cutoff radius $r_{cut} = r_l$.

Naturally, a well constructed pseudopotential firstly leaves most physical and chemical properties of the true atom unchanged and is secondly independent from the set chemical environment ensuring its transferability. It has therefore to meet the following conditions: the atomic all-electron eigenvalues do not differ from those obtained with the help of the pseudopotential ($\epsilon^{AE} = \epsilon^{PP}$), the

wavefunctions of the actual and the pseudo-atom are equal beyond a certain cutoff radius r_l (for each angular momentum l) marking the spatial edge of the pseudo-atom and the charge density of the real atom has to be the same as the pseudo charge within the radius r_l accounting for norm conservation of the wavefunction.

Pseudopotentials of this kind for the solid state were first introduced by Hamann, Schlüter and Chiang [73] and are known as so-called norm-conserving pseudopotentials. They are usually derived by solving the inverse radial Schrödinger (2.1) or (for the inclusion of relativistic effects) Dirac equation (2.55) for each angular momentum l , at which a suitable initial fit of the wavefunction in close proximity to the core is assumed. Hence, the pseudopotential will depend on l as well.

However, the condition for the norm-conservation can be relaxed creating softer pseudopotentials. This allows for very accurate treatment of the first row elements as well as atoms that contain d -electrons (e.g. transition metal elements) while reducing the number of necessary plane waves to a minimum. Examples are the so-called ultrasoft pseudopotential (US) suggested by Vanderbilt [74] and pseudopotentials stemming from the application of the projector augmented-wave scheme (PAW) [75, 76]. The latter are used in this thesis, since they are generally more accurate due to a smaller radial cutoff and an exact reconstruction of the nodes of the valence function in the core region. However, those approaches demand for a correction of the wrong pseudo charge by either introducing a depletion (for US) or augmentation charge (for PAW) utilizing a non-local overlap operator to account for these charges.

2.5 Optimization and solid-state properties

The preceding sections introduced the basic concepts. However, so far only methods to determine the electronic system were described. This chapter shall therefore cover how to describe the dynamics of the nuclei as well and explain the fundamental procedure of how to actually obtain the crystal properties of a system.

2.5.1 Optimization

Until now only the determination of the optimized electronic system was described. According to the Born-Oppenheimer approximation the ground-state density of the electrons as well as the total energy are depending parametrically on the positions of the atoms or ions. Looking at a periodic system a potential energy surface $E_{tot}(\{\mathbf{R}_a\})$ is spanned for the coordinates of the atoms in a unit cell (Born-Oppenheimer surface, see chapter 2.1.2).

Therefore, as a first step to obtain the ground-state energy and properties of a system the total energy $E_{tot}(\{\mathbf{R}_a\})$ is calculated for the electronic system optimizing just the electronic degrees of freedom with respect to the position of the ions or atoms of the investigated system. This can happen within the framework of density functional theory solving the Kohn-Sham equation (2.33) to yield the Born-Oppenheimer potential energy surface.

After this procedure however, one has to consider the dynamics of the ionic system, which can be done by calculating the forces acting on the nuclei from the potential energy surface

$$\mathbf{F}_a = -\nabla_{\mathbf{R}_a} E_{tot} = \mathbf{F}_a^{ion} + \mathbf{F}_a^{el}. \quad (2.61)$$

They vanish as soon as the system reaches its equilibrium state.

By introducing a fictitious time t on which the trajectories $\mathbf{R}_a(t)$ depend, it is possible to calculate those interatomic forces in certain time intervals. This does not only allow for rather simple techniques to optimize the geometry of crystals, even with quite a few atoms in the unit cell, but can even be used to describe solids at higher temperatures (melting) and to investigate phonons further.

$\mathbf{R}_a(t)$ can be determined for instance by treating the nuclei as point particles, applying classical mechanics in form of Newtons equation of motion for the ions of the mass M_a

$$M_a \frac{d^2}{dt^2} \mathbf{R}_a(t) = \mathbf{F}_a, \quad (2.62)$$

where \mathbf{F}_a is given by (2.61).

Generally speaking, therefore having an initial guess for the atomic arrangement $\mathbf{R}_a(t)$, the Kohn-Sham equations are solved within the framework of DFT to

calculate the ground-state energy $E[n]$ and hence $E_{tot}(\{\mathbf{R}_a\})$. This is used to obtain the forces \mathbf{F}_a , which in turn using (2.62) gives the next time step

$$\mathbf{R}_a(t + \Delta t) = \mathbf{R}_a(t) + \mathbf{v}_a(t)\Delta t + \frac{1}{2}\mathbf{a}_a(t)\Delta t^2 + \dots \quad (2.63)$$

representing an atomic configuration that is closer to the equilibrium ensemble. Based on this, the equations (2.33) have to be solved again to find the adequate electronic state.

The method is known as ab-initio molecular dynamics (AIMD) and comprises two interlocked iteration schemes. However, after each calculation of the new atomic arrangement a new BO energy surface has to be calculated. To reduce computational effort it is therefore feasible to estimate the direction and if possible even the velocity of how the energetic minimum will be approached using the calculated forces. It is known as the method of steepest descent. Even faster convergence is achieved using a conjugated gradient scheme, which is primarily used for the calculations presented here.

2.5.2 Equilibrium properties of crystals

The successful calculation of the ground-state energy for a certain arrangement of atoms is the starting point for the determination of various solid-state properties such as crystal structure, lattice constants, density of states and charge densities, cohesive energy and bulk modulus. Furthermore, the coefficient of thermal expansion, elastic constants and interatomic forces (and therefore phonon frequencies) can easily be obtained.

Initially from an experimental point of view all material properties are derived at a given pressure p and temperature T . Hence, the suitable thermodynamic potential is the free enthalpy or Gibbs free energy (for constant particle number)

$$G(T, p) = U - TS + pV \quad (2.64)$$

and its optimization will lead to the thermodynamic equilibrium state. The separate terms specify the internal energy U , the entropy S and the volume of the crystal V . For the purpose of theoretical computations however, this full thermodynamic treatment is challenging due to finite temperature effects and determining the entropy of the system. Hence, several approximations are used.

Firstly, the bulk is assumed to be stress-free, therefore showing little change of volume for nearly constant pressure. This means that the equilibrium state is mainly determined by the free energy

$$F(T, V) = U(T, V) - TS(T, V) \quad (2.65)$$

depending on the temperature and volume, thereby giving a definition for the term stress-free as

$$p = - \left(\frac{dF}{dV} \right)_T = 0.^7 \quad (2.66)$$

On the other hand, an approximation concerning the phonons is made by idealizing the entropy of the electrons to be small. Therefore, the temperature dependency of the internal electronic energy should be negligible. Hence, it is possible to substitute $U_{el}(T \rightarrow 0, V)$ approximately by the total energy of the system $E(V)$. This quasi-harmonic approach yields the following expression

$$F(T, V) = E(V) + U_{vib}^0(V) + F_{vib}(V, T), \quad (2.67)$$

where U_{vib}^0 is the zero temperature vibrational energy and F_{vib} is the free energy of the oscillators. According to Debye for temperatures smaller than the Debye temperature Θ both phonon contributions can be approximated to be $9/8Sk_B\Theta$, which usually amounts to only a few percent of the electronic contribution. If those terms are therefore neglected, we obtain the equilibrium volume from (2.66)

$$\left. \frac{dE(V)}{dV} \right|_{V=V_0} = 0. \quad (2.68)$$

To determine the bulk modulus, experimentally given by

$$B(T, V) = -V \left(\frac{dp(V, T)}{dV} \right)_T, \quad (2.69)$$

by means of quantum chemical methods a sensible equation of state for the solid system has to be derived. It has been shown that in a pressure range of up to 10^{10} Pa the pressure derivative

⁷From this relation between volume and temperature the thermal expansion coefficient $\alpha(T) = (dV/dT)/V$ can be derived.

$$B' = \left(\frac{dB}{dp} \right)_T \quad (2.70)$$

varies little with pressure. The bulk modulus can therefore be assumed to be linearly dependent on the pressure

$$B(T, p) = B_0(T) + B'_0(T)p, \quad (2.71)$$

where the zero indicates values at $p = 0$.

Rearranging and integrating this equation while applying $p = -\frac{dE(V)}{dV}$ according to the quasi-harmonic approximation one obtains the so-called Murnaghan equation of state (EOS) [77]

$$E(V) = E_0 + \frac{B_0 V}{B'_0} \left(\frac{(V_0/V)^{B'_0}}{B'_0 - 1} + 1 \right) - \frac{B_0 V_0}{B'_0 - 1}, \quad (2.72)$$

where the pressure is given by

$$p = \frac{B_0}{B'_0} \left[\left(\frac{V_0}{V} \right)^{B'_0} - 1 \right]. \quad (2.73)$$

This equation has proven to be a very valuable tool in the fitting of total energy versus volume dependencies in order to obtain the properties in question. However, for a wider pressure range one is referred to either use the Birch-Murnaghan equation [78] or the universal Vinet equation of state [79, 80].

Furthermore, the calculation of the total energy enables the determination of binding and cohesion energies, defined as the work per unit cell that is necessary to decompose a crystal of the volume V into its atoms under isothermal conditions

$$E_{coh} = - \int_V^\infty dV' p(T=0, V') = \int_V^\infty dF|_{T=0} = \int_V^\infty dU|_{T=0}. \quad (2.74)$$

Ideally, $U(T=0, V_0)$ is calculated as the sum of the electronic and vibrational part. $U(T=0, V=\infty)$ is determined by adding up the groundstate energies for each isolated atom in the unit cell. In general, by means of the approximations introduced above an overestimation of the cohesion energies is very common [81], which mainly originates in the underestimation of the atomic energies in the

framework of LDA.

2.5.3 Determination of the crystal structure and phase transitions

So far only stress free solids have been discussed. However, equations (2.72) and (2.73) now also provide a tool to discuss the crystal structure under hydrostatic pressure and enable the determination of the solid-state structure of a system at equilibrium conditions as well as at higher pressures if phonon contributions are neglected. It is furthermore possible to determine the pressure at which transitions between the different crystal structures occur. This is realized as follows.

For simple structures, like cubic crystals, the total energy is calculated for different volumes and different structures in question. The equilibrium structure of ground-state and high-pressure phases is given by the minima of the subsequent graphs for $E = E(V)$ as indicated by (2.68), which defines the minimum volume V_0 . For those simple structures this automatically yields the lattice constant a , since the positions of the atoms are fixed.

However, more sophisticated structures are usually characterized by the whole set of the lattice constants a , b and c and several other parameters that define the positions of the cat- and anions within the unit cell. Usually in that case, the equilibrium volume is determined first and subsequently, the ratios c/a and b/a plus the additional ionic degrees of freedom, have to be optimized separately for the according volume. Therefore, when using VASP it is common procedure to carry out a full geometry optimization, i.e. the cell-shape as well as the internal parameters of the respective structure's unit cell are optimized over a range of fixed unit-cell volumes. This is to avoid complicated calculations to evaluate the Pulay-stress corrections. Pulay stress occurs if a volume relaxation is carried out using a constant basis set and leads to error in the stress tensor.

To predict possible high pressure phases of the investigated solids, the energy-volume dependency can give a first estimate employing the common tangent method. After the calculation of the energy-volume dependencies of two different crystal structures, a common tangent for the two curves in question is constructed. Hence, the transition pressure results from the negative slope of the tangent, since $p = -dE/dV$. Furthermore, a transition of two phases is

characterized by the concordance of the Gibbs free energy of the modifications. However, at the low (zero) temperature limit neglecting the entropy term, this can be simplified and the relevant thermodynamic potential is then given by the enthalpy $H = E + pV$, which is known if one considers an EOS like (2.73). This method also allows for the prediction of second order transitions, where the two respective enthalpy versus pressure curves meet and hence the transition is indicated by the crossing of the curves of the pressure derivative. Usually a phase transition goes along with a volume reduction.

Chapter 3

Structural and computational details

This chapter will give some explanatory notes about the group 12 chalcogenides, mainly the description of the different crystal structures investigated, as well as a description of the computational method used to investigate the problem.

3.1 Structures

This section introduces the crystal structures commonly found in the group 12 chalcogenides, giving some guidance and information with respect to the crystallographic classification, the construction of the corresponding unit cell and structural parameters. Those structures are usually labelled in various ways, the most common alternatives being by either historically evolved names (diamond, zinc blende, ...), by the chemical formula of the prototype (e.g. NaCl, CsCl, ...), by the labels in a phase diagram (α -mercury, HgSe-III, ...), by space-group symmetry (like Cmcn, Pmmn, ...), by the Pearson notation (e.g. oP4, cF4) or even, if available, by the Strukturbericht designation. The latter characterizes the structure of a crystal in a semi-systematic way by using a specific combination of letters and numbers (A1, B3, ...), at which the letter A refers to monoatomic structures and B to diatomic crystals with an equal numbers of atoms of each type, whereas other letters are assigned to more complicated structures. The numbers were added depending on the historical order, in which the lattices were investigated and the designation is therefore not always consistent.

Here a mixture of notations will be used according to the terms most commonly

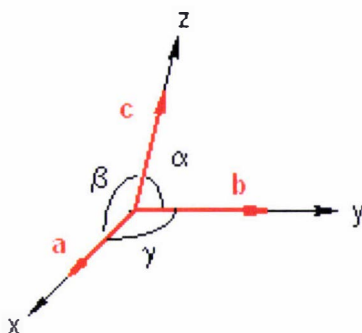


Figure 3.1: The unit vectors and angles of a unit cell defined in the context of a right-handed coordinate system giving the x , y and z axes of a crystal.

used in the literature. Italics are used for pointing out the symmetry of a system, whereas standard text is employed to correspond to the actual name of a structure. A more detailed description of the structures can be found in refs. [12], [82] or [83].

Only the specification of the atomic positions uniquely defines a crystal structure. The atomic positions are usually referred to as so-called Wyckoff positions and are chosen in agreement with the Bilbao Crystallographic server or the International Tables for Crystallography [84–86]. They are given as fractional coordinates of the lattice constants of the unit cell. The lattice parameters are always specified as a , b and c and the angles as α , β and γ in a right-handed coordinate system (see fig. 3.1).

Table 3.1 gives an overview about which structures were considered for the investigated compounds. In general, an indication of which crystal structure will be preferred by one or the other compound is the ratio of volumes of the component atoms.

3.1.1 Cubic lattices

As one of the seven crystal systems, the cubic crystal system is very common and the simplest structure found amongst minerals. One distinguishes three Bravais lattices: simple (sc), face-centred (fcc) and body-centred (bcc) cubic. They are the basis for many typical structures adopted by binary compounds.

Denotations	Lattice, basis, space group	Lattice parameter	Chalcogenides investigated
CsCl	sc	a	ZnX, CdX, HgX,
CC	2 atoms		ZnO, CdO, HgO
B2	$Pm\bar{3}m$		
NaCl	fcc	a	ZnX, CdX, HgX,
RS	2 atoms		ZnO, CdO, HgO
B1	$Fm\bar{3}m$		
ZnS	fcc	a	ZnX, CdX, HgX,
ZB	2 atoms		ZnO, CdO, HgO
B3	$F\bar{4}3m$		
SC16	sc	$a,$	ZnX, CdX, HgX
	16 atoms	v	
	$Pa\bar{3}$		
Wurtzite	h	$a, c,$	ZnX, CdX, HgX,
W	4 atoms	u	ZnO, CdO, HgO
B4	$P6_3mc$		
(α -)HgS	h	$a, c,$	ZnX, CdX, HgX,
C2	6 atoms	u, v	HgO
B9	$P3_121/ P3_221$		
I4/mmm	bct	a, c	HgO
bct	2 atoms		
A_a	$I4/mmm$		
C222 ₁	bco	$a, b, c,$	HgSe, HgTe
	4 atoms	x_1, y_2	
	$C222_1$		
Cmcm	bco	$a, b, c,$	ZnX, CdX, HgX
	4 atoms	y_1, y_2	
	$Cmcm$		
Montroydite	o	$a, b, c,$	HgO
M	8 atoms	x_1, z_1, x_2, z_2	
Pnma	$Pnma$		
Pmmm	o	$a, b, c,$	CdS, HgS
	4 atoms	z_1, z_2	
	$Pmmn$		

Table 3.1: Structures adopted by and investigated for the group 12 chalcogenides. Listed are different denotations such as prototype, abbreviation and Strukturbericht designation as well as lattice type, number of atoms in the atomic basis, space group in Hermann-Mauguin notation, the according lattice parameters and the according chalcogenides for which this structure was investigated. It is $X = S, Se, Te$. The abbreviations sc, fcc, h, bct, bco and o stand for simple cubic, face-centred cubic, simple hexagonal, body-centred tetragonal, base-centred orthogonal and simple orthogonal, respectively.

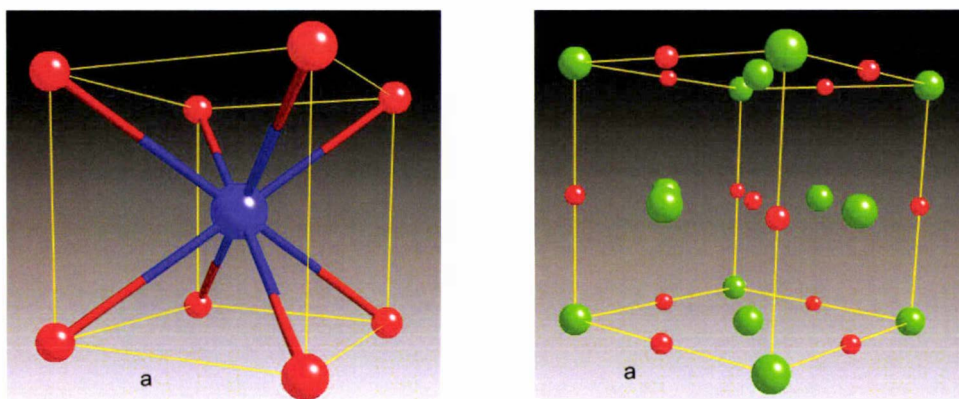


Figure 3.2: The units cells of the cesium chloride (left) and the rocksalt (right) structure.

Cesium chloride

Cesium chloride is a common cubic structure named after its prototype CsCl. However, it is found in several other alkali halides (e.g. CsBr, CsI, RbCl, AlCo, AgZn, BeCu, MgCe, RuAl and SrTl) even though often formed under high pressure. It has not yet been found in too many group 12 chalcogenides, but is expected to emerge at very high pressures. In general, this structure is preferred in binary compounds, where the ions of two elements are of approximately the same size.

The unit cell of the CsCl structure is based on two interpenetrating simple cubic lattices, which form a bcc structure, yet with two different atomic species. The space group is 221 or $Pm\bar{3}m$ with the atomic sites 1(a) at $(0, 0, 0)$ and 1(b) at $(1/2, 1/2, 1/2)$. The origin is the centre of inversion. Hence, the unit cell accommodates two atoms (Pearson symbol cP2) with a perfect eight-fold coordination as indicated by fig. 3.2. The Strukturbericht designation is B2.

Rocksalt

Another cubic formation named after its prototype is rocksalt or NaCl structure, which is found in CdO at ambient pressure along with many alkali halides (KBr, LiCl, LiF, NaBr, NaF, RbF) and various metal oxides, sulfides, selenides, and tellurides (BaS, CaO, CeSe, MgO, NiO, SrO, YbO, ZrO, TbTe). Other compounds showing this structure are AgCl, DyAs, GdN, PrBi, PuC, ScN, UC and YN. It occurs as a high pressure phase in AlN, GaN, InN, InP, ZnO, HgO, ZnX, CdX and HgX ($X = S, Se, Te$).

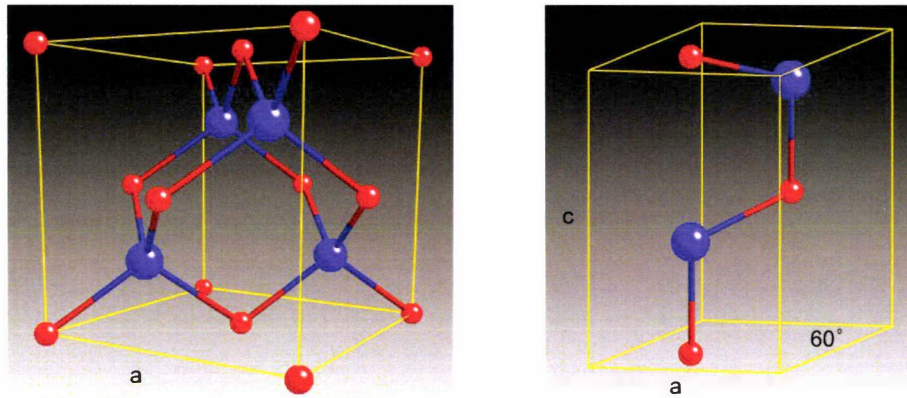


Figure 3.3: The units cells of the zinc blende (left) and the wurtzite (right) structure.

The space group is 225 or $Fm\bar{3}m$ with the atoms of one species sitting at $4(a)$ $(0, 0, 0)$ and the atoms of the other species at $4(b)$ $(1/2, 1/2, 1/2)$, which means that the lattice is built from two interpenetrating fcc lattices. The structure is centrosymmetric with the centre of inversion at the origin and usually preferred if the cation is slightly smaller than the anion (cation/anion radius ratio of 0.414 to 0.732).

The coordination number of each atom is 6, where the anions are surrounded by cations in the fashion of the corners of an octahedron and vice versa giving rise to the Pearson notation $cF8$. The Strukturbericht designation is B1. The conventional unit cell is shown in fig. 3.2.

Zinc blende

Zinc blende is a very common structure not only amongst the group 12 chalcogenides, but is in general the dominant structure under ambient conditions for a variety of III-V and II-VI semiconductors and several binary compounds (e.g. AgI, AlAs, AlP, AlSb, BaS, BN, BP, BeS, BeSe, BeTe, CdS, CuBr, CuCl, CuF, CuI, GaAs, GaP, GaSb, HgS, HgSe, HgTe, InAs, InP, MnS, MnSe, SiC, ZnSe, ZnTe). It derives its name from the zinc sulfide mineral zinc blende (or sphalerite).

It is classified by the space group $F\bar{4}3m$ or 216, hence inheriting a cubic symmetry with one atomic species located at the $4(a)$ site $(0, 0, 0)$ and the other one at the $4(c)$ site $(1/4, 1/4, 1/4)$. The structure could therefore be described as two interpenetrating fcc lattices, shifted by one quarter along the cubic diagonal. Hence, each atom is tetrahedrally coordinated with four unlike nearest

neighbours. The unit cell as can be seen in fig. 3.3 is therefore uniquely described by just the lattice constant a . There are 8 atoms in the unit cell leading to the Pearson symbol cF8. The Strukturbericht designation is B3.

If all atoms are identical, the analog is the diamond structure. It is furthermore, the cubic analog of the wurtzite lattice, similar to the analogy between the fcc and hcp close packed structures, where the only difference is the stacking of the atoms or dimers, respectively, which is ABCABC along the [111]-direction in the case of zinc blende (i.e. fcc) and ABAB for wurtzite (i.e. hcp).

SC16

The SC16 structure characterizes a simple cubic structure that accommodates 16 atoms in the unit cell. Hence, the Pearson notation is cP16. The space group is $Pa\bar{3}$ or 205 with the centre of inversion at $(1/4, 1/4, 1/4)$. No Strukturbericht designation is available.

After several theoretical predictions of a SC16 high-pressure phase in GaAs, GaP, AlSb and InAs, this structure was first observed in CuCl and CuBr [87] and later in GaAs by McMahon *et al.* [88], who established the positions of the two atomic species both at the 8(c) site with coordinates of (u, u, u) and (v, v, v) , respectively. In the case of GaAs it is $u \sim 0.15$ and $v \sim 0.65$.

Interestingly, this structure packs more efficiently than diamond making it preferable at higher pressures. This, however, comes with a slight distortion from the diamond bond length, leading to an almost tetragonally bonded structure with a bond type A to the first-nearest neighbour and a bond type B for the three second-nearest neighbours. Yet, it causes an optimized tetrahedral angle compared to the diamond structure, which is different for the two atomic species if $u - v \neq 0.5$ [89].

Furthermore, the structure is linked to the BC8 structure (body-centred cubic with 8 atoms in the unit cell) found in germanium and silicon by being its binary analog. This means the two structures are related to each other in the same way that zinc blende is related to the diamond structure.

3.1.2 Hexagonal structures

Another one of the seven crystal systems is the hexagonal lattice, but there is actually only one Bravais lattice (hP). It is specified by the lattice constants a and c , where the angle enclosed by the two in-plane lattice vectors is 60° . Several

elements and compounds crystallize in this structure with graphite as one of the more prominent examples.

Furthermore, the hexagonal close-packed structure should be mentioned, since at least 30 elements are known to crystallize in this formation. It is based on the simple hexagonal Bravais lattice with the positions of the atoms given by $(1/3, 2/3, 1/4)$ and $(2/3, 1/3, 3/4)$ both at a (2c) site. This can also be described by two simple hexagonal lattices shifted by $\mathbf{a}_1/3 + \mathbf{a}_2/3 + \mathbf{a}_3/2$, hence achieving the highest space filling of $\eta = V_a/V_u = 0.74$, where V_a is the volume of the atoms in the unit cell with the volume V_u .

Wurtzite

The wurtzite structure is named after the zinc iron sulfide mineral (Zn.Fe)S and is adopted by several binary compounds like AgI, InN, ZnO, ZnS, CdS, CdSe, α -SiC, GaN and AlN at ambient conditions. For other semiconductors, where the wurtzite structure is not the most stable phase it might be preferred in the nano-crystal forms.

It is a hexagonal lattice with the space group $P6_3mc$ or 186 and is built up from two interpenetrating hcp lattices for each atomic species with the atoms located at the 2(b) site at $(1/3, 2/3, 0)$ and the 2(b) site at $(1/3, 2/3, u)$, for the according atomic species. Ideally $u = 3/8$, which is the case if a c/a ratio equivalent to $\sqrt{8/3} = 1.6\bar{3}$ is reached, characterizing an 'ideal' wurtzite structure. Note that the parameter u for the first atomic species is arbitrarily set to zero, which fixes the actually arbitrary origin along z .

As mentioned earlier, wurtzite is the hexagonal analog to the zinc blende structure, where those two structures are related in the same way as is the hcp lattice to the fcc. This is expressed in the stacking of the binaries: a ABCABC-layering is adopted along the (111)-axis for zinc blende, whereas in wurtzite a ABAB-stacking is achieved. Given this structural similarity, it is to be expected that for all group 12 chalcogenides the energy as well as the unit-cell volume difference between the two structures is rather small, which should induce very similar properties, especially regarding the cohesive energy.

In the wurtzite structure each atom is tetrahedrally coordinated in a unit cell that includes four atoms (Pearson symbol hP4) as can be seen in fig. 3.3. The Strukturbericht designation is B4. It is furthermore a non-centrosymmetric structure. This lack of inversion symmetry generally implies properties such as piezoelectricity and pyroelectricity.

If the two atomic species are the same, the hexagonal diamond structure (so-called lonsdaleite) is formed.

3.1.3 Trigonal structures

Cinnabar

The cinnabar structure is named after the naturally occurring mineral of HgS. Under ambient conditions it is furthermore found in HgO as a metastable phase and in HgSe, HgTe, CdTe, ZnTe and GaAs as a high-pressure phase.

The structure is trigonal and non-centrosymmetric with the space group $P\bar{3}_121$ or 152 as first found by Auvray *et al.* in HgS [90]. However, a description of the structures is also possible employing the enantiomorphic space group $P\bar{3}_121$ (154), which is usually utilized, since one cannot distinguish between the enantiomorphic structures using powder data. Furthermore, a hexagonal unit cell can be used to describe the structure. If the latter space group is used, the atoms are positioned at the 3(a) site at $(u, 0, 1/3)$ and the 3(b) site at $(v, 0, 5/6)$, for the two species respectively. The unit cell can be viewed in fig. 3.4, showing six atoms, which gives the Pearson symbol hP6. The Strukturbericht designation is B9.

Comparing the illustrations (a), (c) and (e) in fig. 3.5, it becomes obvious that cinnabar is merely a distortion of the rocksalt structure and therefore a subgroup of this structure. Both formations are identical if $c/a = \sqrt{6} = 2.449$ and $u = v = 2/3$.

How strong the distortion from the rocksalt structure is, can be estimated by the change in the coordination number, where the transition from a six-fold coordination to a 2+4 coordination means that the two nearest neighbours in the cinnabar structure are much closer than the next four nearest neighbours. For instance for HgS, where $u(\text{Hg}) = 0.7199$ and $v(\text{S}) = 0.4889$ [90], this means a nearest-neighbour distance of 2.368 Å, and second nearest-neighbour distances of 3.094 and 3.287 Å.

As a consequence, the two closest nearest neighbours lead to a build-up of S-Hg-S spiral chains running parallel to the z -axis (see fig. 1.3), in which the S-Hg-S groups are linear. In the cinnabar structure the interactions of atoms within a chain are usually much stronger than those between the chains. Therefore, they are thought to be of Van der Waals character in trigonal HgSe and HgTe [91].

However, the coordination number is strongly dependent on the parameters u

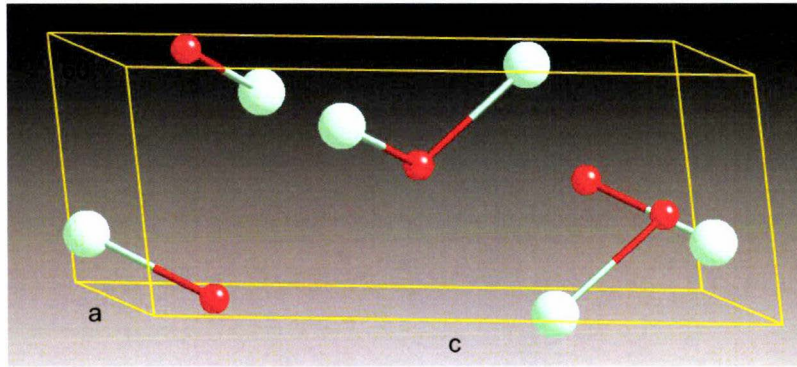


Figure 3.4: The unit cell of the cinnabar structure.

and v . Except for the case of HgO and HgS they are quite similar (and a little less than $2/3$), inducing a 2+2+2 coordination in HgSe and a 4+2 coordination in HgTe and CdTe [92]. The intra-chain distances then become comparable to the inter-chain distances. Looking at e.g. ZnTe u and v are almost the same (around 0.5) and an approximately four-fold coordination is reached. Characterizing those chalcogenide structures by the prototype cinnabar is often questioned due to the strong structural deviation.

Still, HgO and HgS have a true 2+4 coordination meaning two close bond distance neighbours within the chain and 4 neighbours in adjacent chains. The transition in coordination from cinnabar to rocksalt can be viewed in fig. 3.5 [91].

3.1.4 Orthorhombic structures

$C222_1$

The $C222_1$ structure belonging to the space group indicated by its name (alternatively space group 20) is a non-centrosymmetric structure appearing as an intermediate phase between zinc blende and cinnabar in HgSe and HgTe.

The atoms are positioned at the 4(a) and 4(b) sites at $(x, 0, 0)$ and $(0, y, 1/4)$, respectively. This means there are 8 atoms in the unit cell, hence the Pearson symbol oP8. A Strukturbericht designation does not exist.

The structure is regarded as an orthorhombic distortion of the zinc blende formation. The two structures are identical if $a = b = c$ and $x = 0.25 = y$. In HgSe and HgTe the distortion is minimal, therefore maintaining the fourfold coordination of the atoms. However, the bond angles are distorted considerably.

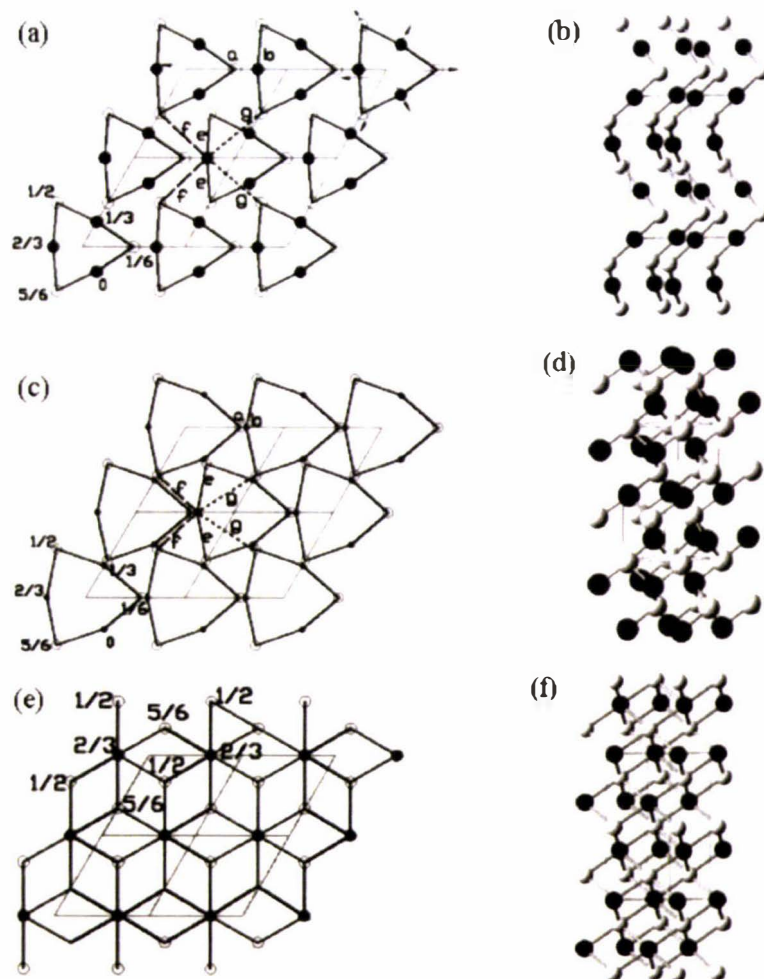


Figure 3.5: The structural transition of the group 12 chalcogenides starting from a 2+4 coordination in HgO and HgS ((a) and (b)), changing to a 4+2 coordination in e.g. CdTe ((c) and (d)) towards the rocksalt structure of HgS with its typical sixfold coordination ((e) and (f)). The pictures (a), (c) and (e) show the plane perpendicular to the c -axis, while (b), (d) and (f) are views taken parallel to the c -axis. Dark atoms and open circles indicate the transition metals and chalcogenides, respectively. The z -coordinate for each atom is represented by the numbers next to the atoms. The picture is taken from ref. [91].

Cmcm

The Cmcm structure is named after its space group and found in various binary structures, such as ZnSe, ZnTe, CdS, CdSe, CdTe, HgSe, HgTe, AlSb, GaP, GaAs, InP and InAs. The space group number is 63 with the Pearson notation

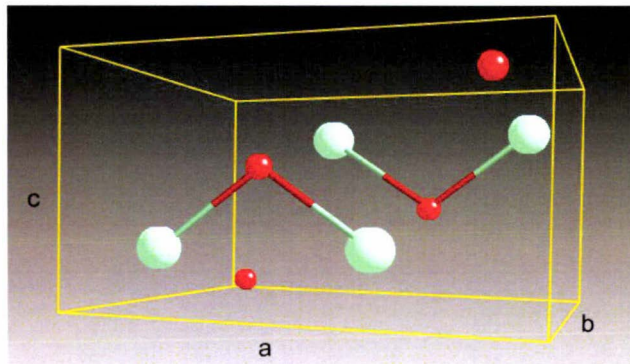


Figure 3.6: The unit cell of the montroydite structure.

oC8. Here, the atoms in the units cell are both sitting at the $4(c)$ sites at $(0, y_1, 1/4)$ and $(0, y_2, 1/4)$, respectively.

The structure is an orthorhombic distortion of the NaCl structure and identical if $a = b = c$, $y_1 = 3/4$ and $y_2 = 1/4$. This distortion is characterized by a displacement along $\pm y$ leading to x - y planes different from rocksalt. A further distortion however appears if $y_1 - y_2 \neq 0.5$, which can be seen in the appearance of zigzag chains along the x -axis, meaning the shortest cation-cation distance is either less or more than the shortest anion-anion distance if $y_1 - y_2 < 0.5$ or > 0.5 , respectively.

Accordingly, the coordination number strongly depends on the values of the lattice parameters as well as the coordinates y_1 and y_2 . A $5 + 3$ coordination can be observed if $y_1 - y_2 < 0.5$, like in ZnTe and CdTe, although it becomes less pronounced in HgTe.

Pnma

Pnma is an orthorhombic structure with the space group 62 or *Pnma*. An example is the Montroydite phase of HgO, where both the Hg and O atoms can be found at the $4(c)$ site at $(x, 1/4, z)$. This means the structural degrees of freedom are $a, b, c, x(\text{Hg}), z(\text{Hg}), x(\text{O})$ and $z(\text{O})$. The unit cell can be viewed in fig. 3.6, which shows a total of 8 atoms in the unit cell.

For HgO, where $x(\text{Hg}) = 0.115$, $z(\text{Hg}) = 0.245$, $x(\text{O}) = 0.36$ and $z(\text{O}) = 0.58$, this results in a built-up of the crystal from planar -O-Hg-O-Hg- zigzag chains running parallel to the x -axis in the ac -plane showing a twofold coordination. The O-Hg-O group is linear, whereas the Hg-O-Hg group is bent with an angle of 108.8° and a Hg-O bond distance of 2.028 \AA . For the full structure see fig. 1.2.

The Pearson symbol is oP8.

Pmmm

Pmmm is an orthorhombic structure named after its space group (alternatively number 59). The atoms are sitting at the 2(b) and 2(a) sites at $(0, 1/2, z_1)$ and $(0, 0, z_2)$, respectively.

It can be viewed as an orthorhombic distortion of the rocksalt structure, Both structures are identical if $a = c = b/\sqrt{2}$ and the atomic positions are $(0, 1/2, 1/4)$ and $(0, 0, 1/4)$, respectively. A centre of inversion is found at $(1/4, 1/4, 0)$ and the Pearson symbol is oP4.

3.1.5 Tetragonal structures

I4/mmm

The I4/mmm structure has the space group 139 with the Hg and O atoms being at the 2(a) and 2(b) at $(0, 0, 0)$ and $(0, 0, 1/2)$, respectively. It has a body-centred unit cell, hence the Pearson symbol is tI2 and the Strukturbericht symbol is A_a .

This structure can be viewed as a rather small distortion of the rocksalt structure, where the crystal is compressed along the z -axis. The two are identical if $c/a = \sqrt{2} = 1.414$. For a picture of the unit cell refer to the picture on the right-hand side of fig. 3.2, but slightly shortened along the z -axis.

3.2 Computational details

Generally, all calculations in the course of this thesis were carried out using density functional theory within a periodic boundary framework as implemented in the Vienna Ab-initio Simulation Package VASP [70].

Here, the electron-electron interaction is treated within the generalized gradient approach (GGA) [58] for the exchange-correlation energy according to the parametrization by Perdew and Wang (PW91) [93] and a plane wave basis set is employed as explained in chapter 2.4.1. Furthermore, the atomic core region is described by means of the projector augmented-wave (PAW) method [75, 76], which allows to reduce the number of plane waves per atom for transition metals

as well as first row elements to a minimum. Here only the outermost $(n-1)$ d - plus n s -electrons are used in the valence space. The integration over the Brillouin zone was carried out by summing over a uniform k -point mesh including the Γ -point, where the number of k -points was chosen to obtain a converged total energy.

Relativistic effects were allowed by including them within the pseudopotential approximation, which only accounts for scalar-relativistic (mass-velocity) contributions. Yet, comparable nonrelativistic calculations were only carried out for the mercury chalcogenides. This is justified as the relativistic impact on the zinc as well as cadmium chalcogenides is much smaller and therefore negligible within the accuracy of the density functional treatment chosen here.

Even though the study at hand discusses the relativistic influences on the mercury chalcogenides only, both structural and electronic properties were calculated for the zinc and cadmium chalcogenides as well, which primarily enables a direct comparison of the nonrelativistically treated mercury chalcogenides to those compounds. It furthermore has the positive side effect of providing a tool to test the quality of the computational specifications used, by comparing the results to previously published work.

3.2.1 Cutoff energy and k -point mesh

In order to obtain reliable results, their convergence with respect to the number of plane waves as well as the size of the k -point mesh needs to be assured prior to the actual calculations (see also chapter 2.4.1). Tests were carried out for every considered crystal structure of each chalcogenide system both at the experimental equilibrium lattice constant and at a volume expected to be well below the transition into the next phase. If no experimental data was available short benchmarking calculations were performed beforehand. It was aimed to keep the deviation in the total energy with respect to the tested parameters below 1 meV.

In general, the plane-wave expansion could be restricted to a maximum kinetic energy of 450 eV, except for the relativistic HgO montroydite structure where a 585 eV cutoff was necessary. Even if the required energy was below those values, it was increased to 450 eV in order to provide for optimum comparability.

Even more critical is the number of k -points necessary for a calculation, since the integration over the Brillouin zone is substituted by a summation over a uniform k -point mesh. The errors due to this problem are not transferable, meaning the

<i>Transition metals</i>	Zn	Cd	Hg	Hg (nonrel.)
<i>E (eV)</i>	0.002	0.005	-0.014	0.013
<i>Chalcogenides</i>	O	S	Se	Te
<i>E (eV)</i>	-1.748	-0.928	-0.773	-0.641

Table 3.2: Atomic total energies in eV. The values for the chalcogenides were calculated including spin polarization.

same k -point mesh leads to completely different errors for different investigated structures. Hence, several bulk calculations were executed using the previously determined plane wave cutoff, to check for the total energy convergence with respect to the dimension of the needed k -point mesh.

3.2.2 Ground-state properties and transition pressures

To obtain the equilibrium crystal properties a full geometry optimization was carried out for different crystal structures of the group 12 chalcogenides allowing the program VASP to optimize the positions of the ions by minimizing the forces on those ions as mentioned in chapter 2.5.2. More specifically, the cell shape as well as the internal Wyckoff parameters of the respective crystal structures were allowed to relax while the cell volume was kept constant, hence calculating the total energy for different cell volumes. This method allows for independent optimization of the lattice parameters, where more than one structural variable characterizes the structure of the according polymorph.

The energy-volume relationships generated by those means, were employed to determine the structural properties by fitting them to the Murnaghan EOS. From this, one immediately obtains the pressure as $p = -dE/dV$, the equilibrium volume V_0 , the total energy per cation-anion pair E_0 , the bulk modulus B and the pressure coefficient B' (see also chapter 2.5.2).

Furthermore, from the total energy per cation-anion pair the cohesive energy was calculated by subtracting the respective atomic total energies. This means that experimental data for comparison is identical to the so-called heat of vapourization or atomization energy. The atomic total energies were obtained by carrying out single atom calculations for the according atoms in a well-defined box size using a plane-wave cutoff equivalent to the one used in the bulk calculations. Usually, a reference state inheriting spherical symmetry is chosen to create the pseudopotential for the atoms, which is subsequently set to zero energy. This works well for most atoms in their ground state. However, in contrast to the tran-

sition metals, the ground state for the chalcogenides is spin polarized according to Hund's law. Therefore, spin polarization was included in the treatment of O, S, Se and Te. Table 3.2 shows the respective energies for the atoms.

Unless otherwise stated, the transition pressure was estimated for the low temperature limit only, i.e. instead of the Gibbs free energy $G = U + pV - TS$ defining the crystal stability for a given temperature and pressure the enthalpy $H = E + pV$ is used, where $U(V) \approx E(V)$. The zero-point energy is neglected. The transition pressure then is received from the enthalpy-vs-pressure plot as the crossing of two curves of different crystal structures (see also chapter 2.5.3).

3.2.3 Determination of the electronic structure

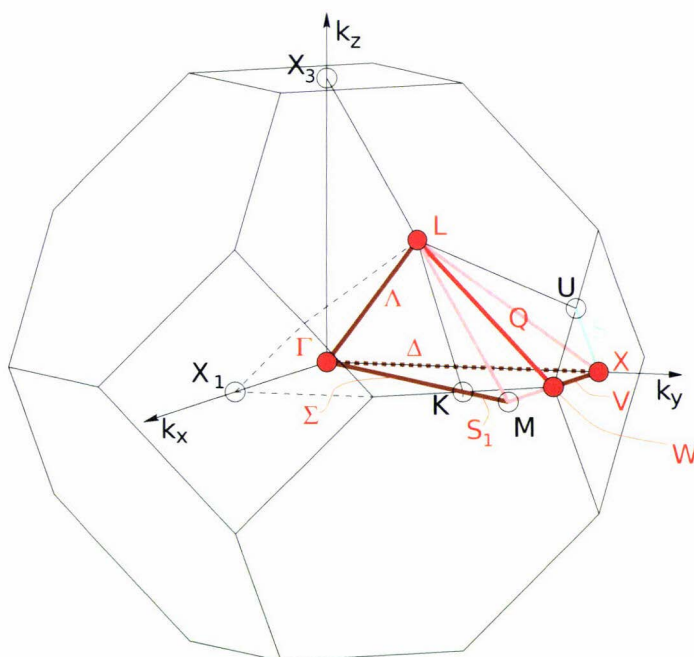


Figure 3.7: The Brillouin zone of the fcc lattice along with important k -points and paths within the Brillouin zone [84, 85].

Concerning the electronic structure calculations of the various crystals investigated, the corresponding band structures are derived directly from the eigenvalues of the Kohn-Sham equation [51]. Due to the density functional being chosen within the single-particle picture, this method implies an underestimation of the band gap and interband-transmission energies due to the neglect of excitations [94, 95]. However, it usually leads to surprisingly reasonable results for the dispersion and orbital character of the valence and conduction bands.

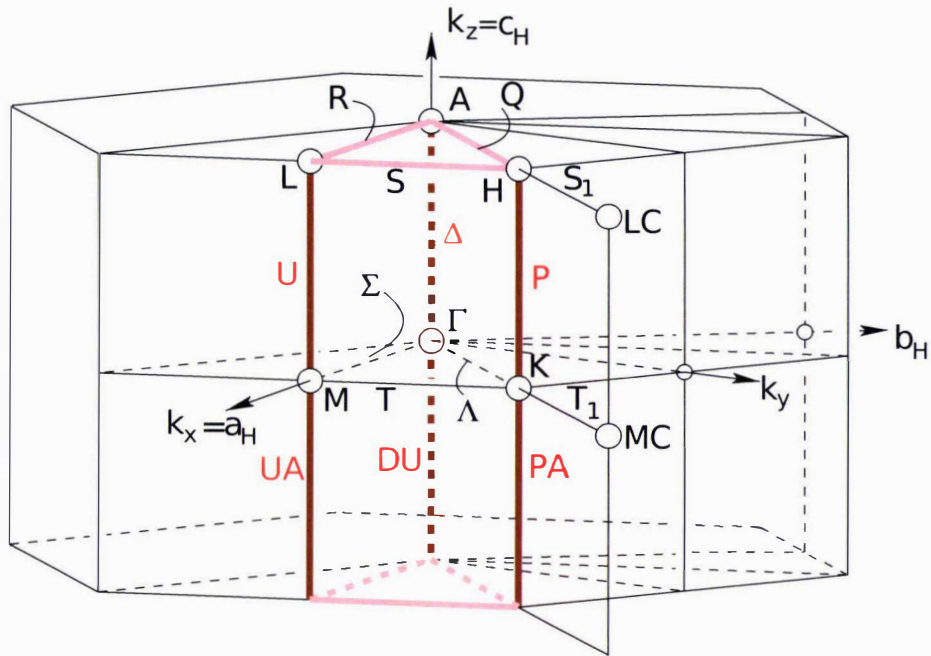


Figure 3.8: The Brillouin zone of the hexagonal primitive lattice along with important k -points and paths within the Brillouin zone [84, 85] .

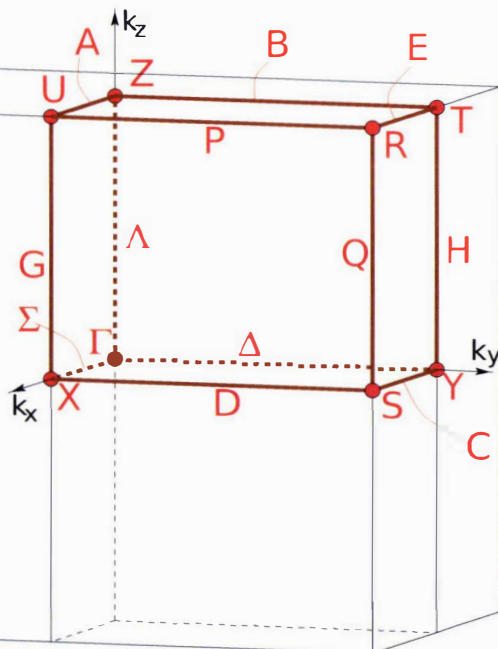


Figure 3.9: The Brillouin zone of the orthorhombic side-face centred lattice along with important k -points and paths within the Brillouin zone [84, 85] .

Hence, this method also allows for the calculation of the electronic density of states (DOS).

The path for the calculations of the band structure was chosen according to the Bilbao Crystallographic Server [84, 85]. For the picture of the Brillouin zone along with the respective k -vectors see fig. 3.7 for the fcc structures (rocksalt and zinc blende), fig. 3.8 for all primitive hexagonal lattices including cinnabar (due to the chosen hexagonal description) and fig. 3.9 for the orthorhombic side-face centred montroydite structure.

To calculate the electronic DOS, the tetrahedron method [96] is employed to integrate over the Brillouin zone while increasing the k -point mesh to $25 \times 25 \times 25$ for the fcc structures, $22 \times 22 \times 9$ for the primitive hexagonal lattices and to $15 \times 15 \times 23$ for the montroydite structure.

Note that the respective computations were only carried out for the ambient pressure structures of each group 12 chalcogenide. Furthermore, it is mentioned that the electronic gap depends considerably on the lattice constant. Hence, this limits the accuracy of the calculated gap energies and makes them very much dependent on the accuracy of the calculated lattice constant.

Chapter 4

The group 12 oxides

4.1 Occurring crystal structures

4.1.1 Zinc oxide

At room conditions zinc oxide exists in a wurtzite-type structure ($a = 3.2495 \text{ \AA}$ and $c = 5.2069 \text{ \AA}$ [12]) and can usually be found as a white powder. The naturally occurring mineral ranges in colour depending on defects and is called zincite. Bates *et al.* first described a transition upon appliance of pressure ($p_t = 10 \text{ GPa}$) into a site-ordered rocksalt structure and furthermore established that this phase can be stable at ambient conditions as well (by quenching from the transition pressure) [97]. Others however, report the transition to be fully reversible [98] despite a quite large hysteresis [99, 100], which made this transition very well investigated [99–106]. The transition is accompanied by a volume change ($\Delta V/V_0$) of 16.6 % [102] and the new phase has a lattice constant of $a = 4.280 \text{ \AA}$ [105]. Several theoretical studies confirm the properties of the ZnO phases and transition pressures are usually in good agreement. Qteish predicted RS-ZnO to be a wide band gap indirect semiconductor [107]. Another theoretical study by Azzaz *et al.*, who extended their investigation to the cinnabar, Cmc₂m, β -tin, NiAs, Immm and Imm2 structures as well, proved none of them to be stable compared to the wurtzite and rocksalt structure [108].

In chapters 4.2.1 and 4.3.1 the results for the zinc oxide equilibrium and high-pressure modifications are listed. There, the tables 4.1 and 4.4 will include the structural parameters and transition pressures determined by previous investigators (experimentally as well as theoretically) of the various structures as discussed

here as well.

4.1.2 Cadmium oxide

Cadmium oxide under ambient conditions adopts the rocksalt structure with a lattice constant of $a = 4.6942 \text{ \AA}$ [12]. It occurs naturally, yet rarely, as the mineral montepelite, which appears in the form of brown to red crystals.

For a long time, very little work had been done investigating the high-pressure behaviour of cadmium oxide. Even from a theoretical point of view only few data is available. Here the work of Majewski and Vogl should be mentioned, predicting a transition into the cesium chloride structure at 118.3 GPa [109]. Finally in 2004 Liu *et al.* confirmed the stability of the rocksalt phase experimentally up to 90 GPa, followed by a transition into the cesium chloride structure [110]. This is an excellent example of the importance of theoretical calculations stimulating experimental investigations.

Furthermore, the structures NiAs, Cmcm, cinnabar were ruled out as stable phases for CdO in the course of a comprehensive FP-LAPW DFT-GGA study by Guerrero-Moreno *et al.* [111].

Later (see chapters 4.2.2 and 4.3.2), the structural parameters and transition pressures of the cadmium oxide polymorphs obtained in the course of this thesis are summarized in tables 4.2 and 4.5. Those will also list the results of previous theoretical as well as experimental work for comparison.

4.1.3 Mercury oxide

At ambient pressure mercury oxide adopts two different structures. The low-temperature form has an orthorhombic structure with the space group $Pnma$, referred to as the montroydite phase after its naturally (but rarely) occurring mineral, which is known to have a yellow to reddish brown colour, depending on the grain size of the crystals. On the other hand there is the cinnabar form of HgO, stable at temperatures above 220°C and orange in colour.

Both forms are described by Aurivillius *et al.*, who found the structural parameters of the montroydite phase to be $a = 6.612 \text{ \AA}$, $b = 5.520 \text{ \AA}$ and $c = 3.521 \text{ \AA}$ with $x(\text{Hg}) = 0.115$, $z(\text{Hg}) = 0.245$, $x(\text{O}) = 0.36$ and $z(\text{O}) = 0.58$ [5]. The lattice constants of the cinnabar structure are $a = 3.577 \text{ \AA}$ and $c = 8.681 \text{ \AA}$, where $u(\text{Hg}) = 0.745$ and $v(\text{O}) = 0.46$, accordingly [6].

If the two structures are compared, the montroydite crystal consists of planar O-Hg-O-Hg zigzag chains lying in the a - c -plane and running parallel to the x -axis, while the cinnabar form consists of spiral chains running parallel to the z -axis. In both cases the O-Hg-O group is linear, but the Hg-O-Hg group is bent with the angle being 108.8° and 107.9° for montroydite and cinnabar, respectively. The Hg-O bond is 2.028 Å for the Pnma phase and 2.030 Å for the cinnabar form.

According to studies based on measuring the resistivity the cinnabar phase transforms into a metallic state at 10 GPa, possibly to the NaCl structure [112].

The orthorhombic montroydite form however, is first reported to transform into a tetragonal phase under compression of up to 20 GPa [10]. Zhou *et al.* support this observation in a combined Raman/ADX study ($p_t = 14$ GPa) and reported the structure to be site-ordered with the space group $I4/mmm$ and the lattice constants $a = 3.370$ Å and $c = 4.651$ Å at 19.3 GPa [11] (for atomic position see chapter 3.1). Despite the structure being incompatible with their Raman data, due to no other better suitable option $I4/mmm$ was regarded as the suitable description of the average structure, which was confirmed by Nelmes *et al.* ($p_t = 11.6$ GPa) later on [12].

Further pressure increase reveals yet another transition at 26-28 GPa (Raman and ADX measurements, respectively) to a metallic rocksalt phase [11, 12].

Tables 4.3 and 4.6 in chapters 4.2.3 and 4.3.3 will conclude the results for the structural parameters and transition pressures of the different mercury oxides phases. A summary of the parameters obtained in preceding experimental and theoretical investigations as discussed above will be included as well.

4.2 Equilibrium structures

4.2.1 Zinc oxide

Fig. 4.1 concludes the calculated energy-volume curves for the different crystal structures of ZnO, which confirm that zinc oxide at ambient conditions crystallizes in a wurtzite structure ($E_{coh} = 7.294$ eV/pair). With a ground-state volume of 24.70 Å³/pair the two lattice constants are determined to be $a = 3.279$ Å and $c = 5.304$ Å, and the internal Wyckoff parameter is $u = 0.3785$. Those structural parameters are in very good agreement with experimental ($a = 3.258$ Å, $c = 5.220$ Å and $u = 0.382$ [117]) and other published theoretical work ($a =$

Property	This work	Other theoretical	Experiments
<i>Wurtzite</i>			
a	3.279	3.283 ^a , 3.292 ^c , 3.198 ^d	3.258 ^e , 3.250 ^f
c	5.304	5.309 ^a , 5.292 ^c , 5.167 ^d	5.220 ^e , 5.204 ^f
c/a	1.618	1.617 ^a , 1.608 ^c , 1.616 ^d	1.602 ^e , 1.601 ^f
u	0.3785	0.3786 ^a , 0.3802 ^c , 0.379 ^d	0.382 ^e
V_0	24.70	24.78 ^a , 24.83 ^c , 22.88 ^d	23.99 ^e , 23.80 ^f
B_0	131.1	131.5 ^a , 133.7 ^c , 159.5 ^d	181 ^e , 183 ^f
B'	4.4	4.2 ^a , 3.8 ^c , 4.5 ^d	4 ^e , 4 ^f
E_{coh}	7.294	7.20 ^a , 7.69 ^c	7.52 ^b
p_t to RS	13.31	11.8 ^a , 13.3 ^g , 6.6 (9.3) ^h	8.7 ^f , 10 ⁱ , 9.8 ^j
<i>Zinc blende</i>			
a	4.622	4.627 ^a , 4.633 ^c , 4.504 ^d	-
V_0	24.68	24.77 ^a , 24.86 ^c , 22.84 ^d	-
B_0	130.9	131.6 ^a , 135.3 ^c , 160.8 ^d	-
B'	4.6	3.3 ^a , 3.7 ^c , 5.7 ^d	-
E_{coh}	7.282	7.19 ^a , 7.68 ^c	-

^aPAW-GGA from ref. [113], ^bfrom ref. [114], ^cfrom ref. [115], ^dfrom ref. [116],
^efrom ref. [117], ^ffrom ref. [102], ^gfrom ref. [107], ^hLDA (GGA) from ref. [104],
ⁱfrom ref. [97], ^jfrom ref. [99, 100]

Table 4.1: Ground-state properties of the equilibrium phases of ZnO. Presented are the lattice constants a and c (Å), internal parameter u , axial ratio c/a , ground-state volume V_0 (Å³/pair), bulk modulus B_0 (GPa) and its pressure derivative B' as well as the cohesive energy E_{coh} (eV/pair) and the transition pressure p_t (GPa) where applicable.

3.283 Å, $c = 5.309$ Å, $u = 0.3786$ [113]). For further properties see also table 4.1. The bulk modulus obtained amounts to 131.1 GPa (experimental value: 181 GPa [117]), whereas its pressure derivative is 4.4. The deviations in the bulk modulus are recorded in other theoretical investigations as well [113], and are most likely a finite temperature effect.

The zinc blende structure of ZnO was investigated as well, and we obtain a lattice constant of $a = 4.622$ Å ($V_0 = 24.68$ Å³/pair) and a cohesive energy of $E_{coh} = 7.282$ eV/pair. Hence, this crystal arrangement is very close to the wurtzite structure [113]. Yet, the energy difference of 12 meV/pair is big enough to confirm that the zinc blende structure is not accessible as an equilibrium phase. The bulk modulus is calculated to be 130.9 GPa and B' equals 4.6. Again, those results are in excellent agreement with previous theoretical studies (table 4.1), but there is no experimental data available.

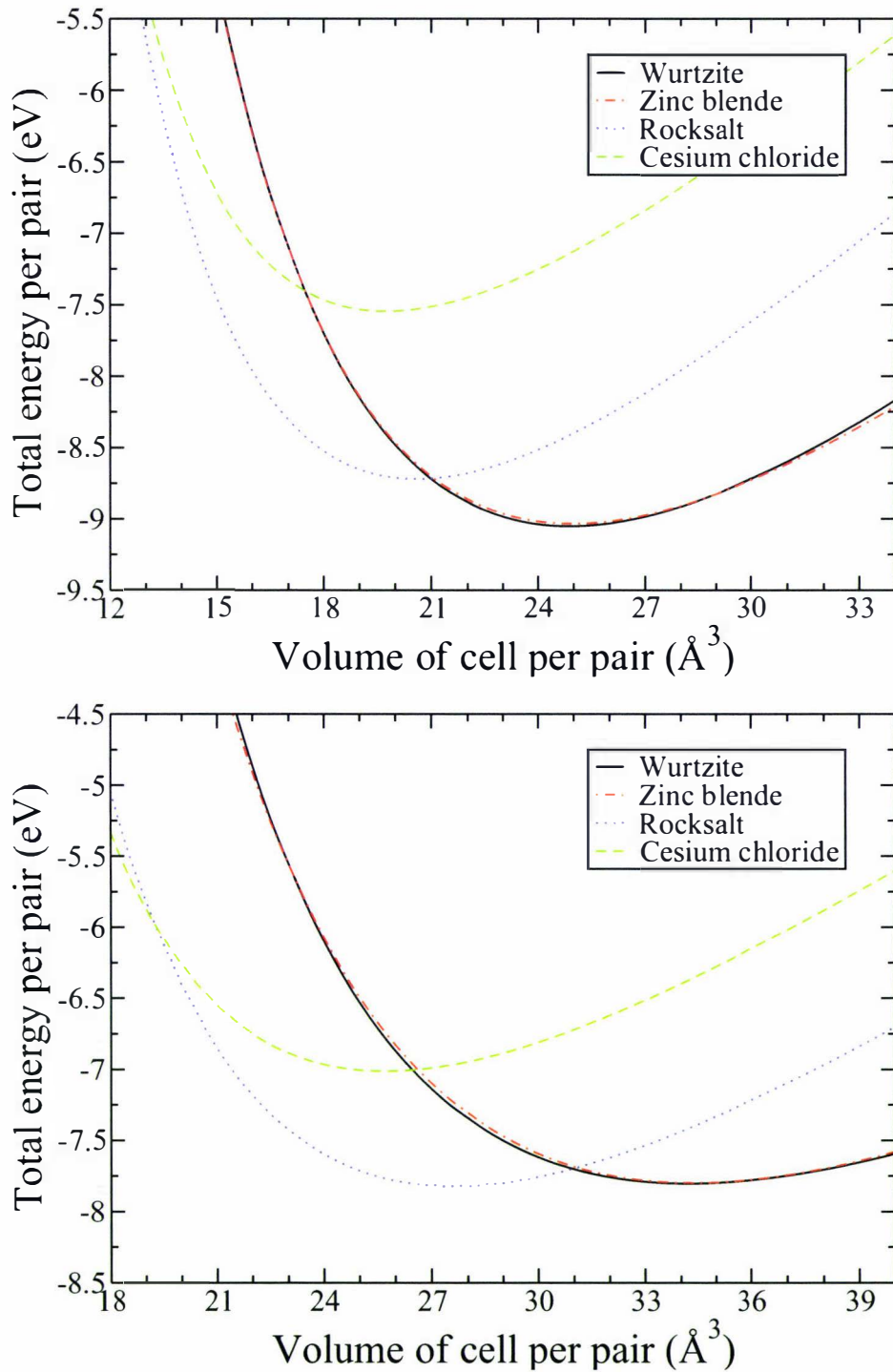


Figure 4.1: The total energy versus volume per cation-anion pair for different crystal structures of ZnO (upper panel) and CdO (lower panel).

Property	This work	Other theoretical	Experiments
<i>Rocksalt</i>			
a	4.779	4.779 ^a , 4.770 ^c	4.696 ^d , 4.694 ^e
V_0	27.29	27.29 ^a , 27.13 ^c	25.89 ^d , 25.86 ^e
B_0	130.1	130.5 ^a , 130 ^c	148 ^d ,
B'	4.0	35.0 ^a , 4.1 ^c	4 ^d
E_{coh}	6.091	6.00 ^a , 5.30 ^c	6.40 ^b
p_t to CC	84.24	85 ^a , 89 ^d	90 ^f
<i>Wurtzite</i>			
a	3.641	3.678 ^a , 3.660 ^c	-
c	5.946	5.825 ^a , 5.856 ^c	-
c/a	1.633	1.584 ^a , 1.600 ^c	-
u	0.3767	0.3849 ^a , 0.3500 ^c	-
V_0	34.14	34.12 ^a , 33.97 ^c	-
B_0	93.9	92.7 ^a , 86 ^c	-
B'	4.1	4.7 ^a , 4.5 ^c	-
E_{coh}	6.067	5.97 ^a , 5.30 ^c	-
<i>Zinc blende</i>			
a	5.149	5.148 ^a , 5.150 ^c	-
V_0	34.13	34.11 ^a , 34.15 ^c	-
B_0	94.3	93.9 ^a , 82 ^c	-
B'	4.4	5.0 ^a , 3.0 ^c	-
E_{coh}	6.046	5.96 ^a , 5.18 ^c	-

^aPAW-GGA from ref. [113], ^bfrom ref. [114], ^cfrom ref. [111], ^dfrom ref. [118],
^efrom ref. [12], ^ffrom ref. [110]

Table 4.2: Ground-state properties of the equilibrium phases of CdO. Presented are the lattice constants a and c (Å), internal parameter u , axial ratio c/a , ground-state volume V_0 (Å³/pair), bulk modulus B_0 (GPa), its pressure derivative B' as well as the cohesive energy E_{coh} (eV/pair) and the transition pressure p_t (GPa) where applicable.

4.2.2 Cadmium oxide

The results presented here, correctly predict the equilibrium structure of CdS to be rocksalt with a cohesion energy of 6.091 eV, as can be derived from fig. 4.1. A lattice parameter of $a = 4.779$ Å is obtained along with a ground-state volume of 27.20 Å³/pair in good agreement with experimental values ($a = 4.696$ Å [118]). Other theoretical calculations yield very similar results ($a = 4.779$ Å [113]). The determined cohesion energy, the bulk modulus and its pressure derivative ($B_0 = 130.1$ GPa, $B' = 4.0$) also compare rather well to previously published data. For details see table 4.2.

Furthermore, the investigation of the energy-volume curves for the wurtzite and

zinc blende phase were included in the calculations. The property values are listed in table 4.2 as well and are in excellent agreement with other theoretical studies. Again, the cohesive energies of both phases are fairly alike with a difference of 21 meV/pair, indicating their structural similarity.

The cohesive energies are also rather similar to the one obtained for rocksalt. The difference in energy is 25 meV/pair. However, from the energy differences obtained between for instance the wurtzite and zinc blende structure concerning the discussion of the group 12 chalcogenides in general and comparing it to what is experimentally observed, it is safe to say that the energy difference is large enough to rule out the zinc blende as well as the wurtzite structure as an equilibrium phase in CdO.

4.2.3 Mercury oxide

As explained above HgO exists under normal conditions in a so-called montroydite as well as a cinnabar form. This is confirmed by figure 4.2, which shows two very close lying energy curves for the two modifications with cohesive energies of 4.036 and 4.029 eV/pair, respectively. The energy difference is very small with only 7 meV/pair.

For the montroydite phase lattice constants of $a= 6.747$ Å, $b= 5.779$ Å, and $c= 3.697$ Å are obtained with the parameters $x(\text{Hg})= 0.112$, $z(\text{Hg})= 0.243$, $x(\text{O})= 0.360$, $z(\text{O})= 0.571$ for the orthorhombic structure. This compares very well to experiments, where the following structural parameters are determined: $a= 6.612$ Å, $b= 5.520$ Å, $c= 3.521$ Å, Wyckoff positions $x(\text{Hg})= 0.112$, $z(\text{Hg})= 0.243$, $x(\text{O})= 0.358$ and $z(\text{O})= 0.587$ [10]. It is also in good agreement with another theoretical PBE study attaining lattice constants of $a= 6.74$ Å, $b= 5.68$ Å and $c= 3.68$ Å [7]. However, in this work no other parameters and properties are given. For the bulk modulus and its pressure derivative the values $B_0 = 20.7$ GPa and $B' = 9.7$ are obtained, compared to $B_0 = 44$ GPa and $B' = 7$ in an experimental reference [11]. However, in the experiment the same Murnaghan fit was used for the montroydite modification as well as for the high-pressure phase.

Turning now to the cinnabar phase, the calculations presented here, find the lattice parameters $a= 3.745$ Å and $c= 8.968$ Å along with the Wyckoff parameters $u(\text{Hg})= 0.745$, and $v(\text{O})= 0.414$, all in reasonable agreement with the experimental results [6].

In general, the discrepancies in the values are acceptable considering the very shallow potential curve (see fig. 4.2) expressed by the very small bulk moduli.

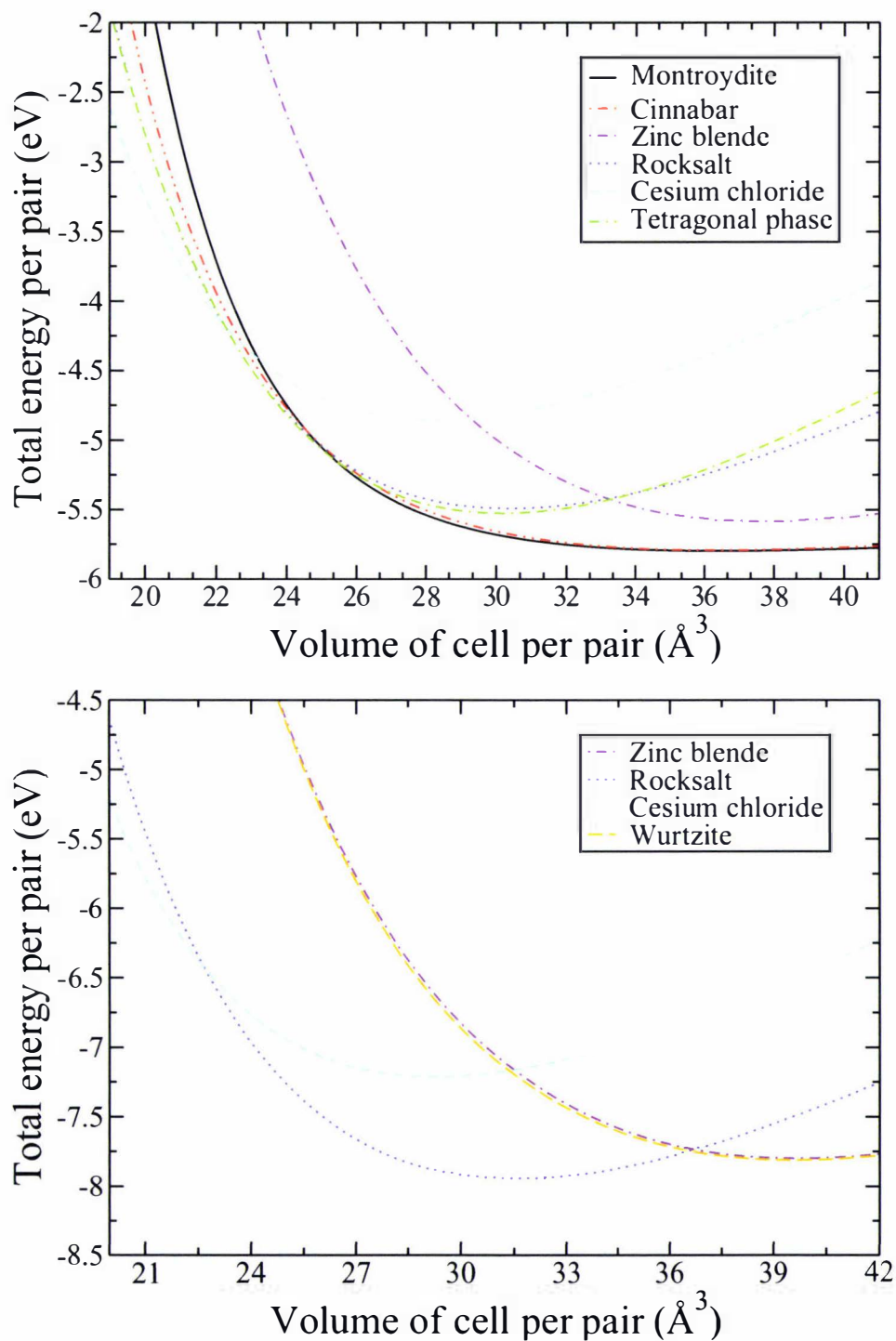


Figure 4.2: The total energy versus volume per cation-anion pair for different crystal structures of relativistic (upper panel) and nonrelativistic Hg₀ (lower panel).

Property	This work	Other theoretical	Experiments
<i>Montroydite</i>			
a	6.747	6.74 ^a	6.612 ^b
b	5.784	5.68 ^a	5.520 ^b
c	3.693	3.68 ^a	3.521 ^b
b/a	0.857	0.843 ^a	0.835 ^b
c/a	0.547	0.546 ^a	0.533 ^b
$x(\text{Hg})$	0.1120		0.112 ^b
$z(\text{Hg})$	0.2430		0.243 ^b
$x(\text{O})$	0.3595		0.358 ^b
$z(\text{O})$	0.5707		0.587 ^b
V_0	36.04	35.22 ^a	32.13 ^b
B_0	20.7		44 ^c
B'	9.7		7 ^c
E_{coh}	4.036		
p_t to I4/mmm	25		10 ^b , 14 ^c , 11.6 ^d
<i>Cinnabar</i>			
a	3.745		3.577 ^e
c	8.968		8.681 ^e
c/a	2.395		2.427 ^e
$u(\text{Hg})$	0.7450		0.745 ^e
$v(\text{O})$	0.4141		0.460 ^e
V_0	36.39		32.07 ^e
B_0	20.5		
B'	5.9		
E_{coh}	4.029		
<i>Zinc blende</i>			
a	5.309		5.43 ^f
V_0	37.41		40.03 ^f
B_0	82.1		
B'	5.5		
E_{coh}	3.825		
^a PAW-PBE from ref. [7], ^b from ref. [10], ^c from ref. [11], ^d from ref. [12], ^e from ref. [6], ^f from ref. [119]			

Table 4.3: Ground-state properties of the equilibrium phases of HgO. Presented are the lattice constants a , b and c (Å), respective internal parameters, ground-state volume V_0 (Å³/pair), bulk modulus B_0 (GPa) and its pressure derivative B' as well as the cohesive energy E_{coh} (eV/pair) and the transition pressure p_t (GPa) where applicable.

Nevertheless, we accurately predict these two crystal structures as low pressure modifications. Further details can be viewed in table 4.3.

Mercury oxide in a zinc blende structure was also calculated in the course of this

study. The lattice constant obtained is $a = 5.309 \text{ \AA}$ along with $B_0 = 82.1 \text{ GPa}$ and $B' = 5.5$. Proposed as a metastable sphalerite phase in shock-compression experiments on HgO by Ovsyannikova *et al.* ($a = 5.43 \text{ \AA}$) [119], the calculated bond distances are overestimated. This is most likely due to the difficulties in examining metastable phases in general, or to the density functional approximation used. Compared to the cinnabar and montroydite form its cohesive energy of 3.825 eV/pair is too high to find this modification as an equilibrium phase.

4.3 High-pressure phases

4.3.1 Zinc oxide

Property	This work	Other theoretical	Experiments
<i>Rocksalt</i>			
a	4.334 (4.225)	4.334 ^a , 4.345 ^b	4.271 ^c , 4.211 ^d 4.275 ^e
V_0	20.35 (18.85)	20.35 ^a , 20.51 ^b	19.48 ^c , 18.67 ^d , 19.53 ^e
B_0	168.5	167.8 ^a , 172.7 ^b	228 ^c , 194 ^e
B'	5.5	5.3 ^a , 3.7 ^b	4 ^c , 9 ^d , 4.8 ^e
E_{coh}	6.997	6.91 ^a , 7.46 ^b	
p_t to CC	261.25	261 ^a , 256 ^b , 265 ^f	
<i>Cesium chloride</i>			
a	2.690 (2.350)	2.690 ^a , 2.705 ^b	
V_0	19.46 (12.98)	19.46 ^a , 19.79 ^b	
B_0	161.9	162.4 ^a , 156.9 ^b	
B'	4.6	4.7 ^a , 3.8 ^b	
E_{coh}	5.838	5.76 ^a , 6.33 ^b	

^aPAW-GGA from ref. [113], ^bfrom ref. [115], ^cfrom ref. [102], ^dat 10 GPa from ref. [105], ^e from ref. [103], ^fFP-LAPW LDA from ref. [108].

Table 4.4: Ground-state properties of the high-pressure phases of ZnO. Presented are the lattice constant a (Å), ground-state volume V_0 (Å³/pair), bulk modulus B_0 (GPa) and its pressure derivative B' as well as the cohesive energy E_{coh} (eV/pair) and the transition pressure p_t (GPa) where applicable. Values in brackets indicate higher pressure.

Looking at the energy-volume relationship shown in fig. 4.1 it already becomes obvious that the equilibrium wurtzite phase undergoes a transition to the cubic rocksalt structure with increasing pressure. The enthalpy-pressure dependencies derived from those results confirm this and predict the pressure for this transition to be 13.31 GPa, which is in reasonable agreement with previous theoretically

and experimentally obtained transition pressures (see table 4.1).

The structural ground-state properties for this high-pressure modification are: $a = 4.334$ Å, $B_0 = 168.5$ GPa and $B' = 5.5$, whereas the cohesive energy is 6.997 eV in accordance with other theoretical work (e.g. $a = 4.334$ Å, $B_0 = 167.8$ GPa, $B' = 5.3$, $E_{coh} = 6.91$ eV using the PW91 functional as well [113]). The deviations from experimental values are slightly higher, see table 4.4. However, if the lattice constant is determined at 15.98 GPa ($a = 4.225$ Å), the agreement improves. Furthermore, the pressure derivative B' is not in agreement with the findings by Gerward and Staum Olsen, but the unusually high value of 9 reported by them for the wurtzite and rocksalt polymorphs¹, was partially blamed on experimental difficulties in measuring the pressure in the transition region [105].

At 261.25 GPa, the results presented here predict another pressure-induced transition, which is in excellent concordance with earlier published calculations [108, 113]. The crystallographic arrangement changes towards the cesium chloride structure with a lattice constant of 2.690 Å at zero pressure and 2.235 Å at 162.67 GPa. This and other properties again compare very well to other theoretical work. For details see table 4.4. However, due to the extremely high pressure predicted no experimental data is available yet.

4.3.2 Cadmium oxide

Property	This work	Other theoretical	Experiments
<i>Cesium chloride</i>			
a	2.938 (2.650)	2.94 ^a	2.86 ^b
V_0	25.37 (18.61)	25.41 ^a	23.39 ^b
B_0	130.5	114 ^a	169 ^b
B'	4.4	4.66 ^a	4.66 ^b
E_{coh}	5.291	4.47 ^a	

^aGGA from ref. [111], ^bfrom ref. [110].

Table 4.5: Ground-state properties of the high-pressure phases of CdO. Presented are the lattice constant a (Å), ground-state volume V_0 (Å³/pair), bulk modulus B_0 (GPa) and its pressure derivative B' as well as the cohesive energy E_{coh} (eV/pair). Values in brackets indicate higher pressure.

With increasing pressure CdO undergoes a phase transition from the equilibrium rocksalt phase to the cesium chloride structure, see fig. 4.1. Concluded from

¹A typical value for materials like ZnO is 4.

Property	This work	Experiments
<i>I₄/mmm</i>		
<i>a</i>	3.517	3.370 ^a
<i>c</i>	4.854	4.651 ^a
<i>c/a</i>	1.380	1.380
<i>V</i>	30.02	32.15 ^a
<i>B</i> ₀	110.6	44 ^a
<i>B</i> '	5.9	7 ^a
<i>E</i> _{coh}	3.754	
<i>Rock:salt</i>		
<i>a</i>	4.937	
<i>V</i>	30.08	
<i>B</i> ₀	112.3	
<i>B</i> '	3.8	
<i>E</i> _{coh}	3.742	
<i>Cesium chloride</i>		
<i>a</i>	3.028	
<i>V</i>	27.77	
<i>B</i> ₀	120.8	
<i>B</i> '	5.3	
<i>E</i> _{coh}	3.116	
^a Raman/ADX from ref. [11] at 19.3 GPa.		

Table 4.6: Ground-state properties of the high-pressure phases of HgO. Presented are the lattice constants *a* and *c* (Å), axial ratio *c/a*, bulk modulus *B*₀ (GPa) and its pressure derivative *B*', together with the transition pressure *p*_t (GPa). No other theoretical data is available.

the enthalpy versus pressure curves, the transition occurs at 84.24 GPa, which supports the experiment carried out by Liu *et al.* [110], who obtained 90 GPa. The structural parameters (*a* = 2.938 Å, *B*₀ = 130.5 GPa, *B*' = 4.4) as well as the transition pressure are in excellent agreement with a theoretical investigation by Guerrero-Moreno *et al.* [111], but show the general underestimation of the bulk modulus compared to the experiment. At a higher pressure of 83.70 GPa the lattice constant is *a* = 2.650 Å. For a listing of all parameters the reader is referred to table 4.5. Hence, there is nothing surprising for CdO. It is however less stable than ZnO.

4.3.3 Mercury oxide

Compared to ZnO and CdO a completely different picture is found for the high-pressure phases of mercury oxide, just like for the equilibrium phases. Here, a

transition at 25 GPa from the orthorhombic montroydite form into the tetragonal I4/mmm structure is determined.

The lattice constants are $a = 3.517$ and $c = 4.854$ Å, which confirms that the c/a ratio in this structure differs only slightly from the optimum value of $\sqrt{2}$. Those values are furthermore in good agreement with experiment ($a=3.370$ Å, $c=4.651$ Å, $c/a=1.380$ at 19.3 GPa; $p_t=14$ GPa [11]). The agreement of the experimentally obtained bulk modulus and B' , where the calculations presented here derive values of 110.6 GPa and 5.9, respectively, is not as good. However, this can be attributed to the use of the same fit for both the montroydite and I4/mmm phase in the experiment. To the best of our knowledge no theoretical references are available.

Another pressure induced transition is predicted to happen around 28 GPa into the metallic rocksalt structure with an according ground-state lattice constant of 4.937 Å.

Subsequently, the rocksalt structure undergoes a transition into the cesium chloride structure with a lattice constant of $a = 3.028$ Å at zero pressure. This transition predicted at 57 GPa has not been found or predicted yet, but fits perfectly into the lineup of those semiconductors. However, another transition into an intermediate phase following the rocksalt modification cannot be ruled out. Other structural parameters for the high-pressure phases rocksalt and cesium chloride can be obtained from table 4.6.

4.4 Electronic structure

4.4.1 Zinc oxide

The band structure and DOS calculated for the wurtzite structure using the scalar-relativistic approach is shown in the upper panel of fig. 4.3.

According to this graph this equilibrium phase of ZnO needs to be categorized as a typical semiconductor, which exhibits a direct gap with an energy of 0.75 eV at the Γ -point of the Brillouin zone. However, further local valence-band maxima (VBM) at A (-0.37 eV) and H (-1.19 eV) are found as well as other conduction-band minima (CBM), which appear at A (3.37 eV) and between L and M (5.38 eV), making the next direct transition possible at the A -point with a significantly higher gap energy.

The band structure calculated is in very good agreement with other theoretical

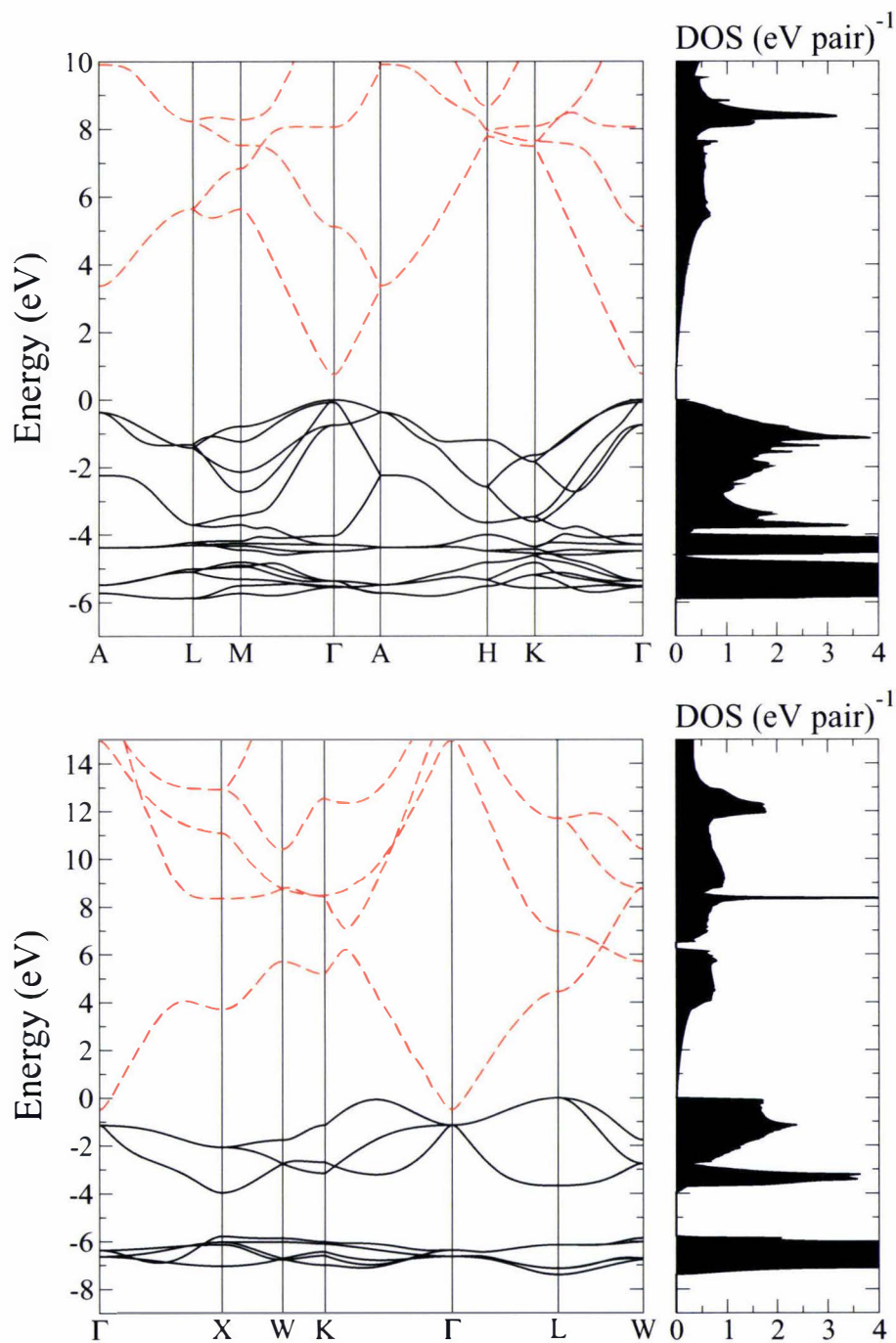


Figure 4.3: Band structure and density of states (normalized per pair) at zero pressure for the ZnO polymorph wurtzite (upper panel) and the CdO polymorph rocksalt (lower panel) calculated within the scalar-relativistic DFT-GGA framework. The valence-band maximum is set to zero energy. The black solid lines indicate the valence and the red dashed lines the conducting bands, respectively.

findings, e.g. Schleife *et al.* with $E_g(\Gamma) = 0.73$ eV [113]. Yet, the method used largely underestimates the band gap, which is measured to be about 3.44 eV in a two-photon absorption experiment at 6 K [120]. This value is confirmed by Vogel *et al.*, who employed the more sophisticated self-interaction-corrected scheme [120].

4.4.2 Cadmium oxide

The electronic structure as depicted in the lower panel of fig. 4.3 shows the equilibrium rocksalt modification of CdO at the scalar-relativistic level as a half-metal.

A direct gap of 0.66 eV is found at the centre of the Brillouin zone in excellent agreement with another calculated result using DFT-GGA (0.66 eV [113]). The VBM are located at the L -point (set to 0 eV) and along the Σ -line between Γ and K (-0.07 eV). Both of those maxima however, lie above the CBM causing negative indirect band-gaps of -0.49 and -0.42 eV, respectively. The CBM is found at the Γ -point. Those values are in accordance with another GGA study, where 0.51 and 0.43 eV are obtained [113].

In contrast, experiments suggest a semiconductor, which has positive direct as well as indirect gaps ($E_g^{dir}(\Gamma) = 2.28$ eV, $E_g^{ind}(L - \Gamma) = 0.84$ eV, $E_g^{ind}(\Sigma - \Gamma) = 1.09$ eV [120]). Self-interaction corrected calculations determine $E_g^{ind}(L - \Gamma) = 1.7$ eV, hence predicting the correct electronic behaviour. The deviations to the present study are due to the severe underestimation of band gaps in the DFT formalism. Furthermore, a DFT study by Boettger shows that, while relativistic corrections have little impact on the bulk properties, they do influence the electronic structure. Using a nonrelativistic description, CdO is predicted to have a small band gap, whereas the scalar-relativistic picture incorrectly suggests a semi-metallic state. The effect of spin-orbit splitting was proven to be negligible [121].

4.4.3 Mercury oxide

HgO in its ground-state montroydite form through photoconductivity measurements is established to be a n-type II-VI semiconductor [11] with a band gap of approximately 2.19 [122] to 2.80 eV [123]. Even though this result is qualitatively confirmed by a theoretical LDA study by means of the scalar-relativistic

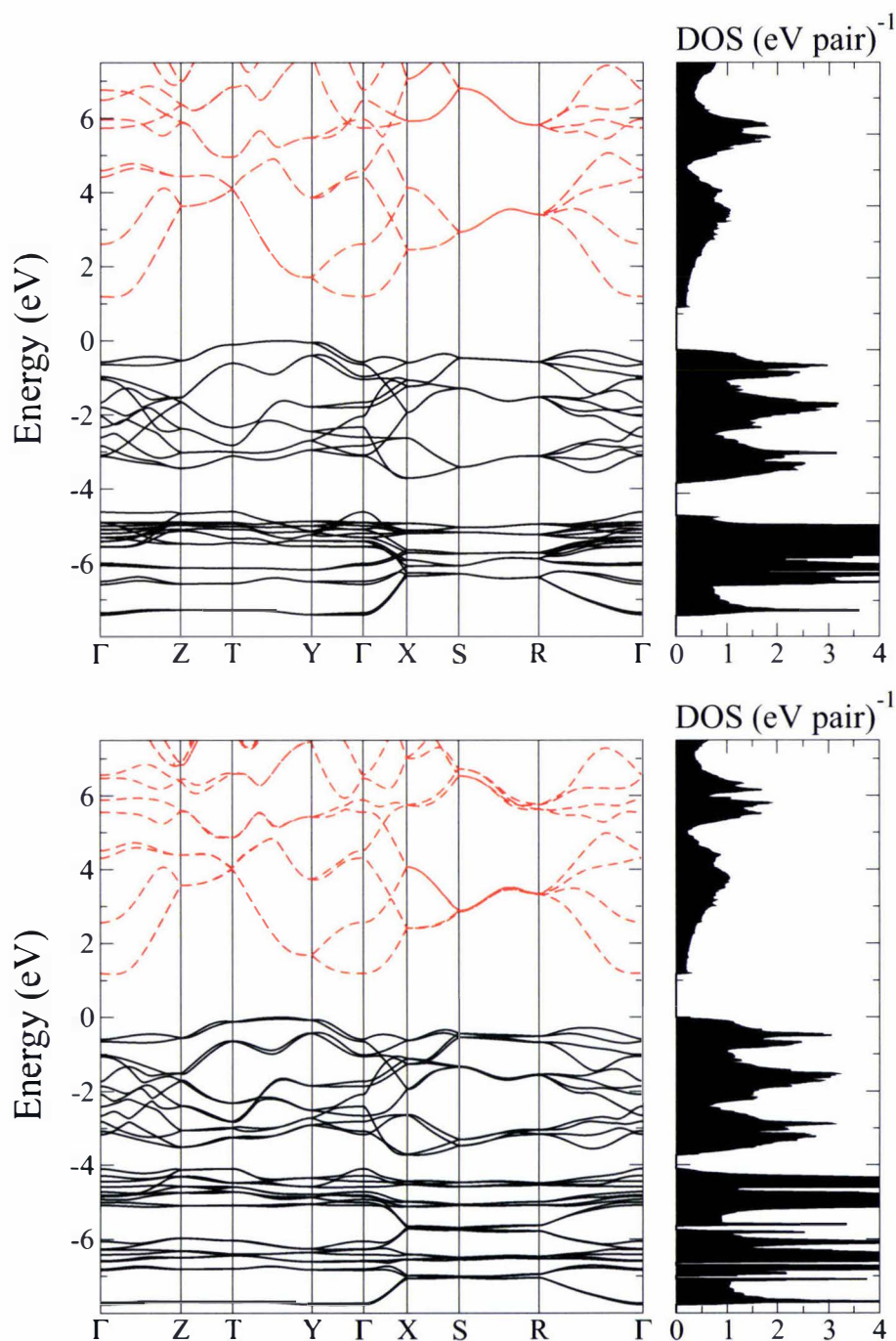


Figure 4.4: Band structure and density of states (normalized per pair) at zero pressure for the HgO montroydite polymorph calculated within the scalar-relativistic DFT-GGA framework (upper panel) as well as upon inclusion of spin-orbit effects (lower panel). The valence-band maximum is set to zero energy. The black solid lines indicate the valence and the red dashed lines the conducting bands, respectively.

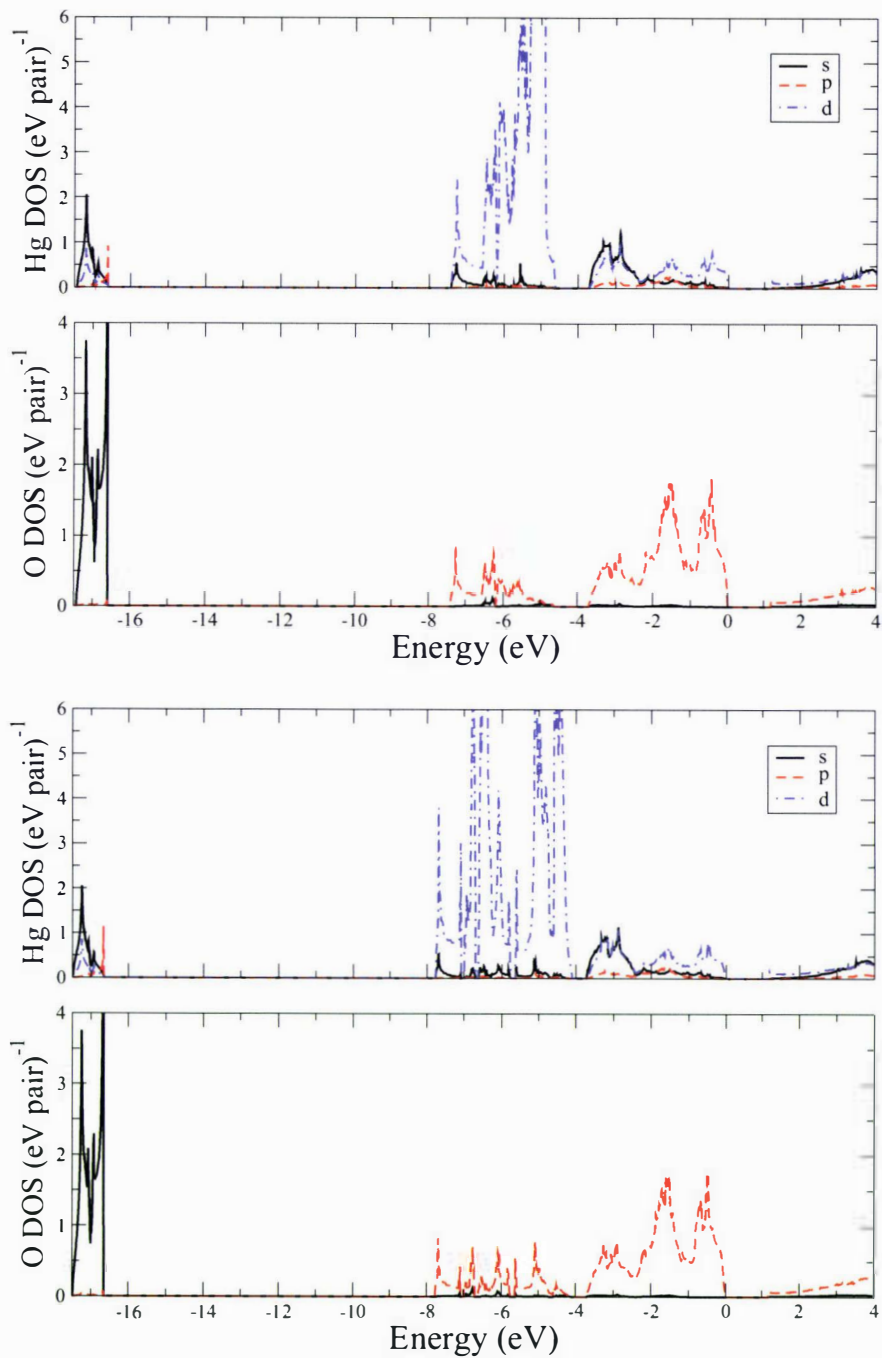


Figure 4.5: Site-projected density of states at zero pressure for the HgO montroydite polymorph calculated within the scalar-relativistic DFT-GGA framework (upper panel) as well as upon inclusion of spin-orbit effects (lower panel). The black solid, red dashed and blue dash-dotted line indicate the s, p and d site-projected DOS, respectively.

tight-binding linear muffin-tin orbital atomic sphere approximation as cited in ref. [11], it nevertheless features the underestimation of the band gap, commonly occurring for the applied DFT methods. Hence, they yield an indirect band gap of 1.33 eV only.

Using the scalar-relativistic approach, the semiconductor character as well as the indirect band gap are confirmed with the VBM and CBM occurring at the H line between T and Y and at the Λ line between Γ and Z , respectively. Consequently, a fundamental gap of 1.18 eV is calculated in good agreement with ref. [11]. Several other indirect as well as direct transitions are possible at slightly higher energies, the first possible direct transition at the Δ line between Y and Γ at an energy of 1.49 eV. To view the scalar-relativistic electronic structure of HgO in its montroydite phase as well as the site-projected DOS see the upper panels of figs. 4.4 and 4.5.

Even though this is in concordance with the theoretical findings mentioned above, it neglects spin-orbit coupling. The relativistic expansion of the $5d_{5/2}$ -band in mercury is expected to lead to a substantial mixing with the $6s$ -band and one has to consider the spin-orbit splitting in the empty $6p$ bands as well. Looking at the band structure and DOS calculated with the inclusion of spin-orbit coupling (cf. lower panel of fig. 4.4) the VBM and CBM are still located at the H line between T and Y and the Λ line between Γ and Z . However, the band gap is marginally decreased to 1.17 eV. This also holds for a possible direct transition (at the Δ line between Y and Γ with a gap energy of 1.50 eV), meaning the values develop even further away from the experimental values.

This result deviates from the statement in a publication [124], where as a first-order approximation the charge density relaxed within the scalar-relativistic approach was used leading to the false conclusion that the method used characterizes HgO as a metal if spin-orbit coupling is included. This false description of GGA in terms of an underestimation of the band gap, is actually well-known in Mott-insulators in transition metal oxides [125] and for the δ -phase of solid plutonium [126] as discussed in detail in ref. [125]. Rather strong correlation effects in these transition metal oxides are to be blamed and make further investigations using methods like LDA+U desirable [127]. Yet, it does not explain the strong deviation in the band structure calculation if the scalar-relativistic charge density is used as a starting point for the spin-orbit coupling calculations. Further investigations are under way to explain this behaviour.

Turning now to the cinnabar modification of HgO, an indirect semiconductor is found as the result of both the calculations excluding and including spin-orbit

effects as indicated by fig. 4.6. In both cases the VBM is situated between the A - and L -point, followed by two very close lying maxima between A and H at (-0.01 and -0.009 eV with and without spin-orbit coupling, respectively) and A and Γ (-0.03 and -0.009 eV with and without spin-orbit coupling, respectively). The CBM is located close to the centre of the Brillouin zone (to be more specific towards the M -direction) leading to a fundamental gap energy of 1.29 and 1.32 eV considering and neglecting spin-orbit coupling, respectively. The first possible direct transition is extremely close in energy (1.38 and 1.39 eV with and without spin-orbit coupling, respectively).

In general, the electronic structure looks rather similar to the one obtained for the montroydite phase, which can be explained by the structural similarity of the chain-like constitution, confirmed in the close lying energy-volume curves (see fig. 4.2). Seemingly, no other data of the band structure of cinnabar-HgO could be found to compare with.

From the display of the Hg site-projected DOS in figs. 4.5 and 4.7 it becomes obvious that for both the montroydite and the cinnabar modification the electronic structure upon inclusion of spin-orbit coupling becomes far more complex. However, since the spin-orbit splitting mainly occurs in the lower lying d -bands, the semiconducting character as well as the gap energy are not significantly altered. A prominent splitting of the Hg core- $5d$ band into the $5d_{3/2}$ and $5d_{5/2}$ contributions is evident, where the energy difference is about 2 eV. This agrees nicely with the atomic level splitting of 1.86 eV in the Hg^+ atom [128]. However, an additional superposition with the crystal-field splitting can be seen. This should be investigated further by spectroscopic methods. The Fermi edge has dominantly O $2p$ and Hg $5d$ character.

4.5 Relativistic influences

4.5.1 Equilibrium structure

If relativistic effects for mercury oxide are neglected we find a completely different structural behaviour. Figure 4.2 shows that in this case, the structure found under ambient conditions is the rocksalt arrangement.

Here the obtained lattice constant a is 4.996 Å, which is in fact by 15% and by 4% larger than the lattice constant for the respective modification in ZnO and CdO, indicating the suppression of the typical relativistic contraction by the crystal

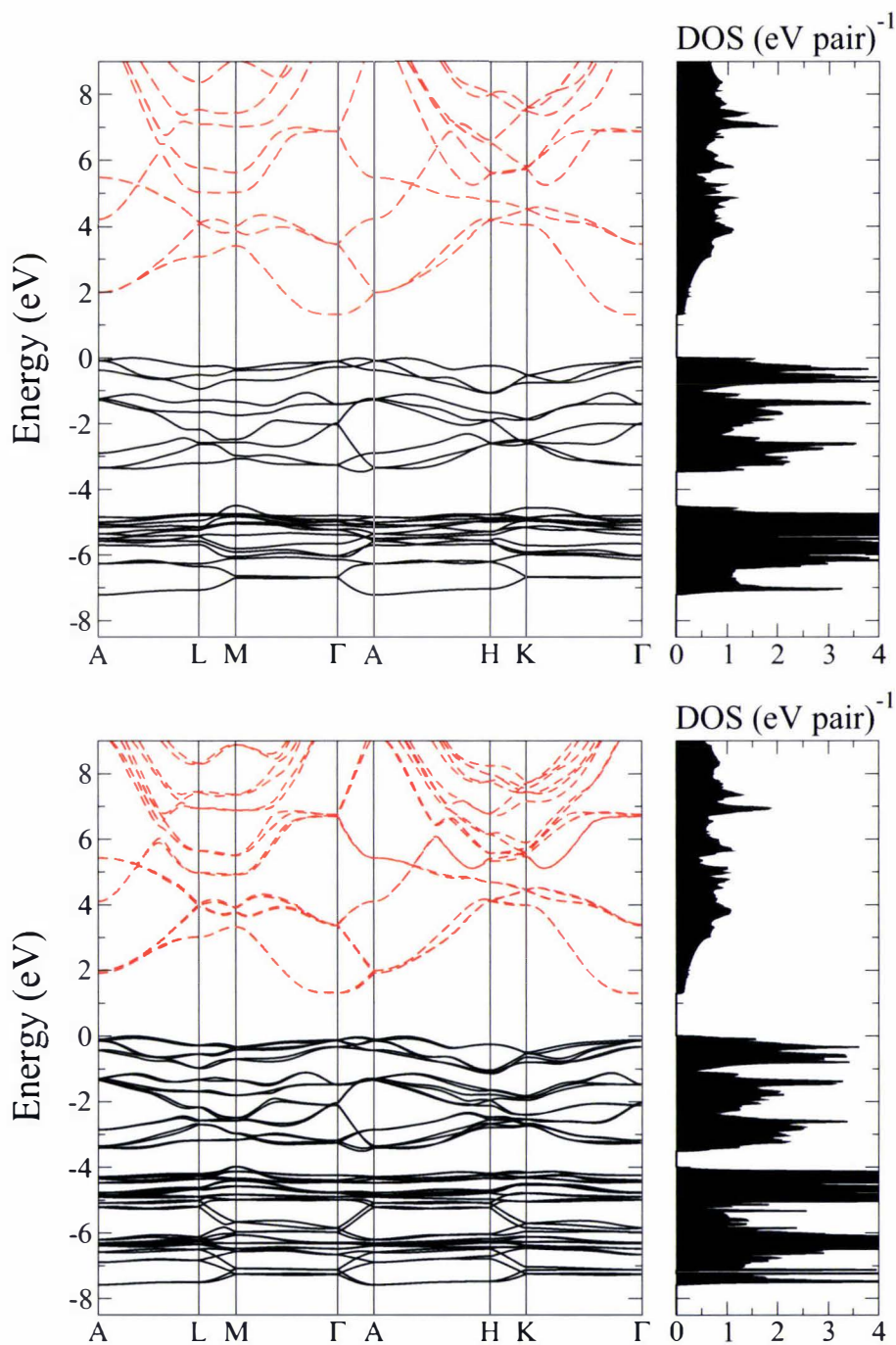


Figure 4.6: Band structure and density of states (normalized per pair) at zero pressure for the HgO cinnabar polymorph calculated within the scalar-relativistic DFT-GGA framework (upper panel) as well as upon inclusion of spin-orbit effects (lower panel). The valence-band maximum is set to zero energy. The black solid lines indicate the valence and the red dashed lines the conducting bands, respectively.

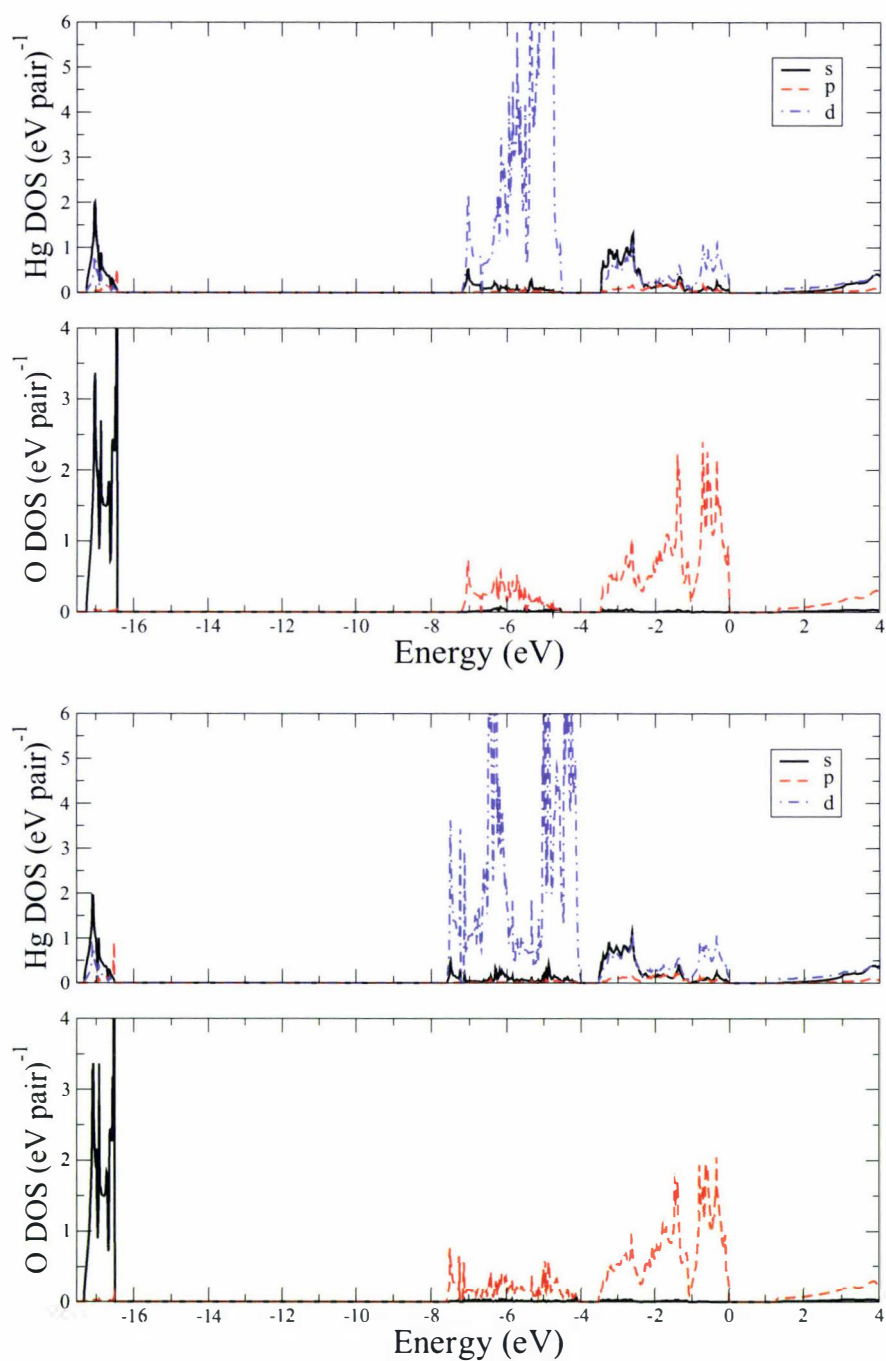


Figure 4.7: Site-projected density of states at zero pressure for the HgO cinnabar polymorph calculated within the scalar-relativistic DFT-GGA framework (upper panel) as well as upon inclusion of spin-orbit effects (lower panel). The black solid, red dashed and blue dash-dotted line indicate the s, p and d site-projected DOS, respectively.

System	ZnO		CdO		HgO		nonrel. HgO	
	d_{MO}	d_{MM}	d_{MO}	d_{MM}	d_{MO}	d_{MM}	d_{MO}	d_{MM}
Wurtzite	2.00	3.26	2.23	3.61			2.33	3.85
exp.	1.98	3.21	-	-	-	-	-	-
Zinc blende	2.00	3.27	2.23	3.64	2.30	3.75	2.34	3.82
exp.	-	-	-	-	2.35	3.84	-	-
Rocksalt	2.17	3.07	2.39	3.38	2.47	3.49	2.50	3.53
exp.	2.14	3.02	2.35	3.32	-	-	-	-
Montroydite	-	-	-	-	2.06	3.38	-	-
exp.	-	-	-	-	2.03	3.31	-	-
Cinnabar	-	-	-	-	2.07	3.33	-	-
exp.	-	-	-	-	2.03	3.30	-	-

Table 4.7: Closest metal-oxygen bond distance d_{MO} and closest metal-metal distance d_{MM} in Å of the respective equilibrium structures of the group 12 oxides.

field. In addition, the nonrelativistic cohesive energy of 6.20 eV/pair exceeds the relativistic value by more than 2 eV/pair. This is especially interesting, since this rather large relativistic lattice destabilization goes along with a huge relativistic *contraction* of 0.343 Å in the intra-chain Hg-O bond distance compared to the montroydite equilibrium structure of relativistic HgO (see table 4.7 for metal-oxygen and metal-metal distances). For the purpose of comparison, this fact causes the bond distance in HgO to be actually just as small as the ZnO bond distance for the wurtzite structure.

However, it should be mentioned that this intra-chain contraction evokes an inter-chain expansion in b -direction, increasing the inter-chain Hg-O distance to 2.964 Å. Thus, the overall volume is actually expanded from 31.2 to 36.0 Å³ due to the change in crystal symmetry, leading to a consequent density decrease from 11.54 to 9.98 g cm⁻³ upon inclusion of relativistic effects. To compare with, this only just exceeds the densities of ZnO and CdO with values of 5.6 and 8.15 g cm⁻³ [114], respectively. The experimental value found for the density of HgO in its equilibrium structure is 11.14 g cm⁻³ [114].

Even more surprising is the fact that both the montroydite as well as the cinnabar phases relax into the rocksalt structure upon structure optimization utilizing the nonrelativistic description. Therefore, those two modifications clearly become unstable at the nonrelativistic level, meaning that the existence of the montroydite and cinnabar structure in HgO can be credited to relativistic effects.

An explanation for this behaviour originates in the decrease of ionicity in HgO due to relativistic effects and a consequent significant increase of the covalent

bonding in the solid state. Calculations show a substantial reduction of the HgO dipole in the diatomic molecule from 8.0 to 5.6 Debye due to relativistic effects. This is calculated at the Hartree-Fock level, where electron correlation is treated within a second-order many-body perturbation theory. Indeed, the calculations carried out reveal that the Mulliken charge for the mercury atom in solid HgO decreases from 1.10 to 0.90 going from the nonrelativistic level (rocksalt phase) to the relativistic description (montroydite structure). This in turn, causes typical ionic structures like rocksalt to become less favourable.

Furthermore, it should be noted that the large relativistic destabilization of solid HgO mentioned above (decrease in cohesive energy from 6.2 to 4 eV upon inclusion of relativity) is also substantially increased compared to the HgO molecule. Here the change in dissociation energy is 1.0 eV at the nonrelativistic level as compared to only 0.17 eV at the relativistic level [1] and gives rise also to the easy decomposition of HgO in the gas phase, which was mentioned in chapter 1 already.

Since spin-orbit coupling is suppressed in the ionic lattice field, the structural change is assumed to originate almost exclusively from scalar-relativistic (mass-velocity) effects. However, spin-orbit effects are important to determine the exact band gap in HgO (see discussion in chapter 4.5.3). Note also that the sublimation energies of group 12 chalcogenides have recently been discussed in detail by Szentpály [129].

4.5.2 High-pressure structure

System	a	c	u	B_0	B'	E_{coh}	V_0
Rocksalt	4.996	-	-	113.6	5.5	6.198	31.17
Wurtzite	3.851	6.112	0.3850	79.4	3.5	6.056	39.28
Zinc blende	5.400	-	-	81.5	5.4	6.033	39.36
Cesium chloride	3.066	-	-	117.4	4.8	5.479	28.83

Table 4.8: Ground-state properties of equilibrium and high-pressure phases of HgO within the nonrelativistic approach. Presented are the lattice constants a and c (Å), internal parameter u , ground-state volume V_0 (Å³/pair), bulk modulus B_0 (GPa) and its pressure derivative B' as well as the cohesive energy E_{coh} (eV/pair).

Turning now to the high-pressure phases, the tetragonal I4/mmm phase found in HgO is not stable anywhere in the nonrelativistic regime studied here. Therefore, a direct transition into the cesium chloride phase is observed at 62 GPa with

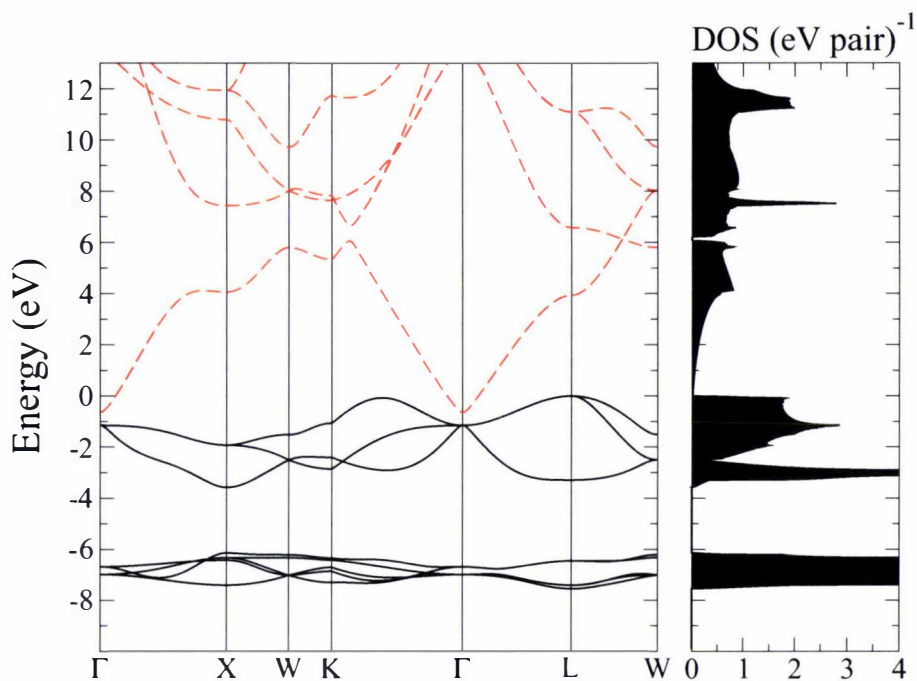


Figure 4.8: Band structure and density of states (normalized per pair) at zero pressure for the HgO polymorph rocksalt calculated within the nonrelativistic DFT-GGA framework. The valence-band maximum is set to zero energy. The black solid lines indicate the valence and the red dashed lines the conducting bands, respectively.

an according ground-state lattice constant of 3.066 Å. Hence, the nonrelativistic structural transition path closely resembles that of CdO.

In addition, the structural parameters for the zinc blende and wurtzite phase were calculated for nonrelativistic HgO as well, see table 4.8. In general a slight increase in the lattice constants compared to the respective phases at the relativistic level can be observed due to the omission of relativistic contraction.

4.5.3 Electronic structure

Looking at the electronic behaviour of the nonrelativistic equilibrium state of HgO, the rocksalt structure, the differences to the relativistic picture are quite significant.

The VBM is now located at the Σ line between Γ and K and at the L point, and the CBM occurs at the Γ point as indicated by fig. 4.8. The results presented suggests a half metal at the nonrelativistic level, since the VBM lie above the CBM inducing negative indirect band gaps of -0.56 and -0.64 eV, respectively.

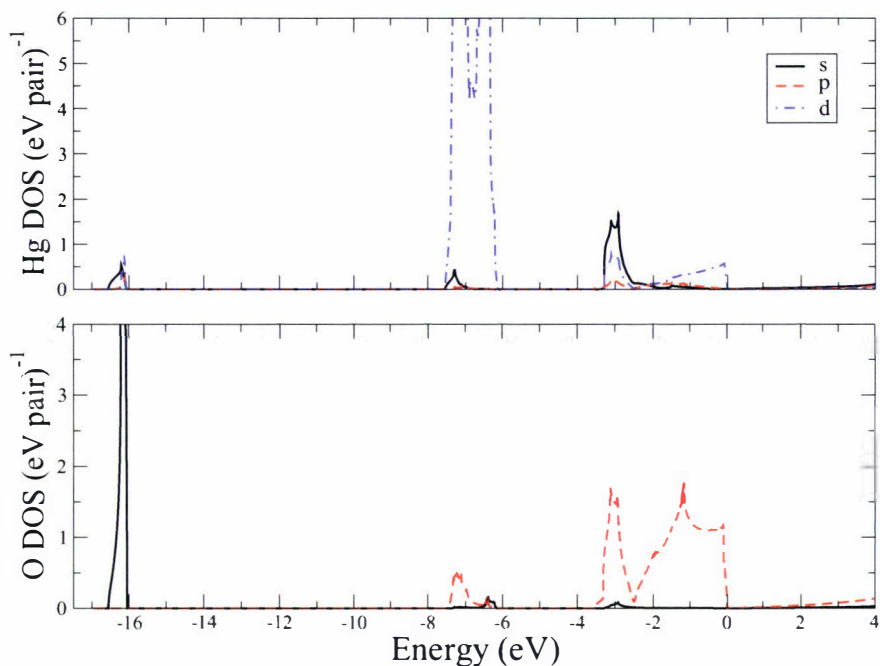


Figure 4.9: Site-projected density of states at zero pressure for the HgO polymorph cinnabar calculated within the nonrelativistic DFT-GGA framework. The black solid, red dashed and blue dash-dotted line indicate the s, p and d site-projected DOS, respectively.

The smallest direct gap occurs at the Γ point with an energy of 0.52 eV. This behaviour is rather similar to the characteristics found for CdO (see chapter 4.4.2) and in stark contrast to the semiconducting nature of the cinnabar and montroydite structure when using the relativistic approach.

The Hg site-projected DOS for nonrelativistic HgO depicted in fig. 4.9 shows a well-defined crystal-field splitting for the *d*-bands of approximately 0.8 eV, which is typical for an octahedral arrangement like in the rocksalt structure. In contrast, the Hg site-projected DOS upon inclusion of spin-orbit coupling for the montroydite as well as the cinnabar structure becomes far more complex (see figs. 4.5 and 4.7). Here, the spin-orbit splitting dominates over the crystal-field splitting.

4.6 Summary

The lattice properties and transition pressures obtained for the group 12 oxides in the course of this thesis are in excellent agreement with other theoretical and

experimental studies available. The only exception are the bulk moduli where the discrepancies are slightly larger. Yet other theoretical work suggest similar deviations. Concerning the transition pressure, only the value for the montroydite to I4/mmm transition is overestimated which is to be blamed on the minute energy and structural difference between the rocksalt and tetragonal structure in the transition region. Hence, the transition pressure is pushed towards the theoretical $M \rightarrow RS$ transition value. Furthermore, the electronic structure is qualitatively in good agreement with experiments, with the usual DFT-like underestimation of the band gaps. In the case of CdO it is so severe that a half-metal is predicted instead of the experimentally observed semiconducting behaviour.

To the best of our knowledge the high-pressure behaviour of mercury oxide has been investigated by theoretical means in this thesis for the first time and no other theoretical studies could be found to compare with. In addition, a new cesium chloride phase of HgO is predicted following the rocksalt modifications. The transition pressure is rather low with 57 GPa in order to be confirmed experimentally. Yet, intermediate phases will have to be excluded by theoretical or experimental means.

The influence of relativistic effects on the structure of HgO is rather dramatic for the equilibrium as well as the high-pressure behaviour. First and foremost, the montroydite and cinnabar equilibrium phases become unstable if relativity is neglected. Instead the rocksalt structure is predicted similar to CdO. This is due to the large relativistic lattice destabilization of 2.2 eV and a relativistic decrease in ionicity, suppressing the typical ionic rocksalt structure. Considering the high-pressure behaviour, the I4/mmm phase is not stable anymore causing a transition path that is very similar to CdO.

Chapter 5

The group 12 sulfides

5.1 Occurring crystal structures

5.1.1 Zinc sulfide

Zinc sulfide is known to adopt two different crystalline structures at ambient conditions. This is on the one hand the stable zinc blende structure, where ZnS itself delivers the prototype, with a lattice constant of $a = 5.4102 \text{ \AA}$ [12]. On the other hand it crystallizes in a metastable wurtzite structure, where the lattice parameters are $a = 3.8226 \text{ \AA}$ and $c = 6.2605 \text{ \AA}$ [12]. This structure was observed to transform into the zinc blende structure at appliance of pressure [130]. Many intermediate polytypes have been found.

Various studies concerning the high-pressure behaviour of the zinc blende structure were conducted. Minomura *et al.* [131] for the first time observed a transition at higher pressures to a structure, which was later identified in ref. [132] to have a rocksalt arrangement. Using different diffraction and optical techniques the value for the transition pressure is reported to be between 11.7 and 15.4 GPa (see table 5.1). Even though Minomura *et al.* reported the NaCl phase to be metallic, it is an indirect-gap semiconductor with a gap of about 2 eV [133, 134]. The lattice constant is 4.839 Å at 17.1 GPa [134].

However, the situation is not absolutely clear from a theoretical point of view, where Nazzal *et al.* using a PP-PW approach in conjunction with DFT-LDA predicted a transition from the zinc blende to the cinnabar structure (11.4 GPa) first and only then the passage into the rocksalt structure (14.5 GPa) [135]. But two X-ray diffraction studies [12, 130] rule out the intermediate cinnabar phase

for ZnS, as does a later theoretical study by Qteish *et al.* [136]. Nelmes and McMahon [12] did, however, observe a transition at 69 GPa into a most likely Cmc \bar{m} -like structure, but could not resolve the structural parameters. No further transition was found up to 84 GPa. Desgreniers *et al.* [130] support those findings experimentally, as well as López-Solano *et al.* theoretically [137]. Furthermore, Qteish and Parinello predicted a new phase intermediate between zinc blende and rocksalt [138]. This ZnS form has the SC16 structure and was confirmed by another calculation of ref. [139]. However, the transition might be hindered by energy barriers, since this new arrangement of ZnS has not been found experimentally yet.

In chapters 5.2.1 and 5.3.1, the structural parameters and transition pressures obtained for the zinc sulfide phases in the course of this thesis will be presented in tables 5.1, 5.4 and 5.5. Those will also list the results of previous theoretical as well as experimental work for comparison.

5.1.2 Cadmium sulfide

Polytypism also applies to cadmium sulfide, where again two stable phases are found at room conditions. Equivalent to zinc sulfide, those two structures are wurtzite (stable and semiconducting) with lattice constants $a = 4.1362 \text{ \AA}$ and $c = 6.714 \text{ \AA}$ and metastable zinc blende ($a = 5.818 \text{ \AA}$) [12].

Detailed studies under high pressure are, however, only available for the wurtzite phase, where a transition at 2.75 GPa was first observed by Edwards and Drickamer [140] (optical measurements). This new phase was later identified to have a rocksalt structure ($a = 5.42 \text{ \AA}$ [141]). The transition goes along with a sudden decrease in resistivity [142] and an over all volume decrease ($\Delta V/V_0$) of 16% is noted [143]. The rocksalt structure was found to be semiconducting with an indirect band gap of 1.6 eV [144].

A further transformation into CdS-III was observed at 50-58 GPa by Suzuki *et al.* (combining EDX and ADX), which characterized the new phase as an orthorhombic (low-pressure KCN-type) structure with the space group $Pm\bar{m}n$ [145] which is stable at least up to 68 GPa. However, no atomic positions were reported. A reinvestigation of the structure [12] confirmed findings in general, but the absence of the NaCl(111)-peak splitting was criticized. Therefore, in analogy of the Cmc \bar{m} phase in CdTe and ZnSe, the data was fitted to that structure as well, which however led to a poorer fit. For lattice parameters see table 5.6.

The stability of the $Pm\bar{m}n$ or Cmc \bar{m} phase was investigated theoretically as well,

with, however, differing outcomes [146, 147]. No post-Cmcm high-pressure behaviour is reported yet, neither experimentally nor theoretically.

The chapters 5.2.2 and 5.3.2, where the results for the cadmium sulfide equilibrium and high-pressure modifications are summarized in tables 5.2, 5.6 and 5.7, will include the structural parameters and transition pressures determined by previous investigators (by experimental and theoretical means) of those structures as well.

5.1.3 Mercury sulfide

At ambient conditions mercury sulfide can be found in its stable mineral form, which delivers the prototype for the so-called cinnabar structure. This is a red crystal with the lattice parameters $a = 4.145 \text{ \AA}$ and $c = 9.496 \text{ \AA}$ and internal parameters $u(\text{Hg}) = 0.7198$ and $v(\text{S}) = 0.4889$ [90]. However, a second metastable low-pressure black coloured form exists which adopts a zinc blende structure with $a = 5.851 \text{ \AA}$. It transforms into the cinnabar phase at 5 GPa. The cinnabar structure is again built from S-Hg-S spiral chains lying parallel to the z -axis, implying a 2+4 coordination equivalent to the situation found in cinnabar-HgO. At higher pressures a transformation to the rocksalt structure ($a = 5.070 \text{ \AA}$) occurs, which was first described by Huang *et al.* and Werner *et al.* [148, 149]. The pressure range of the structure change created a debate between the two groups, but was confirmed by Nelmes and McMahon to take place at 20.5 GPa (high-resolution ADX) [12]. During the course of those studies a further transition was observed at around 52 GPa into HgS-III, where a Cmcm-structure was proposed in accordance with the knowledge about HgSe and HgTe.

Later, the structural parameters and transition pressures of the different mercury sulfide phases calculated in this study are concluded in tables 5.3 and 5.8 (see chapters 5.2.3 and 5.3.3). Those results will be compared to the parameters obtained in preceding experimental and theoretical investigations as just discussed.

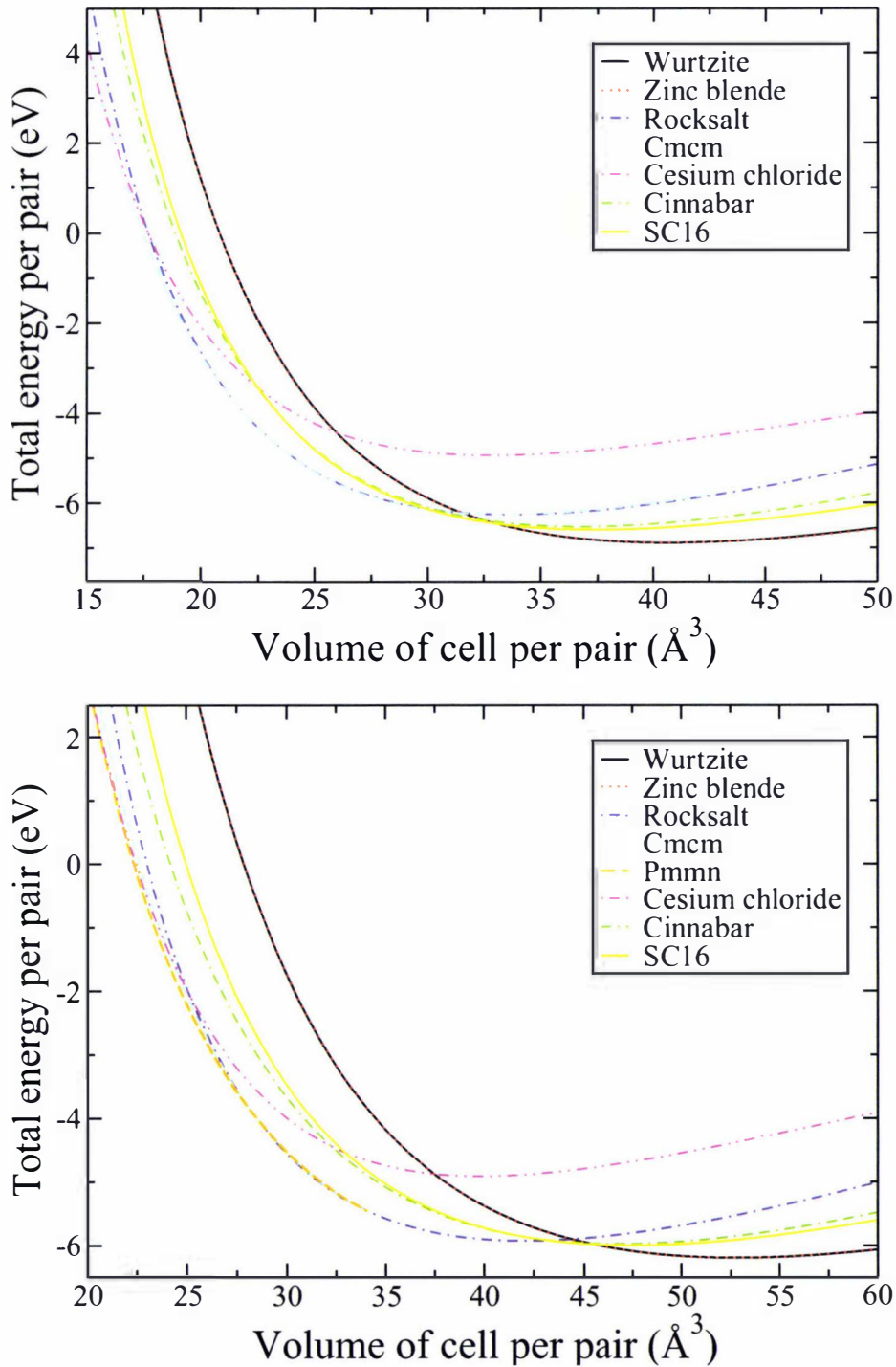


Figure 5.1: The total energy versus volume per cation-anion pair for different crystal structures of ZnS (upper panel) and CdS (lower panel).

Property	This work	Other theoretical	Experiments
<i>Zinc blende</i>			
a	5.446	5.449 ^a , 5.404 ^b , 5.58 ^c	5.410 ^d , 5.412 ^f
V_0	40.38	40.45 ^a , 39.45 ^b , 43.44 ^c	39.59 ^d , 39.63 ^f
B_0	70.4	69.8 ^a , 71.22 ^b , 75.9 ^c	76.9 ^d , 79.5 ^e
B'	4.6	4.4 ^a , 4.7 ^b , 4.7 ^c	4.9 ^d , 4 ^e
E_{coh}	5.971	4.66 ^c , 5.88 ^r	6.33 ^d , 6.36 ^r
p_t to SC16	16.73	12.8 ^p , 12.25 ^q	
p_t to RS	16.97	18.50 ^a , 15.4-17.5 ^b , 16.1 ^c , 14.35 ^p	17.4 ^d , 11.7 ^g , 12 ^h , 14.5-15.4 ⁱ
p_t to C2	18.53	11.4 ⁿ , 17.8 ^o	
<i>Wurtzite</i>			
a	3.848	3.852 ^a , 3.840 ^j , 3.982 ^m	3.823 ^d , 3.811 ^k
c	6.308	6.313 ^a , 6.267 ^j , 6.500 ^m	6.261 ^d , 6.234 ^k
c/a	1.639	1.639 ^a , 1.632 ^j , 1.632 ^m	1.638 ^d , 1.636 ^k
u	0.3747	0.375 ^a , 0.375 ^j , 0.377 ^m	0.3748 ^l , 0.375 ^a
V_0	40.44	40.56 ^a , 40.01 ^j , 44.63 ^m	39.62 ^d , 39.21 ^k
B_0	69.7	68.5 ^a , 68.96 ^j	76.2 ^d , 80.1 ^h , 75.8 ^a
B'	4.4	4.1 ^a , 4.39 ^j	4 ^h , 4.4 ^a
E_{coh}	5.963		
p_t to RS	16.61	14.84 ^a , 17.2 ^j	14.1-14.6 ^h , 16 ^a

^aPAW-GGA from ref. [150] and refs. therein; ^bPP-GGA from ref. [151]; ^cHF-LCAO from ref. [152]; ^dfrom ref[153]; ^efrom ref. [130]; ^ffrom ref. [143]; ^gfrom ref. [132]; ^hfrom ref. [130]; ⁱfrom ref. [12]; ^jPW-GGA from ref. [154]; ^lfrom ref. [155]; ^kfrom ref. [143]; ^mfrom ref. [156]; ⁿPP-PW-LDA from ref. [135]; ^oPP-PW from ref. [136]; ^pPP-PW from ref. [138]; ^qTB-LMTO [139]; ^rsemi-empirical TB calc. from ref. [157] and refs. therein.

Table 5.1: Ground-state properties of the equilibrium phases of ZnS. Presented are the lattice constants a and c (Å), internal parameter u , axial ratio c/a , ground-state volume V_0 (Å³/pair), bulk modulus B_0 (GPa) and its pressure derivative B' as well as the cohesive energy E_{coh} (eV/pair) and the transition pressure p_t (GPa) where applicable.

5.2 Equilibrium structures

5.2.1 Zinc sulfide

Figure 5.1 shows the total energies per ZnS pair plotted against the volume of the unit cell per pair. The graph clearly confirms the polytypism found in zinc sulfide, as the curves for the zinc blende as well as the wurtzite structure are in very close proximity with a cohesive energy of 5.971 eV/pair and 5.963 eV/pair, respectively. This means that the B3 structure is slightly more stable having the

lower energy. At the same time, the difference in energy (8 meV/pair) agrees with the calculations by Yeh *et al.*, who obtained 3.1 meV/atom [158].

The calculations presented here give a ground-state lattice constant of $a = 5.446$ Å (corresponding to a volume $V_0 = 40.38$ Å³/pair) for the prototype zinc blende structure, which is in accordance with other experimental and theoretical investigations (see table 5.1). Compared to very recent theoretical investigations using similar methods (PAW-GGA) the agreement is excellent (see refs. [150] and [151] in table 5.1). The corresponding bulk modulus and its pressure derivative are 70.4 GPa and 4.6. Those values again match other results.

For the metastable wurtzite phase the derived lattice constants are $a = 3.848$ Å and $c = 6.308$ Å, whereas the internal Wyckoff parameter was calculated to be $u = 0.3747$ and the ground-state unit-cell volume is $V_0 = 40.44$ Å³/pair, accordingly. Compared to zinc blende, the ground-state unit-cell volume is very similar. The ratio $c/a=1.639$ is therefore very close to the ideal value of 1.633. The bulk modulus for the wurtzite structure is determined to be 67.8 GPa with a pressure derivative of 3.9. Looking at table 5.1 the determined properties agree very well with other work.

5.2.2 Cadmium sulfide

Similar to zinc sulfide, the calculations presented here confirm that as mentioned before under normal conditions cadmium sulfide exists in two forms, the cubic zinc blende and the hexagonal wurtzite form. Again, the minute difference in cohesive energy of 3 meV/pair ($E_{coh}^{ZB} = 5.266$ eV/pair, $E_{coh}^W = 5.269$ eV/pair) indicates that both crystal arrangements are very similar. This very small energy difference lies within the methodical uncertainty of DFT, making it very difficult to predict, which phase is energetically most stable. This can also be gathered from the energy-volume dependencies of fig. 5.1. However, rather few experimental data are available for the investigation of the zinc blende form at normal conditions as well as at higher pressure, which might indicate that it is slightly less stable or common than the wurtzite form. This is confirmed by the results presented here. Furthermore, the energy difference of only 3 meV/pair compares well to investigations of Yeh *et al.* where $\Delta E^{W-ZB} = -1.1$ meV/atom and Wei *et al.* who obtained $\Delta E^{W-ZB} = -2$ meV/pair [158, 161].

For the zinc blende phase a zero pressure volume of 52.29 Å³/pair is calculated, going along with a lattice constant of 5.936 Å. A bulk modulus of $B_0 = 53.9$ GPa together with a B' of 4.7 are obtained. Those results compare well to previous

Property	This work	Other theoretical	Experiments
<i>Wurtzite</i>			
a	4.199	4.108 ^a , 4.19 ^b , 4.101 ^c	4.136 ^d , 4.14 ^e
c	6.853	6.66 ^b , 6.687 ^c	6.714 ^d , 6.72 ^e
c/a	1.632	1.589 ^b , 1.631 ^c	1.623 ^d , 1.623 ^e
u	0.3758	0.3757 ^c	0.3777 ^f
V_0	52.31	50.71 ^b , 48.69 ^c	49.73 ^d , 49.89 ^e
B_0	53.7	68.8 ^a , 66.4 ^b , 46.7 ^g	62 ^a , 62.8 ^b
B'	4.7	4.5 ^a	
E_{coh}	5.269		
p_t to RS	4.15	3.2 ^h	2.8 ^d , 2.34 ^e , 3 ⁱ , 2.3 ^j
<i>Zinc blende</i>			
a	5.936	5.808 ^a , 5.87 ^b , 5.83 ^k	5.818 ^d
V_0	52.29	48.98 ^a , 50.55 ^b , 49.54 ^k	49.23 ^d
B_0	53.9	69.44 ^a , 65.5 ^b , 62.3 ^l	64.4 ^m , 66.0 ^b
B'	4.7	4.6 ^a , 5.4 ^l	
E_{coh}	5.266	4.874 ^l , 5.78 ^m	5.68 ^m
p_t to RS	4.11	3.2 ^h , 4.48 ⁿ	

^aFP-LMTO-LDA from ref. [159]; ^binteratomic potentials from ref. [160]; ^cLAPW-LDA from ref. [161]; ^dfrom ref. [153]; ^efrom ref. [143]; ^ffrom ref. [120]; ^g*ab-initio* GDSP/DFT from ref. [162]; ^hFP-LMTO-LDA from ref. [146]; ⁱX-ray diffraction from ref. [145]; ^jADX from ref. [12]; ^kPP-LDA from ref. [147]; ^lMD from ref. [163]; ^msemi-empirical TB calc. from ref. [157] and refs. therein; ⁿab-initio PP calculation from ref. [164].

Table 5.2: Ground-state properties of the equilibrium phases of CdS. Presented are the lattice constants a and c (Å), internal parameter u , axial ratio c/a , ground-state volume V_0 (Å³/pair), bulk modulus B_0 (GPa) and its pressure derivative B' as well as the cohesive energy E_{coh} (eV/pair) and the transition pressure p_t (GPa) where applicable.

experimental data ($a = 5.818$ Å, $V_0 = 49.23$ Å³/pair, $B_0 = 64.4$ GPa [153, 157]) and are in good agreement with other theoretical investigations (see table 5.2). However, the deviation from experimental data for the bulk modulus of at least 19% is rather big.

In the case of the wurtzite structure the determined lattice properties are $a = 4.199$ Å, $c = 6.853$ Å and $u = 0.3758$, in good agreement with other results. The lattice constants vary within a few percent as is to be expected within the framework of DFT. The c/a ratio is again very close to the optimal value of $\sqrt{8/3}$. In addition, the bulk modulus and its pressure derivative ($B_0 = 53.7$ GPa, $B' = 4.7$) are within limits compared to other calculations as well as experimental investigations (see table 5.2).

5.2.3 Mercury sulfide

Property	This work	Other theoretical	Experiments
<i>Cinnabar</i>			
a	4.395	4.294 ^a	4.149 ^b , 4.074 ^c , 4.145 ^d
c	9.729	9.885 ^a	9.495 ^b , 9.395 ^c , 9.496 ^d
c/a	2.214	2.302 ^a	2.289 ^b , 2.306 ^c , 2.291 ^d
u	0.7515	0.7192 ^a	0.7189 ^d , 0.720 ^e
v	0.4633	0.4960 ^a	0.4889 ^d , 0.480 ^e
V_0	55.16	51.32 ^a	47.18 ^b , 45.02 ^c , 47.10 ^d
B_0	8.8 (17.3)	22.48 ^a	19.4 ^b , 18-37 ^c
B'	8.9 (5.4)	4.8 ^a	11.1 ^b
E_{coh}	3.657		3.64 ^f
p_t to RS	28.7	26.57 ^a	24 ^b , 13 ^g , 20.5 ^h , 29 ⁱ
<i>Zinc blende</i>			
a	6.009	5.975 ^j , 5.83-6.03 ^k	5.851 ^f
V_0	54.67	53.33 ^j , 49.5-54.8 ^k	50.08 ^f
B_0	50.4	55.3 ^j , 64.9-67.0 ^k	68.6 ^f
B'	4.9		
E_{coh}	3.680		3.47 ^f
p_t to C2	1.38		5 ^l
p_t to RS	5.60	0.36 ^m	

^aAPW+LO-GGA at zero pressure from ref. [91]; ^bX-ray diffraction at zero pressure from ref. [149]; ^cX-ray diffraction at 0.4 GPa from ref. [165]; ^dfrom ref. [90]; ^efrom ref. [166]; ^ffrom ref. [120]; ^gX-ray diffraction from ref. [148]; ^hADX from ref. [12]; ⁱconductivity measurements from ref. [167]; ^j*ab-initio* GDSP/DFT from ref. [162]; ^kFP-LMTO LDA and GGA from ref. [168]; ^lfrom ref. [169]; ^m*ab-initio* pseudo-potential calculations from ref. [164].

Table 5.3: Ground-state properties of the equilibrium phases of HgS. Presented are the lattice constants a and c (Å), internal parameters u and v , axial ratio c/a , ground-state volume V_0 (Å³/pair), bulk modulus B_0 (GPa) and its pressure derivative B' as well as the cohesive energy E_{coh} (eV/pair), and the transition pressure p_t (GPa) where applicable.

The energy-volume curves for the different crystal structures of mercury sulfide can be viewed in fig. 5.10. As mentioned above, under ambient conditions mercury sulfide crystallizes in both a cinnabar as well as a zinc blende form. This is confirmed by our calculations considering that those two structures lead to the lowest energies with cohesive energies of 3.657 eV/pair and 3.680 eV/pair, respectively.

Hence, the zinc blende structure seems to be energetically more favourable by 23 meV/pair, which is significantly higher than the energy deviation between

wurtzite and zinc blende in e.g. ZnS and CdS. However, the picture changes quickly with pressure increase and we find a transition into the cinnabar modification at a rather low pressure of 1.4 GPa, in concordance with the experimental transition pressure of 5 GPa [169]. Since the cinnabar structure is observed to be the stable equilibrium form of HgS, the differences are most likely due to temperature effects.

Yet, the wurtzite structure is in close proximity ($E_{coh} = 3.673$ eV/pair) to those two structures, but up to at least 100 GPa zinc blende is always more stable. A possible wurtzite phase would undergo the transition into cinnabar at even lower pressures of just 1.0 GPa.

The lattice parameters obtained for the cinnabar phase are $a = 4.395$ Å and $c = 9.729$ Å with $u(\text{Hg}) = 0.7515$ and $v(\text{S}) = 0.4633$. The minimum volume is reached at 54.23 Å³ per HgS pair. The bulk modulus and its pressure derivative are determined to be 8.8 GPa and 8.9, respectively. Whereas the structural properties are in reasonable agreement with other work, the bulk modulus seems to be extremely low compared to other calculations and the experimental value (see table 5.3). However, if more data points are included into the fit the obtained bulk modulus quickly rises to 17.3 GPa ($B' = 5.4$), showing how much the compressibility depends on the pressure. This in turn means that the Murnaghan and Vinet EOS might not be the optimal choice for the fit. Comparability of the lattice and internal parameters can be improved if one looks at a pressure of 1.27 GPa, which is just below the transition pressure of the ZB→C2 transition, where the following parameters are obtained: $a = 4.207$ Å, $c = 9.569$ Å, $c/a = 2.274$, $u = 0.7150$, $v = 0.4962$ and $V = 48.91$ Å³/pair. Those values are in excellent agreement with the other theoretical and experimental results which again shows how sensitive the internal parameters are to pressure.

On the other hand, for the zinc blende form a lattice constant of $a = 6.009$ Å ($V_0 = 54.23$ Å³/pair) is found, which is in good agreement with experimental and theoretical investigations. This is, within the limitations of the applied methodology, true for the bulk modulus as well ($B_0 = 50.4$ GPa), where other groups obtained values of 68.6 GPa (experimentally) and 55.3-67.0 GPa (theoretically). The pressure derivative B' was determined to be 4.9. See table 5.3 for details.

For the non-existent wurtzite phase the following properties are obtained: $V_0 = 54.28$ Å³/pair $a = 4.256$ Å, $c = 6.923$ Å, $u = 0.3777$, $B_0 = 50.0$ GPa and $B' = 5.0$. Almost no difference is observed for the three different ground-state volumes.

5.3 High-pressure phases

5.3.1 Zinc sulfide

The thesis at hand predicts that the zinc blende form of ZnS undergoes a phase transition into the SC16 structure at approximately 16.73 GPa. This is at a significantly higher pressure than determined by Gangadharan *et al.* and Qteish *et al.* (12.25 and 12.8 GPa), who investigated this phase as well. The transformation from SC16 into the rocksalt structure takes place at 17.23 GPa. This leaves a stability range of only 0.5 GPa as compared to 3.4 GPa obtained by Qteish *et al.*, who calculated the pressure for the SC16→RS transformation to be 16.2 GPa.

In contrast, the lattice properties of $a = 6.688 \text{ \AA}$, $u(\text{Zn}) = 0.1560$, $v(\text{S}) = 0.6442$ compare quite well to the other theoretical studies (see table 5.4 for details). This is also true for the bulk modulus and its pressure derivative ($B_0 = 65.1 \text{ GPa}$, $B' = 5.4$), if the difference in methodology is considered.

However, according to the study at hand, at 16.97 GPa the zinc blende form of ZnS transforms into the rocksalt structure. The estimated pressure is in good agreement with other theoretical (15.4-18.5 GPa) as well as experimental (11.7-17.4 GPa) work. This means that the pressure derived for the ZB→SC16 transition is in very close proximity to the one obtained for ZB→RS transition. Hence, it is difficult to estimate whether SC16 would actually exist as an intermediate phase, especially since it has not been observed experimentally yet. The transition might also be kinetically hindered.

For the rocksalt structure the following solid-state properties are derived: $a = 5.108 \text{ \AA}$, $V_0 = 33.32 \text{ \AA}^3/\text{pair}$, $B_0 = 86.8 \text{ GPa}$ and $B' = 4.8$ along with a cohesion energy of 5.336 eV/pair. The agreement in particular with other theoretical investigations is excellent with deviations of only a few percent. Having a look at the obtained parameters at a pressure above the transition pressure ($p = 19.44 \text{ GPa}$), the lattice constant is 4.850 \AA with a unit-cell volume of $V = 28.52 \text{ \AA}^3/\text{pair}$.

On the basis of the calculations presented here, the rocksalt phase of ZnS is predicted to undergo a transition into the Cmcm structure at approximately 59.5 GPa. This transition was investigated by only two groups so far¹ and the

¹Desgreniers *et al.*, who used x-ray diffraction and López-Solano *et al.*, who employed a plane wave pseudo-potential approach in combination with DF1-LDA.

Property	This work	Other theoretical	Experiments
<i>SC16</i>			
a	6.688	6.555 ^a , 6.586 ^b	
$u(\text{Zn})$	0.1560	0.1541 ^a	
$v(\text{S})$	0.6442	0.6431 ^a	
V	37.40	35.21 ^a , 35.709 ^b	
B_0	65.1	78.4 ^a , 89.53 ^b	
B'	5.4	4.7 ^a	
E_{coh}	5.672		
p_t to RS	17.23	16.2 ^a	
<i>Rocksalt</i>			
a	5.108	5.107 ^c , 5.07 ^d , 5.21 ^e	5.060 ⁱ , 5.21 ^{j,†} , 5.13 ^{j,‡}
V	33.32	33.30 ^c , 32.58 ^d , 35.36 ^e	32.38 ⁱ , 35.36 ^{j,†} , 33.75 ^{j,‡}
B_0	86.8	85.11 ^c , 89.54 ^d , 83.1 ^e	103.6 ⁱ , 47.5 ^{j,†} , 85.0 ^{j,‡}
B'	4.8	4.5 ^c , 4.6 ^d , 10.0 ^e	4 ⁱ , 6.2 ^{j,†} , 4 ^{j,‡}
E_{coh}	5.336		
p_t to Cmcn	59.5	65 ^h	69 ^f , 65 ^g
<i>Cmcm</i>			
a	(4.482)	(4.45 ^h)	(4.45 ^g)
b	(4.537)	(4.49 ^h)	(4.49 ^g)
c	(4.429)	(4.40 ^h)	(4.43 ^g)
b/a	(1.012)	(1.01 ^h)	(1.01 ^g)
c/a	(0.988)	(0.99 ^h)	(1.00 ^g)
$y(\text{Zn})$	(0.7020)	(0.71 ^h)	
$y(\text{S})$	(0.2099)	(0.22 ^h)	
V	(22.51)	(21.98 ^h)	(22.13 ^g)
V_0	33.43	30.99 ^h	
B_0	104.6	115.3 ^h	
B'	3.1	3.5 ^h	
E_{coh}	5.314		
p_t to CsCl	215		

^aPP-PW from ref. [138]; ^bTB-LMTO [139]; ^cPAW-GGA from ref. [150]; ^dPP-GGA from ref. [151]; ^eHF-LCAO from ref. [152]; ^ffrom ref. [12]; ^gat 90 GPa from ref. [130]; ^hPW-PP-LDA at 77.7 GPa from ref. [137]; ⁱfrom ref. [133] (B' kept fixed); ^jfrom ref. [134]; where B' kept fixed using the Vinet fit (†) and B' relaxed using a 3rd order Birch-Murnaghan fit (‡).

Table 5.4: Ground-state properties of the high-pressure phases of ZnS. Presented are the lattice constants a , b and c (Å), respective internal parameters, ground-state volume V_0 (Å³/pair), bulk modulus B_0 (GPa) and its pressure derivative B' as well as the cohesive energy E_{coh} (eV/pair) and the transition pressure p_t (GPa) where applicable. Values in brackets indicate higher pressure.

Property	This work	Other theoretical
<i>Cesium chloride</i>		
a	3.202	
V	32.82	
B_0	74.5	
B'	4.4	
E_{coh}	4.018	
<i>Cinnabar</i>		
a	3.807	3.765 ^a , 3.784 ^b , 3.761 ^c
c	8.745	8.786 ^c
c/a	2.297	2.336 ^c
$u(\text{Zn})$	0.5016	0.455 ^c
$v(\text{S})$	0.5004	0.480 ^c
V	36.57	
B_0	76.5	89.3 ^a , 81.02 ^b , 92 ^c
B'	4.3	4.5 ^a , 3.1 ^c
E_{coh}	5.595	
p_t to RS	15.31	14.5 ^c

^aPP-PW from ref. [138]; ^bTB-LMTO [139]; ^cPP-PW-LDA from ref. [135].

Table 5.5: Ground-state properties of the high-pressure phases of ZnS. Presented are the lattice constants a , b and c (Å), respective internal parameters, ground-state volume V_0 (Å³/pair), bulk modulus B_0 (GPa) and its pressure derivative B' as well as the cohesive energy E_{coh} (eV/pair) and the transition pressure p_t (GPa) where applicable. Experimental data are not available.

transitions pressure is in good agreement with their results of $p_t = 65 - 69$ GPa (see also table 5.4).

Since the Cmc m structure is a distortion of the rocksalt arrangement, it relaxes directly into this structure for lower pressures, and a listing of the crystal properties at zero pressure is not possible. A seamless transition of the structural parameters towards rocksalt occurs, meaning all three lattice constants become equal and the values for $y(\text{Zn})$ and $y(\text{S})$ are developing towards 0.75 and 0.25, respectively. Therefore, the structural parameters are evaluated at a pressure well above the transition: at 80.7 GPa equivalent to a unit-cell volume of 22.51 Å³/pair the lattice constants are $a = 4.482$ Å, $b = 4.537$ Å, $c = 4.429$ Å (hence, $b/a = 1.012$ and $c/a = 0.988$) with $y(\text{Zn}) = 0.7020$ and $y(\text{S}) = 0.2099$. Even with increasing pressure the orthorhombic distortion is rather small. It should also be noted that the volume difference between the rocksalt and Cmc m phases is rather small (see fig. 5.1), which is not surprising due to the similarity of the two structures.

Comparison of the lattice constants and structural parameters with previous results is rather difficult, since refs. [130] as well as [137] contain figures only. The data presented in table 5.4 are therefore estimated from those graphs and rather approximate. Furthermore, Desgreniers *et al.* mention that, due to the very small orthorhombic distortion, the data points are quite scattered, making an accurate determination of the lattice constants very hard (and possible only above 78 GPa) and an estimate of the internal parameters impossible. Bearing in mind these problems, the agreement between the values presented here and other experimental and theoretical results is reasonable (see table 5.4). López-Solano *et al.* already mention that the deviations are due to the limits of DFT and non-zero temperature effects. Turning now to the bulk modulus and its pressure derivative, the agreement with a PW-PP-LDA study by López-Solano *et al.* is good (table 5.4) and deviations can be blamed on the use of the different functionals.

At an extremely high pressure of 215 GPa a transition from Cmcm into the cesium chloride structure occurs. This is also in concordance with the studies mentioned above, who rule out a further transition only up to pressures of 120 GPa [137]. The lattice parameters obtained for this phase are $a = 3.202 \text{ \AA}$ representing an equilibrium volume of $32.82 \text{ \AA}^3/\text{pair}$. The calculated bulk modulus is 74.5 GPa along with a pressure derivative of 4.4.

However, no other reference data are available yet. Since a distortion of the CsCl phase would be possible as well, as it is the case for HgTe, the existence as well as stability of the cesium chloride structure at high pressures for ZnS will have to be investigated further theoretically as well as experimentally. The latter would be very challenging due to the high pressure required.

After initially converse statements of an intermediate phase between zinc blende and rocksalt, now the consensus is reached that the cinnabar phase is not stable for zinc sulfide. It was included in the calculations carried out and the discussion presented here due to the general importance of this structure within the group 12 chalcogenides. Furthermore, in GaAs cinnabar is found as a metastable phase only [138]. This could be the case here as well.

In this study lattice constants of $a = 3.807 \text{ \AA}$ and $c = 8.745 \text{ \AA}$ are obtained ($V_0 = 36.6 \text{ \AA}^3/\text{pair}$), leading to a ratio of $c/a = 2.297$, which is in good agreement with the previous theoretical results (see table 5.5). The bulk modulus ($B_0 = 76.5 \text{ GPa}$) and its pressure derivative ($B' = 4.3$) compare equally good ($B_0 = 81.0 \text{ GPa}$ [139], $B' = 4.5$ [138]). In contrast, the internal parameters $u = 0.5016$

and $v = 0.5004$ deviate from the values obtained by Nazzal *et al.* with $u = 0.455$ and $v = 0.480$ [135]. The reason for this remains unclear. However, it means that the coordination in cinnabar-ZnS is four-fold like in zinc blende, unlike HgS, which Qteish *et al.* found as well.

However, the results also confirm the non-stability of the cinnabar structure with respect to SC16: The transition pressure of 15.31 GPa into the rocksalt form, consistent with the results obtained by Nazzal *et al.* ($p_t = 14.5$ GPa) [135], is well below the pressure for the transition ZB→RS ($p_t = 17$ GPa).

5.3.2 Cadmium sulfide

The results presented here show that both the wurtzite and the zinc blende structure become thermodynamically unstable with respect to the rocksalt form of CdS. The transition pressure for the ZB→RS transition is 4.11 GPa, as opposed to 4.15 GPa for the W→RS transition. A recent DFT-LDA study by Benkhattou *et al.* found a transition pressure of 3.2 GPa in both cases while experimental results are available for the W→RS transition only and range from 2.3-3 GPa.

For the rocksalt structure a lattice constant of 5.503 Å is determined along with a volume of 41.66 Å³/pair, whereas the bulk modulus and its pressure derivative are 73.3 GPa and 4.9, respectively. At a slightly elevated pressure of 4.02 GPa we obtain the following parameters: $a = 5.414$ Å, $V_0 = 39.67$ Å³/pair. Those values compare very nicely to the lattice parameters obtained in experimental investigations.

For the post-rocksalt behaviour of CdS two different orthorhombic distortions of rocksalt have been discussed, that is either a Pmmn or Cmcm structure (see chapter 5.1). The calculations presented here support a transition into the Cmcm structure at approximately 43.99 GPa first, followed by a structure change towards Pmmn at 61.56 GPa. This transition pressure is in excellent agreement with Kirin *et al.*, who obtain 47 GPa for the RS→Cmcm transition [147].

However, considering that both structures are very close in energy in the range where a transition would be possible and keeping in mind the deviations to experimental results due to non-zero temperature effects, the results presented here cannot with absolute certainty state the existence of the Cmcm phase in CdS. Hence both structures could be possible. Assuming the non-existence of the Cmcm phase, the RS→Pmmn transition would occur at 56.35 GPa, which

Property	This work	Other theoretical	Experiments
<i>Rocksalt</i>			
a	5.503 (5.414)	(5.353 ^a , 5.353 ^b)	(5.42 ^c)
V_0	41.67 (39.67)	(38.35 ^a), (38.34 ^b)	(39.81 ^c)
B_0	73.3	97.3 ^a , 99.68 ^b	86.7 ^d
B'	4.9	4.5 ^a , 4.0 ^b	4.4 ^d
E_{coh}	5.010		
p_t to Cmc m	43.99	47.0 ^e	51 ^f
p_t to Pm mn	56.35	58.6 ^b	56 ^d , 51 ^f
<i>Cmcm</i>			
a	(4.896)		(4.883 ^f)
b	(4.940)		(4.881 ^f)
c	(4.845)		(4.875 ^f)
b/a	(1.009)		(1.000 ^f)
c/a	(0.990)		(0.998 ^f)
$y(\text{Cd})$	(0.7036)		(0.699 ^f)
$y(\text{S})$	(0.2076)		(0.174 ^f)
V	(29.30)		(29.05 ^f)
B_0	89.8		
B'	3.3		
E_{coh}	5.008		
p_t to Pm mn	61.56		
<i>Pmmn</i>			
a	(3.560)	3.480 ^b	(3.471 ^d), (3.493 ^f)
b	(4.758)	5.138 ^b	(4.873 ^d), (4.877 ^f)
c	(3.369)	3.550 ^b	(3.399 ^d), (3.412 ^f)
b/a	(1.337)	1.476 ^b	(1.404 ^d), (1.396 ^f)
c/a	(0.946)	1.020 ^b	(0.979 ^d), (0.977 ^f)
$z(\text{Cd})$	(0.3439)	0.3555 ^b	(0.319 ^f)
$z(\text{S})$	(0.1664)	0.1615 ^b	(0.148 ^f)
V	(28.54)	63.47 ^b	(57.06 ^d), (58.12 ^f)
B_0	55.8	107.0 ^b	
B'	3.4	3.7 ^b	
E_{coh}	5.248		
p_t dist. CsCl	129		
p_t CsCl	361		

^aFP-LMTO-LDA from ref. [159]; ^bFP-LMTO-LDA from ref. [146]; ^cat 4 GPa from ref. [141]; ^dX-ray diffraction at 61 GPa from ref. [145]; ^ePP-LDA from ref. [147]; ^fADX at 60 GPa from ref. [12].

Table 5.6: Ground-state properties of the high-pressure phases of CdS. Presented are the lattice constants a , b and c (Å), respective internal parameters, ground-state volume V_0 (Å³/pair), bulk modulus B_0 (GPa) and its pressure derivative B' as well as the cohesive energy E_{coh} (eV/pair) and the transition pressure p_t (GPa) where applicable. Values in brackets indicate higher pressure.

Property	Cesium chloride	Cinnabar	SC16
a	3.415	4.092	7.246
c	-	9.598	-
c/a	-	2.346	-
$u(\text{Cd})$	-	0.5081	0.1542
$v(\text{S})$	-	0.5035	0.6428
V_0	39.83	46.41	47.55
B_0	70.5	60.1	51.4
B'	4.8	4.6	4.6
E_{coh}	3.988	5.041	5.068
p_t to RS	-	0.89	1.56

Table 5.7: Ground-state properties of the high-pressure phases of CdS. Presented are the lattice constants a and c (Å), internal parameters u and v , ground-state volume V_0 (Å³/pair), bulk modulus B_0 (GPa) and its pressure derivative B' as well as the cohesive energy E_{coh} (eV/pair) and the transition pressure p_t (GPa) where applicable. No previous data are available.

compares very well to the X-ray diffraction data of Suzuki *et al.* (56 GPa) [145] and other theoretical results [146].

In contrast, McMahon *et al.* [12] in the course of their ADX studies observe only one transition at 51 GPa which would suit both of the pressures calculated here for either the RS to Cmcm or Pmmn transition. Unfortunately, Kirin *et al.* do not investigate the stability of the Pmmn structure and the only other comparative theoretical study claims Cmcm to be unstable [146]. The presence of the Cmcm structure as an intermediate phase between rocksalt and Pmmn therefore remains an open question and should be investigated further experimentally.

Concerning the Cmcm structure of CdS the following lattice parameters are derived at 57.30 GPa: $a = 4.896$, $b = 4.940$, $c = 4.845$ Å ($V = 29.30$ Å³/pair, $b/a = 1.009$, $c/a = 0.990$) along with $y(\text{Cd}) = 0.7036$ and $y(\text{S}) = 0.2076$. Those values compare rather well to the ones fitted by McMahon *et al.* ($a = 4.883$, $b = 4.881$, $c = 4.875$ Å, $V = 29.05$ Å³/pair, $b/a = 1.000$, $c/a = 0.998$, $y(\text{Cd}) = 0.699$ and $y(\text{S}) = 0.174$ at 60 GPa [12]). The bulk modulus estimated from the data points available is 89.8 GPa and its pressure derivative 3.3 from the Murnaghan fit.

The solid-state properties for the Pmmn phase obtained are 3.560, 4.748 and 3.369 Å for the lattice constants a , b and c , respectively, together with the internal parameters $z(\text{Cd}) = 0.3439$ and $z(\text{S}) = 0.1664$ at a pressure of 61.02 GPa and an estimate of 55.8 GPa for the bulk modulus at 0 GPa ($B' = 3.4$) is taken from the Murnaghan fit using the data points available. Those values are in good

agreement with experimental and theoretical data. While the lattice constants seem to compare better to the experimental results, the internal parameters are closer to data obtained in other theoretical work (for further details see table 5.6). In contrast, the bulk modulus deviates extremely, which is easily justified considering that no data points are available around 0 GPa (where the Murnaghan fit is most reliable) and due to the unreliability of LDA when it comes to bulk moduli.

Interestingly enough at even higher pressures a seamless transition from Pmmn into a distorted CsCl structure is observed. This is indicated by fig. 5.2, where the development of the lattice constants calculated for the Pmmn phase is depicted depending on the pressure. Here one can see the pressure range in which the Pmmn form of CdS is actually stable, and that at 129 GPa the lattice constants a and b become equal. At this pressure the parameters are $a = 3.997$, $b = 4.002$, $c = 2.978$ Å ($V_{pt} = 23.82$ Å³/pair) with $z(\text{Cd}) = 0.4993$ and $z(\text{S}) = 0.0740$, which means a lattice constant ratio of $b/a = 1.001$ and $c/a = 0.745$. The ideal cesium chloride structure would be reached if $a = b$ and $c/a = 1/\sqrt{2} = 0.707$, with the atoms being positioned at $z(\text{Cd}) = 0.5$ and $z(\text{S}) = 0.0$. Therefore, it is concluded that a small distortion along the z -axis remains, where the lattice constants a and b given above would be equal to a CsCl lattice constant of 2.83 Å.

However, a further transition into the exact cesium chloride structure is predicted at extremely high pressures of around 361 GPa ($V_{pt} = 18.04$ Å³/pair) with a lattice constant of 2.623 Å. To the best of our knowledge neither the distorted nor the exact cesium chloride phase have been detected yet, neither experimentally nor theoretically, but fit very well within the line-up of other group 12 chalcogenides.

There is no evidence for a cinnabar phase in cadmium sulfide. But due to reports claiming its existence in zinc sulfide and for reasons of consistency it was included in this study. The lattice parameters obtained are 4.092 and 9.598 Å for a and c , respectively, whereas the internal parameters are calculated to be $u(\text{Cd}) = 0.5081$ and $v(\text{S}) = 0.5035$. Furthermore, the bulk modulus, its pressure derivative and the cohesive energy are $B_0 = 60.1$ GPa, $B' = 4.6$ and $E_{coh} = 5.041$ eV (at zero pressure). To the best of our knowledge no theoretical investigations have been carried out to compare with.

However, as expected the cinnabar phase is not a stable phase in CdS according to the study presented here, as the pressure for the wurtzite to cinnabar transition with 6.75 GPa as well as for the zinc blende to cinnabar transition with 6.69 GPa

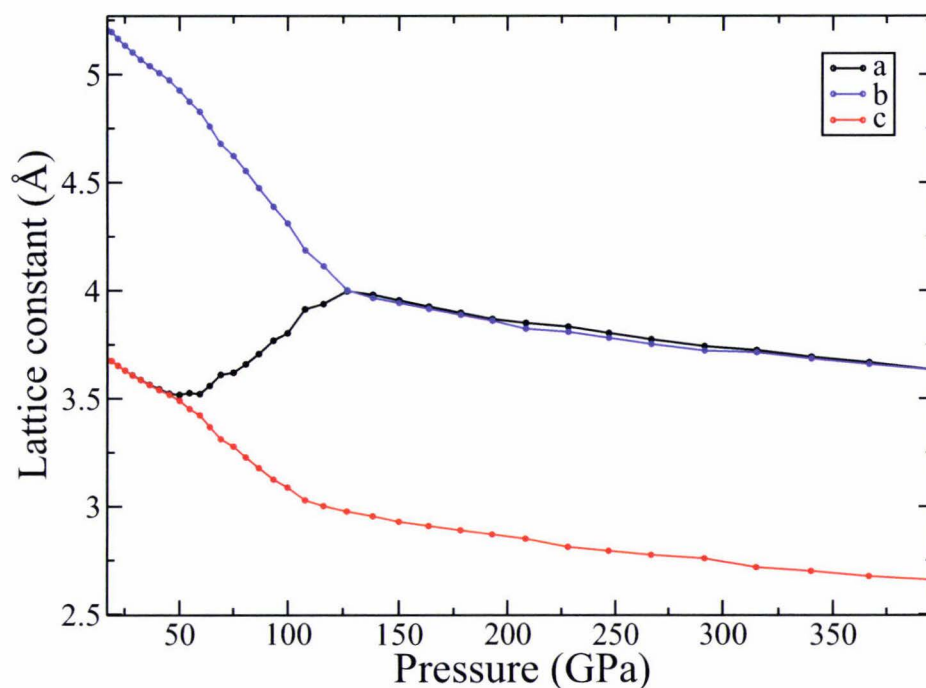


Figure 5.2: Lattice parameters depending on the pressure calculated for the $Pnmm$ structure of CdS.

is well above the pressures for the respective transitions into the rocksalt structure with 4.15 and 4.11 GPa, respectively.

In addition the SC16 structure was investigated as well due to the lack of its study in CdS. However, the $ZB \rightarrow SC16$ and $W \rightarrow SC16$ transition occurs at 6.97 and 7.03 GPa and would therefore happen after the transition to RS. Yet, it should be mentioned that the structure would be extremely close in energy to the cinnabar structure. The lattice parameters obtained for the SC16 structure are listed in table 5.7.

5.3.3 Mercury sulfide

The first transition under high pressure in HgS according to the study at hand takes place at 28.7 GPa, which is in excellent concordance with e.g. the GGA results of Sun *et al.* (26.57 GPa) [91] and shows good resemblance with various experimental investigations (13-29 GPa, see table 5.3), too. It should be mentioned that the transition is rather smooth, with a corresponding change of the internal parameters towards the trigonal description of rocksalt, meaning the

Property	This work	Other theoretical	Experiments
<i>Rocksalt</i>			
a	5.582 (5.150)	(5.052 ^a)	(5.180 ^b), (5.070 ^c)
V_0	43.47 (34.15)	(32.23 ^a)	(34.74 ^b) (32.58 ^c)
B_0	67.3	67.3 ^a	
B'	5.2	4.6 ^a	
E_{coh}	3.337		
p_t to Cmcn	54.55		52 ^d
p_t to Pmmn	63.51		
<i>Cmcn</i>			
a	(4.895)		
b	(4.898)		
c	(4.907)		
b/a	(1.001)		
c/a	(1.003)		
$y(\text{Hg})$	(0.7356)		
$y(\text{S})$	(0.2365)		
V	(29.41)		
B_0	113.2		
B'	2.9		
E_{coh}	3.294		
p_t to Pmmn	57.85		
<i>Pmmn</i>			
a	(3.633)		
b	(4.930)		
c	(3.312)		
b/a	(1.357)		
c/a	(0.912)		
$z(\text{Hg})$	(0.3150)		
$z(\text{S})$	(0.1903)		
V	(29.66)		
B_0	89.5		
B'	3.2		
E_{coh}	3.343		
p_t CsCl	210.87		

^aAPW+L●-GGA from ref. [91]; ^bX-ray diffraction at 23.4 GPa from ref. [165];
^cX-ray diffraction at 30 GPa from ref. [148]; ^dADX from ref. [12].

Table 5.8: Ground-state properties of the high-pressure phases of HgS. Presented are the lattice constants a , b and c (Å), respective internal parameters, ground-state volume V_0 (Å³/pair), bulk modulus B_0 (GPa) and its pressure derivative B' as well as the cohesive energy E_{coh} (eV/pair) and the transition pressure p_t (GPa) where applicable.

E-V curves superpose at this point. This was also observed by Sun *et al.* and indicates a second order transition.

The ground-state properties obtained for the rocksalt modification of HgS are $a = 5.582$ Å, $V_0 = 44.03$ Å³/pair, $B_0 = 67.3$ GPa and $B' = 5.2$. The cohesive energy is 3.337 eV/pair. Comparing with the theoretical and experimental values of other work listed in table 5.8, the lattice constant is strongly overestimated. Bulk modulus and B' are in excellent concordance with the GGA study of Sun *et al.* They give a ground-state volume of 32.23 Å³/pair, which would go along with a lattice constant of 5.052 Å. This deviates from the value calculated here by quite a few percent. However, this value is for the rocksalt structure treated as the cinnabar structure using $u = v = 2/3$, hence avoiding the error due to change of symmetry. At a pressure of 30.24 GPa the calculations presented in this work give a lattice constant of 5.150 Å, which certainly agrees with the experimental values. A recent publication also mentions that the authors observed the rocksalt and cinnabar phase to coexist between 15-23 GPa. This gives rise to relatively large errors for the unit-cell parameters, explaining the deviation between experiments and the results presented here [165].

Since in the case of CdS, both Cmcm and Pmmn were suggested as high-pressure structures and not much is known of the post-RS behaviour of HgS, calculations were carried out determining both of those structures for HgS as well. The stability of the Cmcm phase over the Pmmn modification is supported by the results presented here. The transition from rocksalt into the Cmcm phase actually takes place at 54.55 GPa compared to 63.51 GPa for the Pmmn form. The Cmcm→Pmmn transition is predicted at 57.85 GPa. Both structures are, however, close in energy. Yet, the pressure predicted for the first transition agrees very well with the one measured by Nelmes and McMahon, who obtained 52 GPa. But too little is known yet, as they did not resolve the structure, but merely suggested 'a distortion of the NaCl structure, possibly Cmcm' [12].

Calculating the lattice parameters for the Cmcm structure gives $a = 4.895$ Å, $b = 4.898$ Å, $c = 4.907$ Å ($b/a = 1.001$, $c/a = 1.003$) and $V = 29.41$ Å³/pair as well as $y(\text{Hg}) = 0.7356$ and $y(\text{S}) = 0.2365$ at 67.77 GPa. Bulk modulus and pressure derivative are estimated from the data points available (see table 5.8). The lattice constants obtained for the possible Pmmn phase are $a = 3.633$ Å, $b = 4.930$ Å, $c = 3.312$ Å along with the following internal parameters: $z(\text{Hg}) = 0.3150$ and $z(\text{S}) = 0.1903$. All those values are determined at a pressure of 63.54 GPa. Unfortunately, no data to compare with is available and further

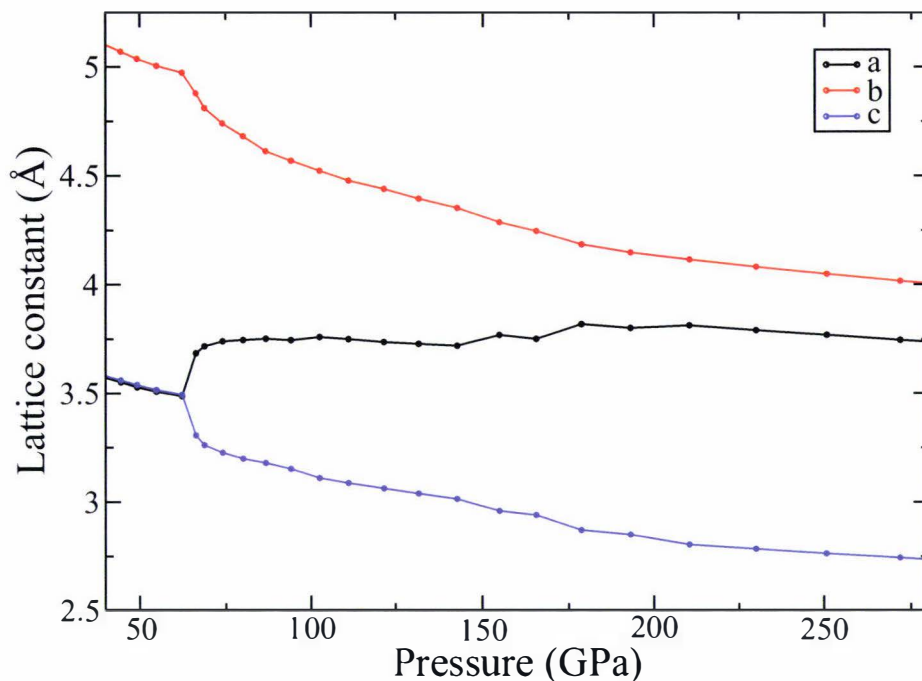


Figure 5.3: Lattice parameters depending on the pressure calculated for the Pmmn structure of HgS.

investigations by theoretical means would be strongly recommended.

Finally, we predict the transition into the CsCl structure at about 210 GPa. However, subjective to the few structures investigated we cannot rule out the transition into intermediate phases between Pmmn and CsCl that yet have to be discovered either experimentally or theoretically. In addition, the pressure necessary is extremely high making it difficult for experimentalists to obtain this structure. No evidence is found in HgS for the distorted CsCl structure occurring intermediate between Pmmn and CsCl in CdS (see fig. 5.3).

Furthermore, the SC16 structure was calculated for HgS as well, which has not been done before. However, it is always at least 0.1 eV higher in enthalpy compared to the cinnabar phase and therefore unlikely to appear in HgS. The ground-state properties were obtained anyway and are $V_0 = 48.81 \text{ \AA}^3/\text{pair}$, $a = 7.309 \text{ \AA}$, $u = 0.1471$ and $v = 0.6462$, $B_0 = 45.67 \text{ GPa}$, $B' = 6.0$ and $E_{coh} = 3.500 \text{ eV}$.

5.4 Electronic structure

5.4.1 Zinc sulfide

Looking at the electronic structure of the ZnS equilibrium phases while using the discussed scalar-relativistic approach, the band structures and density of states depicted in fig. 5.4 indicate a wide-gap semiconductor with a direct fundamental gap for both polymorphs.

It occurs at the Γ -point in the Brillouin zone and is 2.00 and 2.06 eV for zinc blende and wurtzite, respectively, showing a rather similar electronic structure despite the different structure and coordination. It should be mentioned that further local minima of the conduction bands are located at the L -, X - and K -points and at the A -point as well as between L and M for the cubic and hexagonal modification, respectively. Additional local valence-band maxima (VBM) can be found at the L -point for the zinc blende form and at A , M and H for the wurtzite phase of ZnS.

As expected those results underestimate the experimental gap of 3.8 and 3.9 eV severely [153], but agree very well with other theoretical DFT work, where the band gap is calculated to be 1.82 (LDA) [170] and 2.0 eV (GGA) [150] for ZB-ZnS and 1.97 eV (LDA) [171] for the hexagonal structure. Furthermore, comparability with experiments can be improved using the GW approximation, where Fleszar *et al.* obtained fundamental gaps of 3.38-3.99 eV for the zinc blende form [170].

5.4.2 Cadmium sulfide

Concerning the equilibrium structures of CdS, the method employed here gives a band gap of 1.08 and 1.00 eV for the wurtzite and zinc blende form, respectively. Like for ZnS, the valence-band maximum as well as the conduction-band minimum are at the centre of the Brillouin zone, thus making both polymorphs direct wide-gap semiconductors (see fig. 5.5).

However, for the cubic form further local minima of the first conduction band are located at the L -, X - and K -points. Another local maximum of the last filled valence-band can be found at the L -point. In the case of the wurtzite form more conduction-band minima are found at the A -point and between L and M , whereas another local valence-band maximum is located at A , M and H .

Again, values estimated by experimental means with a gap of $E_g(\Gamma) = 2.58$ eV (at 1.8 K) for hexagonal and $E_g(\Gamma) = 2.48$ eV (at 1.6 K) [120] for cubic CdS

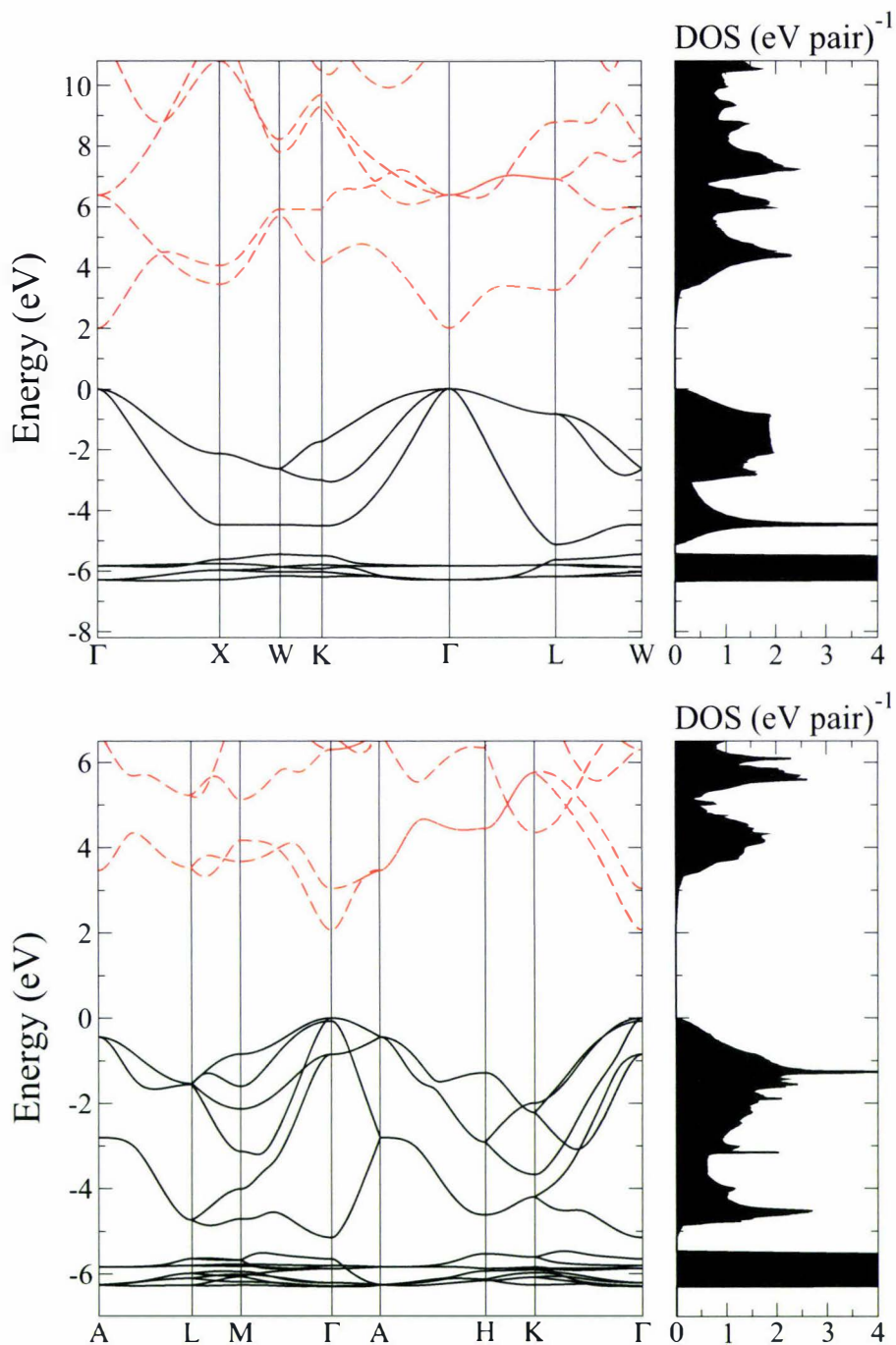


Figure 5.4: Band structure and density of states (normalized per pair) at zero pressure for the ZnS polymorphs zinc blende (upper panel) and wurtzite (lower panel) calculated within the scalar-relativistic DFT-GGA framework. The valence-band maximum is set to zero energy. The black solid lines indicate the valence and the red dashed lines the conducting bands, respectively.

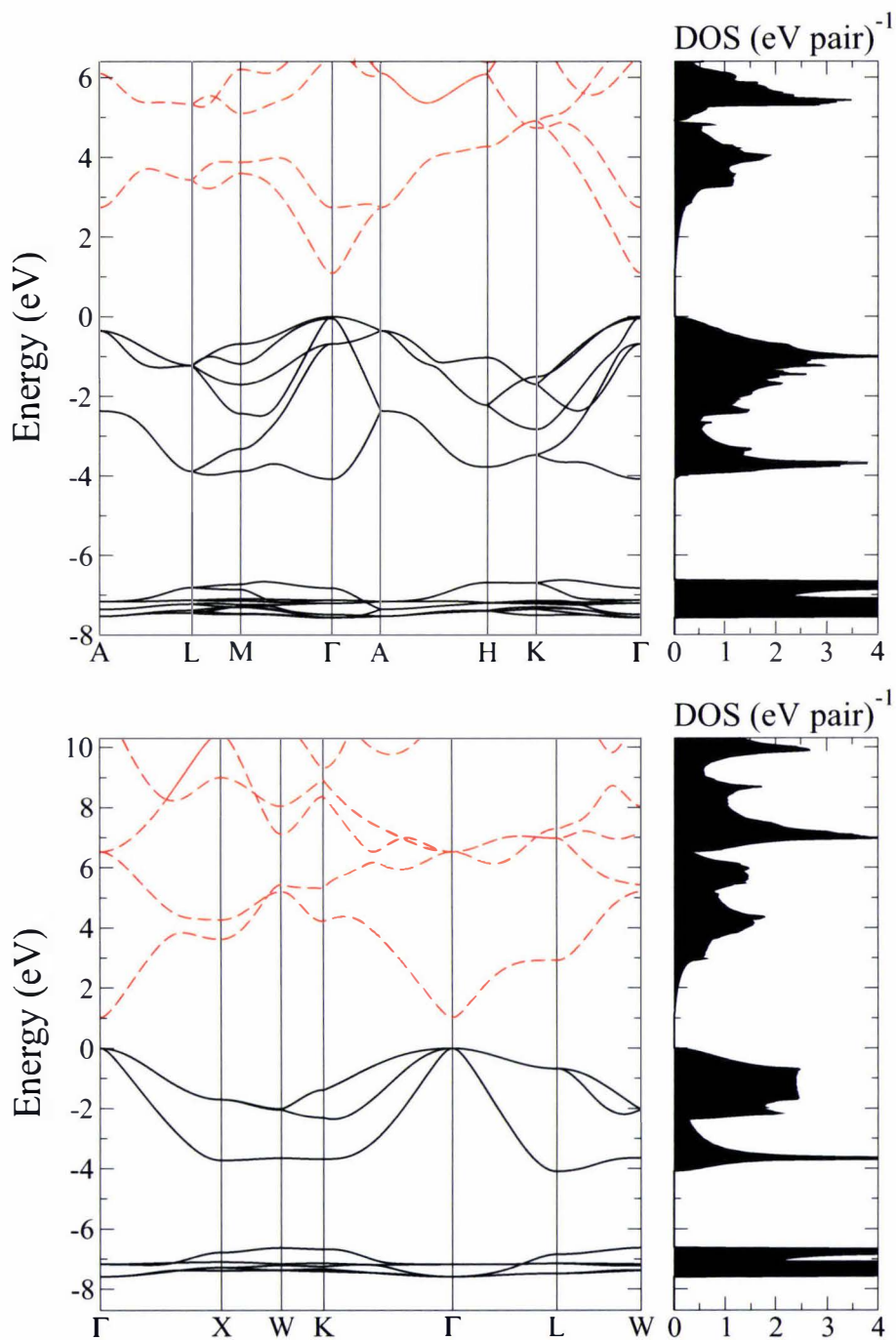


Figure 5.5: Band structure and density of states (normalized per pair) at zero pressure for the CdS polymorphs wurtzite (upper panel) and zinc blende (lower panel) calculated within the scalar-relativistic DFT-GGA framework. The valence-band maximum is set to zero energy. The black solid lines indicate the valence and the red dashed lines the conducting bands, respectively.

at zero pressure are very much underestimated, but the electronic structure is in good qualitative agreement. Another theoretical LDA calculation by Fleszar *et al.* finds a direct bandgap of $E_g(\Gamma) = 0.80$ eV for the zinc blende modification similar to the value obtained here, but the authors refine their result using different GW approximation approaches ($E_g(\Gamma) = 2.11 - 2.63$ eV) [170]. Calculations using so-called self-interaction-corrected pseudopotentials approximate the band-gap value for the hexagonal polymorph to $E_g(\Gamma) = 2.5$ eV [120].

5.4.3 Mercury sulfide

Like for mercury oxide, again the band structure and density of states was calculated at different levels of theory, employing a pure scalar-relativistic approach as well as including the effects of spin-orbit coupling. The results can be found in figs. 5.6 and 5.8 for the cinnabar and zinc blende modification, respectively. HgS in its prototype cinnabar modification has according to various luminescence experiments a band gap of 2.275 eV, which is most likely direct [120]. It is therefore classified as a large-gap semiconductor [172].

When facilitating a scalar-relativistic approach, the trigonal modification of mercury sulfide is technically an indirect band gap semiconductor (see upper panel of fig. 5.6). The CBM occurs at the Γ -point at 1.60 eV with other local minima to follow at M (2.17 eV) and L (2.27 eV). The VBM can be found along the Δ -line between Γ and A along with further local maxima between A and L (-0.005 eV) and between A and H (-0.005 eV) as well as at Γ (-0.020 eV).

However, this means that the smallest direct fundamental gap occurs at the Γ -point with $E_g(\Gamma) = 1.62$ eV. This is extremely close in energy to the indirect gap, which explains why experiments classify it as direct.

Furthermore, those results (including the DOS) are in excellent qualitative agreement with the GGA calculations of Sun *et al.* using a APW+lo plane-wave basis set [173]. According to their graphs the band gap is around 1.6 eV as well (hard to estimate from just pictures).

Taking into account spin-orbit splitting, the picture does not change dramatically, as can be seen in the lower panel of fig. 5.6. However, the CBM is now slightly shifted and two minima open up extremely close to Γ at an energy of 1.585 eV. They are located at the Δ -line between Γ and A and between M and Γ . Further minima can be found around M (2.124 eV) and shortly before L between A and L (2.243 eV). Concerning the VBM, the local maximum A and H in the scalar-relativistic calculations becomes more prominent, but a further maxima

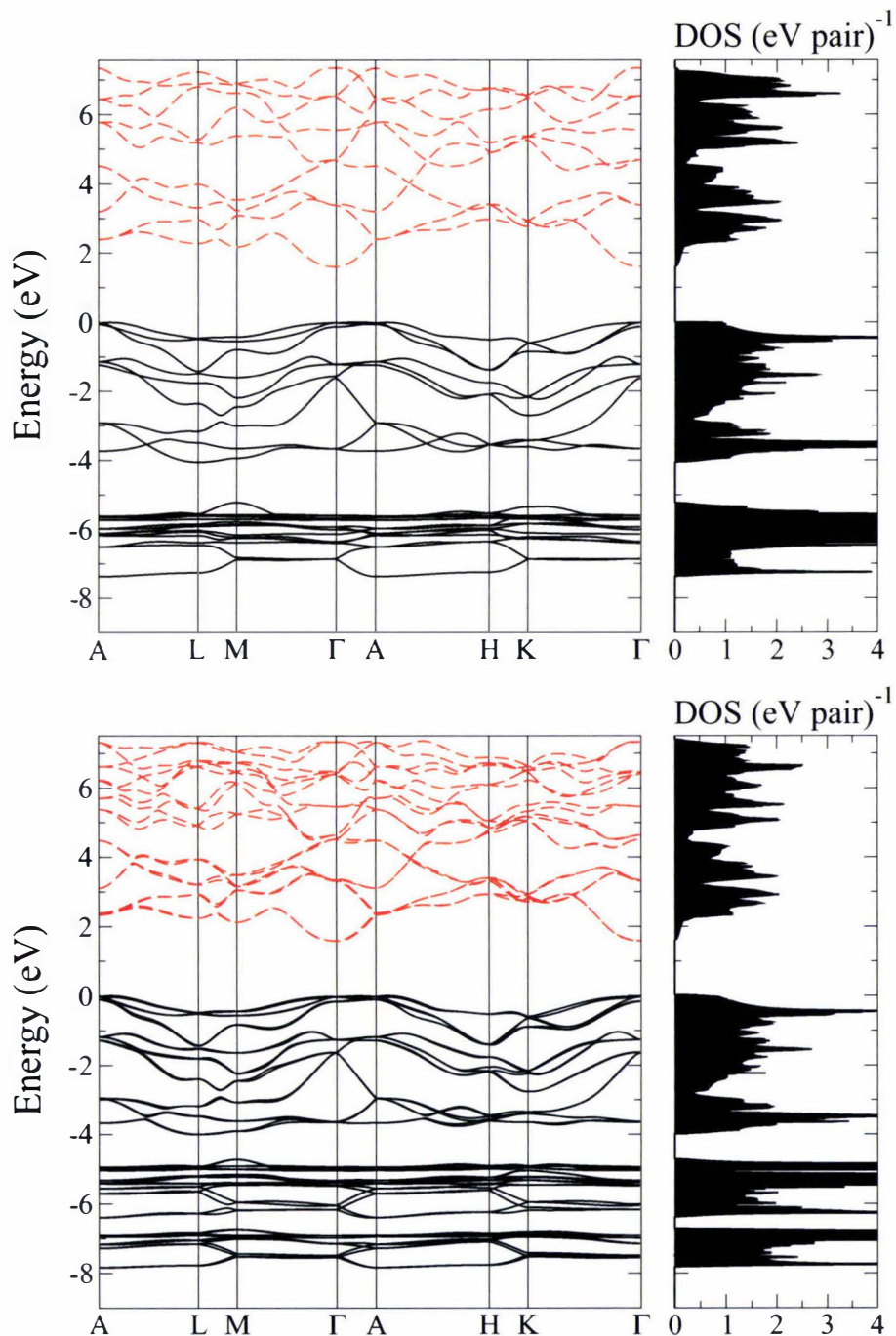


Figure 5.6: Band structure and density of states (normalized per pair) at zero pressure for the HgS cinnabar polymorph calculated within the scalar-relativistic DFT-GGA framework (upper panel) as well as upon inclusion of spin-orbit effects (lower panel). The valence-band maximum is set to zero energy. The black solid lines indicate the valence and the red dashed lines the conducting bands, respectively.

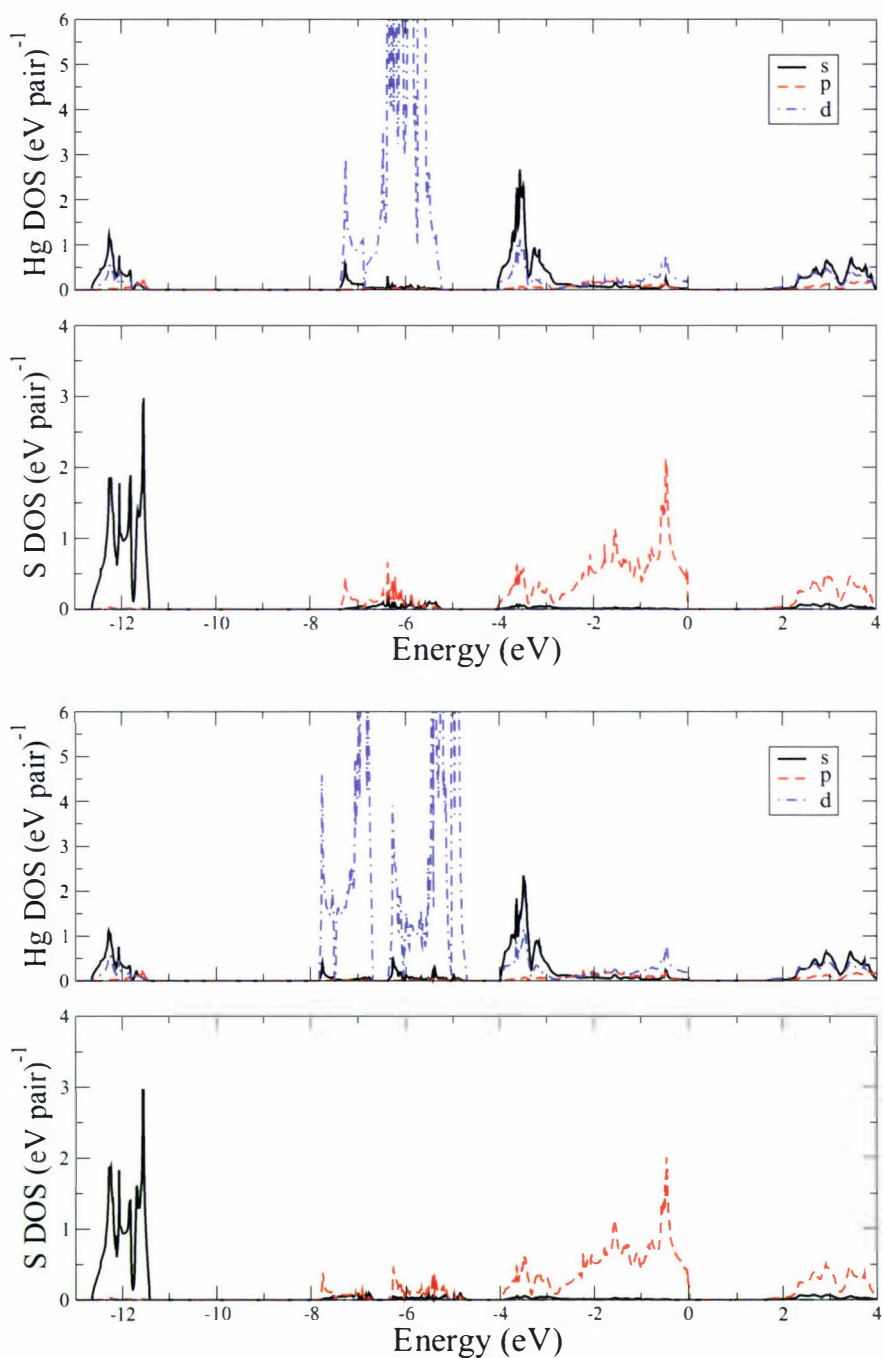


Figure 5.7: Site-projected density of states at zero pressure for the HgS cinnabar polymorph calculated within the scalar-relativistic DFT-GGA framework (upper panel) as well as upon inclusion of spin-orbit effects (lower panel). The black solid, red dashed and blue dash-dotted line indicate the s, p and d site-projected DOS, respectively.

between A and L occurs almost at the same energy. More follow between Γ and A and between K and Γ still very close in energy. The first direct transition is possible around Γ with a gap energy of 1.614 eV. Further theoretical results on this level of theory would be desirable to compare with.

The site-projected DOS are depicted as well using both the scalar-relativistic approach and upon inclusion of spin-orbit coupling (see fig. 5.7). The scalar-relativistic DOS agrees well with the results of Sun and Dong [173]. The d -bands feature the typical crystal field splitting pattern of the trigonal bonded structures, where the three peaks are separated by approximately 0.1 and 0.4 eV respectively in accordance with experimental values (0.10 and 0.39 eV calculated from $D_q = 0.05$ eV [120]). The most prominent feature of the spin-orbit corrected site-projected DOS is again the spin-orbit splitting in the d -bands of the Hg atom of about 2 eV resembling the one found for the atomic splitting (1.86 eV [128]).

Turning now to the zinc blende modification of mercury sulfide, it is particularly interesting because of its rather unique electronic structure. It was first described as a zero-gap semiconductor, i.e. semimetal, evoked by a band degeneracy due to symmetry [120]. However, a band gap of 0.54 eV is measured through absorption at 300 K [120]. Other measurements through plasma edge reflectivity and interband absorption conclude an inverted band structure along with a negative band gap -0.110 to -0.150 eV [172]. The inverted structure can be explained by the large effective positive charge of the Hg core, which causes the bands of the Γ_6 symmetry to be shifted below the Γ_8 level. Therefore, only two of the four Γ_8 bands are occupied, while the other two contribute to the conduction band. The hence induced degeneracy with the highest valence band gives rise to a zero gap [168].

Interestingly enough, the scalar-relativistic calculations carried out (see upper panel of fig. 5.8) confirm the non-existence of the fundamental gap. However, if one looks at the electronic structure determined by the inclusion of spin-orbit coupling, depicted in the lower panel of fig. 5.8, counting bands a small band-gap opens up close to the Γ -point. The VBM occurs at the Σ -line between K and Γ . But two more local VBM, which are almost as high appear along the Λ -line between Γ and L and at the Δ -line between Γ and X , all of which are very close to the centre of the Brillouin zone. The CBM can be found at the Γ -point at 0.028 eV. Hence, this HgS phase at ambient conditions has an indirect energy gap of $E_g(\Gamma - \Sigma) = 0.028$ eV, whereas the smallest direct gap can be found at the

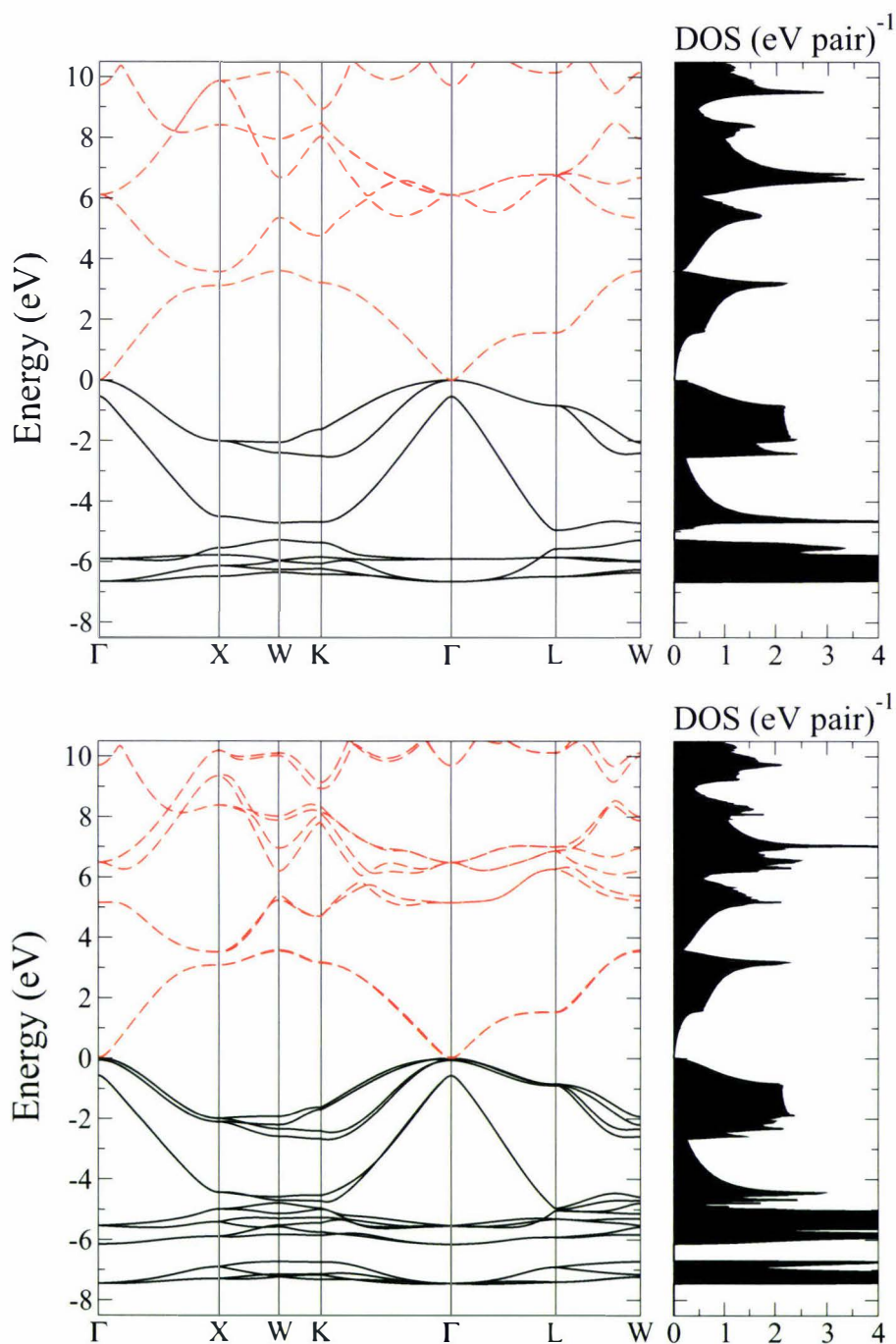


Figure 5.8: Band structure and density of states (normalized per pair) at zero pressure for the HgS zinc blende polymorph calculated within the scalar-relativistic DFT-GGA framework (upper panel) as well as upon inclusion of spin-orbit effects (lower panel). The valence-band maximum is set to zero energy. The black solid lines indicate the valence and the red dashed lines the conducting bands, respectively.

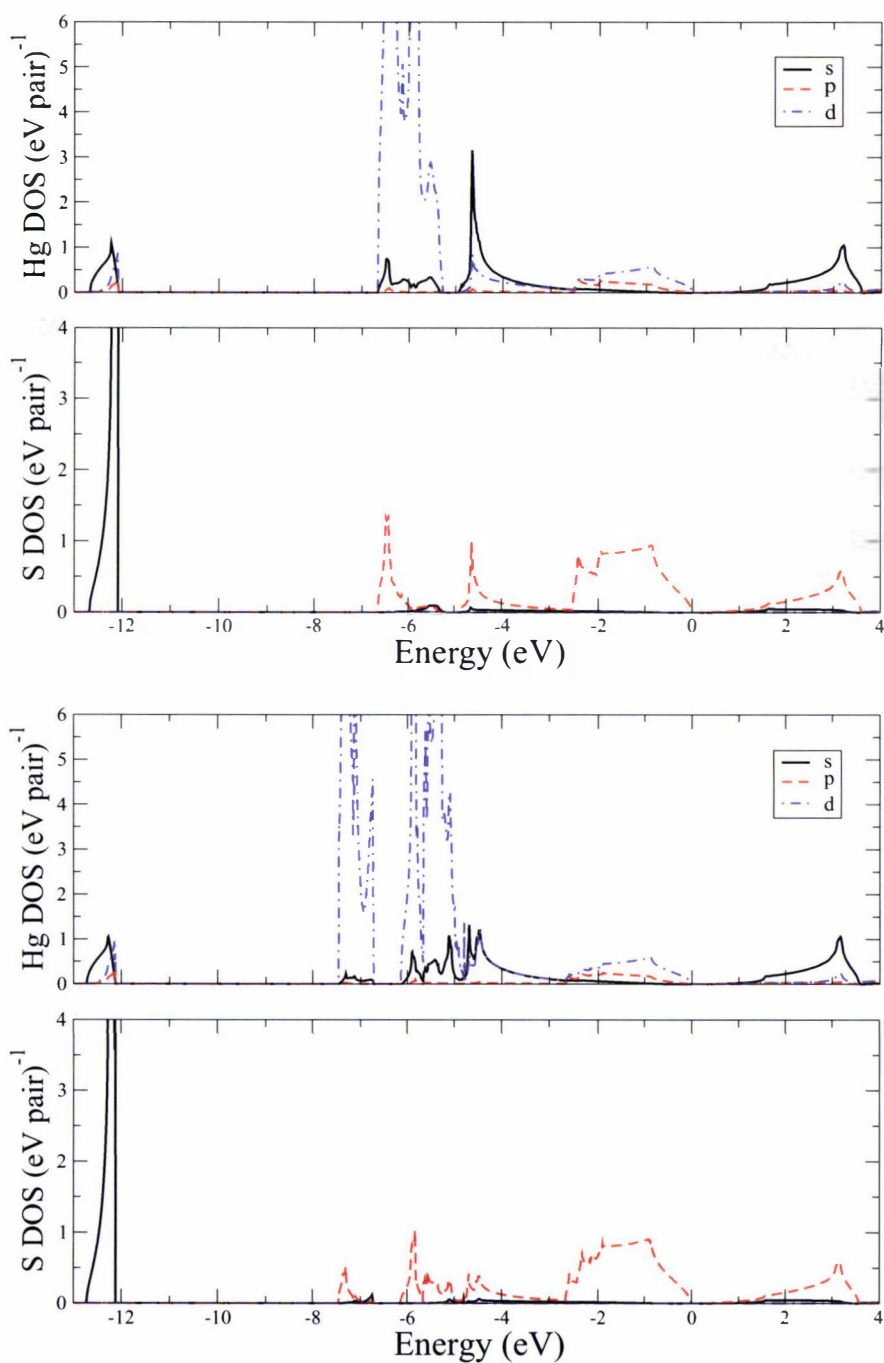


Figure 5.9: Site-projected density of states at zero pressure for the HgS zinc blende polymorph calculated within the scalar-relativistic DFT-GGA framework (upper panel) as well as upon inclusion of spin-orbit effects (lower panel). The black solid, red dashed and blue dash-dotted line indicate the s, p and d site-projected DOS, respectively.

Σ -line and is determined to be $E_g(\Gamma)=0.090$ eV. This agrees very well with the result of Cardona *et al.* ($E_g^{direct} = 0.091$ eV [174], VASP-GGA) and Delin *et al.* ($E_g^{direct} < 0.1$ eV [168], FP-LMTO LDA). According to the authors those values also match the experimental results of Zallen and Slade (0.25 eV) reasonably well.

However, the negative spin-orbit splitting needs to be accounted for, which inverts the band structure. This means the energy gap is found between Γ_6 and Γ_8 . In that case, according to the calculation presented here, the direct energy gap obtained is -0.57 eV, which is in excellent agreement with the reference cited above ($E_g^{direct,GGA} = -0.483$ eV, $E_g^{direct,LDA} = -0.573$ eV). Interestingly enough Cardona *et al.* also point out that, according to the GW calculations of e.g. Fleszar and Hanke [170], the Γ_1 state of HgX compounds calculated within LDA needs to be corrected by 0.75 eV. If one adds this value to the obtained gap energy, the fundamental gap of zinc blende HgS actually becomes positive. This means it has to be characterized as a semiconductor. The site-projected DOS are shown in fig. 5.9.

Comparing the scalar-relativistic calculations presented here with other theoretical reports [162, 168], the resemblance is good. In general like for HgO, a further investigation of those band structures using LDA+U or the GW approximation would be recommended.

5.5 Relativistic influences

5.5.1 Equilibrium structure

System	a	c	u / v	B_0	B'	E_{coh}	V_0
Wurtzite	4.398	7.091	0.3792 / -	48.1	4.5	5.383	59.37
Zinc blende	6.192	-	- / -	47.9	4.7	5.377	59.35
Rocksalt	5.711	-	- / -	67.4	4.7	5.302	46.57
Cesium chloride	3.523	-	- / -	67.4	4.8	4.432	43.73
Cinnabar	4.233	10.085	0.5060 / 0.5032	53.8	4.6	5.213	52.17
SC16	7.537	-	0.1539 / 0.6417	46.3	5.1	5.215	53.52

Table 5.9: Ground-state properties of equilibrium and high-pressure phases of HgS within the nonrelativistic approach. Presented are the lattice constants a and c (Å), respective internal parameters, ground-state volume V_0 (Å³/pair), bulk modulus B_0 (GPa) and its pressure derivative B' as well as the cohesive energy E_{coh} (eV/pair).

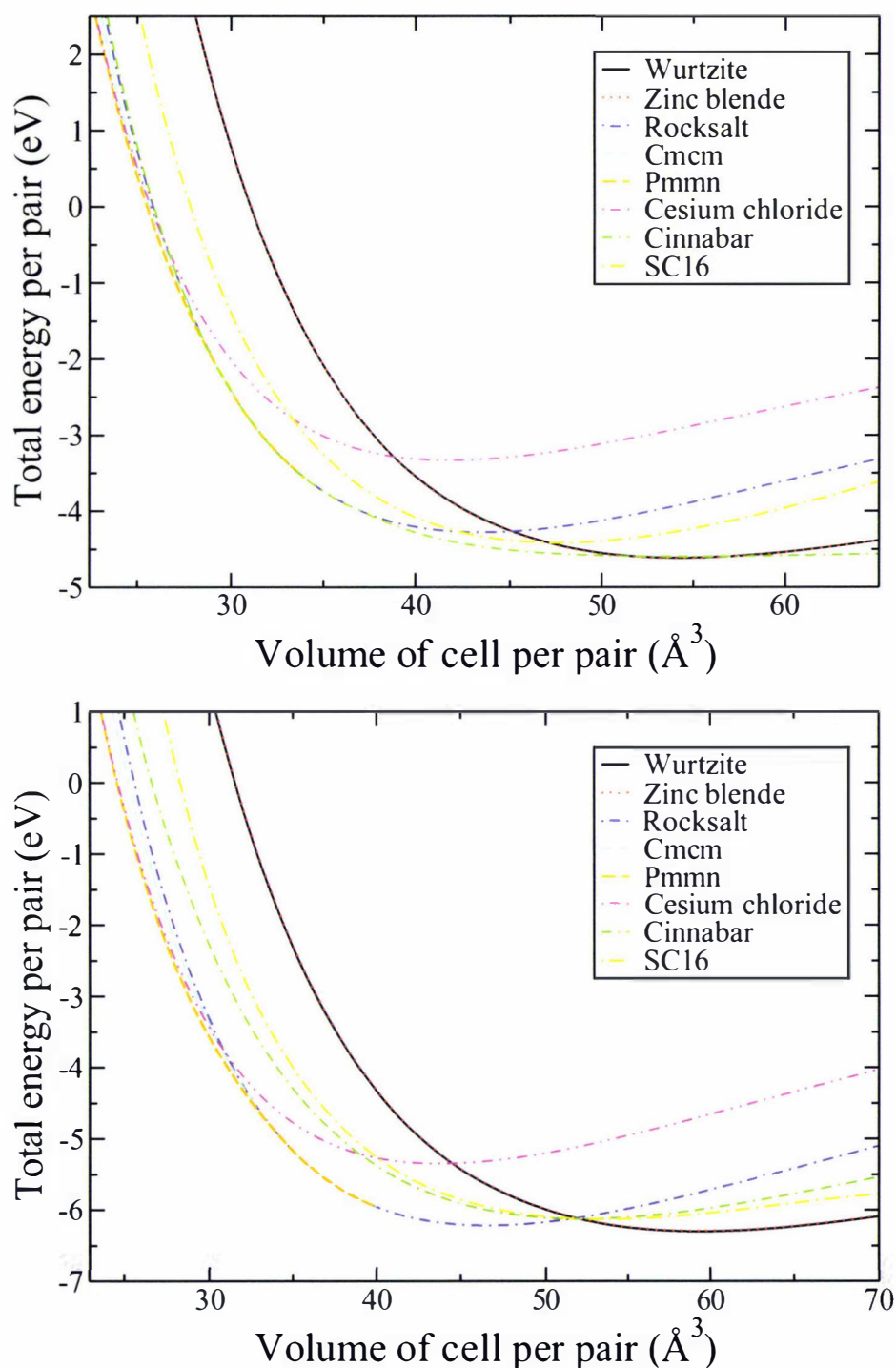


Figure 5.10: The total energy versus volume per cation-anion pair for different crystal structures of relativistic (upper panel) and nonrelativistic HgS (lower panel).

Looking at the nonrelativistic energy-volume curves for HgS, depicted in the lower panel of fig. 5.10, the equilibrium behaviour changes dramatically. The cinnabar structure disappears not only as the equilibrium phase, but completely. In summary a similar behaviour as in ZnS and CdS is found, meaning the structures lying lowest in total energy are wurtzite and zinc blende. Yet, the wurtzite structure is slightly preferred with an energy difference of only 6 meV/pair. This means, assuming the non-relativistic description of HgS, the relative stability of the wurtzite form compared to zinc blende structure actually increases going from ZnS via CdS to HgS, whereas the relativistic influences change that picture favouring the cinnabar structure over wurtzite instead.

The lattice properties determined for the wurtzite structure are $a = 4.398$ Å, $c = 7.091$ Å and $V_0 = 59.37$ Å³/pair (see table 5.9). Hence, the lattice constant is 14% and 5% larger than for the respective structure in ZnS and CdS. This is opposed to a value of 4.256 Å in relativistic wurtzite-HgS, making the lattice constant almost comparable to the one in CdS and therefore showing the typical relativistic contraction.

This effect becomes even more obvious, if one looks at the bond distances (see table 5.10): Induced by the structure change due to relativistic effects, the metal-sulphur bond distance of cinnabar-HgS (2.40 Å) is comparable to the one obtained for the equilibrium structure of ZnS (2.35 Å). This means a huge relativistic contraction in the intra-chain Hg-S distances of 0.28 Å, if one compares the relativistic to the nonrelativistic value (2.68 Å). However, this comes at the cost of increasing the inter-chain Hg-S bond distance to 3.36 Å. Hence, the overall volume expands from 55.16 (relativistic) to 59.37 Å³/pair (nonrelativistic) decreasing the density from 7.19 to 7.00 g cm⁻³. The experimental value for cinnabar-HgS is 8.2 g cm⁻³ as compared to 4.0 g cm⁻³ in ZB-ZnS and 4.8 cm⁻³ in W-CdS [114].

Looking at the cohesive energies, a deviation of over 1.73 eV/pair is determined changing from the relativistic ($E_{coh} = 3.657$ eV/pair) to the nonrelativistic ($E_{coh} = 5.383$ eV/pair) picture, hence indicating a strong lattice destabilization due to relativistic influences.

Furthermore, the extreme contraction in bond length is even applicable if one compares the metal-sulphur distances of HgS with the hypothetical cinnabar forms of ZnS and CdS. Even then the value is almost comparable to the 2.39 Å obtained in cinnabar-ZnS and significantly lower than in nonrelativistic cinnabar-HgS ($d_{HgS} = 2.70$ Å). This is due to a significant change in the internal parameters u and v , leading to a fourfold coordination instead of the 2+4 coordination

found in relativistic HgS (see fig 3.5 for visualization).

The solid-state properties of the possible equilibrium phases of nonrelativistic HgS as well as the cohesive energies are summarized in table 5.9.

System	ZnS		CdS		HgS		nonrel. HgS	
	d_{MS}	d_{MM}	d_{MS}	d_{MM}	d_{MS}	d_{MM}	d_{MS}	d_{MM}
Wurtzite	2.35	3.84	2.57	4.20	2.60	4.24	2.68	4.36
exp.	2.34	3.82	2.53	4.12	-	-	-	-
Zinc blende	2.36	3.85	2.56	4.19	2.60	4.25	2.68	4.38
exp.	2.34	3.82	2.52	4.11	2.53	4.14	-	-
Cinnabar	2.39	3.48	2.59	3.79	2.40	4.39	2.70	3.97
	-	-	-	-	2.41	4.20	-	-
exp.	-	-	-	-	2.37	4.14	-	-

Table 5.10: Closest metal-sulphur bond distance d_{MS} and closest metal-metal distance d_{MM} in Å of the respective equilibrium structures of the group 12 sulfides.

5.5.2 High-pressure structure

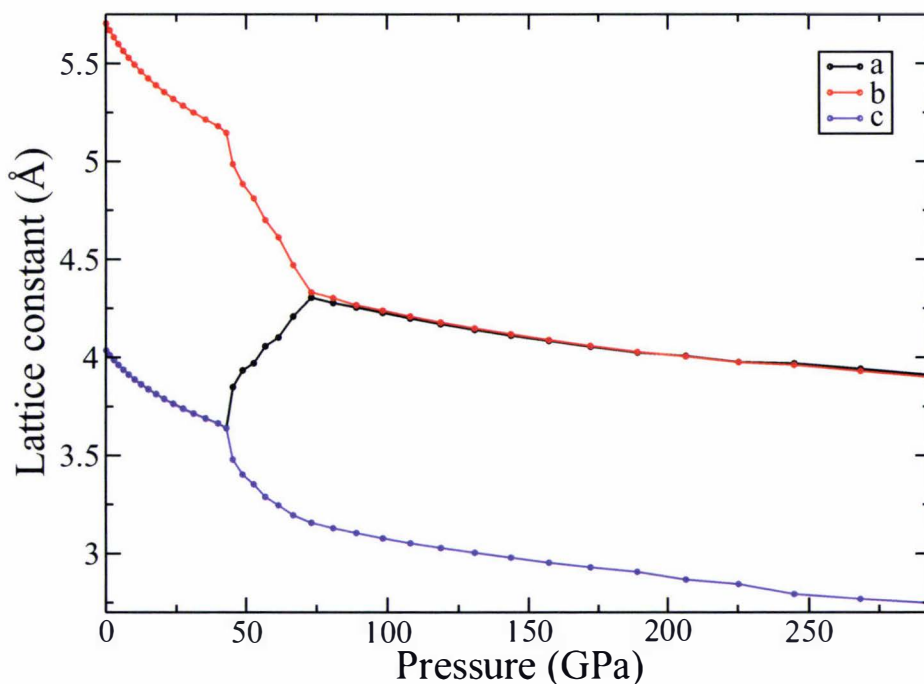


Figure 5.11: Lattice parameters depending on the pressure calculated for the Pmmn structure of nonrelativistic HgS.

While the change in the equilibrium structure accompanying the neglect of relativistic effects is rather dramatic, nothing special can be said about the high-pressure phases of HgS in those circumstances.

A transition to the rocksalt structure is predicted to happen at 1.07 GPa ending the stability range for the wurtzite form ($p_t = 0.97$ GPa for zinc blende). The ground-state lattice constant of this phase is calculated to be 5.711 Å, which is significantly larger than the respective values for the wurtzite form of ZnS (5.108 Å), CdS (5.503 Å) and relativistic HgS (5.582 Å). The bulk moduli decrease in the same order, but are almost identical for relativistic and nonrelativistic HgS.

Subsequently, a transition to the Cmc m structure takes place at 37.97 GPa. The Pmm m structure is unstable in the presence of Cmc m and the respective transition (RS \rightarrow Pmm m) would only occur at 43.80 GPa. However, in the transition region the three structures are less than 2 meV apart from each other in enthalpy, making it difficult to make predictions due to the precision of the calculations.

The solid-state properties for the Cmc m structure are $V = 34.59$ Å³/pair, $a = 5.172$ Å, $b = 5.175$ Å, $c = 5.169$ Å (hence $b/a = 1.000$ and $c/a = 0.999$) as well as $y(\text{Hg}) = 0.7388$ and $y(\text{S}) = 0.2393$ at 40.70 GPa. For the Pmm m modification the following values are obtained at 44.86 GPa: $V = 33.36$ Å³/pair, $a = 3.848$ Å, $b = 4.985$ Å, $c = 3.478$ Å, $b/a = 1.295$, $c/a = 0.904$, $z(\text{Hg}) = 0.3590$ and $z(\text{S}) = 0.1508$. The transition from Cmc m to Pmm m takes place at 43.94 GPa.

Finally, at 73.6 GPa the lattice constants a and b become equal and the c/a ratio indicates a transition towards distorted CsCl (see fig. 5.11) having an approximate lattice constant of 2.972 Å at 108 GPa, with a further transition to CsCl at 280.25 GPa, where a lattice constant of 2.767 Å is calculated ($V = 21.18$ Å³/pair).

It should be mentioned that neither the cinnabar nor the SC16 structure are stable in nonrelativistic HgS. All properties are summarized in table 5.9.

5.5.3 Electronic structure

Considering the small energy difference and following the trend from ZnS and CdS it is likely that both the zinc blende and the wurtzite phase would exist as an equilibrium phase for nonrelativistic HgS. Therefore, electronic structure calculations for both of those potential nonrelativistic equilibrium states of HgS were carried out. Fig. 5.12 indicates that the band structure and DOS for nonrelativistic HgS are rather similar to the ones obtained for CdS.

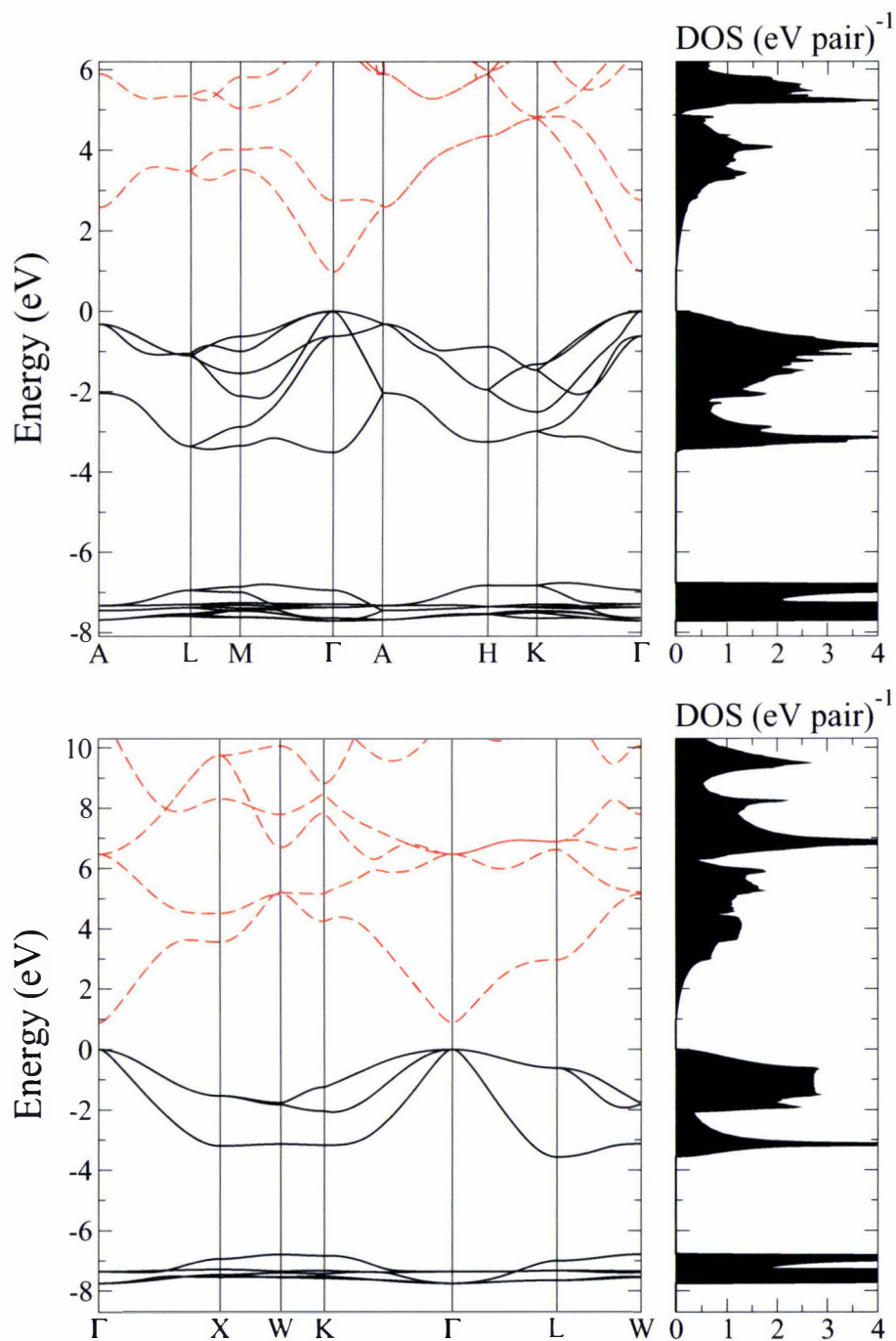


Figure 5.12: Band structure and density of states (normalized per pair) at zero pressure for the HgS polymorphs wurtzite (upper panel) and zinc blende (lower panel) calculated within the nonrelativistic DFT-GGA framework. The valence-band maximum is set to zero energy. The black solid lines indicate the valence and the red dashed lines the conducting bands, respectively.

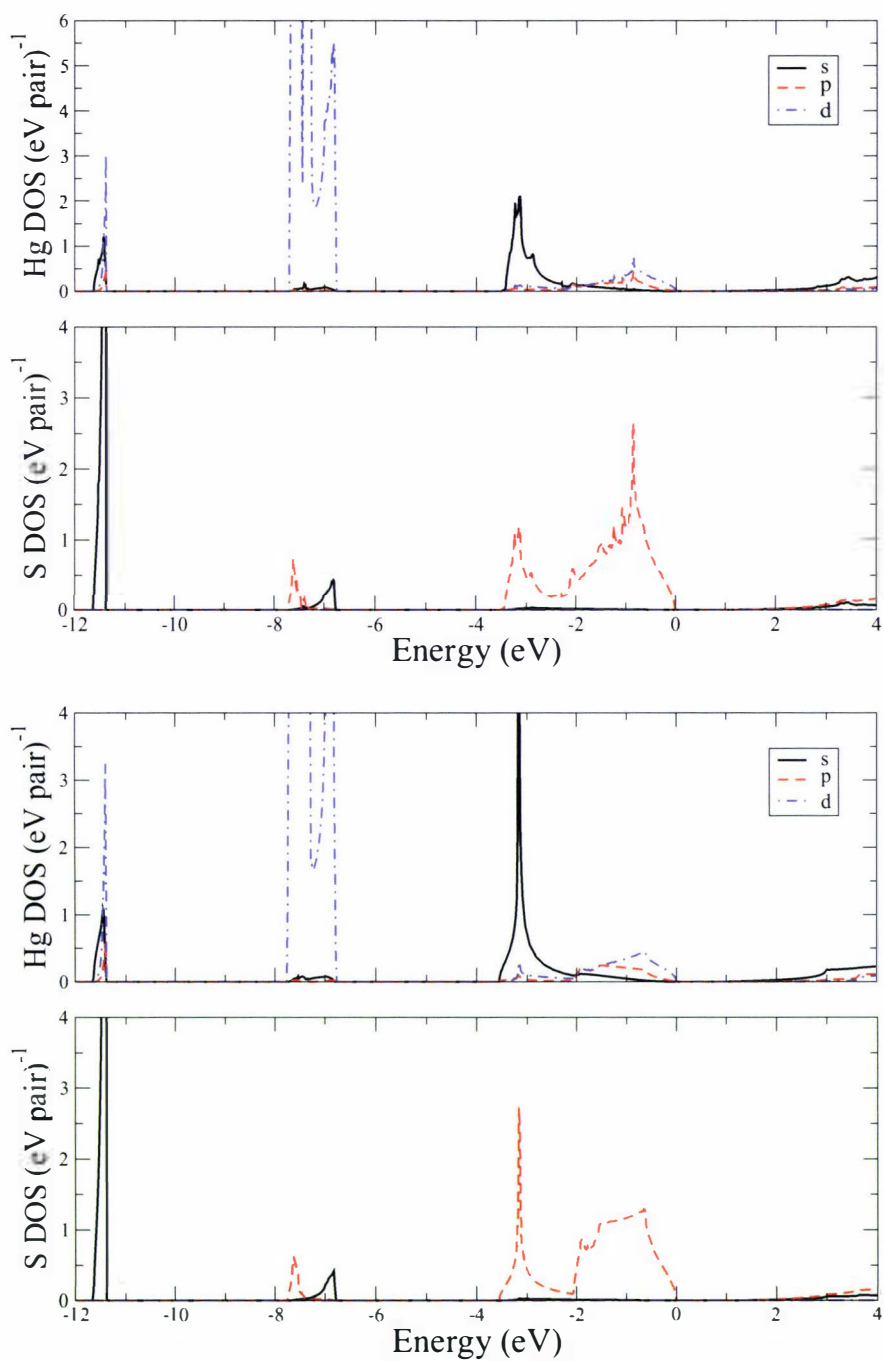


Figure 5.13: Site-projected density of states at zero pressure for the HgS polymorphs wurtzite (upper panel) and zinc blende (lower panel) calculated within the nonrelativistic DFT-GGA framework. The black solid, red dashed and blue dash-dotted line indicate the s, p and d site-projected DOS, respectively.

The wurtzite modification of HgS would have a semiconducting character with a direct band gap of 0.97 eV at the centre of the Brillouin zone. Additional local VBM and CBM can be found. This means compared to the stable relativistic equilibrium form (cinnabar) the band gap is significantly reduced, imitating the behaviour in wurtzite-CdS. However, the semiconducting properties are maintained.

For the zinc blende structure the changes due to relativistic effects are even more severe. The inverted band structure is now abolished, leaving nonrelativistic cubic HgS as a rather ordinary small-gap semiconductor. The VBM as well as the CBM, similarly to CdS, can be found at Γ , hence giving rise to a direct band-gap with $E_g(\Gamma) = 0.89$ eV, again similar to ZB-CdS. Other local CBM, however much higher in energy, can be found at X and K .

The site-projected DOS of both possible equilibrium forms of nonrelativistic HgS are shown in fig. 5.13. For both polymorphs the site-projected DOS is rather simplified compared to the relativistic equivalents. The crystal field splitting can be clearly seen, which is around 0.23 eV for W-HgS as well as for ZB-HgS and is typical for the tetrahedral bonding in those structures. In both cases the Fermi edge is characterized mainly by the Hg-5*d* and S-2*p* orbitals.

5.6 Summary

In general, the properties for the group 12 sulfides are in good agreement with experimental and other theoretical work, where available. This is true for the equilibrium as well as high pressure phases. Concerning the electronic structure, the band gap is generally drastically underestimated due to the known shortcomings of DFT in this context, yet qualitative agreement is ensured.

The predicted transitions paths are mostly in concordance with experiments. However, for ZnS the stability of the SC16 structure as an intermediate phase between the zinc blende and rocksalt form is supported in accordance with other theoretical work. Furthermore, a transition from the Cmc*m* to a cesium chloride structure has been newly predicted. However, the new structure still needs to be confirmed experimentally, especially with respect to possible intermediate phases. Furthermore, the previously discussed Cmc*m* and Pmm*n* structures of CdS are for the first time investigated together with the same method and compared. In addition, the Cmc*m* and Pmm*n* structures found in CdS are investigated theoretically for HgS and are calculated to be stable in HgS under higher pressure as

well, which has not been done before. Since in both cases the two structures are rather close in energy, it is likely that both phases might exist in a mixed form in experiments. This would explain why both structures only partially explain the diffraction pattern found experimentally in CdS. Furthermore, a possibly new phase following the Pmmn structure in CdS is predicted and identified as a distorted CsCl form stretched along the c -axis. A high-pressure cesium chloride form in HgS has been predicted as well, which should be confirmed experimentally as well as theoretically to rule out intermediate phases.

Concerning the influence of relativistic effects, it is found that especially the equilibrium structure of HgS is significantly altered if a nonrelativistic treatment is chosen. In this case the cinnabar phase, similar to what was observed in HgO, becomes unstable and even disappears not only as an equilibrium phase, but as a possible high-pressure phase as well. Hence, this modification suppresses the wurtzite form, which nonrelativistically would increase in stability going from ZnS via CdS to HgS. Yet, a relativistic lattice destabilization of 1.73 eV/pair is already less than in HgO, where the difference amounts to more than 2 eV/pair. This shows for instance in the fact that the relative stability of the cinnabar form compared to the zinc blende form is already less, i.e. the zinc blende structure is found as a high-temperature equilibrium phase in HgS.

The high-pressure behaviour for HgS as well as the electronic structure become more similar to CdS, which is indicated by a similar transition path and smaller band gaps.

Chapter 6

The group 12 selenides

6.1 Occurring crystal structures

6.1.1 Zinc selenide

Zinc selenide crystallizes in a zinc blende structure with a lattice constant of $a = 5.668 \text{ \AA}$ under ambient conditions. It can be found as a grey microscopic mineral known as stilleite. Depending on the preparation conditions it may, however, also adopt its high-temperature (metastable) wurtzite structure with the lattice constants $a = 4.003 \text{ \AA}$ and $c = 6.540 \text{ \AA}$ [120].

A transition under pressure was observed at around 13 GPa by means of optical [175, 176] as well as resistivity [177, 178] measurements, and the new phase was reported to have a (site-ordered) rocksalt structure ($a = 5.110 \text{ \AA}$ at 13.6 GPa) with a reported volume change ($\Delta V/V_0$) of 13% [12, 102].

It should also be noted that, after Raman studies by Lin *et al.* and Greene *et al.*, the issue was raised, whether the NaCl phase is actually an approximately equal mixture of rocksalt and a simple hexagonal phase based on diffraction data anomalies at around 5 GPa or whether it transforms completely into this phase at 48 GPa. However, Raman studies of Arora *et al.* and ADX studies of Nelmes and McMahon show no such evidence [12].

At 30.5 GPa a very slow Cmc m -type distortion of the rocksalt structure is described by McMahon and Nelmes with the final transition at about 48 GPa [179]. The lattice parameters for ZnSe-III at 60 GPa are $a = 4.728 \text{ \AA}$, $b = 4.800 \text{ \AA}$, $c = 4.703 \text{ \AA}$, $y(\text{Zn}) = 0.704$ and $y(\text{Se}) = 0.196$. Nelmes and McMahon also report a very weak further distortion somewhere above 48 GPa.

Furthermore, a potentially stable but fourfold coordinated cinnabar phase is suggested by a theoretical pseudopotential study of Côté *et al.* in a region of 10.2-13.4 GPa [180], which however is close to the resolution of the calculations. It is also supported by a theoretical investigation of Qteish and Muñoz [181] and experimental findings of Pellicer-Porres *et al.* [182]. The latter, however, observe the cinnabar phase in a region of 10.1-10.9 GPa only.

Theoretical reports have furthermore suggested the SC16 structure as an intermediate phase between the zinc blende and the rocksalt modification [139, 181, 183]. Later, the results for both structural parameter data as well as transition pressures of the different zinc selenide phases are summarized in tables 6.1, 6.4 and 6.5 (see chapters 6.2.1 and 6.3.1). For comparison the above discussed theoretical and experimental reference data is listed in those tables as well.

6.1.2 Cadmium selenide

Like cadmium sulfide, cadmium selenide at room conditions exists in a stable wurtzite as well as a metastable zinc blende structure. The lattice parameters are $a = 4.300 \text{ \AA}$ and $c = 7.010 \text{ \AA}$ and $a = 6.052 \text{ \AA}$, respectively [12]. The naturally occurring mineral of cadmium selenide is known as cadmoselite, which is a black to pale grey opaque yet very rare crystal.

The wurtzite form of CdSe was first reported to transform at 2.7 GPa (optical study) [140], which later turned out to be a nonmetallic (site-ordered) rocksalt structure [184, 185] with a lattice constant of $a = 5.08 \text{ \AA}$ at 10 GPa and an indirect band gap of 0.65 eV at 3 GPa ([120, 186]). The transition is indicated by a drastic decrease in electrical resistivity [187] as well as a volume change ($\Delta V/V_0$) of 16.4 % [143].

Not many high pressure studies of CdSe are available, but a pseudopotential calculation [188] predicts a transition into a cesium chloride structure at about 94 GPa. However, a transition into an intermediate phase between NaCl and CsCl is possible and later studies suggest the cinnabar as well as the Cmcn structure. A transition from rocksalt to Cmcn was predicted by first-principles calculations at 29 GPa [180] and subsequently confirmed by ADX studies of Nelmes and McMahon ($p_t = 27.0 \text{ GPa}$). The refined (site-ordered) structure at 34.4 GPa has the following lattice parameters: $a = 5.200 \text{ \AA}$, $b = 5.222 \text{ \AA}$, $c = 5.159 \text{ \AA}$, $y(\text{Cd}) = 0.703$ and $y(\text{Se}) = 0.214$ [12].

They further observed a possible transition into a distorted Cmcn structure at approximately 36 GPa, which seems to be stable up to the highest pressure

measured (85 GPa), but the structure could not be resolved.

In chapters 6.2.2 and 6.3.2 the structural parameters and transition pressures obtained in this study for the cadmium selenide phases will be discussed. The according tables 6.2, 6.6 and 6.7 can also be used as a summary for the parameters determined in the previously discussed theoretical and experimental reference data.

6.1.3 Mercury selenide

Under ambient conditions mercury selenide adopts a semimetallic zinc blende structure [189], which is naturally found as a dull grey (to reddish brown or black) mineral called tiemannite in hydrothermal veins in association with other selenides and calcite. It has a lattice constant of $a = 6.084$ Å. This is signalling a change in the structural behaviour of the mercury chalcogenide to favouring less complicated lattices.

However, a (site-ordered) cinnabar structure is still existent in HgSe, where Bridgeman first observed a transition at a rather low pressure of 0.74 GPa [169]. The transition goes along with a strong increase in resistivity, indicating the changeover into a semiconducting behaviour with a gap of 0.5-0.9 eV [189–192], and a volume change ($\Delta V/V_0$) of 9.0 % [193]. In the course of their ADX studies Nelmes and McMahon report the lattice parameters to be $a = 4.120$ Å, $c = 9.560$ Å, $u(\text{Hg}) = 0.662$ and $v(\text{Se}) = 0.550$ at 4.0 GPa [194]. Therefore, the coordination is 2+2+2 with 3 pairs of unlike neighbours, at which the bond distances are 2.541, 2.891 and 3.240 Å, respectively. Hence, the cinnabar structure in HgSe differs significantly from the one obtained in HgO and HgS.

In addition, McMahon *et al.* discovered another transition of the zinc blende HgSe phase, which they identified as a (site-ordered) orthorhombic distortion of zinc blende with the space group C222₁. It appears due to pressure increase during a very slow ZB to cinnabar transition, is stable in only a small pressure range (2.1-2.25 GPa) and therefore labelled as a 'hidden' intermediate phase between zinc blende and cinnabar [195]. The following lattice parameters were determined at 2.25 GPa: $a = 5.992$ Å, $b = 5.879$ Å, $c = 6.045$ Å, $x(\text{Hg}) = 0.302$ and $y(\text{Se}) = 0.207$.

Upon further increase of pressure the cinnabar form was found to adopt a (site-ordered) rocksalt structure at 15.5 GPa with $a = 5.360$ Å at 21 GPa [191, 192, 196]. The volume change is 0.2 % at 15.7 GPa [12].

Possibly a further high temperature phase exists in a pressure regime of 15-

17 GPa, which is however unidentified [191, 192].

At 28 GPa another phase (HgSe-IV) was observed [196]. After a discussion of possible structures (including orthorhombic, body-centred (β -tin) or hexagonal), it has been characterized as (site-ordered) orthorhombic Cmc m by ADX studies, at which the lattice parameters and atomic positions are $a = 5.153$ Å, $b = 5.559$ Å, $c = 4.972$ Å, $y(\text{Hg}) = 0.644$ and $y(\text{Se}) = 0.141$ at 35.6 GPa [194]. The transition is accompanied by a 0.9 % volume change.

No further transition has been found up to 50 GPa. The different phases of mercury sulfide calculated within the scope of this thesis including structural parameters and the transition pressures are summarized in chapters 6.2.3 and 6.3.3. In those chapters tables 6.3, 6.8 and 6.9 will also list the according data of previous work as introduced above.

6.2 Equilibrium structures

6.2.1 Zinc selenide

The energy-volume relationships of the various ZnSe modifications are displayed in the upper panel of fig. 6.1. They clearly show that zinc blende is the preferred structure under normal conditions with a cohesive energy of 5.310 eV/pair. However, the wurtzite modification is separated in energy by only 9 meV/pair, which fits nicely with an ab-initio LAPW calculation by Yeh *et al.*, who noted a difference of 5.3m eV/atom [158]. The properties derived for the equilibrium phases of ZnSe are summarized in table 6.1.

Using the Murnaghan EOS a lattice constant of 5.734 Å is derived, which is overall in good agreement with other theoretical work and overestimates the experimental value (5.668 Å) by only 1 %. Good comparability is also given for the bulk modulus, where a value of $B_0 = 57.3$ GPa is obtained (see table 6.1). For the pressure derivative the calculated value of $B' = 4.7$ lies within the relatively wide range of experimental and theoretical results.

For the metastable wurtzite modification lattice constants of $a = 4.049$ Å and $c = 6.646$ Å are calculated, which means that the ground-state volume of $V_0 = 47.20$ Å³/pair barely differs from the one obtained for ZB-ZnSe (47.13 Å³/pair). Those values are in excellent agreement with both experimental and other computational work. However, the bulk modulus $B_0 = 57.1$ GPa and its pressure derivative $B' = 4.6$ for unknown reasons deviate rather strongly from the ex-

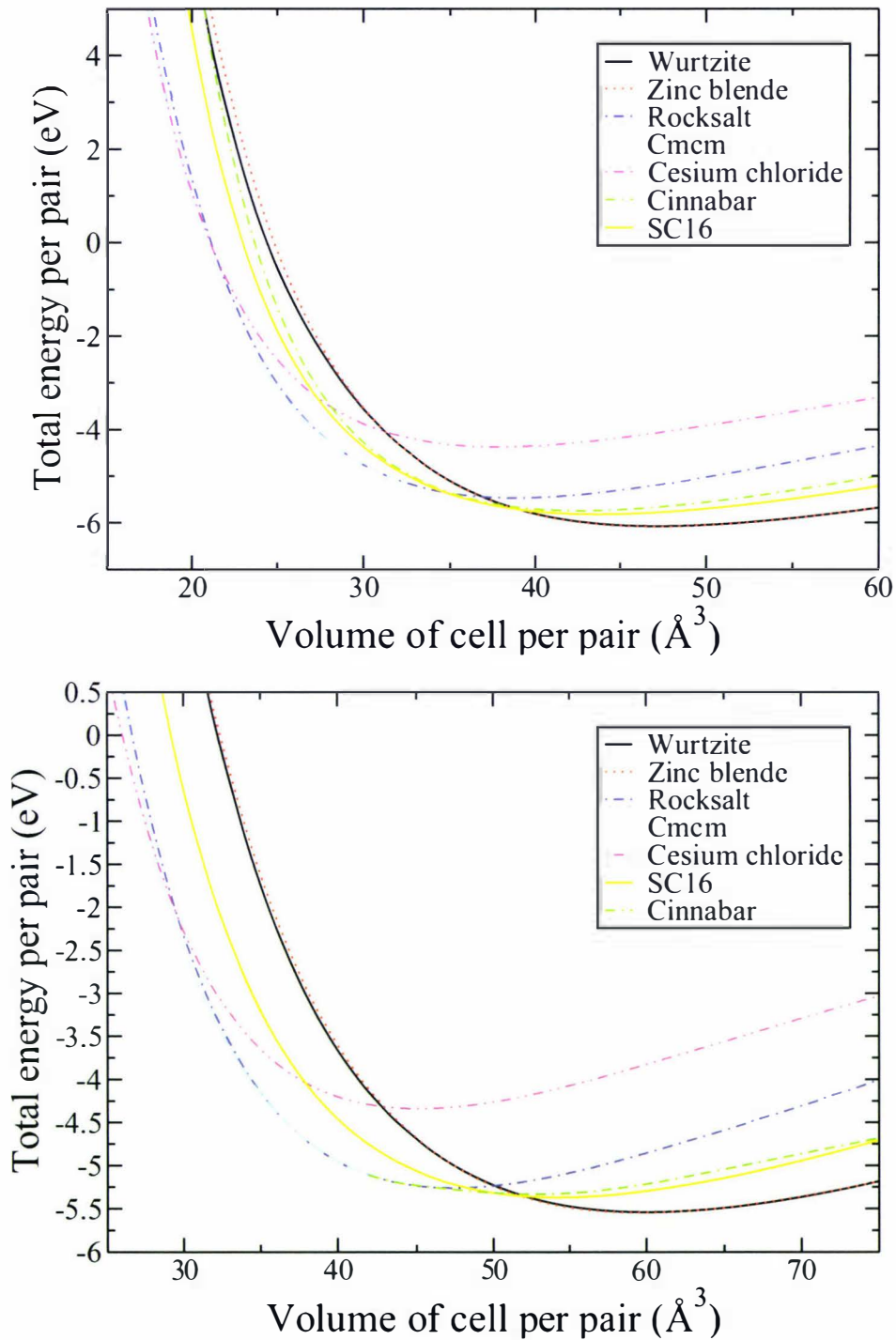


Figure 6.1: The total energy versus volume per cation-anion pair for different crystal structures of ZnSe (upper panel) and CdSe (lower panel).

Property	This work	Other theoretical	Experiments
<i>Zinc blende</i>			
a	5.734	5.606 ^a , 5.669 ^b , 5.820 ^c	5.668 ^d , 5.667 ^{e,f}
V_0	47.13	44.05 ^a , 45.55 ^b , 49.28 ^c	45.52 ^d , 45.504 ^g
B_0	57.3	70.5 ^a , 63.07 ^b , 52.92 ^c	64.7 ^e , 69.3 ^f , 58 ^h
B'	4.7	3.9 ^b , 4.05 ^g , 4.88 ⁱ	4.77 ^e , 5.5 ^h
E_{coh}	5.310	4.574 ^j , 5.20 ^k	4.38 ^d , 5.16 ^k
p_t to RS	13.76	11 ^a , 15-21 ^c , 12.6 ^l	12 ^m , 10-16.5 ⁿ
p_t to C2	13.96	10.2 ^a , 13.1 ^l	
p_t to SC16	12.50	13 ^b , 9.2 ^l , 8.7 ^o	
<i>Wurtzite</i>			
a	4.049	3.974 ^p	4.003 ⁿ
c	6.646	6.506 ^p	6.540 ⁿ
c/a	1.641	1.637 ^p	1.634 ⁿ
u	0.3743	0.375 ^p	
V_0	47.20	44.49 ^p	45.38 ⁿ
B_0	57.1		80 ⁿ
B'	4.6		3.7 ⁿ
E_{coh}	5.301		
p_t to ZB	2.25		
p_t to RS	12.94	4.4 ^g	13.0 ^g
p_t to C2	12.51		

^aPW-PP LDA from ref. [180]; ^bPW-PP GGA from ref. [183]; ^cFP-LAPW and NAO+GC from ref. [197]; ^dfrom ref. [153]; ^efrom ref. [198]; ^ffrom ref. [88]; ^gfrom ref. [102]; ^hX-ray diffraction from ref. [182]; ⁱFP-APW+lo LDA from ref. [199]; ^jMD calculations from ref. [163]; ^ksemi-empirical TB calculations from ref. [157] and refs. therein; ^lPP Kohn-Sham LDA from ref. [181]; ^m from ref. [200]; ⁿfrom ref. [120]; ^oTB-LMTO from ref. [139]; ^pLAPW-LDA from ref. [158].

Table 6.1: Ground-state properties of the equilibrium phases of ZnSe. Presented are the lattice constants a and c (Å), internal parameter u , axial ratio c/a , ground-state volume V_0 (Å³/pair), bulk modulus B_0 (GPa) and its pressure derivative B' as well as the cohesive energy E_{coh} (eV/pair) and the transition pressure p_t (GPa) where applicable.

perimental values (see table 6.1), but only one study is available to compare with.

6.2.2 Cadmium selenide

The equilibrium phases of CdSe are known to be the zinc blende and wurtzite structures as well. This again is confirmed by the calculations presented here, as can be seen in the lower panel of fig. 6.1. The energy difference of 4 meV/pair

Property	This work	Other theoretical	Experiments
<i>Zinc blende</i>			
a	6.202	6.050 ^a , 6.055 ^b , 6.035 ^c	6.052 ^d , 6.077 ^e
V_0	59.64	55.36 ^a , 55.50 ^b , 54.95 ^c	55.36 ^d , 56.11 ^e
B_0	45.0	57.2 ^a , 54.6 ^b , 66.5 ^c	55.0 ^f
B'	4.5	5.57 ^b	
E_{coh}	4.778	4.448 ^b , 4.78 ^f	3.334 ^e (E_{sub})
p_t to RS	4.01	2.5 ^a , 2.33 ^e , 2.62 ^g	2.8 ^h
p_t to C2	5.70		
p_t to SC16	5.53		
<i>Wurtzite</i>			
a	4.386	4.293 ⁱ , 4.272 ^j	4.291-4.309 ^e
c	7.168	7.038 ⁱ , 6.979 ^j	7.007-7.03 ^e
c/a	1.634	1.639 ⁱ , 1.634 ^j	1.630-1.638 ^e
u	0.3753	0.374 ⁱ , 0.3756 ^j	0.3760 ^e
V_0	59.70	56.17 ⁱ , 55.15 ^j	56.05-56.47 ^e
B_0	45.0	53.6 ⁱ , 57.9 ^j	53.4 ^e
B'	4.8	4.6 ⁱ	3.17 ^e
E_{coh}	4.774		
p_t to RS	4.03	2.0 ^g	2.7 ^k
p_t to C2	5.68		
p_t to SC16	5.51		

^aPW-PP LDA from ref. [180]; ^bMD from ref. [163]; ^c*ab-initio* GDSP/DFT from ref. [162]; ^dfrom ref. [12]; ^efrom ref. [120]; ^fsemi-empirical TB calc. from ref. [157] and refs. therein; ^gFP-LMTO from ref. [146]; ^h from ref. [193]; ⁱFP-LMTO DFT-LDA from ref. [201]; ^jLAPW-LDA from ref. [161]; ^kfrom ref. [140].

Table 6.2: Ground-state properties of the equilibrium phases of CdSe. Presented are the lattice constants a and c (Å), internal parameter u , axial ratio c/a , ground-state volume V_0 (Å³/pair), bulk modulus B_0 (GPa) and its pressure derivative B' as well as the cohesive energy E_{coh} (eV/pair) and the transition pressure p_t (GPa) where applicable.

between the two phases is very small, but according to the results presented here the zinc blende structure seems to be slightly favoured ($E_{coh}^{ZB} = 4.778$ eV/pair versus $E_{coh}^W = 4.774$ eV/pair). A LAPW-LDA study by Yeh *et al.* also finds the zinc blende structure to be lower in energy by 1.4 meV/atom [158], whereas ref. [161] gives $\Delta E^{W-ZB} = 2$ meV/pair. Yet, this prediction is in contrast to experiments, where the zinc blende phase is only metastable. It can most likely be blamed on temperature effects and it should also be noted that the calculated energy difference between the two phases is definitely smaller than for ZnSe and HgSe, where zinc blende is the stable form.

The determined lattice constant of 6.202 Å for the zinc blende polymorph com-

pares well to other theoretical and experimental ($a = 6.052 \text{ \AA}$) results, yet again is by a few percent too large. This is a consequence of the method used. Values of 45.0 GPa and 4.5 for the bulk modulus and its pressure derivative, respectively, are in reasonable agreement with other work (see table 6.2 for details).

For the wurtzite modification the lattice parameters are $a = 4.386 \text{ \AA}$, $c = 7.168 \text{ \AA}$ and $u = 0.3753$, whereas the bulk modulus and its pressure derivative are calculated to be 45.0 GPa and 4.8. Within the limits of the method employed, those values compare well to experimental as well as other theoretical results (see again table 6.2) despite the overestimation of the lattice constants.

Note that wurtzite is the high temperature phase of CdSe with the transition occurring at 95 °C [120]. Table 6.2 summarizes the results.

6.2.3 Mercury selenide

The upper panel of fig. 6.6 shows the energy-volume dependencies for HgSe within the scalar-relativistic treatment. The zinc blende structure yields the lowest total energy and with a cohesive energy of 3.373 eV/pair is proven to be the preferred polymorph under normal conditions.

The lattice constant of 6.272 Å ($V_0 = 61.68 \text{ \AA}^3/\text{pair}$) is in excellent concordance with other DFT calculations, but shows the typical overestimation in comparison with experimental data ($a = 6.085 \text{ \AA}$ [120]). The opposite effect is achieved for the bulk modulus, where a value of 43.0 GPa is determined compared to 57.6 GPa found in ultrasound velocity experiments [120]. Bigger discrepancies are noted for the pressure derivative of the bulk modulus, where a value of 4.8 is obtained ($B' = 2.6$ by ultrasound measurements). However, agreement with other theoretical work is good.

Looking at the wurtzite structure with $E_{coh} = 3.359 \text{ eV/pair}$, it is energetically close. This means an energy difference of 14 meV/pair, which fits nicely with the results of Yeh *et al.*, who obtained a difference of 6.9 meV/atom [158]. The bulk properties are $a = 4.433 \text{ \AA}$, $c = 7.263 \text{ \AA}$, $V_0 = 61.81 \text{ \AA}^3/\text{pair}$, $B_0 = 42.3 \text{ GPa}$ and $B' = 5.0$. Similar values for the ground-state volume and the bulk modulus as well as its pressure derivative indicate the structural similarity to the zinc blende form. However, very few data are available to compare with (see table 6.3), and even though it is occasionally claimed in literature that HgSe crystallizes in both the zinc blende and the wurtzite form, no experimental structural parameters could be found.

The results are concluded along with some previous work in table 6.3.

Property	This work	Other theoretical	Experiments
<i>Zinc blende</i>			
a	6.272	6.077-6.303 ^a , 6.194 ^b , 6.255 ^c	6.085 ^d , 6.084 ^e
V_0	61.68	56.1-62.6 ^a , 59.41 ^b , 61.18 ^c	56.33 ^d , 56.30 ^e
B_0	43.0	58.1-59.2 ^a , 41.8 ^b	51.66 ^d
B'	4.8		2.6 ^d
E_{coh}	3.373		3.856 ^d (E_{sub})
p_t to C2	1.96		0.74-1.5 ^e , 1.15-2.20 ^f
p_t to C222 ₁	1.35-3.06		2.1 ^e
<i>Wurtzite</i>			
a	4.433	4.310 ^g	
c	7.263	7.064 ^g	
c/a	1.638	1.639 ^g	
u	0.3747	0.375 ^g	
V_0	61.81	56.82 ^g	
B_0	42.3		
B'	5.0		
E_{coh}	3.359		

^aFP-LMTO LDA and GGA from ref. [168]; ^b*ab-initio* GDSP/DFT from ref. [162];
^cPW-PP GGA from ref. [174]; ^dfrom ref. [120]; ^efrom ref. [12]; ^ffrom ref. [200]
(C222₁ mixed with ZB between 2.1 and 2.25 GPa); ^gLAPW-LDA from ref. [158].

Table 6.3: Ground-state properties of the equilibrium phases of HgSe. Presented are the lattice constants a and c (Å), internal parameter u , axial ratio c/a , ground-state volume V_0 (Å³/pair), bulk modulus B_0 (GPa) and its pressure derivative B' as well as the cohesive energy E_{coh} (eV/pair) and the transition pressure p_t (GPa) where applicable.

6.3 High-pressure phases

6.3.1 Zinc selenide

The high-pressure transition of ZnSe in its zinc blende form was investigated and a change into the rocksalt structure is predicted to happen at 13.76 GPa. This is in excellent agreement with both experimental and theoretical investigations (see table 6.1).

The ground-state lattice constant obtained for this new phase is 5.372 Å, which compares rather well to the literature values (e.g. $a^{exp} = 5.292$ Å at 0 GPa [102]). This is true for the bulk modulus $B_0 = 71.7$ GPa and $B' = 4.7$, too, if compared to other theoretical results. Comparison with experimental values is difficult, since the bulk moduli were fitted with a fixed B' . However, the bulk modulus

Property	This work	Other theoretical	Experiments
<i>SC16</i>			
a	7.041	6.903 ^a , 6.881 ^b , 6.987 ^c	
u	0.1568	0.1563 ^b , 0.1453 ^c	
v	0.6432	0.6421 ^b , 0.6473 ^c	
V_0	43.64	41.12 ^a , 40.73 ^b , 42.64 ^c	
B_0	54.27	63.55 ^a , 63.9 ^b , 53.78 ^c	
B'	4.6	5.5 ^b , 4.1 ^c	
E_{coh}	5.049		
p_t to RS	15.16	16.4 ^b , 17 ^c	
<i>Rocksalt</i>			
a	5.372	5.304 ^a , 5.319 ^c	5.08 ^d , 5.292 ^e
V_0	38.76	37.30 ^a , 37.62 ^c	32.77 ^d , 37.01 ^e
B_0	71.7	77.84 ^c , 74-91 ^f	104 ^e , 54 ^g
B'	4.7	3.75 ^c , 3.5-4.9 ^f	4.0 ^e , 5.5 ^g
E_{coh}	4.697		
p_t to Cmc m	29.602	29.8 ^c , 36.5 ^h	30 ⁱ
<i>Cmcm</i>			
a	(4.735)	5.276 ^c	4.728 ⁱ
b	(4.965)		4.800 ⁱ
c	(4.533)		4.703 ⁱ
b/a	(1.049)		1.015 ⁱ
c/a	(0.957)		0.995 ⁱ
$y(\text{Zn})$	(0.6607)		0.704 ⁱ
$y(\text{Se})$	(0.1850)		0.196 ⁱ
V	(26.64)		26.68 ⁱ
B_0	79.56	70.0 ^c	
B'	3.4	4.32 ^c	
E_{coh}	4.709		
p_t to CC	234.96		

^aTB-LMTO from ref. [139]; ^bPP Kohn-Sham LDA from ref. [181] at 0 GPa; ^cPW-PP GGA from ref. [183]; ^dfrom ref. [120] at 10 GPa; ^efrom ref. [102] (B' fixed); ^fFLAPW from ref. [197]; ^gX-ray diffraction from ref. [182] (B' fixed); ^hPW-PP LDA from ref. [180]; ⁱADX from ref. [179] at 60 GPa.

Table 6.4: Ground-state properties of the high-pressure phases of ZnSe. Presented are the lattice constants a , b and c (Å), respective internal parameters, ground-state volume V_0 (Å³/pair), bulk modulus B_0 (GPa) and its pressure derivative B' as well as the cohesive energy E_{coh} (eV/pair) and the transition pressure p_t (GPa) where applicable. Values in brackets indicate higher pressure.

is within the experimental range of 54-104 GPa. Looking at the bulk properties at a post-transition pressure of 10.4 GPa results in the following parameters: $a = 5.175$ Å and $B_0 = 120.24$ GPa, meaning agreement with experiments is

Property	This work	Other theoretical	Experiments
<i>Cesium chloride</i>			
a	3.356		
V_0	37.81		
B_0	64.1		
B'	4.8		
E_{coh}	3.604		
<i>Cinnabar</i>			
a	3.808	3.987 ^a , 3.932 ^b , 3.971 ^c	3.789 ^a , 3.785 ^d
c	8.819	8.992 ^b	8.844 ^d
c/a	2.316	3.287 ^b , 2.26 ^e	2.34 ^d
$u(\text{Zn})$	0.4966	0.5 ^e	0.63 (0.5) ^d
$v(\text{Se})$	0.4979	0.5 ^e	0.55 (0.5) ^d
V_0	36.91	40.13 ^b	36.58 ^d
B_0	62.4	69.03 ^a , 72.6 ^b , 68.33 ^c	65.7 ^a
B'	3.4	5.5 ^b , 3.71 ^c	
E_{coh}	4.777		
p_t to RS	13.50	13.4 ^e	

^aTB-LMTO from ref. [139]; ^bPP Kohn-Sham LDA from ref. [181]; ^cPW-PP GGA from ref. [183]; ^dX-ray diffraction from ref. [182]; ^ePW-PP LDA from ref. [180].

Table 6.5: Ground-state properties of the high-pressure phases of ZnSe. Presented are the lattice constants a , b and c (Å), respective internal parameters, ground-state volume V_0 (Å³/pair), bulk modulus B_0 (GPa) and its pressure derivative B' as well as the cohesive energy E_{coh} (eV/pair) and the transition pressure p_t (GPa) where applicable. Values in brackets indicate higher pressure.

good for higher pressures as well (see table 6.4). Yet, the calculated lattice constant is somewhat overestimated.

For the wurtzite to rocksalt transition the pressure estimated is 12.94 GPa which compares well to the experimental result ($p_t = 13.0$ GPa [102]). However, this transition is not well investigated since wurtzite is known to transform into the zinc blende structure at 3 GPa. The transition pressure is determined to be 2.25 GPa matching other theoretical results.

However, in addition, the simple cubic SC16 structure introduced as a possible high-pressure phase by theoretical means [181] has been taken into consideration as well and indeed is found to be an intermediate structure between the transition from zinc blende to rocksalt. The ZB→SC16 transition occurs at 12.50 GPa, which is in excellent agreement with other theoretical work, where the transition pressure ranges from 8.7-13 GPa [139, 181, 183].

The bulk properties found are $a = 7.041$ Å, $V_0 = 43.64$ Å³/pair, $u = 0.1568$,

$v = 0.6432$, $B_0 = 54.27$ GPa and $B' = 4.6$ at ambient conditions along with a cohesive energy of 5.049 eV/pair. Looking at the data obtained by Cui *et al.* agreement is extremely good, but unfortunately this ZnSe modification will still have to be discovered experimentally. Yet, the possibility of energy barriers hindering the transition needs to be considered. The lattice parameters at the transition pressure are given as well: $a = 6.675$ Å, $V_0 = 37.18$ Å³/pair, $u = 0.1486$, $v = 0.6437$.

Eventually, SC16-ZnSe changes over into the rocksalt structure at 15.16 GPa, again in concordance with other theoretical work. Hence, the range of stability (2.66 GPa) is on the lower end of the scale of previous predictions (4-7.2 GPa) (see table 6.4) but close to the range found for SC16-ZnS (3.4 GPa) [138].

Looking at even higher pressures, a rocksalt to Cmcm transition is observed at 29.60 GPa. Since this is a second order transition the structure slowly relaxes towards the rocksalt parameters for lower pressure, meaning that no ground-state properties can be obtained. Instead, the bulk properties are determined at 59.90 GPa, where lattice constants of $a = 4.735$, $b = 4.965$ and $c = 4.533$ Å are determined along with $y(\text{Zn}) = 0.6607$ and $y(\text{Se}) = 0.1850$. In particular the lattice constants agree very well with an experiment ($a = 4.728$, $b = 4.800$ and $c = 4.703$ Å at 60 GPa) as do derived properties such as the c/a - and b/a -ratios as well as the unit-cell volume [179]. The bulk modulus and its pressure derivative are 79.56 GPa and 3.4 in accordance with theoretical investigations (for details refer to table 6.4).

At an extremely high pressure of 235 GPa a transition into the cesium chloride structure would be possible according to the calculations discussed here with the ground-state properties listed in table 6.5. At 235 GPa the following values would be observed: $V = 18.61$ Å³/pair and $a = 2.650$ Å. The ground-state bulk modulus and B' are 64.1 GPa and 4.8. However, whether this transition is genuine should be subject to further investigations to make sure no intermediate structure change occurs between the Cmcm and cesium chloride phase.

In addition, the cinnabar phase was investigated, which was claimed by Côté *et al.* to be stable between 10.2 and 13.4 GPa. However, according to the calculations presented here, this is not the case. Over the whole volume range investigated the SC16 structure is lower in enthalpy, making it the preferred structure. But even in the absence of the SC16 phase, the transition from zinc blende to cinnabar would happen at 13.96 GPa, at which pressure transition from zinc blende to rocksalt would have already occurred ($p_t = 13.76$ GPa).

Also, the transition from cinnabar to rocksalt is predicted to start at 13.5 GPa already. For this possible cinnabar modification properties of $a = 3.808 \text{ \AA}$ and $c = 8.819 \text{ \AA}$ along with the Wyckoff parameters $u \approx 0.5 \approx v$ are derived at 12.3 GPa. The properties at zero pressure can be viewed in table 6.5. They are very consistent with the pseudopotential study of Côté *et al.* [180] as well as the X-ray diffraction data of Pellicer-Porres *et al.*, for whom the cinnabar phase is only accessible in downstroke experiments [182]. Their experimental data lead to better results using the Wyckoff parameters derived by Côté *et al.* However, it is mentioned that at 14.7 GPa the calculations presented here result in values of $u = 0.5616$ and $v = 0.5386$, similar to the ones measured by ref. [182] and deviating from 0.5 at an increased c/a ratio of 2.337. The ground-state bulk modulus and its pressure derivative are $B_0 = 62.4 \text{ GPa}$ and $B' = 3.4$. Another study shows calculations of the ground-state properties as well, but find the cinnabar phase not to be stable [183] (see also table 6.5).

The fact that the cinnabar phase is experimentally only observed in downstroke measurements, reinforces the possibility of the structure being in fact a metastable phase [180]. This might be an explanation that despite experimental observation, the cinnabar modification is not stable in ZnSe according to the results presented here.

6.3.2 Cadmium selenide

CdSe is very similar to ZnSe in its high-pressure behaviour. Again first of all, both the zinc blende and the wurtzite phase become unstable towards the rocksalt structure at 4.01 GPa and 4.03 GPa in reasonable accordance with previous work (see table 6.2). The cohesive energy at ambient conditions is 4.493 eV/pair.

For this modification a lattice constant of 5.743 Å at 0 GPa and 5.625 Å at 4.33 GPa along with a ground-state volume of 47.35 Å³/pair at 0 GPa and 44.49 Å³/pair at 4.33 GPa is determined. The ground-state bulk modulus and the pressure derivative are 60.9 GPa and 4.9 respectively. This matches experimental and theoretical values where available as listed in detail in table 6.6.

With increasing pressure a transition into the Cmc₂m structure is predicted at 26.17 GPa according to the calculations presented here. This pressure is in good agreement with experimental as well as theoretical results. This also holds for the lattice properties, where values of $a = 5.250 \text{ \AA}$, $b = 5.317 \text{ \AA}$, $c = 5.178 \text{ \AA}$ with $y(\text{Cd}) = 0.6999$ and $y(\text{Se}) = 0.2064$ are determined at a pressure of 30.5 GPa.

Property	This work	Other theoretical	Experiments
<i>Rocksalt</i>			
a	5.743 (5.625)	5.576 ^a , 5.72 ^b	(5.49) ^c , (5.5) ^d , 5.71 ^b
V	47.35 (44.49)	43.34 ^a , 46.79 ^b	(41.4) ^c , (41.59) ^d , 46.54 ^b
B_0	60.9	85.0 ^a , 57.7 ^b	
B'	4.9	4.0 ^a	
E_{coh}	4.493		
p_t to Cmcn	26.17	29.0 ^e	27.0 ^f
<i>Cmcm</i>			
a	(5.250)	5.195 ^a	(5.200) ^f
b	(5.317)	5.916 ^a	(5.222) ^f
c	(5.178)	5.545 ^a	(5.159) ^f
c/a	(0.986)	0.707 ^a	(0.992) ^f
b/a	(1.013)	0.211 ^a	(1.004) ^f
$y(\text{Cd})$	(0.6999)		(0.703) ^f
$y(\text{Se})$	(0.2064)		(0.214) ^f
V	(36.14)	42.60 ^a	(35.02) ^f
B_0	54.1	80.6 ^a	
B'	3.7	4.6 ^a	
E_{coh}	4.576		
p_t to ?			37 ^g
p_t to CC	108.22		
<i>Cesium chloride</i>			
a	3.562 (2.975)	3.443 ^a	
V_0	45.19 (26.33)	40.82 ^a	
B_0	58.6	81.6 ^a	
B'	4.8	4.6 ^a	
E_{coh}	3.571		

^aFP-LMTO from ref. [146]; ^bfrom ref. [202]; ^cX-ray at 3.2 GPa from ref. [185];
^dX-ray at 2 GPa from ref. [184]; ^ePW-PP LDA from ref. [180]; ^ffrom ref. [12]
at 34.4 GPa; ^gX-ray scattering from ref. [179].

Table 6.6: Ground-state properties of the high-pressure phases of CdSe. Presented are the lattice constants a , b and c (Å), respective internal parameters, ground-state volume V_0 (Å³/pair), bulk modulus B_0 (GPa) and its pressure derivative B' as well as the cohesive energy E_{coh} (eV/pair) and the transition pressure p_t (GPa) where applicable. Values in brackets indicate higher pressure.

However, the ground-state volume could not be obtained, since for lower pressure in general a relaxation into the rocksalt form is experienced. The parameters are evaluated at a slightly lower value than in the experiment, but comparability with experimental as well as theoretical data is very good. The bulk modulus $B_0 = 54.1$ GPa and its pressure derivative $B' = 3.7$ are estimated from the

Property	This work	Other theoretical
<i>Cinnabar</i>		
a	4.281/4.282	
c	9.9307/9.927	
c/a	2.319/2.318	2.29 ^a
u	0.4983/0.5501	0.57 ^a
v	0.4993/0.5229	0.54 ^a
V_0	53.00/52.74	
B_0	50.4/35.96	
B'	4.3/-4.7	
E_{coh}	4.565/4.564	
<i>SC16</i>		
a	7.569	
u	0.1561	
v	0.6411	
V_0	54.21	
B_0	42.9	
B'	5.8	
E_{coh}	4.601	
^a PW-PP LDA from ref. [180] (estimated from graph).		

Table 6.7: Ground-state properties of the high-pressure phases of CdSe. Presented are the lattice constants a , b and c (Å), respective internal parameters, ground-state volume V_0 (Å³/pair), bulk modulus B_0 (GPa) and its pressure derivative B' as well as the cohesive energy E_{coh} (eV/pair) and the transition pressure p_t (GPa) where applicable. Values in brackets indicate higher pressure. No experimental data are available.

Murnaghan fit only over the volume range accessible for the calculations carried out. They therefore deviate from the values derived by Benkhetton *et al.*

The cesium chloride structure was also included in our calculations being a promising candidate for a high-pressure phase of II-VI semiconductors. The transition from Cmc \bar{m} -CdSe is calculated at 108.2 GPa and the ground-state properties are given in table 6.6. A previous calculation was done by Benkhetton *et al.*, but the authors do not give a pressure for which the results are obtained. However, the lattice parameters are not in agreement especially if compared to values calculated at a post-transition pressure of 117 GPa, where according to the results presented here, the following parameters are valid: $a = 2.975$ Å and $V_0 = 26.33$ Å³/pair. If one uses the values obtained off the graph in ref. [146] it becomes obvious, that a factor of two is missing in the ground-state volume determined by the authors. Using the corrected values, agreement is good (see table 6.6).

Since the cinnabar phase and SC16 structure have been discussed for the zinc and cadmium selenides before, they have been included in the calculation presented here. Both phases are found to be very close lying in enthalpy at the transition pressure from ZB to NaCl, which is in excellent agreement with the findings of Côté *et al.* [180].

However, the pressures for the ZB→C2, W→C2, ZB→SC16 and W→SC16 transitions are calculated to be 4.19, 4.21, 5.53 and 5.51 GPa and therefore slightly above the respective pressure for the transition from zinc blende and wurtzite to rocksalt. Therefore, and since no experimental observations are recorded, these calculations suggest that neither cinnabar nor SC16 are stable phases for CdSe. Yet, it should be kept in mind that the energy differences are small and similar to ZnSe. Thus, the possibility of a metastable phase (i.e. only accessible in downstroke experiments) should be admitted for.

The ground-state properties for both structures are listed in table 6.7. As pointed out by Côté *et al.* generally for the cinnabar structure, there is always a minimum if $u = 0.5 = v$ [180]. This is for instance the only minimum that can be found in ZnSe. In addition to that, in some cases a second energetic minimum is found for $u \neq v \neq 0.5$, like in HgSe (see next chapter). Interestingly enough for CdSe, both minima are very close, so that for higher volumes, the internal parameters slowly converge towards a value of 0.5. This induces a negative value for B' , most likely due to a change in structure (and coordination) between the two minimum structures. Hence, two different sets of values are given in table 6.7.

A comprehensive study of supposed other crystal structures would be desirable to rule out or confirm possible intermediate phases between the Cmc₂m and the cesium chloride structure, especially since Nelmes and McMahon observed a structure change around 37 GPa. This however goes beyond the scope of this thesis, where mainly the relativistic influence is discussed with the focus on the cinnabar and montroydite structure.

6.3.3 Mercury selenide

Unfortunately, HgSe seems to have been studied theoretically mainly in its zinc blende form. Hence, the comparison of the results obtained for the behaviour at higher pressure will be limited to experimental data.

The calculations presented here predict that the equilibrium zinc blende structure of HgSe undergoes a transition into the cinnabar form at about 1.96 GPa. The

Property	This work	Experiments
<i>Cinnabar</i>		
a	4.481 (4.179)	4.120 ^a , 4.32 ^b , 4.174 ^c
c	9.949 (9.708)	9.560 ^a , 9.68 ^b , 9.626 ^c
c/a	2.220 (2.323)	2.320 ^a , 2.24 ^b , 2.306 ^c
u	0.7118 (0.6624)	0.662 ^a , 0.666 ^c
v	0.4966 (0.5491)	0.550 ^a , 0.540 ^c
V	57.69 (48.95)	46.845 ^a , 52.15 ^b , 48.41 ^c
B_0	10.1 (24.01)	
B'	12.1 (4.4)	
E_{coh}	3.300	
p_t to RS	13.56	14.6-15.5 ^a , 16 ^d
<i>C222₁</i>		
a	(6.149)	5.992 ^c
b	(5.980)	5.879 ^c
c	(6.185)	6.045 ^c
b/a	(0.973)	0.981 ^c
c/a	(1.006)	1.009 ^c
$x(\text{Hg})$	(0.3100)	0.302 ^c
$y(\text{Se})$	(0.2082)	0.207 ^c
V	(56.86)	53.24 ^c
B_0	6.9	
B'	4.7	
E_{coh}	(3.319)	
<i>Rocksalt</i>		
a	5.808 (5.275)	5.360 ^d
V	48.98 (36.70)	38.50 ^d
B_0	57.9	
B'	5.2	
E_{coh}	3.066	
p_t to Cmc ₂ m	35.70	28 ^e

^aADX at 4 GPa from ref. [12]; ^bfrom ref. [185] at 1.5 GPa; ^cX-ray diffraction from ref. [179, 195] at 2.25 GPa; ^dfrom ref. [203] at 21 GPa; ^efrom ref [196].

Table 6.8: Ground-state properties of the high-pressure phases of HgSe. Presented are the lattice constants a , b and c (Å), respective internal parameters, ground-state volume V_0 (Å³/pair), bulk modulus B_0 (GPa) and its pressure derivative B' as well as the cohesive energy E_{coh} (eV/pair) and the transition pressure p_t (GPa) where applicable. Values in brackets indicate higher pressure. No other theoretical data are available.

ground-state properties obtained and summarized in table 6.8 are in accordance with experimental data, but again show the for DFT typical overestimation of the lattice constants.

Property	This work	Experiments
<i>Cmcm</i>		
a	(5.215)	5.153 ^a
b	(5.680)	5.559 ^a
c	(4.801)	4.972 ^a
b/a	(1.089)	1.079 ^a
c/a	(0.921)	0.965 ^a
$y(\text{Hg})$	(0.6383)	0.644 ^a
$y(\text{Se})$	(0.1531)	0.141 ^a
V	(35.6)	35.601 ^a
B_0	76.6	
B'	3.8	
E_{coh}	2.842	
p_t to CC	107.67	
<i>Cesium chloride</i>		
a	3.609 (3.025)	
V_0	47.01 (27.68)	
B_0	53.2	
B'	5.7	
E_{coh}	2.263	

^aADX at 35.6 GPa from ref. [194].

Table 6.9: Ground-state properties of the high-pressure phases of HgSe. Presented are the lattice constants a , b and c (Å), respective internal parameters, ground-state volume V_0 (Å³/pair), bulk modulus B_0 (GPa) and its pressure derivative B' as well as the cohesive energy E_{coh} (eV/pair) and the transition pressure p_t (GPa) where applicable. Values in brackets indicate higher pressure. No other theoretical data are available.

At 4.7 GPa, a pressure close to the experimental reference data, lattice constants of $a = 4.179$ Å and $c = 9.708$ Å are determined along with $u = 0.6624$ and $v = 0.5491$ as the Wyckoff positions. This improves comparability with the experiment even more and yields excellent results for the c/a -ratio and unit-cell volume (see table 6.8).

Which also stands out, is the anomalously small bulk modulus of just 10.1 GPa in combination with an extremely high pressure derivative ($B' = 12.1$), which indicates that the bulk material rapidly stiffens with pressure. This is similar to the values obtained for HgO and HgS and is caused by the chain-like structure. However, if more data points are included a bulk modulus of 24.01 GPa with a pressure derivative of 4.4 is determined, meaning a physically more sensible value for B' . This might suggest that the Murnaghan fit is not suitable to describe cinnabar-HgSe. Unfortunately, no data could be found to compare with.

More recent reports however, describe the appearance of a 'hidden' intermediate phase of HgSe, which therefore was taken as encouragement to investigate the transition to this distorted zinc blende structure (C222₁) theoretically. This structure is found to be energetically very close in the transition range between zinc blende and cinnabar. However, using the Murnaghan fit in the first place to determine the enthalpy-pressure curve, it turns out to describe the energy-volume relationship for C222₁ rather poorly. Hence, the transition pressure obtained for the ZB → C222₁ structure change is calculated to be 3.06 GPa while the C222₁ → C2 transition is predicted to occur at 1.75 GPa. This leaves no stability window for the C222₁ phase. However, if a simple spline is used as a first estimate to describe the energy-volume curve the transition pressures change to 1.35 and 1.94 GPa. In that case, this phase would be accessible. Yet, it shows how delicate this system is and that by no means the accuracy of the used method is good enough to make an accurate prediction. It should also be noted that the transition from ZB to C222₁ in the experiments also occurs outside the actual stability range of ZB with respect to cinnabar, pointing out the special status this phase has as a hidden form. Other experimental groups even just measure a mixed state [200].

The bulk properties at 2.85 GPa are determined to be $a = 6.149$ Å, $b = 5.980$ Å, $c = 6.185$ Å, $x(\text{Hg}) = 0.3100$ and $x(\text{Se}) = 0.2082$, with further details listed in table 6.8. The values are in good agreement with experimental data [195], but no ground-state properties can be given since for lower pressures only the relaxation into the zinc blende structure can be observed. The bulk modulus is therefore evaluated using the few data points available. It is again very low. More theoretical work is necessary to solve this structure.

No matter how the structure change to the cinnabar phase is achieved, according to the calculations carried out in the course of this study there is no doubt that upon pressure increase a transition into the rocksalt structure happens at 13.56 GPa. This matches previous experimental work. In the ground state a lattice constant of 5.808 Å is obtained for this structure with a respective unit-cell volume of 48.98 Å³/pair and at 22.4 GPa values of $a = 5.400$ Å and $V = 39.37$ Å³/pair are determined. This is in good agreement with the experimental data available (e.g. $a = 5.360$ at 21 GPa [203]). The bulk modulus and its pressure derivative in the ground state have also been calculated and are $B_0 = 57.9$ GPa and 5.2, respectively.

At an even higher pressure a transition to the orthorhombic Cmcm structure is

predicted, which is found to be stable from 35.70 GPa onwards, in accordance with 28 GPa measured by Huang and Ruoff for the mistakenly denoted bct-phase.

Again no ground-state values can be given due to the tendency of the structure to directly relax into the rocksalt structure for lower pressure. However, at a pressure of 37.5 GPa, shortly after the transition, lattice parameters of $a = 5.215$ Å, $b = 5.680$ Å, $c = 4.801$ Å, $y(\text{Hg}) = 0.6383$ and $y(\text{Se}) = 0.1531$ are obtained. Those values are in excellent concordance with the experimental data by Nelmes and McMahon (see table 6.9). The unit-cell volume is almost identical. The bulk modulus and pressure derivative were fitted using the available data and therefore will most likely underestimate the true value. A bulk modulus of $B_0 = 76.6$ GPa and a pressure derivative of 3.8 are determined.

Furthermore, at 107.67 GPa a transition to the cesium chloride structure is suggested. Ground-state properties for this phase are $a = 3.609$ Å, $V_0 = 47.01$ Å³/pair, $B_0 = 53.2$ GPa, $B' = 5.7$ and $E_{coh} = 2.263$ eV/pair. At a pressure of 115 GPa the lattice constant has decreased to 3.025 Å. However, other possible structures should be investigated to exclude phases intermediate between Cmcn and cesium chloride.

6.4 Electronic structure

6.4.1 Zinc selenide

According to the results presented here, ZnSe at ambient pressures in its zinc blende modification proves to be a direct-gap semiconductor. The smallest band gap appears at the centre of the Brillouin zone with a fundamental gap of 1.14 eV as can be viewed in fig. 6.2 (upper panel). However, further CBM are located at the L - (2.5 eV), X - (3.1 eV) and K -point (3.6 eV).

Experimentalists find a gap energy of 2.82 eV [204], which is as to be expected significantly bigger than the calculated result. Highly accurate calculations using different GW-approximation approaches confirm the measurements ($E_g(\Gamma) = 2.24 - 2.68$ eV [204]). Yet, the band structure presented here compares very well to calculations at a similar level of theory, e.g. $E_g(\Gamma) = 0.88$ eV according to Kohn-Sham LDA by Fleszar and Hanke [170].

Similar to ZB-ZnSe, for the wurtzite modification the results presented here reveal a direct band gap semiconductor as well. The gap energy is 1.18 eV. This

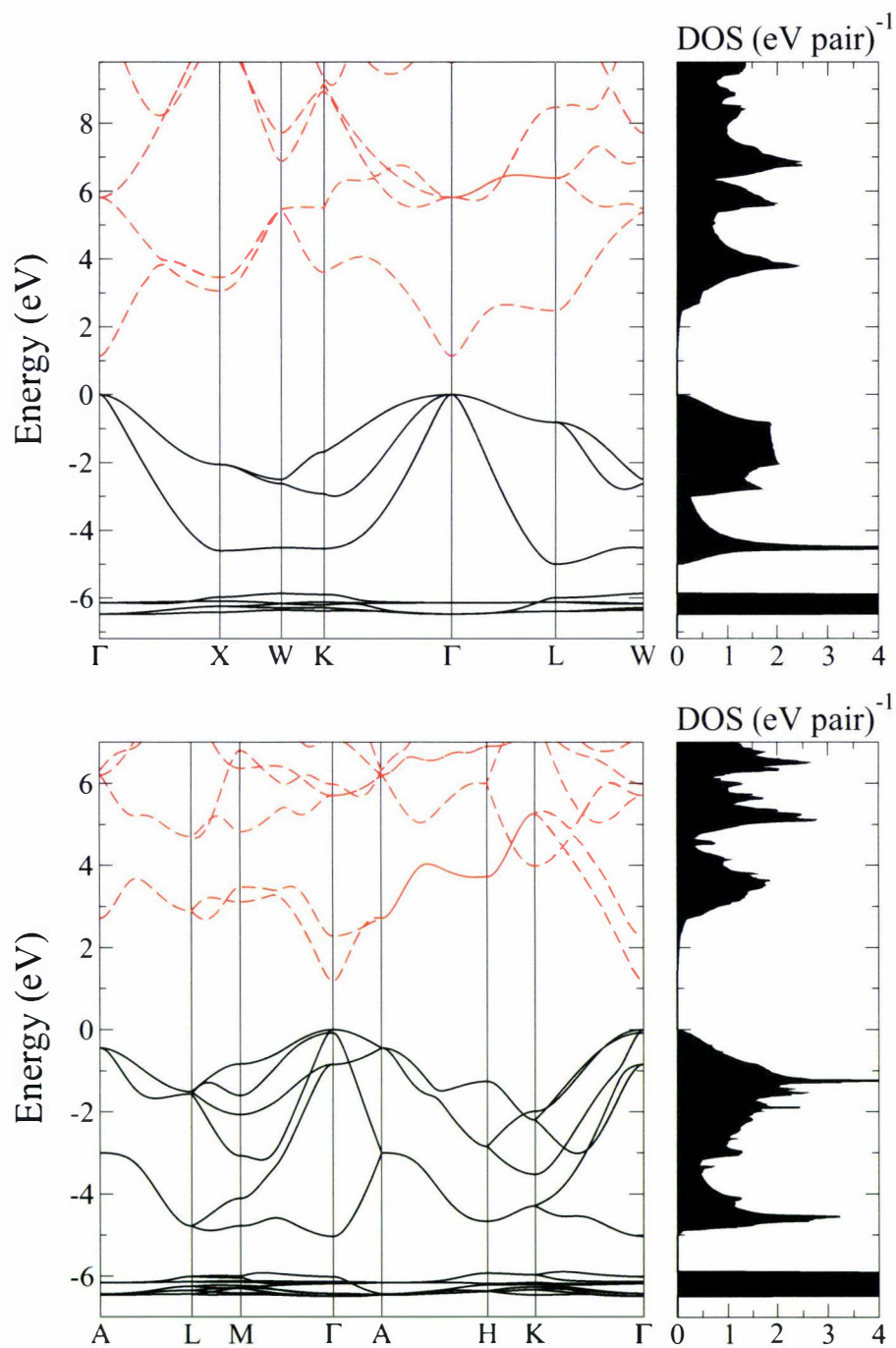


Figure 6.2: Band structure and density of states (normalized per pair) at zero pressure for the ZnSe polymorphs zinc blende (upper panel) and wurtzite (lower panel) calculated within the scalar-relativistic DFT-GGA framework. The valence-band maximum is set to zero energy. The black solid lines indicate the valence and the red dashed lines the conducting bands, respectively.

can be read from the lower panel of fig. 6.2. Both the VBM as well as the CBM appear at the centre of the Brillouin zone, even though other local maxima and minima can be found. However, agreement with the experimentally measured band gap of $E_g(\Gamma) = 2.87$ eV [120] is again diminished by the general shortcoming of DFT for band structure calculations. Yet, the difference in the energy of the fundamental gaps between the zinc blende and wurtzite form compare very well to experimental data.

6.4.2 Cadmium selenide

The bandstructure and DOS for the zinc blende as well as the wurtzite structure of CdSe are depicted in fig. 6.3. Both clearly confirm that CdSe at normal pressure is a direct-gap semiconductor and in both cases the smallest gap occurs at the Γ -point of the Brillouin zone in the style of the behaviour in ZnSe.

However, unlike the ZnSe polymorphs the fundamental gap is rather small with an energy of $E_g(\Gamma) = 0.48$ eV and $E_g(\Gamma) = 0.52$ eV for the zinc blende and the wurtzite case, respectively. But other prominent CBM can be found at L (2.31 eV), X (3.23 eV) and K (3.69 eV) in the zinc blende phase. Further CBM for the wurtzite structure show up at A and between L (2.25 eV) and M (2.67 eV). Lower lying VBM are located at L , K and X for the ZB modification and at A , M and H for the wurtzite polymorph, leaving room for energetically higher transitions.

The data for zinc blende predicts the quantitative electronic structure correctly, yet underestimates the measured band gap ($E_g(\Gamma) = 1.70$ eV [204]) by over 100%, not surprisingly within the DFT Kohn-Sham approach. However, the results are in accordance with other similar calculations, where DFT-LDA predicts an energy of $E_g(\Gamma) = 0.17$ eV [170]. But Fleszar and Hanke also show that additional computational effort can improve the result ($E_g(\Gamma) = 1.25 - 1.70$ eV).

In the case of CdSe-wurtzite structure, experimentalists found an energy gap of 1.71 eV by means of photomodulated transmission spectroscopy [204]. A semi-empirical tight-binding calculation by Kobayashi *et al.* yields 2.0 eV, while a theoretical investigation at similar level of theory as presented here gives $E_g(\Gamma) = 0.43$ eV (FP-LMTO DFT-LDA and GGA) [201] in good agreement with the results presented here.

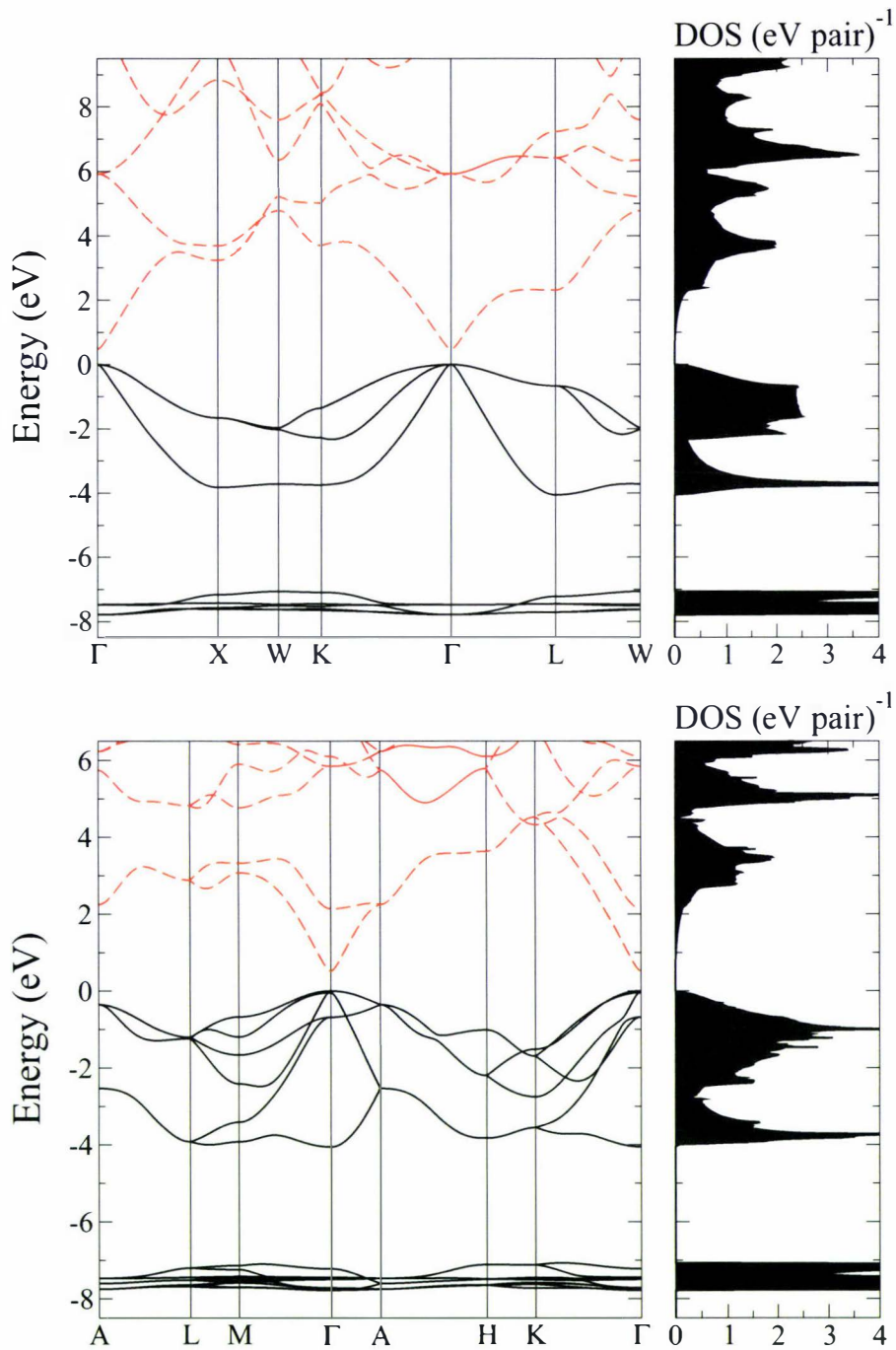


Figure 6.3: Band structure and density of states (normalized per pair) at zero pressure for the CdSe polymorphs zinc blende (upper panel) and wurtzite (lower panel) calculated within the scalar-relativistic DFT-GGA framework. The valence-band maximum is set to zero energy. The black solid lines indicate the valence and the red dashed lines the conducting bands, respectively.

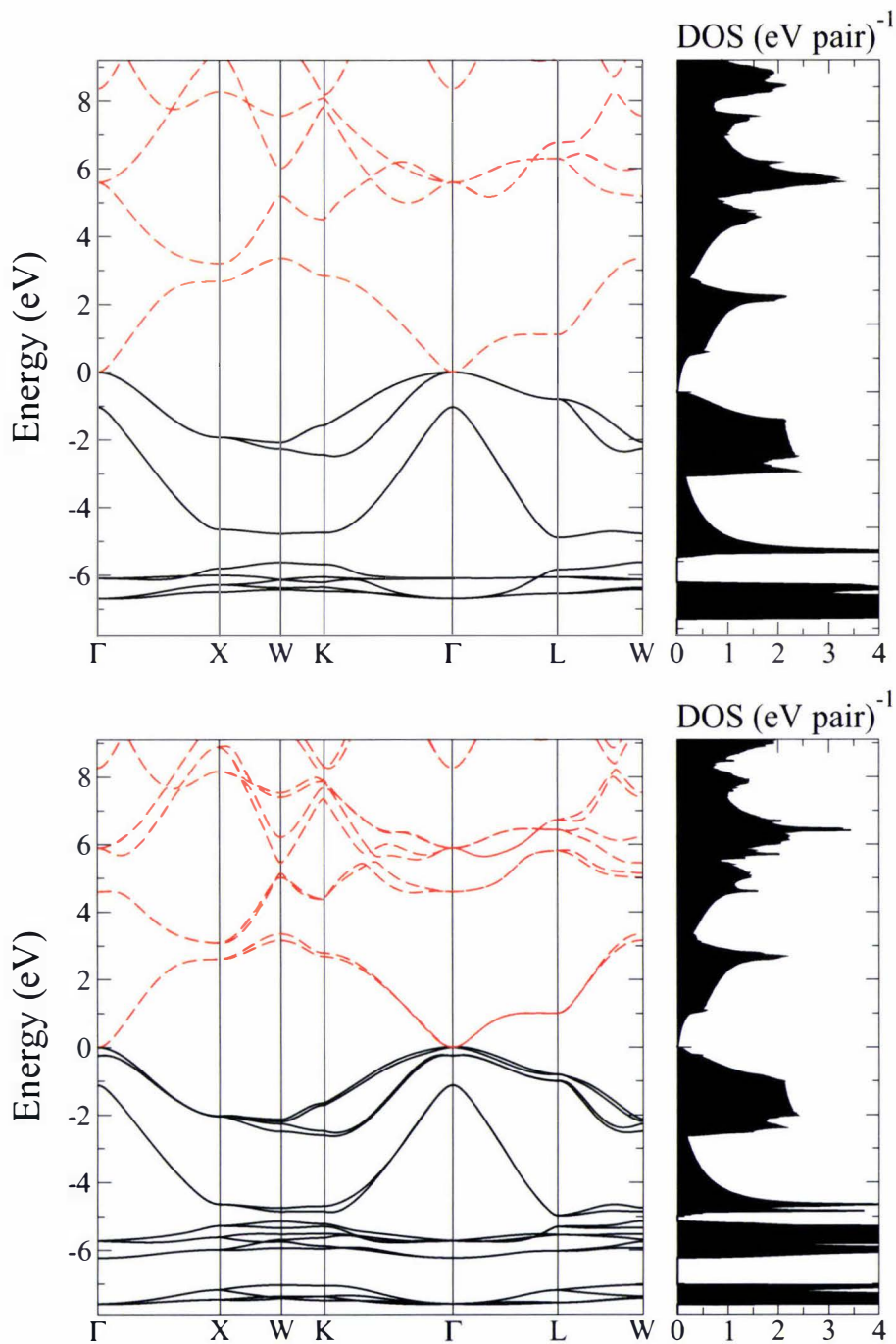


Figure 6.4: Band structure and density of states (normalized per pair) at zero pressure for the HgSe zinc blende polymorph calculated within the scalar-relativistic DFT-GGA framework (upper panel) as well as upon inclusion of spin-orbit effects (lower panel). The valence-band maximum is set to zero energy. The black solid lines indicate the valence and the red dashed lines the conducting bands, respectively.

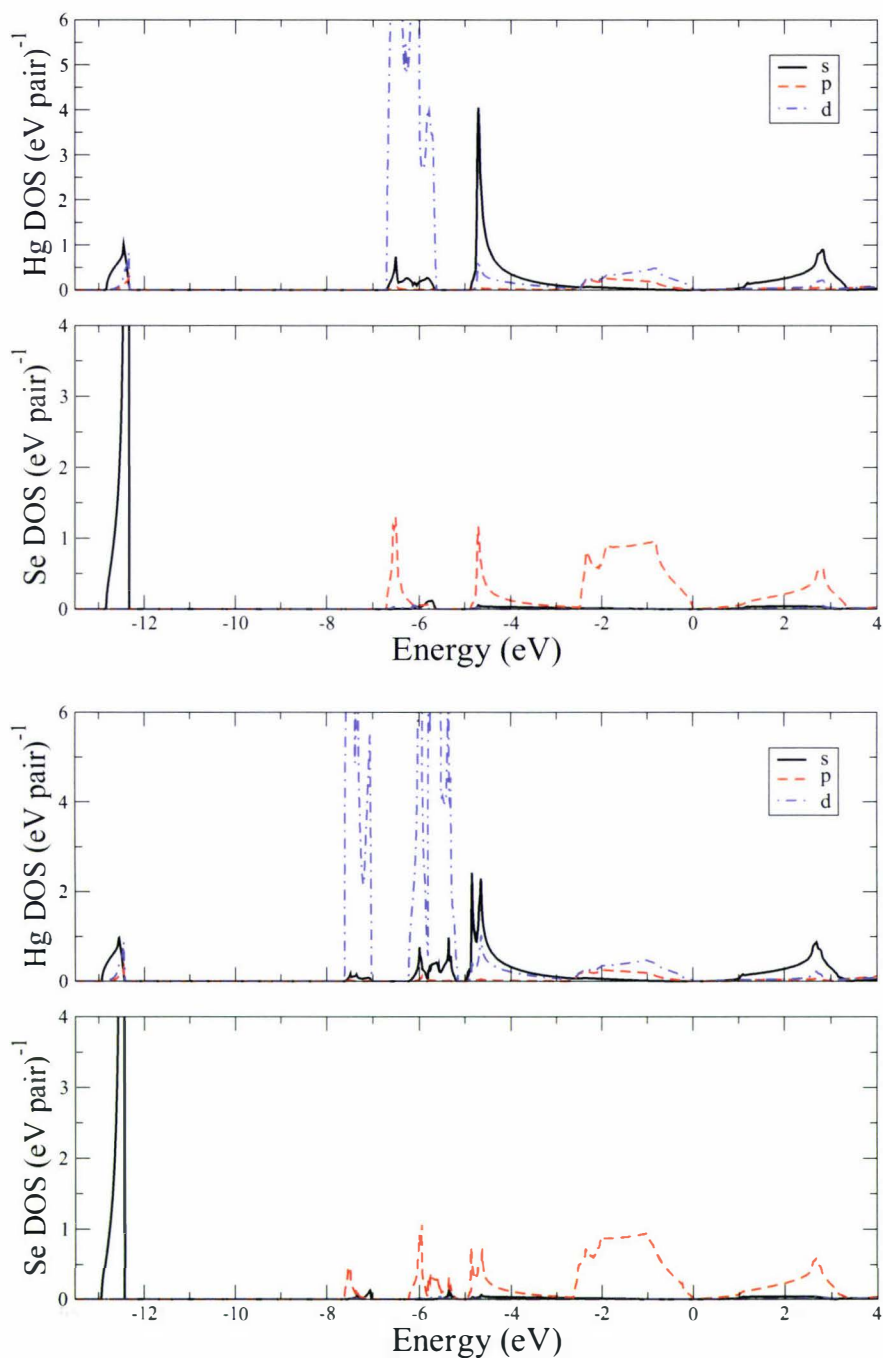


Figure 6.5: Site-projected density of states at zero pressure for the HgSe zinc blende polymorph calculated within the scalar-relativistic DFT-GGA framework (upper panel) as well as upon inclusion of spin-orbit effects (lower panel). The black solid, red dashed and blue dash-dotted line indicate the s, p and d site-projected DOS, respectively.

6.4.3 Mercury selenide

According to ref. [120] HgSe in its zinc blende equilibrium form is a zero-gap material or semimetal, which is caused by the lowest conduction band and the highest occupied valence band being degenerate at the Γ -point of the Brillouin zone. However, ZB-HgSe exhibits a so-called inverted band structure, which means that the for most cubic semiconductors first conduction band, Γ_6 , is found below the Γ_8 -state. Hence, a negative energy gap is created and at 4.2 K a gap energy of -0.27 eV is measured [120].

This is confirmed by the investigations concluded in this thesis and in both, the scalar-relativistic and the spin-orbit corrected description, a zero-gap material is found. The CBM as well as the VBM are calculated to be at the centre of the Brillouin zone evoking a disappearing energy gap. Yet, other local VBM and CBM exist at the L -, K - and X -points in the reciprocal space. Other theoretical investigations of the bandstructure [162, 168, 174] agree rather well with the results obtained. The band structure and DOS in the scalar-relativistic model as well as upon inclusion of spin-orbit effects is shown in fig. 6.4. The site-projected DOS at both levels of theory can be found in fig. 6.5.

By comparing the respective parts of these graphs it can be concluded that, while the lowest lying band with a $4s$ -Se character is not influenced by spin-orbit effects, the following set of $5d$ -Hg bands is split. To begin with, the scalar relativistic calculations show a crystal field splitting of approximately 0.45 eV for the d -bands, which is caused by the tetrahedral arrangement in ZB-HgS. However, improving those results by the inclusion of spin-orbit effects, the lower lying set of $5d$ -Hg bands is split again. The splitting of approximately 1.87 eV is again in good agreement with the level splitting of 1.86 eV found for the atom [128].

For the $E_g(\Gamma_{8v} - \Gamma_{6c})$ -gap values of -1.04 and -1.12 eV are measured in the scalar-relativistic picture and upon inclusion of spin-orbit effects, respectively. This overestimates the experimental result (see above), but is in excellent agreement with values listed in ref. [174] (-1.07 eV for VASP-GGA). Furthermore, Fleszar and Hanke [170] pointed out that gap energies of HgX compounds calculated within LDA need to be corrected by 0.75 eV. If this value is added, the agreement with the experimental result is good.

Looking at the band structure calculated upon inclusion of spin-orbit effects (see lower panel of fig. 6.4), the splitting of the highest lying valence band is determined to be 0.25 eV. This again agrees very well the results of Cardona *et*

al. [174], who obtain the same value at the same level of theory.

6.5 Relativistic influences

6.5.1 Equilibrium structure

System	a	c	u / v	B_0	B'	E_{coh}	V_0
Wurtzite	4.569	7.426	0.3767/ -	40.9	4.5	4.925	67.11
Zinc blende	6.450	-	- / -	40.8	4.5	4.922	67.08
Rocksalt	5.941	-	- / -	57.4	4.8	4.811	52.41
Cinnabar	4.437	10.429	0.5 / 0.5	45.34	4.2	4.759	59.07
Cesium chloride	3.669	-	- / -	57.3	4.7	3.974	49.39
SC16							

Table 6.10: Ground-state properties of equilibrium and high-pressure phases of HgSe within the nonrelativistic approach. Presented are the lattice constants a and c (Å), respective internal parameters, ground-state volume V_0 (Å³/pair), bulk modulus B_0 (GPa) and its pressure derivative B' as well as the cohesive energy E_{coh} (eV/pair).

Looking at HgSe within a nonrelativistic approach leads to the energy-volume curves in the lower panel of fig. 6.6. The changes in the equilibrium structure are less dramatic than in HgO and HgS due to the absence of an equilibrium cinnabar phase in HgSe. However, the summary of the solid-state properties in table 6.10, shows that the wurtzite structure has a minutely higher cohesive energy than the zinc blende structure. Even though the difference is only 3 meV/pair, it indicates that, similarly to the trend in HgS (in the absence of the cinnabar structure), in a nonrelativistic picture the wurtzite modification is preferred in HgSe as well. This means that the relative stability of the wurtzite structure compared to zinc blende increases going from ZnSe via CdSe to HgSe, if relativistic effects are neglected ($\Delta E_{coh}^{W-ZB} = -9$, -4 and 3 meV/pair for ZnSe, CdSe and nonrelativistic HgSe, respectively as compared to -13.97 meV/pair in relativistic HgSe). Considering the small energetic deviation it is likely that both the zinc blende and the wurtzite form would be found as equilibrium structures in a nonrelativistic world.

The lattice constants for the nonrelativistic wurtzite phase of HgSe are $a = 4.569$ Å and $c = 7.426$ Å going along with ground-state volume of 67.11 Å³/pair (for further properties see table 6.10). This implies considerably larger lattice constants than in ZnSe ($a = 4.049$ Å) and CdSe ($a = 4.386$ Å) as well as rela-

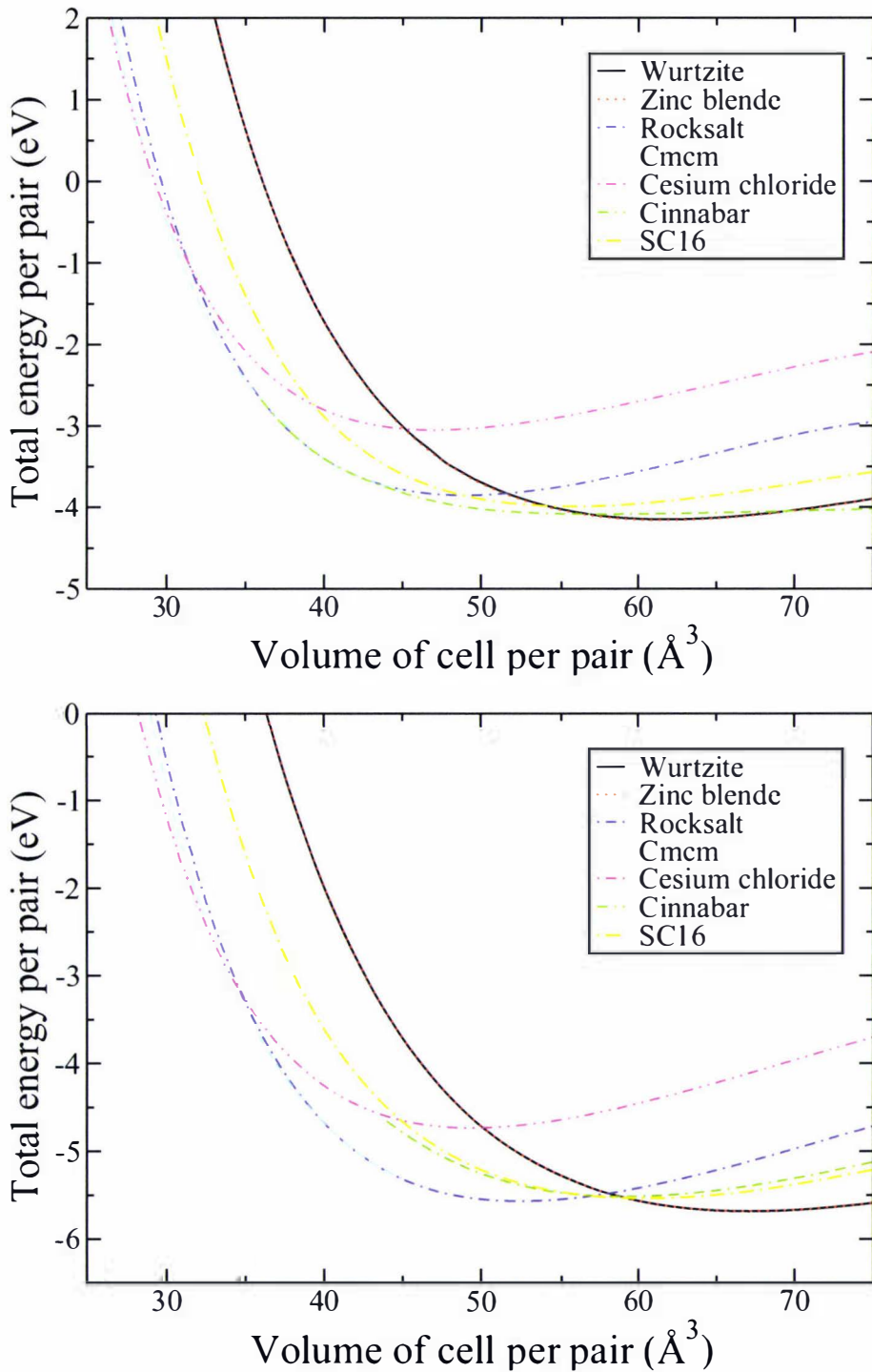


Figure 6.6: The total energy versus volume per cation-anion pair for different crystal structures of relativistic (upper panel) and nonrelativistic HgSe (lower panel).

tivistic W-HgSe ($a = 4.433 \text{ \AA}$), showing the effects of a relativistic contraction. This can also be concluded from the bond distances itemized in table 6.11. This relativistic contraction can also be observed in the overall volume of the unit cell, in stark contrast to the behaviour in HgO and HgS. For those compounds, due to the change in structure (allowing a dramatic contraction in the intra-chain HgO-distances) overall a relativistic volume expansion has been observed, even though the effect of the relativistic contraction in lattice constants and bond distances is even more dramatic than in HgSe.

On the other hand the cohesive energy is increased by 1.55 eV, which means that, even though smaller than in HgO and HgS, still a considerable lattice destabilization by 50% is found when including relativistic effects.

System	ZnSe		CdSe		HgSe		nonrel. HgSe	
	d_{MSe}	d_{MM}	d_{MSe}	d_{MM}	d_{MSe}	d_{MM}	d_{MSe}	d_{MM}
Wurtzite	2.49	4.05	2.68	4.38	2.71	4.43	2.79	4.55
exp.	2.45	4.00	2.64	4.30	-	-	-	-
Zinc blende	2.48	4.05	2.68	4.38	2.72	4.43	2.79	4.56
exp.	2.45	4.01	2.64	4.29	2.63	4.30	-	-
Cinnabar	2.40	3.50	2.67	3.96	2.55	4.00	2.79	4.18
at p_t	-	-	-	-	2.58	4.03	-	-
exp.	-	-	-	-	2.54	4.00	-	-

Table 6.11: Closest metal-selenium bond distance d_{MSe} and closest metal-metal distance d_{MM} in \AA of the respective equilibrium structures (unless indicated otherwise) of the group 12 selenides.

6.5.2 High-pressure structure

The high-pressure behaviour of HgSe treated nonrelativistically is comparable to CdSe leading to the following transition path: ZB/W \rightarrow RS \rightarrow Cmcm \rightarrow CC.

The transition from the wurtzite to the zinc blende structure is bound to happen at 3.38 GPa, whereas both structures undergo a transition to the rocksalt phase at 1.31 and 1.24 GPa for the wurtzite and zinc blende modification, respectively. For the nonrelativistic RS-HgSe modification a ground-state lattice constant of 5.941 \AA is obtained, larger than for all relativistically treated group 12 selenides with lattice constants ranging from 5.372 \AA in ZnSe to 5.808 \AA in HgSe.

At a higher pressure of 22.80 GPa a transition into the Cmcm structure takes place and at 25.00 GPa the following properties are obtained: $V_0 = 40.99 \text{ \AA}^3/\text{pair}$,

$a = 5.476 \text{ \AA}$, $b = 5.490 \text{ \AA}$, $c = 5.454 \text{ \AA}$, $y(\text{Hg}) = 0.7235$ and $y(\text{Se}) = 0.2256$. Subsequently, the transition to the cesium chloride structure is predicted at 66.59 GPa.

The enthalpies of the cinnabar as well as the SC16 structure are always above the one for the rocksalt modification, hence excluding those structures as high-pressure modifications. Furthermore, the C222₁ structure becomes unstable in the nonrelativistic picture as well. The properties are summarized in table 6.10. This means, even though the cinnabar structure does not appear as an equilibrium phase in HgSe, its absence as a high-pressure modification in the nonrelativistic picture in opposition to the relativistic case, demonstrates that relativistic effects indeed play a crucial role to explain the occurrence of the cinnabar structure as such.

Furthermore, if one has a closer look at the Hg-Se bond lengths in the cinnabar structure for the various selenides (see table 6.11), relativistic effects significantly shorten the Hg-Se bond. This is coherent with a very different coordination. In ZnSe for instance, a definite fourfold coordination is found, at which the Zn-Se bond distance is 2.40 Å (Zn-Zn bond distances equals 3.50 Å). For CdSe at the minimum of its E-V-curve, the closest bond Cd-Se distances are 2.67, 2.76 and 3.82 Å with two bonds each, whereas the closest Cd-Cd distance is 3.96 Å. This means that a 2+2+2 coordination is found. This 2+2+2 coordination is also obtained for HgSe, but only if ones looks at a pressure shortly after the ZB → C2 transition. The Hg-Se bond distances at this pressure (4.7 GPa) are 2.58, 2.94 and 3.29 Å (closest Hg-Hg bond distances equals 4.03 Å), which is in excellent accordance with the experimentally observed structure, where the bond distances are determined to be 2.54, 2.89 and 3.24 Å [12]. However, if relativistic cinnabar-HgSe is studied at 0 GPa to enable comparison with ZnSe and CdTe, the chain-like arrangement typical for HgS and HgO is still existent. The closest Hg-Se distances at this pressure are 2.55, 3.29 and 3.53 Å, which means that a 2+4 coordination is still present. This however, is in stark contrast to the coordination obtained if cinnabar-HgSe is treated nonrelativistically. In that case, the Hg-Se bond distances are 2.79, 2.93 and 3.79 Å indicating that the 2+2+2 coordination obtained for CdSe is restored. This change from a 2+4 to a more or less fourfold coordination is depicted in fig. 3.5.

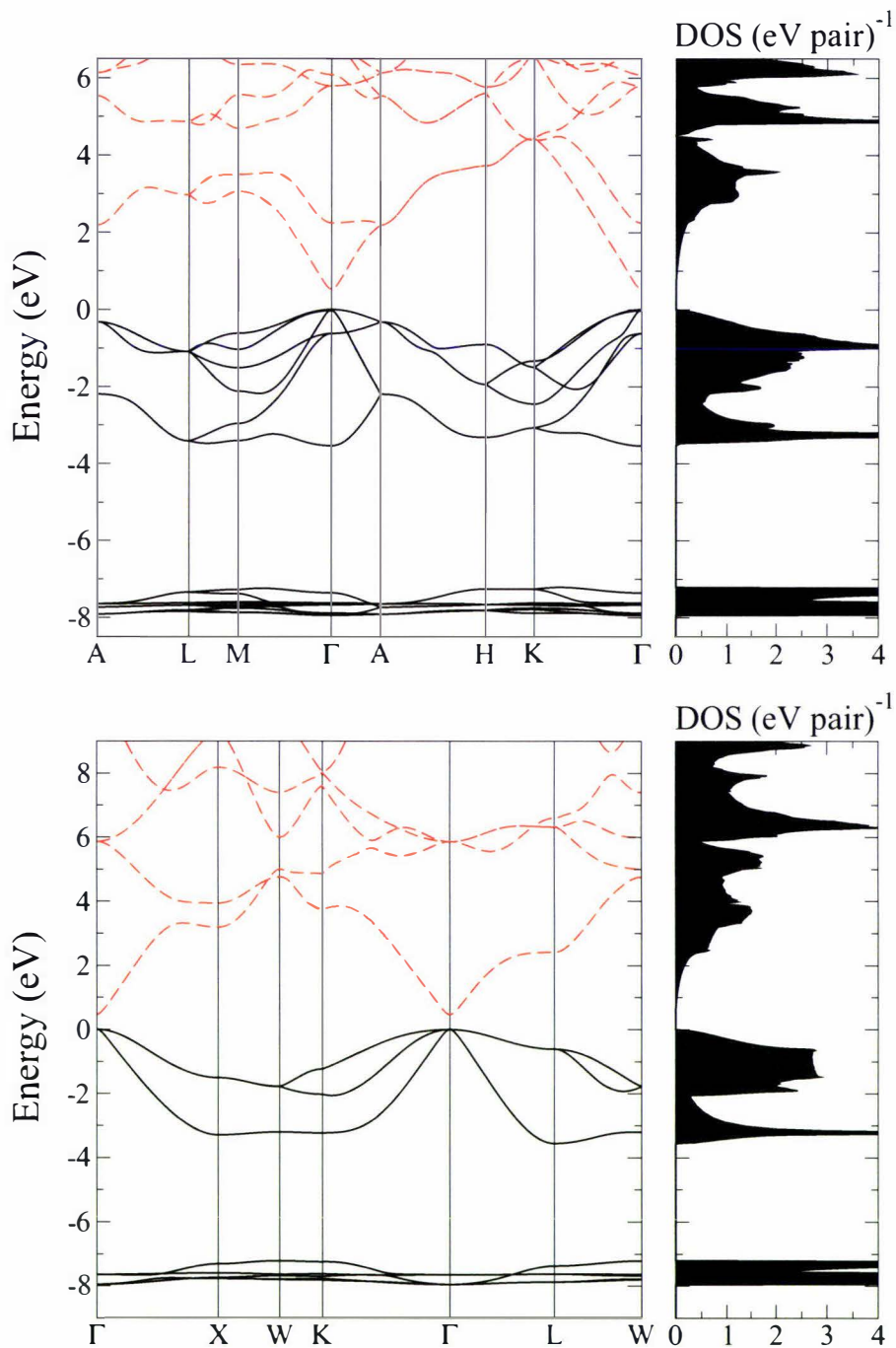


Figure 6.7: Band structure and density of states (normalized per pair) at zero pressure for the HgSe polymorphs wurtzite (upper panel) and zinc blende (lower panel) calculated within the nonrelativistic DFT-GGA framework. The valence-band maximum is set to zero energy. The black solid lines indicate the valence and the red dashed lines the conducting bands, respectively.

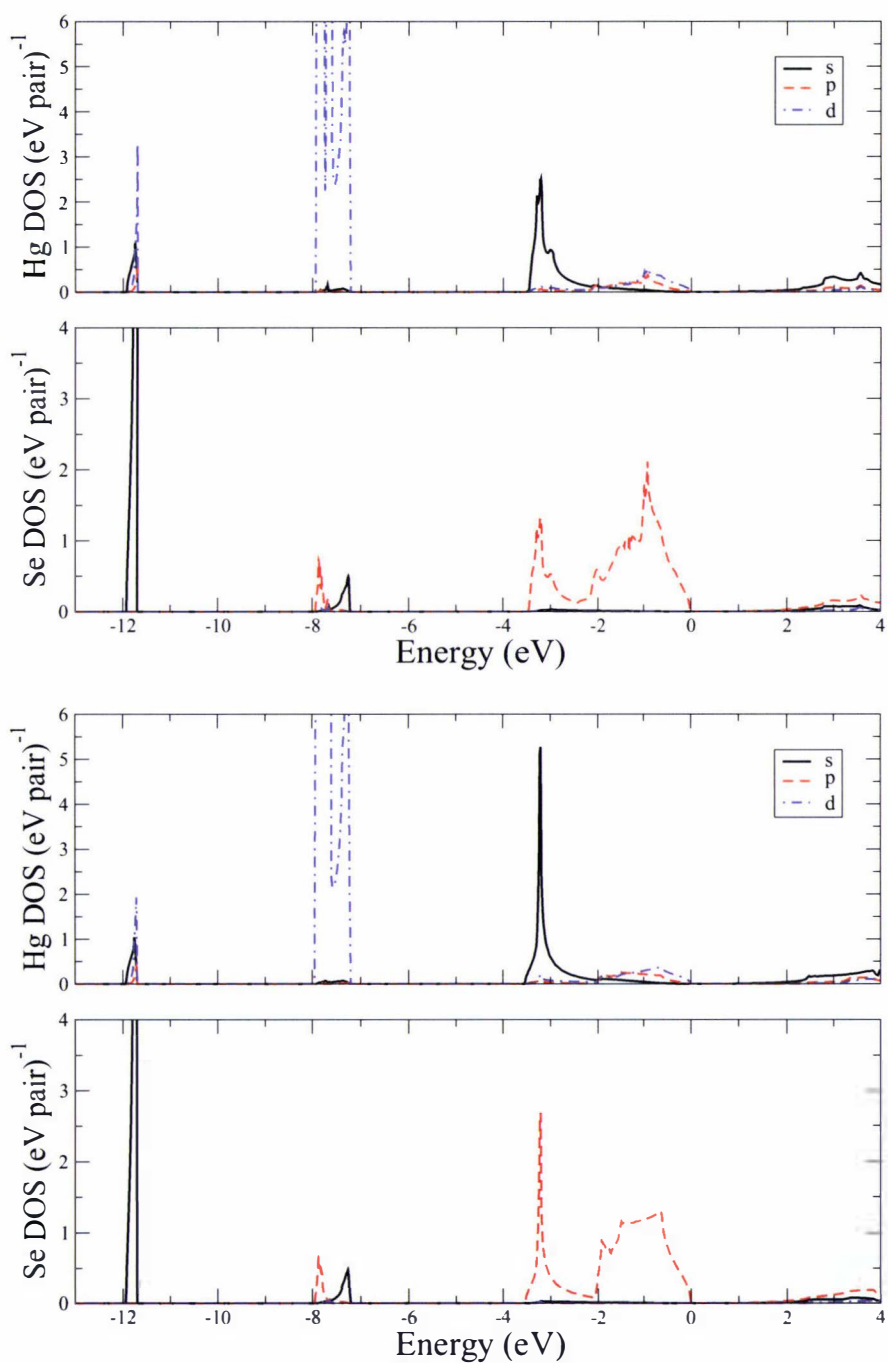


Figure 6.8: Site-projected density of states at zero pressure for the HgSe polymorphs wurtzite (upper panel) and zinc blende (lower panel) calculated within the nonrelativistic DFT-GGA framework. The black solid, red dashed and blue dash-dotted line indicate the s, p and d site-projected DOS, respectively.

6.5.3 Electronic properties

If one looks at the electronic structure of the HgSe equilibrium structure nonrelativistically, dramatic changes happen. From the band structure shown in fig. 6.7 it becomes immediately obvious that the wurtzite as well as the zinc blende modification have semiconducting properties. Specifically for nonrelativistic ZB-HgSe, the $6s$ states of Hg now become degenerate with the higher lying bands close to the Fermi edge at the Γ -point, hence abolishing the inverted band structure. This in turn means that compared to the semimetallic behaviour in the relativistic description the semiconducting properties are now restored.

The band structures and DOS for both the wurtzite and the zinc blende structure look qualitatively very similar to the ones calculated for ZnSe and CdSe. Likewise, the VBM as well as the CBM are located at Γ leading to a direct-gap of 0.48 eV and 0.53 eV for zinc blende and wurtzite, respectively. Those values are quantitatively very close to the gap energies in CdSe, indicating that the electronic structure of HgSe would follow the trend of CdSe if relativistic effects are neglected. Details concerning this trend can also be taken from the site-projected DOS for both possible modifications shown in fig. 6.8.

6.6 Summary

Overall, the structural properties obtained for the equilibrium as well as high-pressure phases of the group 12 selenides compare well to experimental and other theoretical studies, as far as the method used allows for. This applies for the qualitative behaviour in the electronic structure calculations as well. However, as pointed out before, the band gaps determined are strongly underestimated.

The predicted transition paths are in good concordance with other previous work, where available. In addition, a cesium chloride high pressure phase for ZnSe and HgSe is predicted for the first time. However, further work should be carried out to test for phase transitions intermediate between the according $Cmcm$ and cesium chloride modifications. Furthermore, no theoretical work has been carried out to investigate the high-pressure behaviour of HgSe. Hence the results presented here, for the first time confirm the transition path under high pressure observed experimentally for this compound.

Under the neglect of relativistic influences, it is found that the equilibrium structures are not as significantly altered as in HgS and HgO. Yet, a general trend

towards the stability of the wurtzite phase is observed, if one follows the sequence ZnSe, CdSe to nonrelativistic HgSe, which is interestingly enough totally absent in relativistic HgSe. Furthermore, a relativistic lattice destabilization of 1.55 eV/pair is found.

In addition, it is discovered that even though the cinnabar structure is not found as an equilibrium structure anymore in HgSe, it still appears as an high-pressure phase in stark contrast to ZnSe, CdSe and nonrelativistic HgSe. Furthermore, its coordination changes in HgSe, if one switches off relativistic effects, from a 2+2+2 to an almost fourfold coordination.

While the relativistic influence on the structural properties and the transition path of HgSe are less pronounced than in HgO and HgS, the electronic structure of HgSe in the relativistic and nonrelativistic picture differ significantly changing its semimetallic behaviour as far as to restoration of semiconducting properties.

Chapter 7

The group 12 tellurides

7.1 Occurring crystal structures

7.1.1 Zinc tellurides

Zinc telluride is known to crystallize in the zinc blende structure at normal conditions ($a = 6.1037 \text{ \AA}$) [12] and is a semiconductor with a band gap of 2.39 eV (at 0 K) [120].

It transforms to ZnTe-II at about 8.5-9.4 GPa which goes along with a sharp discontinuity in the conductivity [132, 142, 205–207]. Resistivity as well as optical studies have characterized this phase to be a transparent semiconductor with a 2.5 eV band gap [205, 207]. The structure of ZnTe-II has been resolved by means of ADX [208, 209], EDX [210, 211] and combined EDX/EXAFS [212] experiments and appears to have a (site-ordered) cinnabar structure with the following structural parameters: $a = 4.105 \text{ \AA}$, $c = 9.397 \text{ \AA}$, $u(\text{Zn}) = 0.540$ and $v(\text{Te}) = 0.504$ (at 8.9 GPa) [209]. In contrast to cinnabar-HgO and cinnabar-HgS, it shows a more or less fourfold coordination (indicated by the values of u and v being very close to 0.5, see chapter 3.1) with two unequal nearest neighbours at 2.528 Å and 2.646 Å and the next two nearest neighbours both at 3.743 Å. The transition from zinc blende to cinnabar was confirmed in calculations carried out by Lee and Ihm as well as Côté *et al.* [180, 213].

A further high-pressure phase can be detected above 11 GPa (ZnTe-III), first proposed in ref. [132]. Upon subsequent investigation this phase is found to be metallic [205, 206]. Even though the structure proved difficult to solve by diffraction and EXAFS measurements, ADX studies by Nelmes *et al.* [214] finally pin-

pointed it to be a distorted-RS arrangement inheriting the space group $Cmcm$ ¹. At 15.7 GPa the authors determined the lattice constants to be $a = 5.379$ Å, $b = 5.971$ Å and $c = 5.010$ Å and the atomic position $y(\text{Zn}) = 0.640$ and $y(\text{Te}) = 0.190$, respectively. Interestingly, this structure has a surprising fivefold coordination, where the five unlike nearest neighbours have a distance of about 2.7 Å. Again, theoretical studies support this transformation and predict the $Cmcm$ phase to be stable up to 100 GPa [180, 213].

Another change in structure is indicated by new diffraction peaks at 85 GPa, which is supposedly stable up to 93 GPa, the highest investigated pressure by respective authors [12]. However the structure has not been solved so far and is in disagreement with the above theoretical findings. Furthermore, a Raman study by Camacho *et al.* predicts an intermediate phase between cinnabar and $Cmcm$, which has a SC16 structure [215]. This is however not confirmed by the calculations in ref. [139]. No reports on post- $Cmcm$ high-pressure phases have been found.

It is noteworthy to emphasize the absence of the in II-VI semiconductors very common rocksalt structure as a low temperature phase in ZnTe. This is most likely due to the fact that ZnTe has the lowest ionicity in its family [83]. However, diffraction studies (EDX) show a transition to ZnTe-IV with a rocksalt structure for high pressures as well as high temperatures, at which the triple point for the cinnabar, $Cmcm$ and RS phases was determined to be at 13 GPa and 453 K [216]. Later on tables 7.1, 7.4 and 7.5 will summarize the structural parameters and transition pressures for the zinc telluride phases obtained as the outcome of this thesis (see chapters 7.2.1 and 7.3.1). This will include the results of previous experimental and theoretical investigations introduced above.

7.1.2 Cadmium tellurides

At ambient pressure cadmium telluride has a zinc blende structure with a lattice constant of $a = 6.482$ Å [12] and is widely used as a solar cell material. A transition into CdTe-II was first observed at about 3.5 GPa by Edwards and Drickamer (optical measurements) [140] and a second phase transition was discovered at 10 GPa by subsequent conductivity measurements [142].

Upon further investigation by diffraction techniques to identify the structure, CdTe-II was found to have a rocksalt structure [141, 185, 217], with $a = 5.930$ Å

¹This introduced a proper description of the $Cmcm$ structure into the community explaining unresolved structures of various IIIa-Va compounds and GaAs.

(at 3.9 GPa). Gonzalez *et al.* later identified the NaCl phase as a semiconductor with a band gap of 0.08 eV at 6.8 GPa [218]. However, the transition was questioned by ADX measurements of ref. [219], who proposed an actual double transition of zinc blende to cinnabar at 3.4 GPa closely followed by a rocksalt-cinnabar passage at 3.9 GPa introducing an intermediate semiconducting site-ordered cinnabar phase². This double transition is confirmed by calculations of Ahuja *et al.*, who however find a different transition pressure of 10 GPa for the second transition [220].

The volume changes for the two transitions are determined to be 3.4 and 12.2 %, respectively. A mapping of the phase diagram [221] pinpointed the triple point of the zinc blende, cinnabar, rocksalt phase transition at 2.6 GPa and 735 K, showing that a direct ZB to RS passage is possible above this temperature.

The lattice parameters obtained for the cinnabar phase are $a = 4.319$ Å and $c = 10.265$ Å, whereas $u(\text{Cd})$ and $v(\text{Te})$ are 0.622 and 0.565, respectively at 3.2 GPa [222]. Similar to HgTe, and indicated by u and v being so close to 0.5, the cinnabar form has a 4+2 coordination (again very different from HgO and HgS), getting closer to the sixfold NaCl coordination upon pressure increase.

The other transition reported at 10 GPa has shown to be to a phase with a site-ordered Cmc \bar{m} structure, distorting NaCl orthorhombically [223]. The lattice parameters are determined to be $a = 5.573$ Å, $b = 5.960$ Å and $c = 5.284$ Å with $y(\text{Cd}) = 0.650$ and $y(\text{Te}) = 0.180$ (at 18.6 GPa), changing the sixfold NaCl-coordination to a 5+3 coordination. The transition is supported theoretically, but yet again with a different transition pressure ($p_t = 15$ GPa) [220].

Nelmes *et al.* furthermore report another phase transition at 42 GPa, but could not solve the structure [12] and find no further transition up to 55 GPa.

The theoretical study of Ahuja *et al.* predicts a transition to the CsCl structure at 28 GPa [220]. Another theoretical study by Côté *et al.* confirms the order of transitions but slightly overestimates the pressure for the RS-Cmc \bar{m} passage [180].

Chapters 7.2.2 and 7.3.2, where the results for the cadmium tellurides are presented, will directly compare the structural parameters and the transition pressures of the different phases as determined by previous studies to the values obtained in the thesis at hand (see tables 7.2, 7.6 and 7.7).

²Historically, this was the first time the cinnabar phase was found in a compound apart from the mercury chalcogenides.

7.1.3 Mercury tellurides

The low pressure phase of mercury telluride has the zinc blende structure, where $a = 6.4603 \text{ \AA}$, and was found to be semimetallic [189]. The naturally occurring mineral, called coloradoite, is very soft and has an iron-black metallic luster.

In general mercury telluride shows a behaviour very similar to HgSe, meaning it has an analog transition sequence of structures from zinc blende to cinnabar to rocksalt to Cmcn with a 'hidden' intermediate C222₁ phase between the zinc blende and cinnabar modification.

The first transition occurs at 1.3 GPa [169] changing the electronic properties to a semiconducting behaviour as indicated by a steep increase in resistivity [224] with an energy gap of 0.7 eV at 2 GPa (0 eV at 6.5 GPa) [191, 192]. The (site-ordered) cinnabar structure for this phase was first proposed by Mariano and Warekois and has the following structural parameters at 3.6 GPa: $a = 4.383 \text{ \AA}$, $c = 10.022 \text{ \AA}$, $u(\text{Hg}) = 0.641$ and $v(\text{Te}) = 0.562$ [92, 185]. With those parameters HgTe shows a 4+2 coordination with each atom having three pairs of unlike neighbours at 2.732, 2.995 and 3.460 Å. The transition to cinnabar-HgTe goes along with a volume change of 11 % [225].

Upon compression the structure becomes more similar to NaCl, but significant discontinuities in the transition for the structural parameters are observed [225]. At 8 GPa the transition to a metallic rocksalt phase occurs as pointed out by resistivity as well as diffraction studies [191, 192]. The structure was identified in refs. [92, 226]. The new phase is site-ordered with $a = 5.843 \text{ \AA}$ at 8.9 GPa and the volume change for the transition is determined to be 3 % [225].

Like for HgSe however, later on an orthorhombic C222₁ structure was found by McMahon *et al.* as a 'hidden' intermediate phase [195]. It is supposed to occur at 2.25 GPa along with a volume change of 1.2 % and the structural parameters at 2.55 GPa are $a = 6.295 \text{ \AA}$, $b = 6.241 \text{ \AA}$, $c = 6.364 \text{ \AA}$, $x(\text{Hg}) = 0.315$ and $y(\text{Te}) = 0.205$ [195]. This means that the distortion is less than in HgSe, therefore making it hard to be certain of the site-ordered nature of the structure. This structure transforms into the cinnabar form at 2.6 GPa, where $\Delta V/V_0 = 8.7 \%$. At 12 GPa a transition to HgTe-IV occurs [191, 192] which was, like in HgSe, mistaken to be a transition to beta-tin or orthorhombic structure [149, 226], but eventually identified to be site-ordered Cmcn by McMahon *et al.* using ADX techniques [227]. The structure was solved at 18.5 GPa leading to lattice constants of $a = 5.5626 \text{ \AA}$, $b = 6.1516 \text{ \AA}$ and $c = 5.1050 \text{ \AA}$ with the Hg and Te atoms at $y(\text{Hg}) = 0.624$ and $y(\text{Te}) = 0.152$, respectively. This leads to a five-

fold coordination, which is however less pronounced than in CdTe. The volume change for the transition is 1.2 % at 11 GPa.

Furthermore, McMahon *et al.* could explain the data with another slightly better fit of another Cmcn structure. The Hg and Te sites are interchanged resulting in two nearest neighbours. However, it has been eliminated by X-ray absorption investigations of Briois *et al.* [228].

In addition, Huang and Ruoff observed yet another transition at 38.1 GPa to HgTe-V inheriting a distorted-CsCl structure [203]. Nelmes *et al.* confirmed this at a however lower pressure of 28 GPa (50 GPa for a complete transformation) with a volume change of 3.0 % and obtained a lattice constant of $a = 3.299 \text{ \AA}$ (at 51 GPa) [209] for a disordered CsCl (bcc) structure.

Later, in chapters 7.2.3 and 7.3.2, the tables 7.3, 7.8 and 7.9 will give an overview of the different cadmium telluride phases including their structural parameters and the transition pressures. For comparison those include the results of previous experimental investigations and calculations as discussed above.

7.2 Equilibrium structures

7.2.1 Zinc telluride

Looking at the volume-energy relationships for the different modifications of ZnTe in the upper panel of fig. 7.1, the zinc blende structure is obviously the most stable one with a cohesive energy of 4.592 eV. This is consistent with previous experimental as well as theoretical results, as is the obtained lattice constant of $a = 6.179 \text{ \AA}$, especially within the accuracy of the used methodology. For bulk modulus and the according pressure derivative values of $B_0 = 43.6 \text{ GPa}$ and 4.9 are calculated. They compare rather well with other theoretical data, but again underestimate the experimental value ($B_0 = 50.9 \text{ GPa}$, $B' = 5.04$ [153]) by a few percent.

The wurtzite structure of ZnTe was calculated as well and has a cohesive energy of 4.580 eV/pair, which is 12 meV/pair below the one obtained for the zinc blende phase. This difference is slightly bigger than for the selenides and sulfides, which supports that zinc blende is the only equilibrium structure found in ZnTe. This result also matches the energy deviation of 6.4 meV/atom determined in ab-initio LAPW calculations by Yeh *et al.* [158]. The equilibrium parameters obtained for wurtzite are $a = 4.358 \text{ \AA}$, $c = 7.178 \text{ \AA}$ and $u = 0.3733$ and compare well to the

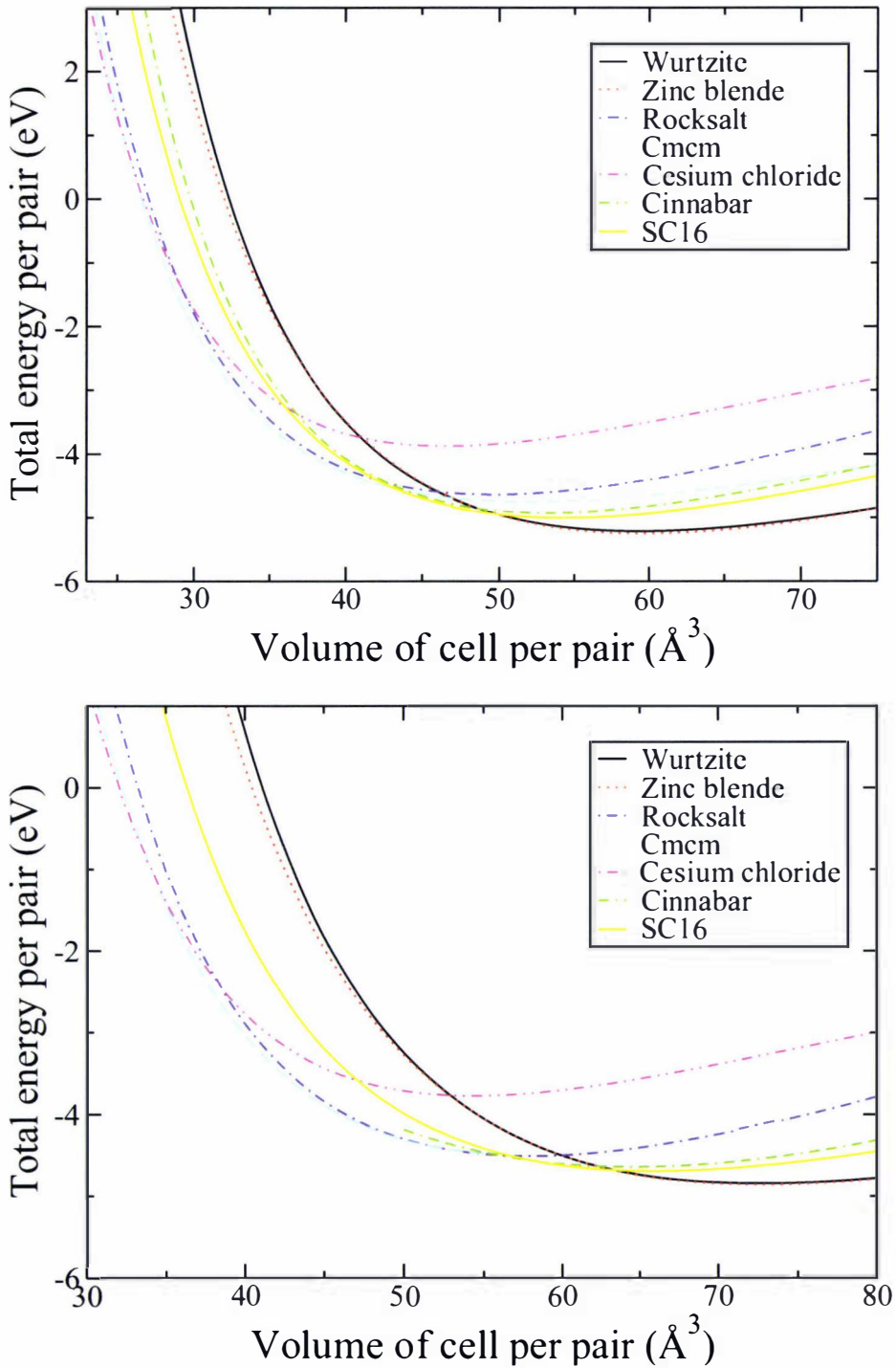


Figure 7.1: The total energy versus volume per cation-anion pair for different crystal structures of ZnTe (upper panel) and CdTe (lower panel).

Property	This work	Other theoretical	Experiments
<i>Zinc blende</i>			
a	6.179	6.013 ^a , 6.020 ^b , 6.174 ^c	6.089 ^b , 6.103 ^e
V_0	58.98	54.35 ^a , 54.54 ^b , 58.84 ^c	56.44 ^b , 56.83 ^e
B_0	43.6	54.7 ^a , 49.2 ^b , 55.21 ^d	50.9 ^e
B'	4.9	4.88 ^c , 4.6 ^d	5.04 ^e
E_{coh}	4.592	4.40 ^f	4.56 ^f
p_t to SC16	9.33	12.7 ^h	
p_t to C2	9.80	5.9 ^a , 8.06 ^j , 11.9 ^l	9.6 ^g , 8.5-9.4 ⁱ
<i>Wurtzite</i>			
a	4.358	4.273 ^k	-
c	7.178	6.989 ^k	-
c/a	1.647	1.636 ^k	-
u	0.3733	0.375 ^k	-
V_0	59.04	55.26 ^k	-
B_0	43.6		-
B'	4.6		-
E_{coh}	4.580		-

^aPW-PP LDA from ref. [180]; ^b*ab-initio* GDSP/DFT from ref. [162]; ^cSCR-LMTO from ref. [229]; ^dFP-APW+lo LDA from ref. [199]; ^efrom ref. [153]; ^fsemi-empirical TB calculation from ref. [157] and refs. therein; ^gRaman study from ref [215]; ^hTB-LMTO from ref. [139]; ⁱfrom ref. [12]; ^jfrom ref. [213]; ^kLAPW-LDA from ref. [158]; ^lDFT from ref. [230].

Table 7.1: Ground-state properties of the equilibrium phases of ZnTe. Presented are the lattice constants a and c (Å), internal parameter u , axial ratio c/a , ground-state volume V_0 (Å³/pair), bulk modulus B_0 (GPa) and its pressure derivative B' as well as the cohesive energy E_{coh} (eV/pair) and the transition pressure p_t (GPa) where applicable.

results of Yeh *et al.* Furthermore, values of 43.6 GPa and 4.6 are calculated for the bulk modulus and its pressure derivative.

For details and to compare the results presented here with previous experimental and theoretical work in detail see table 7.1.

7.2.2 Cadmium telluride

For CdTe, according to the calculations presented here, the zinc blende structure again is the equilibrium phase in accordance with experiments. This can already be deduced from the energy-volume curves in the lower panel of fig. 7.1. The cohesive energy of 4.217 eV/pair matches the experimentally obtained value ($E_{coh} = 4.12$ eV/pair [157]) very well.

Property	This work	Other theoretical	Experiments
<i>Zinc blende</i>			
a	6.620	6.430 ^{a,b} , 6.487 ^c , 6.486-6.573 ^c	6.481 ^c
V_0	72.529	66.46 ^{a,b} , 68.25 ^c , 68.21-71.00 ^c	68.06 ^c
B_0	35.6	46.0 ^a , 29.5 ^b , 41.9 ^c	44.5 ^b , 42.4 ^d
B'	4.8	4.29 ^c , 3.6-4.36 ^c	6.4 ^c
E_{coh}	4.217	4.136 ^c , 3.74 ^d	4.12 ^d
p_t to RS	4.11	3.79 ^h	
p_t to C2	4.16	3.3 ^g	3.4 ^f
p_t to SC16	4.18		
<i>Wurtzite</i>			
a	4.674	4.550 ^e	-
c	7.664	7.451 ^e	-
c/a	1.640	1.638 ^e	-
u	0.3740	0.3754 ^e	-
V_0	72.51	66.79 ^e	-
B_0	35.5	45.4 ^e	-
B'	5.2		-
E_{coh}	4.209		-

^aPW-PP LDA from ref. [180]; ^b*ab-initio* GDSP/DFT from ref. [162]; ^cMD from ref. [231] and refs. therein; ^dsemi-empirical TB calculation from ref. [157] and refs. therein; ^eLAPW-LDA from ref. [161]; ^ffrom ref. [219]; ^gFP-LMTO from ref. [220]; ^hPP-GGA from ref. [232].

Table 7.2: Ground-state properties of the equilibrium phases of CdTe. Presented are the lattice constants a and c (Å), internal parameter u , axial ratio c/a , ground-state volume V_0 (Å³/pair), bulk modulus B_0 (GPa) and its pressure derivative B' as well as the cohesive energy E_{coh} (eV/pair) and the transition pressure p_t (GPa) where applicable.

The lattice properties obtained are $a = 6.620$ Å, $B_0 = 35.6$ GPa and $B' = 4.8$, all of which are in good agreement with previous experimental and theoretical data listed in table 7.2. Again, the variations of a few percent compared to experiments is to be blamed on the method used.

The wurtzite structure was considered as well even though no experimental data is available due to the absence of this structure in CdTe. With the obtained lattice constants of $a = 4.674$ Å and $c = 7.664$ Å and the internal parameter $u = 0.3740$ agreement is reasonable with a LAPW-LDA study by ref. [161] ($a = 4.550$ Å, $c = 7.451$ Å, $u = 0.3754$). The cohesive energy obtained is 4.209 eV/pair. This means the energy difference to the zinc blende structure is 8 meV/pair, which matches another theoretical value extremely well, i.e. 9 meV/pair using LAPW-LDA in ref. [161].

7.2.3 Mercury telluride

Property	This work	Other theoretical	Experiments
<i>Zinc blende</i>			
a	6.660	6.451-6.718 ^a , 6.530 ^b , 6.633 ^c	6.453 ^d , 6.461 ^e
V_0	73.85	67.1-75.8 ^a , 69.61 ^b , 72.96 ^c	67.18 ^d
B_0	34.4	46.4-47.8 ^a , 47.1 ^b	47.6 ^b , 42.3 ^f
B'	5.2		2.1 ^d
E_{coh}	3.059	9.48 ^f	2.176 ^e (E_{sub})
p_t to C222 ₁	3.04		2.55 ^g
p_t to C2	2.30	1.5 ^h	1.3 ⁱ
<i>Wurtzite</i>			
a	4.703		-
c	7.723		-
c/a	1.642		-
u	0.3741		-
V_0	73.95		-
B_0	34.1		-
B'	5.2		-
E_{coh}	3.044		-

^aFP-LMTO LDA and GGA from ref. [168]; ^b*ab-initio* GDSP/DFT from ref. [162];
^cPW-PP GGA from ref. [174]; ^dX-ray diffraction from ref. [149]; ^efrom ref. [120];
^fsemi-empirical TB calculation from ref. [157] and refs. therein; ^gX-ray diffraction
from ref. [195]; ^h PW-US from ref. LDA [233]; ⁱfrom ref. [169].

Table 7.3: Ground-state properties of the equilibrium phases of HgTe. Presented are the lattice constants a and c (Å), internal parameter u , axial ratio c/a , ground-state volume V_0 (Å³/pair), bulk modulus B_0 (GPa) and its pressure derivative B' as well as the cohesive energy E_{coh} (eV/pair) and the transition pressure p_t (GPa) where applicable.

The equilibrium state for HgTe is again the zinc blende structure, which is supported by the energy-volume curves presented in the upper panel of fig. 7.5. The cohesive energy obtained is 3.059 eV/pair, lower than any other investigated structure.

A lattice constant of 6.660 Å is determined along with a ground-state volume of 73.85 Å³/pair, a zero-pressure bulk modulus of $B_0 = 34.4$ GPa and a pressure derivative of 5.2. All properties agree, within the expected accuracy of the method used, with available experimental and theoretical data (see table 7.3 for details), but again overestimate the ground-state volume while underestimating the bulk modulus.

The wurtzite structure, which was investigated as well, is found to be 15 meV/pair higher in energy than the zinc blende phase, which justifies that this modification

does not occur under normal conditions in HgTe. The calculated properties are very similar to the ones obtained for the zinc blende modification, but unfortunately no other studies could be found to compare with.

7.3 High-pressure phases

7.3.1 Zinc telluride

As a result of the calculations presented here, first a transition from the zinc blende structure to the SC16 or the cinnabar structure is obtained. The pressure at which this happens is 9.33 and 9.80 GPa, respectively. Both structures are close in energy. For the cinnabar arrangement a ground-state cohesive energy of 4.290 eV/pair is found, which is about 70 meV lower than the one for the SC16 form. This deviation narrows down for higher pressure. This means that with the methods available at the moment, no statement can be made as to which structure is more stable. In addition, both calculated transition pressures are in very good agreement with other theoretical as well as experimental results as can be concluded from table 7.1. Furthermore, the transition between the SC16 and cinnabar structure is calculated to be possible at 15.50 GPa.

Even though Qteish and Munoz already mention the likelihood of a stable SC16 phase in ZnTe [181], the experimental investigations by Camacho *et al.* [215] as well as the TB-LMTO calculation by ref. [139] conclude the cinnabar phase is preferred over the SC16 phase. However, Camacho *et al.* at least observe the SC16 structure following cinnabar in a narrow pressure range of 12-13.8 GPa, which is extremely close to the stability range of approximately 2.01 GPa obtained here. Refer to table 7.4 for details.

If the SC16→C2 transition is not considered, the results presented here predict that both structures become unstable with respect to the Cmc symmetry (skipping the rocksalt structure in contrast to all other group 12 chalcogenides). This can already be deduced from the upper panel of fig. 7.1. The transition pressures are 11.34 and 9.73 GPa for the SC16 and cinnabar form, respectively, in good agreement with other theoretical and experimental results.

The lattice constant for the SC16 modification under ambient conditions is calculated to be 7.578 Å, which means a ground-state volume of 54.40 Å³/pair. The Wyckoff parameters are $u = 0.1570$ for the Hg atoms and $v = 0.6423$ for the Te atoms, while the bulk modulus and its pressure derivative are 41.5 GPa

Property	This work	Other theoretical	Experiments
<i>SC16</i>			
a	7.578 (7.200)	7.292 ^a	
V_0	54.40 (46.66)		
u	0.1570 (0.1484)		
v	0.6423 (0.6436)		
B_0	41.5	102.35 ^a	
B'	4.5		
E_{coh}	4.363		
p_t to Cmcn	11.34		
<i>Cmcm</i>			
a	5.424 (5.360)	5.655 ^b	5.379 ^c
b	6.852 (6.009)	6.277 ^b	5.971 ^c
c	5.601 (4.913)	5.267 ^b	5.010 ^c
b/a	1.263 (1.121)	1.110 ^b	1.110 ^c
c/a	1.033 (0.917)	0.931 ^b	0.931 ^c
$y(\text{Zn})$	0.6395 (0.6260)		0.640 ^c
$y(\text{Te})$	0.2445 (0.1848)		0.190 ^c
V_0	52.00 (39.56)	46.74 ^b	40.23 ^c
B_0	49.2	62.2 ^b	134 ^d
B'	3.8	4.7 ^b	2.4 ^d
E_{coh}	4.062		
p_t to CC	130.35		
<i>Cesium chloride</i>			
a	3.596 (2.925)		
V_0	46.51 (25.03)		
B_0	50.8		
B'	4.9		
E_{coh}	3.235		

^aTB-LMTO from ref. [139]; ^bDFT from ref. [230]; ^cfrom ref. [214] at 15.7 GPa;
^dX-ray diffraction from ref. [234].

Table 7.4: Ground-state properties of the high-pressure phases of ZnTe. Presented are the lattice constants a , b and c (Å), respective internal parameters, ground-state volume V_0 (Å³/pair), bulk modulus B_0 (GPa) and its pressure derivative B' as well as the cohesive energy E_{coh} (eV/pair) and the transition pressure p_t (GPa) where applicable. Values in brackets indicate higher pressure.

and 4.5. The cohesive energy in the ground state is 4.363 eV/pair. If one looks at the lattice constant at a higher pressure close to the transition (9.20 GPa), a value of 7.200 Å ($V = 46.66$ Å³/pair) is obtained. This means that the results presented here bracket the lattice constant indicated by Gangadharan *et al.* ($a = 7.292$ Å) [139], who unfortunately do not give the pressure at which their

Property	This work	Other theoretical	Experiments
<i>Cinnabar</i>			
a	4.351 (4.101)	4.158 ^a , 4.305 ^b	4.105 ^c
c	9.783 (9.373)	9.899 ^b	9.397 ^c
c/a	2.248 (2.286)	2.299 ^b	2.289 ^c
u	0.4991 (0.5175)		0.540 ^c
v	0.4996 (0.5112)		0.504 ^c
V_0	53.29 (45.51)	52.96 ^b	45.71 ^c
B_0	47.7	62.1 ^a , 51.4 ^b	91.3 ^d
B'	4.9	4.5 ^b	0.8 ^d
E_{coh}	4.290		
p_t to SC16	-		12.2 ^e
p_t to Cmcn	9.73	13.9 ^b , 10.24-11.1 ^f	11-13 ^f
<i>Rocksalt</i>			
a	5.775 (5.500)	5.749 ^b	5.502 ^g
V_0	48.14 (41.59)	47.51 ^b	41.64 ^g
B_0	54.3	57.0 ^b	145 ^g
B'	4.9	5.4 ^b	5 ^g
E_{coh}	3.999		

^aTB-LMTO from ref. [139]; ^bDFT from ref. [230]; ^cfrom ref. [209] at 8.9 GPa;
^dX-ray diffraction from ref. [234]; ^eRaman study from ref [215]; ^ffrom ref. [12];
^gX-ray diffraction at 11.6 GPa from ref. [212].

Table 7.5: Ground-state properties of the high-pressure phases of ZnTe. Presented are the lattice constants a and c (Å), respective internal parameters, ground-state volume V_0 (Å³/pair), bulk modulus B_0 (GPa) and its pressure derivative B' as well as the cohesive energy E_{coh} (eV/pair) and the transition pressure p_t (GPa) where applicable. Values in brackets indicate higher pressure.

data is taken. However, the bulk modulus is not in accordance with their results. This might be due to the different method used. No further data is available to compare with.

On the other hand, the lattice parameters for the cinnabar modification are $a = 4.101$ Å, $c = 9.373$ Å, $u = 0.5175$ and $v = 0.5112$ ($V = 45.51$ Å³/pair) at 10.92 GPa. The corresponding ground-state values are given in table 7.5 and agree considerably well with the results of existing investigations by Nelmes *et al.* and Gangadharan and co-workers [139, 209]. Comparability with ref. [230] is reasonable, considering that the authors fixed the internal parameters with respect to the experimental values.

ZnTe-III has according to the result discussed here a Cmcn structure ($E_{coh} = 4.062$ eV/pair) with lattice constants of $a = 5.424$ Å, $b = 6.852$ Å and $c = 5.601$ Å

along with $y(\text{Zn}) = 0.6395$ and $y(\text{Te}) = 0.2445$ as internal parameters. The lattice constants are in reasonable agreement with the calculations of ref. [230], who have fixed the internal parameters (as well as the lattice constant ratios) to the experimental ones measured by Nelmes *et al.* [214]. This procedure explains the deviations in the bulk modulus as well (see table 7.4). The results are furthermore in concordance with experiments, especially if one looks at the lattice constant at a post-transition pressure: At 16.53 GPa lattice constants of $a = 5.360$ Å, $b = 6.009$ Å and $c = 4.913$ Å and internal parameters of $y(\text{Zn}) = 0.6260$ and $y(\text{Te}) = 0.1848$ are derived (experimental data: $a = 5.379$ Å, $b = 5.971$ Å, $c = 5.010$ Å, $y(\text{Zn}) = 0.640$, $y(\text{Te}) = 0.190$ at 15.7 GPa). However, the bulk modulus seems to be severely underestimated compared to the experiment values. For further details concerning the bulk properties of Cmc \bar{m} -ZnTe see table 7.4.

Furthermore, the present results predict a transition of the Cmc \bar{m} phase to a CsCl-like structure at 130.35 GPa. The ground-state properties can be gathered from table 7.4. At a post-transition pressure of 138.08 GPa, the calculated lattice constant is 2.925 Å. Further work has to be done, to establish whether the CsCl structure becomes unstable in the presence of another intermediate phase. This is very likely, since Nelmes and McMahon observed a phase transition around 85 GPa [12]. Here, especially a distorted CsCl or bcc structure would be worth investigating.

The calculations presented here agree with the interesting fact that the standard transition path for ZnTe does not involve the rocksalt structure in stark contrast to the other zinc chalcogenides. The ground-state cohesive energy of $E_{coh} = 3.999$ eV/pair is considerably higher than the one obtained for the Cmc \bar{m} structure. But since there is evidence of this modification at high temperatures (at 11.5 GPa and 400°C) [212], the bulk properties are included here as well. The ground-state values obtained are: $a = 5.775$ Å, $B_0 = 54.3$ GPa and $B' = 4.9$. At an increased pressure of 11.3 GPa the lattice constant decreases to 5.500 Å ($V = 41.59$ Å³/pair). This is in excellent concordance with the results in ref. [212] ($a = 5.502$ Å at 11.6 GPa). However, the bulk modulus is severely underestimated, which is to be blamed on the fixed value for B' used in the experimental fit and the fact that the authors of ref. [212] give their bulk modulus at higher pressure. Furthermore, the ground-state values are in excellent agreement with previous theoretical work (see table 7.5).

7.3.2 Cadmium telluride

Strictly speaking the transition path calculated for CdTe would go from the zinc blende via the rocksalt to the distorted rocksalt (Cmcm) structure and finally to a caesium chloride arrangement. The according transition pressures are 4.11, 12.4 and 69.5 GPa.

However, the situation is rather complicated with the cinnabar and SC16 structures being energetically in close proximity, especially in the transition region. The transition pressures are very closely spaced with values of 4.11, 4.16 and 4.18 GPa for the ZB→RS, ZB→cinnabar and ZB→SC16 transition, respectively. Therefore, in a pressure range of 4.11 to 4.18 GPa several transitions are possible from a theoretical point of view and the method used is not accurate enough to make a definite statement.

Yet, it is very likely that those structures can be found experimentally, at least as metastable or hidden intermediate phases. The case found here is similar to the situation for the C222₁ phase in HgSe and HgTe. Outside the stability range of ZB with respect to RS (0-4.11 GPa), two possible transitions are found to either the cinnabar or the SC16 structure at 4.16 and 4.18 GPa respectively. But like for C222₁-HgSe an actual stability range cannot be determined, since the C2→RS and SC16→RS transitions are calculated to happen at 3.96 and 4.05 GPa, respectively.

It is mentioned again that only slight energy deviations due to the methodology would change this picture completely, let alone the consideration of differences due to temperature effects. It should also be mentioned that for the cinnabar structure, even though found upon pressure increase as well as decrease, a single phase sample could only be obtained in downstroke experiments [12]. This supports the fact that all structures are energetically very similar.

Concerning the structural properties a ground-state volume of 57.52 Å³/pair is obtained for the rocksalt structure, leading to a lattice constant of 6.128 Å. It decreases to 5.875 Å ($V = 50.69$ Å³/pair) at a pressure of 8.3 GPa in excellent agreement with available experimental data (5.843 Å at 8.9 GPa [226]). The lattice constant is furthermore in good concordance with other theoretical results (see table 7.6). The calculated bulk modulus ($B_0 = 47.5$ GPa) underestimates the experimental value, but is acceptable at the lower end of the theoretical results, as is its pressure derivative ($B' = 5.3$).

The bulk properties determined for the CdTe-IV phase (Cmcm) also match pre-

Property	This work	Other theoretical	Experiments
<i>Rocksalt</i>			
a	6.128 (5.875)	5.787-5.810 ^a , 5.924 ^b	5.930 ^c , 5.843 ^d
V_0	57.52 (50.69)	48.45-49.03 ^a , 51.97 ^b	52.13 ^c , 49.87 ^d
B_0	47.5	74.8-76.2 ^a , 66.4 ^b , 55.3 ^e	69 ^f
B'	5.3	4.29-4.67 ^a , 4.2 ^b , 5.2 ^e	5.1 ^f
E_{coh}	3.868		
p_t to Cmcn	12.41	15 ^e	10.1 ^g , 10 ^h
<i>Cmcm</i>			
a	(5.648)	5.568 ^b	5.573 ^g
b	(6.084)	6.392 ^b	5.960 ^g
c	(5.227)	5.501 ^b	5.284 ^g
b/a	(1.077)	1.148 ^b	1.069 ^g
c/a	(0.926)	0.988 ^b	0.948 ^g
y_1	(0.6396)	0.6532 ^b	0.650 ^g
y_2	(0.1732)	0.1770 ^b	0.180 ^g
V_0	56.90 (44.91)	48.95 ^b	43.9 ^g
B_0	49.02	67.0 ^b	
B'	3.9	4.5 ^b	
E_{coh}	3.816		
p_t to CC	69.53	28 ^e	28 ^g , 42 ⁱ
<i>Cesium chloride</i>			
a	(3.225) 3.788	4.609 ^b , 2.936 ^e	
V_0	(33.54) 54.35	25.31 ^e	
B_0	45.9	66.9 ^b , 108.0 ^e	
B'	5.0	4.72 ^b , 5.3 ^e	
E_{coh}	3.135		

^aLDA and LDA-GGA from ref. [232]; ^bFP-LMTO from ref. [146]; ^cX-ray diffraction at 3.9 GPa from ref. [219]; ^dX-ray diffraction at 8.9 GPa from ref. [226]; ^eFP-LMTO from ref. [220]; ^fX-ray diffraction from ref. [222]; ^gfrom ref. [223] at 18.6 GPa; ^hfrom ref. [142]; ⁱfrom ref. [12].

Table 7.6: Ground-state properties of the high-pressure phases of CdTe. Presented are the lattice constants a , b and c (Å), respective internal parameters, ground-state volume V_0 (Å³/pair), bulk modulus B_0 (GPa) and its pressure derivative B' as well as the cohesive energy E_{coh} (eV/pair) and the transition pressure p_t (GPa) where applicable. Values in brackets indicate higher pressure.

vious data satisfactorily. At 18.99 GPa the lattice constants are 5.648 Å, 6.084 Å and 5.227 Å with a corresponding unit-cell volume of 44.91 Å³/pair. Those values as well as the Wyckoff positions $y(\text{Cd}) = 0.6396$ and $y(\text{Te}) = 0.1732$ are in very good agreement with the experimental data by Nelmes *et al.* ($a = 5.573$ Å, $b = 5.960$ Å, $c = 5.284$ Å, $y(\text{Cd}) = 0.650$, $y(\text{Te}) = 0.180$ at 18.6 GPa). The

Property	This work	Other theoretical	Experiments
<i>Cinnabar</i>			
a	4.618 (4.364)	4.326 ^a	4.338 ^b , 4.292 ^c
c	10.512 (10.285)	10.322 ^a	10.273 ^b , 10.235 ^c
c/a	2.276 (2.357)	2.386 ^a	2.368 ^b , 2.385 ^c
u	0.5193 (0.6209)	0.6540 ^a	0.612 ^b , 0.641 ^c
v	0.5082 (0.5742)	0.675 ^a	0.566 ^b , 0.564 ^c
V	64.64 (56.55)	55.76 ^a	55.81 ^b , 54.43 ^c
B_0	35.1	51.7 ^a	32 ^b
B'	0.18	4.9 ^a	
E_{coh}	4.005		
p_t to SC16	4.13		
p_t to RS	3.96	10 ^d	3.9 ^c
<i>SC16</i>			
a	8.078 (7.800)		
u	0.1576 (0.1514)		
v	0.6395 (0.6404)		
V_0	65.90 (59.32)		
B_0	34.1		
B'	5.3		
E_{coh}	4.054		
p_t to RS	4.05		
^a FP-LMTO from ref. [146]; ^b X-ray diffraction at 2.87 GPa from ref. [222]; ^c X-ray diffraction at 3.6 GPa from ref. [219]; ^d FP-LMTO from ref. [220].			

Table 7.7: Ground-state properties of the high-pressure phases of CdTe. Presented are the lattice constants a and c (Å), respective internal parameters, ground-state volume V_0 (Å³/pair), bulk modulus B_0 (GPa) and its pressure derivative B' as well as the cohesive energy E_{coh} (eV/pair) and the transition pressure p_t (GPa) where applicable. Values in brackets indicate higher pressure.

ground-state values according to the Murnaghan fit are listed in table 7.6 in brackets, but should be regarded with suspicion, since only values up to a volume of 50.54 Å³/pair could be used. This means the minimum is not actually included, therefore the ground-state volume will be over- and the bulk modulus underestimated, since the Murnaghan fit is most reliable for lower pressures. To compare with theoretical data see table 7.6.

For the cesium chloride phase at 73.72 GPa a unit-cell volume of 33.54 Å³/pair along with a lattice constant of 3.225 Å is calculated. However, at this pressure the solid would only be just stable with a very low cohesive energy of 0.154 eV/pair. The ground-state properties were evaluated as well and can be

found in table 7.6. Except for the pressure derivative of the bulk modulus agreement with ref. [220] for unknown reasons is not very good. But the authors also get a very low transition pressure of only 28 GPa, while Nelmes and McMahon reported the Cmcm phase to be stable up to 40 GPa [12]. Comparing this to the transition pressure calculated here (69.3 GPa) it is very likely that another intermediate phase between Cmcm and caesium chloride exists. This should encourage further investigations. but is not the intention of this thesis.

The ground-state properties for the cinnabar structure are listed in table 7.7. At a pressure of 4.13 GPa in the transition region the following properties are determined: $V = 56.55 \text{ \AA}^3/\text{pair}$, $a = 4.364 \text{ \AA}$, $c = 10.285 \text{ \AA}$, $u = 0.6209$ and $v = 0.5742$. The values are in excellent agreement with the respective experimental and theoretical data in table 7.7. The bulk modulus of 35.1 GPa differs from the other computational reference data. but is in excellent concordance with the experimental value (32 GPa [222]). However, the pressure derivative is extremely low with a value of just 0.18.

The structural parameters calculated for the ground state of the SC16 structure in CdTe are: $E_{coh} = 4.054 \text{ eV/pair}$, $a = 8.078 \text{ \AA}$, $V_0 = 65.90 \text{ \AA}^3/\text{pair}$, $u = 0.1576$, $v = 0.6395$, $B_0 = 34.1 \text{ GPa}$ and $B' = 5.3$. At a higher pressure of 4.52 GPa the new lattice parameters are: $a = 7.800 \text{ \AA}$, $V = 59.319 \text{ \AA}^3/\text{pair}$, $u = 0.1514$ and $v = 0.6404$. This phase however, is a pure prediction and no experimental investigations have been reported yet. No other theoretical work could be found either. However, following the predictions for ZnTe, a SC16-CdTe phase is very likely, if not hindered by energy barriers.

7.3.3 Mercury telluride

For the high-pressure behaviour of HgTe a very similar picture to HgSe is found. Similarly, the transition of the equilibrium phase (zinc blende) to the cinnabar phase is predicted at 2.30 GPa, while the method used here fails to predict the intermediate C222₁ phase observed by McMahon *et al.* [195]. The pressure values obtained for the transition are $p_t(\text{ZB} \rightarrow \text{C222}_1) = 3.04 \text{ GPa}$ and $p_t(\text{C222}_1 \rightarrow \text{C2}) = 2.20 \text{ GPa}$ (experimental values: $p_t(\text{ZB} \rightarrow \text{C222}_1) = 2.55 \text{ GPa}$ and $p_t(\text{C222}_1 \rightarrow \text{C2}) = 2.6 \text{ GPa}$ [195]). However, again the C222₁ structure seems to be very sensitive and it is hard to find a Murnaghan fit, since only values over a small volume range are obtained (due to relaxation into other structures). Furthermore, the pressure range for this phase is extremely narrow

Property	This work	Other theoretical	Experiments
<i>Cinnabar</i>			
a	4.695 (4.452)	4.382 ^a	(4.383) ^b , (4.45) ^c
c	10.417 (10.186)	10.028 ^a	(10.022) ^b , (9.89) ^c
c/a	2.219 (2.288)	2.288 ^a	(2.278) ^b , (2.22) ^c
u	0.6639 (0.6489)		(0.641) ^b
v	0.5219 (0.5590)		(0.562) ^b
V	66.28 (58.28)	55.586 ^a	(55.58) ^b , (56.53) ^c
B_0	21.31	55.7 ^a	16.0 ^c , 32-41 ^d
B'	5.1		7.3 ^c , 3.3-5.5 ^d
E_{coh}	2.941		
p_t to RS	5.67		8 ^c
<i>C222₁</i>			
a	(6.531)		(6.295) ^e
b	(6.342)		(6.241) ^e
c	(6.490)		(6.364) ^e
b/a	(0.971)		(0.991) ^e
c/a	(0.994)		(1.011) ^e
$x(\text{Hg})$	(0.3107)		(0.315) ^e
$y(\text{Te})$	(0.2053)		(0.205) ^e
V	(67.21)		
B_0			
B'			
E_{coh}	(2.992)		
p_t to C2	2.20		2.6 ^e
<i>Rocksalt</i>			
a	6.150 (5.875)		(5.83/5.80) ^c , (5.843) ^f
V	58.15 (50.69)		(49.54/48.78) ^c , (49.87) ^f
B_0	47.0		
B'	5.4		
E_{coh}	2.772		
p_t to Cmcn	12.99		10.2 ^g , 12 ^h
^a PW-US LDA from ref. [233]; ^b X-ray diffraction at 3.6 GPa from ref. [92]; ^c X-ray diffraction at 2.6 GPa for the cinnabar and at 8.2/10.5 GPa for the RS form from ref. [149]; ^d X-ray diffraction from ref. [225]; ^e X-ray diffraction at 2.55 GPa from ref. [195]; ^f X-ray diffraction at 8.9 GPa from ref. [226]; ^g from ref. [227]; ^h from refs. [191, 192].			

Table 7.8: Ground-state properties of the high-pressure phases of HgTe. Presented are the lattice constants a , b and c (Å), respective internal parameters, ground-state volume V_0 (Å³/pair), bulk modulus B_0 (GPa) and its pressure derivative B' as well as the cohesive energy E_{coh} (eV/pair) and the transition pressure p_t (GPa) where applicable. Values in brackets indicate higher pressure.

Property	This work	Other theoretical	Experiments
<i>Cmcm</i>			
<i>a</i>	(5.674)	5.612 ^a	(5.563) ^b
<i>b</i>	(6.251)	6.194 ^a	(6.152) ^b
<i>c</i>	(5.163)	5.102 ^a	(5.105) ^b
<i>b/a</i>	(1.102)		
<i>c/a</i>	(0.910)		
<i>y</i> (Hg)	(0.6260)		(0.624) ^b
<i>y</i> (Te)	(0.1546)		(0.152) ^b
<i>V</i>	57.28 (45.78)		
<i>B</i> ₀	49.7	124.7 ^a	
<i>B</i> '	4.2		
<i>E</i> _{coh}	2.705		
<i>p</i> _t to CC	56.74	44.7 ^a	(38.1 ^c , 28-50 ^d)*
<i>Cesium chloride</i>			
<i>a</i>	3.800 (3.325)	3.302 ^a	(3.299) ^d
<i>V</i>	54.87 (36.76)	36.00 ^a	(35.90) ^d
<i>B</i> ₀	54.8	277.2 ^a	
<i>B</i> '	4.1		
<i>E</i> _{coh}	2.236		

^aPW-US from ref. LDA [233]; ^bX-ray diffraction at 18.5 GPa from ref. [227];
^cX-ray diffraction from ref. [203]; ^dX-ray diffraction at 51 GPa from ref. [209].
*The structure is believed to be distorted CsCl or disordered bcc.

Table 7.9: Ground-state properties of the high-pressure phases of HgTe. Presented are the lattice constants *a*, *b* and *c* (Å), respective internal parameters, ground-state volume *V*₀ (Å³/pair), bulk modulus *B*₀ (GPa) and its pressure derivative *B*' as well as the cohesive energy *E*_{coh} (eV/pair) and the transition pressure *p*_t (GPa) where applicable. Values in brackets indicate higher pressure.

(0.05 GPa) and it is actually observed outside the pressure range, where zinc blende is stable with respect to cinnabar. Hence, this phase is not accessible to theoretical calculations.

The structural properties derived for the cinnabar phase of HgTe are *a* = 4.695 Å, *c* = 10.417 Å, *u* = 0.6639, *v* = 0.5219 at zero pressure and *a* = 4.452 Å, *c* = 10.186 Å, *u* = 0.6489, *v* = 0.5590 at 3.69 GPa. Hence, the results are in excellent agreement with the experimental data (see table 7.8). Experiments also measured the bulk modulus for cinnabar-HgTe to be between 16.0 and 41 GPa using different fits, while the pressure dependence is estimated to be in the range of 3.3-7.3. The values determined here, *B*₀ = 21.31 GPa and *B*' = 5.1, are very well within those brackets. Typical for the cinnabar structure among the

mercury chalcogenides is the rather low bulk modulus. The cohesive energy is 2.941 eV/pair, approximately 0.1 eV/pair lower than in zinc blende, meaning that the two structures are very well separated.

Similarly, good results are obtained for the lattice parameters of the $C222_1$ structure, where $a = 6.531$ Å, $b = 6.342$ Å, $c = 6.490$ Å, $x(\text{Hg}) = 0.3107$, $y(\text{Te}) = 0.2053$ at 2.78 GPa. This means that at a similar pressure to experiments, the Wyckoff positions fit nicely, while the lattice parameters show the typical overestimation due to DFT. No structural details are obtained for the ground state due to the direct relaxation into the zinc blende structure for lower pressures. For further details see table 7.8.

Furthermore, at 5.67 GPa a definite structure change from the cinnabar to the rocksalt arrangement is observed. At 5.9 GPa RS-HgTe has the following parameters: $a = 5.875$ Å and $V = 50.69$ Å³/pair. The ground-state properties can be found in table 7.8. They agree well with the experimental data within the limitations of the method used. No other theoretical investigations have been carried out yet. The bulk modulus and pressure derivative are 47.0 GPa and 5.4.

The orthorhombic $Cmcm$ structure is found above pressures of 12.99 GPa and is stable up to 56.74 GPa with respect to the cesium chloride structure. Again no ground-state properties can be given for the $Cmcm$ structure due to relaxation into rocksalt for lower pressures. However, at 18.36 GPa the lattice constants of $a = 5.674$ Å, $b = 6.251$ Å and $c = 5.163$ Å are in good agreement with experimental as well as theoretical work, although no pressure is given for the calculated reference data. The Wyckoff parameters $y(\text{Hg}) = 0.6260$ and $y(\text{Te}) = 0.1546$ match the X-ray diffraction values even better. The few ground-state values given in table 7.9 are estimated from the data points available using the Murnaghan fit and hence will most likely underestimate B_0 .

At still higher pressures of 56.74 GPa a transition to the CsCl structure is predicted with an according lattice constant of 3.325 Å ($V = 36.76$ Å³/pair) at 55.56 GPa. The cohesive energy at this pressure is very low (0.116 eV/pair) and the structure therefore only just stable. However, having said that, one has to bear temperature effects in mind as well. The respective ground-state properties can be found in table 7.9 along with another theoretical study. The results show good comparability to other theoretical work.

Comparison with experimental data is difficult, since the structure of HgTe's post- $Cmcm$ phase is still debated. Huang and Ruoff observed a transition at 38.1 GPa, which they believe to be to a distorted CsCl arrangement. However, Nelmes *et*

al. find a transition at 28 GPa, which could be explained by a disordered CsCl or bcc structure (no long-range order). Yet, a single-phase probe is only obtained at 50 GPa and the lattice constant is $a = 3.299$ Å (at 51 GPa) [209]. This is in excellent concordance with the lattice constant presented for the site-ordered CsCl structure.

Analogous to HgSe, the SC16 structure is too high in energy to be considered a stable phase in HgTe ($E_{coh} = 2.908$ eV/pair). However, the ground-state lattice constant obtained is 8.120 Å along with internal parameters of $u = 0.1623$ and $v = 0.6340$. Hence, the ground-state volume is $V_0 = 66.93$ Å³/pair. Furthermore, the values calculated for the bulk modulus and its pressure dependency are $B_0 = 32.9$ GPa and 6.4 respectively.

7.4 Electronic structure

7.4.1 Zinc telluride

The electronic structure and density of states of ZnTe in its equilibrium state is depicted in fig. 7.2. The VBM and CBM appear both at the centre of the Brillouin zone, and further VBM as well as CBM are located at L , K and X . Hence, it is concluded that the zinc blende form of ZnTe under ambient pressure is a direct-gap semiconducting material with a fundamental gap of 1.07 eV.

Compared to this the experimentally observed energy of 2.39 eV (at 0 K) [120] is significantly higher showing the inadequacy of DFT for the calculation of absolute gap energies. Yet, the qualitative picture compares very well to other investigations. In addition, the values presented agree with calculations at the same level, e.g a LDA calculation discussed in ref. [170] obtaining a value of $E_g(\Gamma) = 0.74$ eV at a lattice constant of $a = 6.088$ Å. A significant improvement of the value could be achieved by using various improved approaches within the computationally extremely expensive GW approximation, leading to values of 1.97 to 2.27 eV [170].

7.4.2 Cadmium telluride

According to the study at hand and in concordance with experimental and other theoretical investigations, CdTe is classified as a small-gap semiconductor, and a direct gap of 0.58 eV is found at the Γ -point in the Brillouin zone. Similarly to

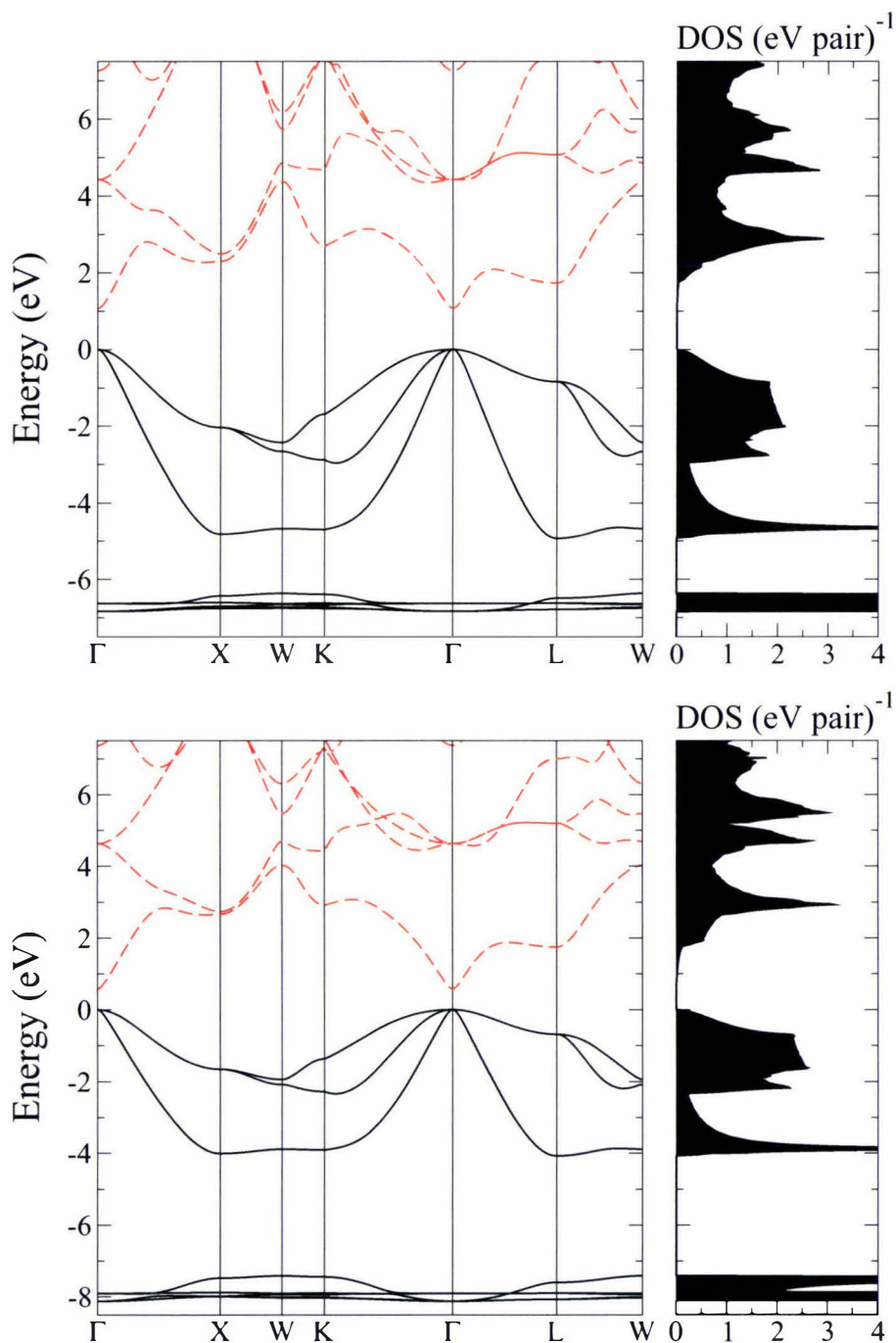


Figure 7.2: Band structure and density of states (normalized per pair) at zero pressure for the ZnTe (upper panel) and CdTe (lower panel) zinc blende polymorph calculated within the scalar-relativistic DFT-GGA framework. The valence-band maximum is set to zero energy. The black solid lines indicate the valence and the red dashed lines the conducting bands, respectively.

ZnTe, other local CBM and VBM are situated at the L , K and X -points. For an illustration of the band structure and DOS the reader is referred to the lower panel of fig. 7.2.

Again the method used here, despite producing qualitatively correct results, severely underestimates the band gap, as a gap energy of 1.59 eV was measured at 1.6 K [120]. Those values can only be obtained computationally, if one employs very expensive methods such as the GW-approximation. In that case ref. [170] calculates an energy of $E_g(\Gamma) = 1.22 - 1.51$ eV. However, comparability with an according LDA calculation is acceptable considering the slightly different lattice constants used as well ($E_g(\Gamma) = 0.21$ eV at a lattice constant of $a = 6.480$ Å) [170].

7.4.3 Mercury telluride

Experimentally, HgTe was found to be a zero-gap material, i.e. a semimetal, with the smallest gap at the Γ -point. Here an inverted band structure is observed since the Γ_6 -level, being the CBM for most cubic semiconductors has a lower energy than the Γ_8 -state (VBM) [120]. Hence, a small negative band gap of -0.304 eV (at 0 K) is measured [120].

This is confirmed by the study at hand, where the results are depicted in figs. 7.3 and 7.4. For both approaches, the scalar-relativistic methodology as well as upon inclusion of spin-orbit coupling, the Hg-6s band are located below the O-5p bands, as can be concluded from the site-projected density of states. Just by counting, the bands should be occupied up to the first O-5p, making HgTe a zero-gap material. Hence, the inverted band structure as well as the semiconducting character of ZB-HgTe are correctly reproduced.

Due to the spin-orbit splitting the picture changes slightly and the situation is similar to HgSe, where spin-orbit splitting of the p -states is large enough and hence the Γ_8 levels are higher in energy than the Γ_7 levels. For the direct $E_g(\Gamma_8 - \Gamma_6)$ -gap an energy of -1.154 eV is calculated. This compares well to other theoretical investigations. For example, Cardona *et al.* [174] obtain a value of $E_g = -1.025 / -1.113$ eV using Vasp LDA and GGA, respectively. The discrepancy can be explained by the slightly different lattice constant used ($a = 6.433 / 6.633$ Å for LDA and GGA, respectively).

Looking at the plot of the relativistic Hg site-projected DOS, a complex picture emerges. Here, a splitting of about 2 eV is found, again indicating the splitting of the 5d band into $5d_{3/2}$ and $5d_{5/2}$ as it was the case for previously described Hg

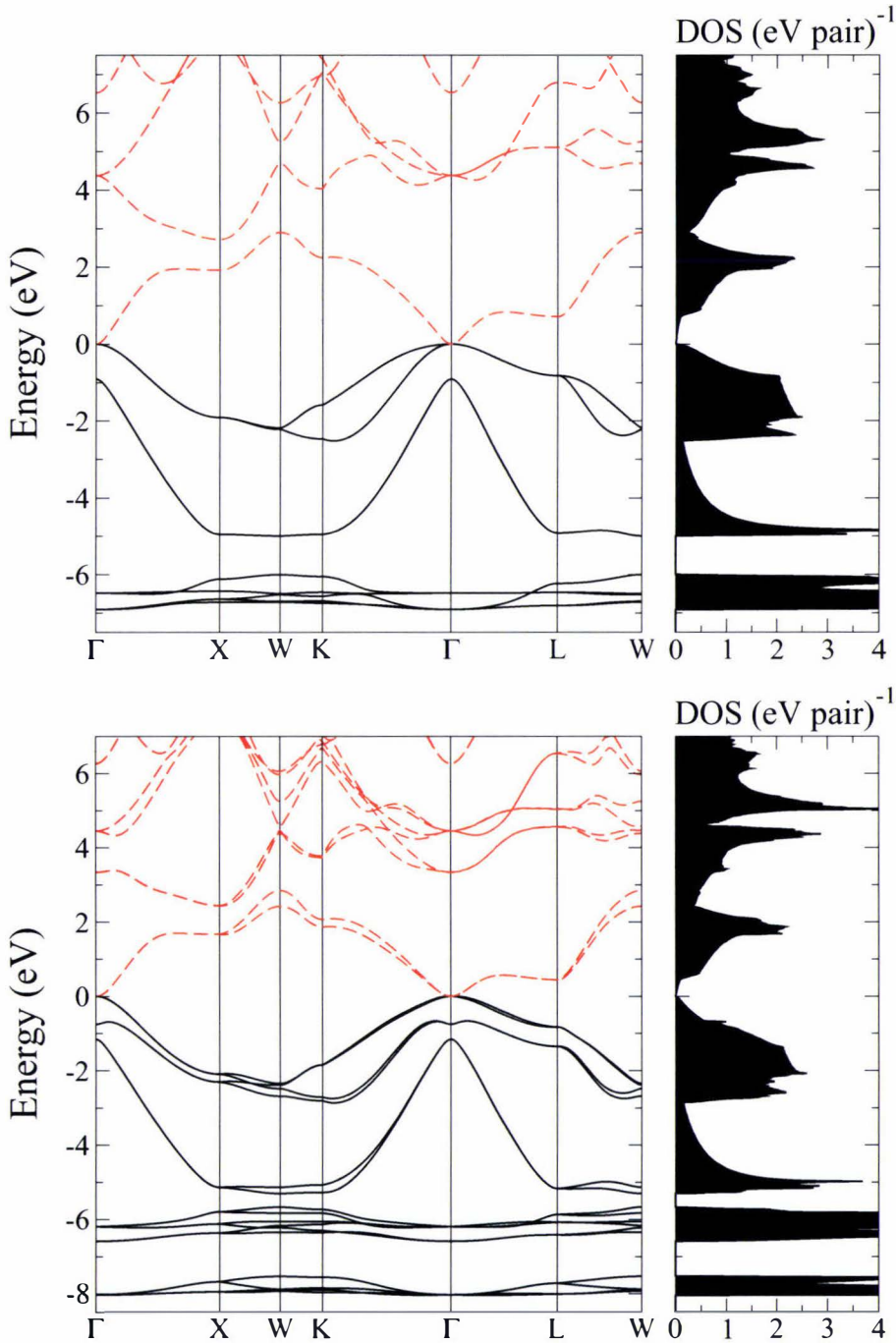


Figure 7.3: Band structure and density of states (normalized per pair) at zero pressure for the HgTe zinc blende polymorph calculated within the scalar-relativistic DFT-GGA framework (upper panel) as well as upon inclusion of spin-orbit effects (lower panel). The valence-band maximum is set to zero energy. The black solid lines indicate the valence and the red dashed lines the conducting bands, respectively.

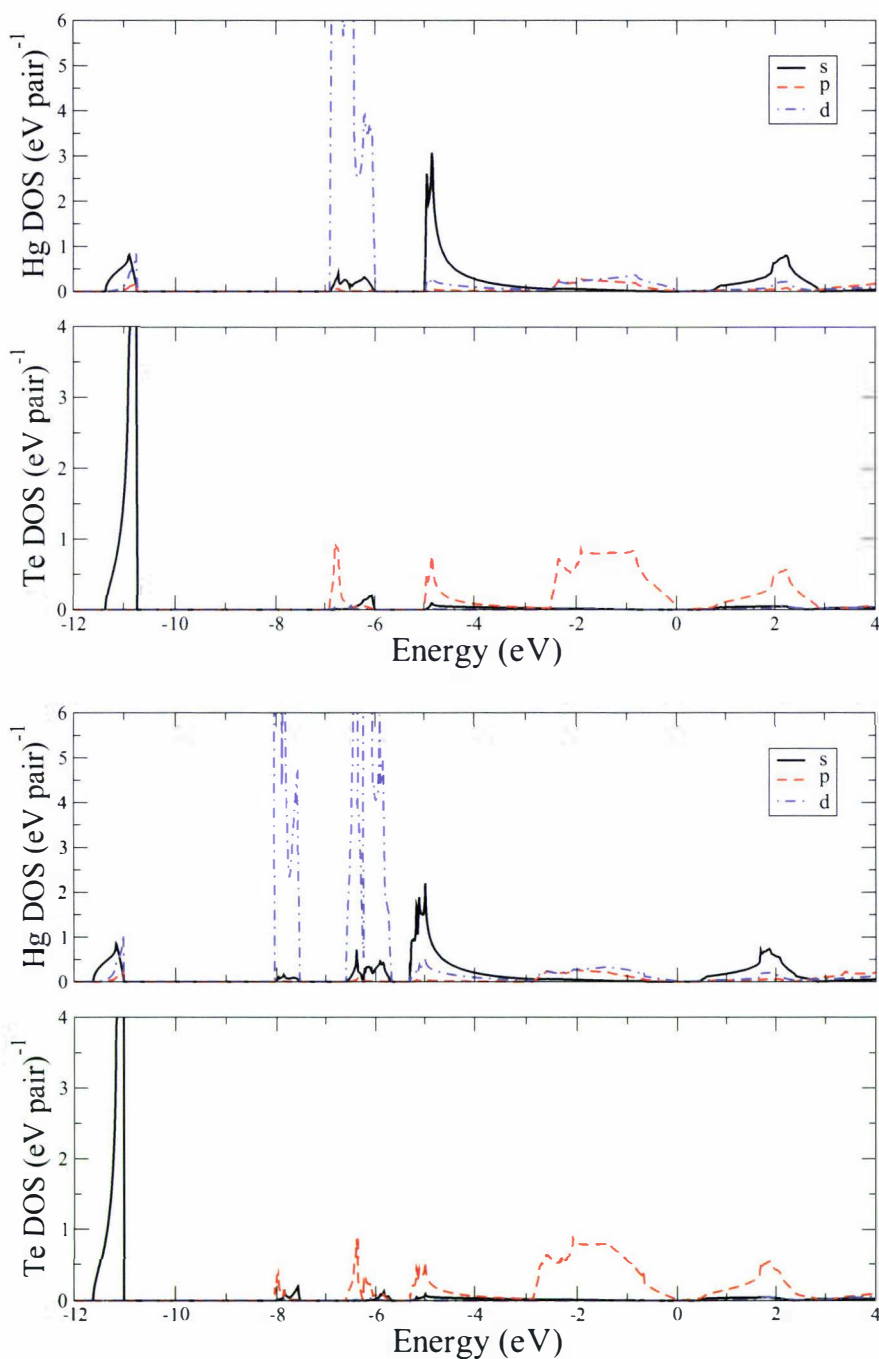


Figure 7.4: Site-projected density of states at zero pressure for the HgTe zinc blende polymorph calculated within the scalar-relativistic DFT-GGA framework (upper panel) as well as upon inclusion of spin-orbit effects (lower panel). The black solid, red dashed and blue dash-dotted line indicate the s, p and d site-projected DOS, respectively.

chalcogenides. An additional influence of the crystal-field splitting can be seen.

7.5 Relativistic influences

7.5.1 Equilibrium structure

System	a	c	u / v	B_0	B'	E_{coh}	V_0
Zinc blende	6.860	-	- / -	32.6	4.9	4.390	80.71
Wurtzite	4.850	7.926	0.3749 / -	32.6	4.9	4.385	80.74
SC16	8.353	-	0.1576 / 0.6386	32.1	4.8	4.250	72.85
Cinnabar	4.742	10.927	0.5397 / 0.5210	22.6	-10.3	4.214	70.95
Rocksalt	6.320	-	- / -	44.9	5.0	4.171	63.12
Cesium chloride	3.897	-	- / -	44.2	4.8	3.422	59.17

Table 7.10: Ground-state properties of equilibrium and high-pressure phases of HgTe within the nonrelativistic approach. Presented are the lattice constants a and c (Å), respective internal parameters, ground-state volume V_0 (Å³/pair), bulk modulus B_0 (GPa) and its pressure derivative B' as well as the cohesive energy E_{coh} (eV/pair).

The volume-energy dependencies of nonrelativistically treated HgTe can be viewed in the lower panel of fig. 7.5. It shows that, similar to what has already been described for HgSe, the zinc blende and wurtzite structure yield the lowest energies. Table 7.10 shows, however, that for the first time within the nonrelativistic Hg chalcogenides the zinc blende structure actually reaches a higher cohesive energy than the wurtzite structure, indicating that this is the preferred equilibrium phase. Yet, the energy difference of just 5 meV/pair is very small and resembles approximately the energy deviation in CdSe, in which case still both structures occur at ambient pressures. Also, looking at the sequence of energy differences between the zinc blende and the wurtzite structure within the group 12 tellurides (12 meV/pair, 8 meV/pair and 15 meV/pair for ZnTe, CdTe and HgTe respectively), it becomes obvious that relativistic influences at least destabilize the wurtzite structure.

The bulk properties obtained for the zinc blende form are $a = 6.860$ Å, $V_0 = 80.71$ Å³, $B_0 = 32.6$ GPa and $B' = 4.9$. This means that yet again the scalar-relativistic calculations for HgTe lead to a typically relativistically contracted lattice constant compared to the nonrelativistic value. This can also be deduced from the bond distances in table 7.11, where relativity causes ZB-HgTe as well as W-HgTe to adopt almost the same values as obtained for CdTe.

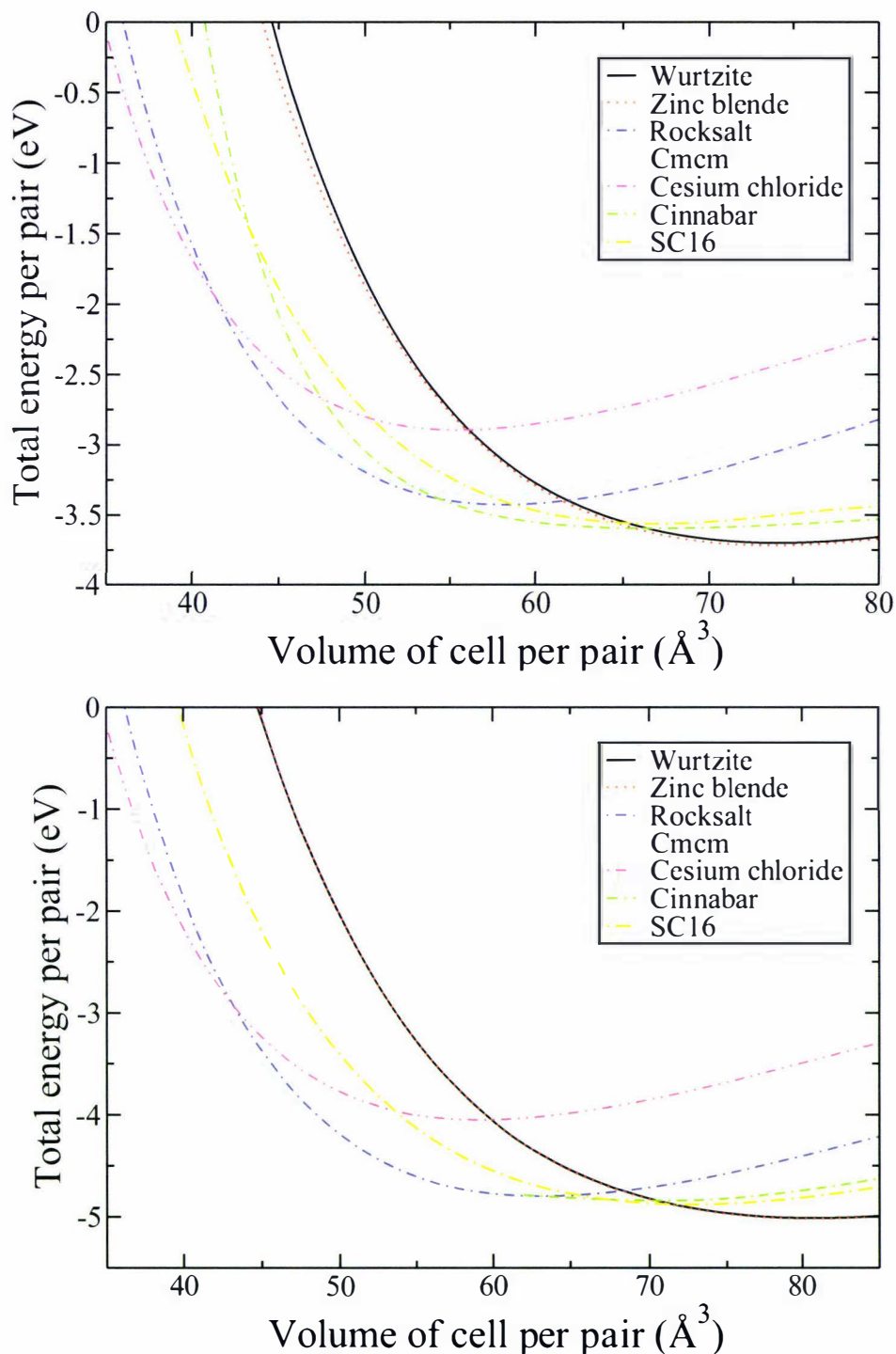


Figure 7.5: The total energy versus volume per cation-anion pair for different crystal structures of relativistic (upper panel) and nonrelativistic HgTe (lower panel).

Furthermore, an energetic lattice destabilization is observed lowering the cohesive energy relativistically from 4.390 to 3.059 eV/pair. The difference of 1.33 eV/pair is even less than in HgSe.

System	ZnTe		CdTe		HgTe		nonrel. HgTe	
	d_{MTe}	d_{MM}	d_{MTe}	d_{MM}	d_{MTe}	d_{MM}	d_{MTe}	d_{MM}
Wurtzite	2.67	4.38	2.86	4.68	2.88	4.72	2.97	4.85
Zinc blende	2.67	4.37	2.87	4.68	2.88	4.71	2.97	4.85
exp.	2.64	4.32	2.81	4.58	2.80	4.57	-	-
Cinnabar	2.72	3.92	2.88	4.20	2.76	4.40	2.96	4.36
at p_t	2.57	4.10	2.79	4.17	2.76	4.34	2.94	4.38
exp.	-	-	2.77	4.14	2.73	4.13	-	-

Table 7.11: Closest metal-tellurium bond distance d_{MTe} and closest metal-metal distance d_{MM} in Å of the respective equilibrium structures (unless indicated otherwise) of the group 12 tellurides.

7.5.2 High-pressure structure

The order of structural transitions at higher pressures for the nonrelativistically treated HgTe is calculated to be ZB→RS→Cmcm→CsCl. The transition pressures obtained are 2.12, 13.30 and 53.71 GPa, respectively.

A transition from the zinc blende structure to a cinnabar form of nonrelativistic HgTe is not achieved until the cinnabar structure already converts into the rocksalt arrangement. However, it is hard to make a prediction since the structures are close in energy and the deviations in the transition pressures ($p_t(\text{ZB} \rightarrow \text{C2}) = 2.33$ GPa and $p_t(\text{C2} \rightarrow \text{RS}) = 1.67$ GPa) smaller than the precision of the method used. Furthermore, for the cinnabar structure again (like in nonrelativistic HgSe) the problem occurs that the structural minimum characterized by $u \approx 0.5 \approx v$ splits up for higher pressures. The energy-volume curve, for which the Wyckoff positions deviate from 0.5, is lower in energy. But since this curve for lower pressures immediately relaxes into the other curve, a negative pressure derivative of the bulk modulus is calculated for nonrelativistic HgTe, making it hard to calculate the correct transition pressure.

This behaviour is similar to CdTe and immediately shows the different nature of the cinnabar phase in nonrelativistic HgTe compared to the relativistic characteristics. In contrast, for the relativistic calculations of cinnabar-HgTe, a strong energy-volume minimum is found, with u and v deviating from 0.5 over the whole pressure range investigated. This leads to a 4+2 coordination almost all

the way through with nearest Hg-Te bond distances of 2.76, 3.07 and 3.50 Å at 3.69 GPa (in good agreement with the experimental distances of 2.73, 3.00 and 3.46 Å [12]), whereas the closest Hg-Hg bond distance is 4.34 Å. The bond distances change only slightly for lower pressures, where values of 2.76, 3.28 and 3.75 Å are obtained, indicating a segue into the 2+2+2 coordination observed in HgSe. In nonrelativistic cinnabar-HgTe however, the nearest Hg-Te bond distances are 2.96, 3.04 and 4.27 Å around the minimum and 2.94, 3.09 and 3.66 Å at a slightly higher pressure (1.87 GPa). This means that even though for higher pressures all group 12 tellurides inherit the 4+2 coordination, the zero pressure structure still varies with a fourfold coordination equivalent to cinnabar-ZnTe and CdTe, but different from relativistically treated cinnabar-HgTe. Yet, this effect is a lot less pronounced than in HgSe, HgS and HgO. All bond distances are listed in table 7.11. For a more visual idea of the transition from a fourfold to the 4+2 coordination in the cinnabar structure the reader is referred to fig. 3.5. In addition, the $C222_1$ structure found in HgTe, becomes significantly less stable due to the neglect of relativistic effects. Furthermore, it should be noted that the SC16 structure is again too high in enthalpy to be considered in the transition path.

The structural parameters and other ground-state properties of the HgTe high-pressure phases in the nonrelativistic picture are summarized in table 7.10. In general, due to the effect of relativistic contraction, the lattice constants are slightly bigger than in their relativistically treated counterparts.

7.5.3 Electronic properties

The zero pressure electronic structure of nonrelativistic ZB-HgTe including the site-projected DOS is shown in figs. 7.6 and 7.7. Compared to figs. 7.3 and 7.4 the striking differences between the relativistic and nonrelativistic picture become immediately obvious: If relativistic effects are neglected, the semi-metallic character of HgTe disappears and a small band-gap semiconductor with a gap energy of 0.63 eV similar to ZB-CdTe occurs instead. Analogously, the CBM and VBM are located at the centre of the Brillouin zone and further maxima and minima are equally located at L , K and X .

The site-projected DOS clarifies the described behaviour, as one can clearly see that the Hg-6s band is now shifted and superposes with the Te-5p band. This leads to a degeneracy at the Γ -point overturning the inverted band structure. Furthermore, the crystal-field splitting in the d -bands is clearly visible in the

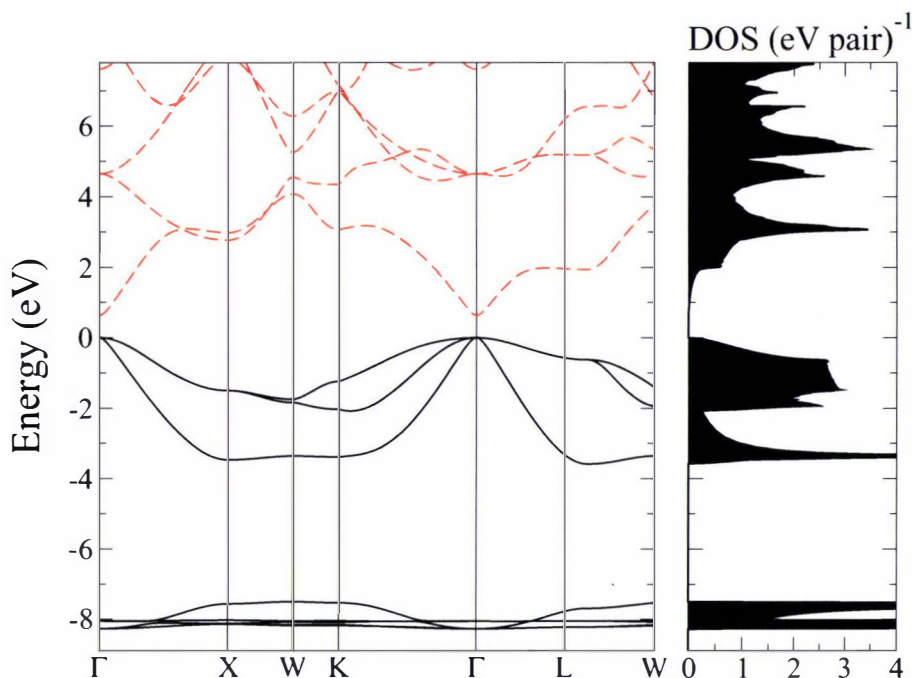


Figure 7.6: Band structure and density of states (normalized per pair) at zero pressure for the HgTe polymorph zinc blende calculated within the nonrelativistic DFT-GGA framework. The valence-band maximum is set to zero energy. The black solid lines indicate the valence and the red dashed lines the conducting bands, respectively.

Hg-spectrum. The separation energy is about 0.15 eV due to the tetrahedral arrangement characteristic for the zinc blende structure.

7.6 Summary

In general, the bulk properties calculated in this study are in good agreement with other theoretical and experimental work. Yet, the bulk moduli are usually somewhat underestimated if compared to experimental results, but are consistent with other computational investigations. The same holds for the qualitative characterization of the electronic structure, even though the gap energies are severely underestimated, which is to be expected using DFT.

Furthermore, the order of the high-pressure phases and the according transition pressures are predicted correctly. Yet, due to the fact that the transitions involving the cinnabar phases are very closely spaced, the method used here might not be accurate enough to make a definite statement. For ZnTe the results

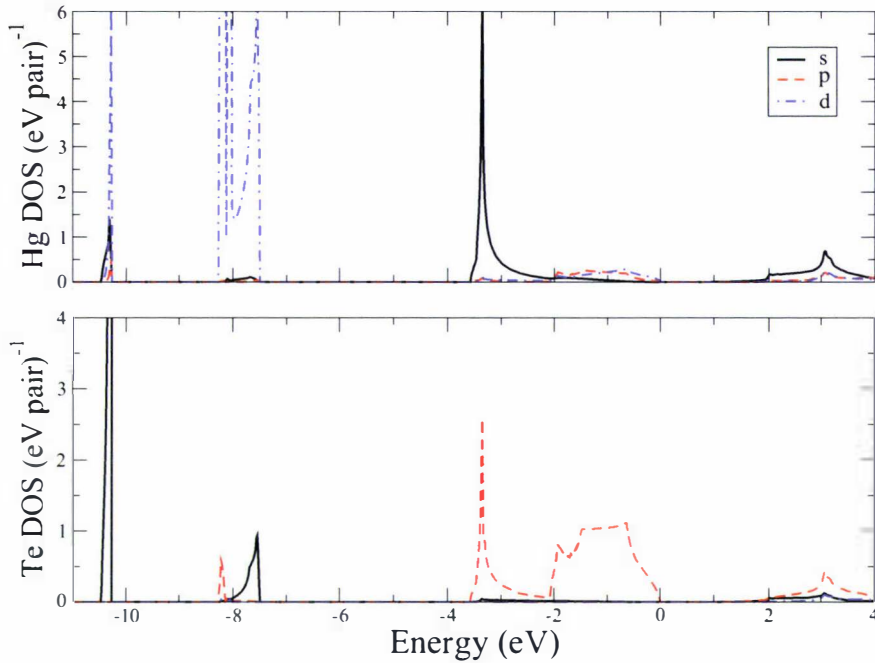


Figure 7.7: Site-projected density of states at zero pressure for the HgTe polymorph zinc blende calculated within the nonrelativistic DFT-GGA nonrelativistic framework. The black solid, red dashed and blue dash-dotted line indicate the s, p and d site-projected DOS, respectively.

presented here confirm its special role in terms of the high-pressure behaviour predicting the absence of the RS structure. This can most likely be explained by the low ionicity of ZnTe compared to similar compounds. However, in contrast to other reports, the SC16 structure is most likely more stable than the cinnabar structure. In addition, a new transition from the $Cmcm$ to the cesium chloride structure is predicted. Whether any intermediate phases between those two modifications are possible should encourage further investigations by theoretical as well as experimental means.

Even though, the stability of the cinnabar phase seems to be slightly underestimated in this investigation, the differences between the relativistic and nonrelativistic treatment of HgTe become obvious. However, the deviations are less obvious than in the other mercury chalcogenides, since the cinnabar phase is observed as a high pressure modification in all three group 12 tellurides. Concerning the structural properties, a difference in coordination is found: For the relativistically treated HgTe a non-fourfold coordination is obtained over the whole range investigated, in contrast to nonrelativistic HgTe.

For the equilibrium phases the relativistic lattice destabilization is calculated to

be 1.33 eV/pair, which is less than in HgO, HgS and HgSe due to the absence of structure change. In addition, it is again determined that the stability of the wurtzite phase is decreased with respect to the zinc blende structure if relativistic effects are included.

Even though the structural difference between nonrelativistic and relativistic HgTe are less pronounced than in HgO and HgS, a significant change in the electronic structure behaviour is observed, where the characteristics change from semimetallic properties in relativistic HgTe to a semiconducting behaviour in nonrelativistic HgTe.

Chapter 8

Conclusion and outlook

In the thesis at hand, for the first time the influence of relativistic effects on the solid-state structure of the mercury chalcogenides has been investigated. To this end, relativistic as well as nonrelativistic density functional theory calculations have been carried out for a considerable range of equilibrium and high-pressure modifications of the group 12 chalcogenides. By those means structural properties of the various chalcogenide phases were obtained, their stabilities calculated and compared.

It was shown, that relativistic effects play indeed a crucial role in the explanation and understanding of the sophisticated chain-like structures, namely cinnabar and montroydite, so typical for the mercury chalcogenides in contrast to the lighter group 12 chalcogenides.

First and foremost, all mercury chalcogenides investigated show relativistic contractions in the bond-distances (for equilibrium as well as high-pressure phases) and a large relativistic lattice destabilization for the equilibrium structure. This destabilization decreases when going from the oxides to the tellurides (ΔE equals 2.15, 1.73, 1.55 and 1.33 eV for HgO, HgS, HgSe and HgTe respectively). An explanation for this behaviour is given by the reduction of the effective charge of the mercury atom due to relativity, i.e. in bulk HgO the Mullikan charge of the mercury atom changes from +0.90 at the relativistic level to +1.10 at the nonrelativistic level. This effect however is balanced out by the decreasing electronegativity descending the 12th group, favouring a more covalent bonding already for the relativistically treated mercury chalcogenides.

Interestingly enough, for the cinnabar phases of HgO and HgS, the above mentioned relativistic contraction is only valid for the inter-chain Hg-chalcogenide

distances. As a big trade-off this contraction is linked to an increase in the intra-chain distances, which in turn leads to a surprising overall volume expansion and a subsequent density decrease upon inclusion of relativistic effects. For relativistically treated HgO, densities as small as the ones found for ZnO and CdO are obtained. This behaviour is in stark contrast to all previous knowledge about the influence of relativistic effects in solids, but is to be blamed on the suppression of the relativistic contraction by the crystal field. However, this effect is not apparent in HgSe and HgTe due to the absence of the pronounced structural change induced by a nonrelativistic treatment (i.e the absence of the cinnabar structure as an equilibrium form). Hence, the relativistic contraction can be identified in the unit-cell volume as well.

Even more surprising is the fact that the montroydite and cinnabar structures found as equilibrium phases in HgO and HgS are solely attributed to relativistic effects and disappear, not only as the ambient pressure phases, but completely, if relativity is neglected. It is found that this can be explained by the decrease in ionicity induced by relativistic effects as well. Hence, typically more ionic bonded structures are favoured in the nonrelativistic picture.

However, this dramatic change in the equilibrium structure becomes less pronounced for mercury selenide and telluride due to the absence of the cinnabar structure as a zero-pressure phase. Yet, significant changes in the coordination of the respective cinnabar modifications are calculated. This trend starts to appear already in HgS where relativity changes a simple fourfold coordination (in non-relativistic HgS) to the unique 2+4 coordination of HgS. The structural change in the Wyckoff parameters u and v here is so large that it has already been challenged whether this arrangement should still be attributed to the prototype cinnabar structure.

Furthermore, it is determined that relativistic effects destabilize the wurtzite structure with respect to the zinc blende structure. This effect is present for all mercury chalcogenides, yet the energetic difference lessens going from HgO via HgS and HgSe to HgTe. It has already been stated in a study that the difference in energy $\Delta E(WZ - ZB)$ increases if the anion atomic number increase from S and Se to Te. As the atomic number decreases, the structures become more ionic, since the Madelung constant for wurtzite ($\alpha_M^{WZ} = 1.6413$) is larger than for zinc blende ($\alpha_M^{ZB} = 1.6381$) [161]. Hence, the less covalent wurtzite phase is preferred in the nonrelativistic picture due to the increase in ionicity upon neglect of relativity.

In general the transition paths of nonrelativistically treated mercury chalcogenides seems to resemble the ones found for the cadmium chalcogenides rather closely.

All structural changes observed due to relativistic effects are expected to originate mainly from scalar-relativistic effects, since spin-orbit coupling is usually suppressed in the ionic lattice field. Yet, spin-orbit effects play an important role to determine an accurate band structure and band gap for the mercury chalcogenides.

It is found that relativistic effects have a major impact on the electronic structure of the mercury chalcogenides as well. For HgO and HgS, the differences between a relativistic and nonrelativistic treatment mainly alter the size of the band gap, which will most likely also be the reason for the red colour found in HgO cinnabar. However, the electronic properties are left unchanged. This is in contrast to HgSe and HgTe, where the neglect of relativistic effects goes as far as changing the experimentally observed semimetallic behaviour to the restoration of semiconducting properties.

Last but not least, the thesis at hand not only exploits the influence of relativistic effects extensively, but also represents a very systematic study of the group 12 chalcogenides in general due to the rather thorough comparative approach. The calculated properties such as lattice constants, internal parameters, bulk moduli, their pressure derivatives and the cohesive energies were calculated and are over all in very good agreement with experimental and other theoretical investigations. Only the bulk moduli at times vary strongly from experimental values. Yet, those deviations are reported in other theoretical studies as well [113] and can most likely be blamed on temperature effects.

With regard to the predicted phase transitions, often several phases are very close in energy in the regions of possible phase transitions. This is particularly true for modifications with many degrees of freedom, e.g. the cinnabar structure. Often the deviations in the total energy are just of the order of typical DFT errors and can easily result in a change of the transition order, therefore making reliable predictions difficult. Yet, it was necessary to rely on DFT as more sophisticated methods are not as well developed for the treatment of solids or rather expensive in computer time. Here, the incremental method developed by Stoll and Fulde [235] should be mentioned as a possible improvement.

Furthermore, it is mentioned that the results presented here are based on a mere thermodynamical treatment and in addition are carried out at zero temperature

only. Hence, an evaluation of phonon dispersions and the inclusion of electron excitations would be desirable, but are beyond the scope of this thesis where the focus lies on the influence of relativistic effects. However, the calculation of exact phase diagrams including temperature induced transitions is very hard and intricate.

The shortcomings of a density functional approach become especially obvious in the severe underestimation of band gaps compared to the available experimental data. However, the results obtained are in very good qualitative agreement and compare excellently to other work at the same level of theory. In order to obtain results comparable to experiments, an improvement of the method such as the GW approximation in conjunction with the random-phase approximation is necessary. However, due to its computational cost and the actual aim of this thesis to estimate the influence of relativistic effects, it was not used here. Major advancement can be achieved, if one goes away from the single particle picture. Here, a more thorough investigation of the electronic structure using highly sophisticated methods such as the Bethe-Salpeter or self-interaction corrected schemes are suggested.

Bibliography

- [1] B. C. Shepler and K. A. Peterson, *J. Phys. Chem. A* **107**, 1783 (2003).
- [2] M. W. Chase Jr., C. A. Davies, J. R. Downey Jr., D. J. Frurip, R. A. McDonald, and A. N. Syverud, *J. Phys. Chem. Ref. Data* **14** (1985).
- [3] M. Filatov and D. Cremer, *Chem. Phys. Chem.* **5**, 1547 (2004).
- [4] K. A. Peterson, B. C. Shepler, and J. M. Singleton, *Mol. Phys.* **105**, 1139 (2007).
- [5] K. L. Aurivillius, *Acta Chem. Scand.* **10**, 852 (1956).
- [6] K. L. Aurivillius and I. B. Carlsson, *Acta Chem. Scand.* **12**, 1297 (1958).
- [7] P. A. Glans, T. Learmonth, K. E. Smith, J. Guo, A. Walsh, G. W. Watson, F. Terzi, and R. G. Egdel, *Phys. Rev. B* **71**, 235109 (2005).
- [8] J. Weissman, *The Photographic Guide to Mineral Species (CD-Rom)* (Excalibur Mineral Cooperation, 2005).
- [9] R. J. Nelmes, M. I. McMahon, N. G. Wright, and D. R. Allan, *Phys. Rev. B* **48**, 1314 (1993).
- [10] V. A. Voronin and V. V. Shchennikov, *Kristallografiya* **34**, 491 (1989).
- [11] T. Zhou, U. Schwarz, M. Hanfland, Z. X. Liu, K. Syassen, and M. Cardona, *Phys. Rev. B* **57**, 153 (1998).
- [12] R. J. Nelmes and M. I. McMahon, in *High Pressure Semiconductor Physics I*, edited by T. Suski and W. Paul (Academic Press, 1998), pp. 146–247.
- [13] J. Maddox, *Nature* **335**, 201 (1988).
- [14] M. L. Cohen, *Nature* **338**, 291 (1989).

- [15] L. Pauling, *The Nature of the Chemical Bond* (Cornell University Press, 1948).
- [16] P. Pyykkö, *P. Chem. Rev.* **88**, 563 (1988).
- [17] P. Schwerdtfeger, ed., *Relativistic Electronic Structure Theory - Part 2: Applications* (Elsevier, 2004).
- [18] P. Schwerdtfeger, *J. Am. Chem. Soc.* **112**, 2818 (1990).
- [19] L. J. Norrby, *J. Chem. Ed.* **68**, 110 (1991).
- [20] P. Schwerdtfeger, P. D. W. Boyd, S. Brienne, J. S. McFeaters, M. Dolg, M. S. Liao, and W. H. E. Schwarz, *Inorg. Chim. Acta* **213**, 233 (1993).
- [21] P. Schwerdtfeger, J. Li, and P. Pyykkö, *Theoret. Chim. Acta.* **87**, 313 (1994).
- [22] H. Nakatsuji, M. Hada, H. Kaneko, and C. C. Ballard, *Chem. Phys. Lett.* **255**, 195 (1996).
- [23] R. Wesendrup, J. K. Laerdahl, and P. Schwerdtfeger, *J. Chem. Phys.* **110**, 9457 (1999).
- [24] P. Schwerdtfeger, R. Wesendrup, G. E. Moyano, A. J. Sadlej, J. Greif, and F. Hensel, *J. Chem. Phys.* **115**, 7401 (2001).
- [25] X. Wang, L. Andrews, S. Riedel, and M. Kaupp, *Angew. Chem. Int. Ed.* **119**, 8523 (2007).
- [26] P. P. Singh, *Phys. Rev. B* **49**, 4954 (1994).
- [27] N. Gaston, B. Paulus, K. Rosciszewski, P. Schwerdtfeger, and H. Stoll, *Phys. Rev. B* **74**, 094102 (2006).
- [28] H. L. Le Chatelier, *Annales des Mines* **13**, 157 (1888).
- [29] A. Schilling, M. Cantoni, J. D. Guo, and H. R. Ott, *Nature* **363**, 56 (1993).
- [30] N. N. Greenwood and A. Earnshaw, *Chemistry of the Elements* (Pergamon, 1984).
- [31] F. Jensen, *Introduction to Computational Chemistry* (John Wiley & Sons Ltd., 1999).

- [32] A. Szabo and N. S. Ostlund, *Modern Quantum Chemistry: Introduction to Advanced Electronic Structure Theory* (Dover Publications, 1996).
- [33] J. Kohanoff, *Electronic Structure Calculations for Solids and Molecules: Theory and Computational Methods* (Cambridge University Press, 2006).
- [34] N. W. Ashcroft and N. D. Mermin, *Solid State Physics* (Brooks/Cole, 1976).
- [35] C. Kittel, *Introduction to Solid State Physics* (John Wiley & Sons Ltd., 1976).
- [36] W. Nolting and W. D. Brewer, *Fundamentals of Many-body Physics: Principles and Methods* (Springer, 2009).
- [37] M. Born and R. Oppenheimer, *Ann. d. Physik* **84**, 457 (1927).
- [38] M. Born, *Rep. Progr. Physics* **9**, 294 (1943).
- [39] J. C. Slater, *Phys. Rev.* **34**, 1293 (1929).
- [40] V. S. Fock, *Z. Physik A* **61**, 126 (1930).
- [41] P. O. Löwdin, *Phys. Rev.* **97**, 1509 (1955).
- [42] C. Møller and M. S. Plesset, *Phys. Rev.* **46**, 618 (1934).
- [43] D. R. Hartree, W. Hartree, and B. Swirles, *Phil. Trans. R. Soc. A* **238**, 229 (1939).
- [44] I. Shavitt, *Mol. Phys.* **94**, 3 (1998).
- [45] O. Sinanoğlu, *J. Chem. Phys.* **36**, 706 (1962).
- [46] J. Čížek, *J. Chem. Phys.* **45**, 4256 (1966).
- [47] C. Pisani, M. Busso, G. Capecchi, S. Casassa, R. Dovesi, L. Maschio, C. Zicovich-Wilson, and M. Schütz, *J. Chem. Phys.* **122**, 094113 (2005).
- [48] C. Pisani and R. Dovesi, *Int. J. Quantum Chem.* **17**, 501 (1980).
- [49] B. Civalleri, P. D'Arco, R. Orlando, V. R. Saunders, and R. Dovesi, *Chem. Phys. Lett.* **348**, 131 (2001).
- [50] P. Hohenberg and W. Kohn, *Phys. Rev. B* **136**, 864 (1964).

- [51] W. Kohn and L. Sham, *Phys. Rev.* **140**, A1133 (1965).
- [52] P. A. M. Dirac, *Proc. Camb. Phil. Soc.* **26**, 376 (1930).
- [53] M. Gell-Mann and K. Brückner, *Phys. Rev.* **106**, 364 (1957).
- [54] D. M. Ceperley and B. J. Alder, *Phys. Rev. Lett.* **45**, 566 (1980).
- [55] S. H. Vosko, L. Wilk, and M. Nusair, *Can. J. Phys.* **58**, 1200 (1980).
- [56] J. P. Perdew and A. Zunger, *Phys. Rev. B* **23**, 5048 (1981).
- [57] Y. Wang and J. P. Perdew, *Phys. Rev. B* **44**, 13298 (1991).
- [58] J. P. Perdew, J. A. Chevary, S. H. Vosko, K. A. Jackson, M. R. Pederson, D. J. Singh, and C. Fiolhais, *Phys. Rev. B* **46**, 6671 (1992).
- [59] J. P. Perdew, K. Burke, and M. Ernzerhof, *Phys. Rev. Lett.* **77**, 3865 (1996).
- [60] A. D. Becke, *Phys. Rev. A* **38**, 3098 (1988).
- [61] C. Lee, W. Yang, and R. G. Parr, *Phys. Rev. B* **37**, 785 (1988).
- [62] R. G. Parr and W. Yang, *Density-Functional Theory of Atoms and Molecules* (Oxford University Press, 1989).
- [63] P. A. M. Dirac, *Proc. R. Soc. London, Ser. A* **123**, 714 (1929).
- [64] P. Schwerdtfeger and M. Lein, in *Gold Chemistry*, edited by F. Mohr (Wiley-VCH, 2009), pp. 183–247.
- [65] N. E. Christensen and B. O. Seraphin, *Phys. Rev. B* **4**, 3321 (1971).
- [66] N. Takeuchi, C. T. Chan, and K. M. Ho, *Phys. Rev. B* **40**, 1565 (1989).
- [67] K. S. Pitzer, *Accounts Chem. Res.* **12**, 271 (1979).
- [68] P. Schwerdtfeger, ed., *Relativistic Electronic Structure Theory - Part 1: Fundamentals* (Elsevier, 2004).
- [69] G. Kresse and J. Furthmüller, *Phys. Rev. B* **54**, 11169 (1996).
- [70] G. Kresse and J. Furthmüller, *Comp. Math. Sci.* **6**, 15 (1996).
- [71] F. Bloch, *Z. Physik* **52**, 555 (1952).

- [72] H. J. Monkhorst and J. D. Pack, *Phys. Rev. B* **13**, 5188 (1976).
- [73] D. R. Hamann, M. Schlüter, and C. Chiang, *Phys. Rev. Lett.* **43**, 1494 (1979).
- [74] D. Vanderbilt, *Phys. Rev. B* **41**, 7892 (1990).
- [75] P. E. Blöchl, *Phys. Rev. B* **50**, 17953 (1994).
- [76] G. Kresse and D. Joubert, *Phys. Rev. B* **59**, 1758 (1999).
- [77] F. D. Murnaghan, *Proc. Nat. Acad. Sci. (USA)* **50**, 697 (1944).
- [78] F. Birch, *J. Geophys. Res.* **57**, 227 (1952).
- [79] P. Vinet, J. Ferrante, J. R. Smith, and J. H. Rose, *J. Phys. C* **19**, L467 (1986).
- [80] P. Vinet, J. H. Rose, J. Ferrante, and J. R. Smith, *J. Phys.: Condens. Matter* **1**, 1941 (1989).
- [81] B. Farid and R. J. Needs, *Phys. Rev. B* **45**, 1067 (1992).
- [82] J. Donohue, *The Structures of the Elements* (John Wiley & Sons Ltd., 1974).
- [83] A. Mujica, A. Rubio, A. Muñoz, and R. J. Needs, *Rev. of Mod. Phys.* **75**, 863 (2003).
- [84] M. I. Aroyo, J. M. Perez-Mato, C. Capillas, E. Kroumova, S. Ivantchev, G. Madariaga, A. Kirov, and H. Wondratschek, *Z. Krist.* **221**, 15 (2006).
- [85] M. I. Aroyo, A. Kirov, C. Capillas, J. M. Perez-Mato, and H. Wondratschek, *Acta Cryst.* **A62**, 115 (2006).
- [86] T. Hahn, ed., *International Tables for Crystallography*, vol. A (Dordrecht: Reidel, 1983).
- [87] S. Hull and D. A. Keen, *Phys. Rev. B* **50**, 5868 (1994).
- [88] M. I. McMahon, R. J. Nelmes, D. R. Allan, S. A. Belmonte, and T. Bovom-ratanaraks, *Phys. Rev. Lett.* **80**, 5564 (1998).
- [89] J. Crain, S. J. Clark, G. J. Ackland, M. C. Payne, V. Milman, P. D. Hatton, and B. J. Reid, *Phys. Rev. B* **49**, 5329 (1994).

- [90] P. Auvray and F. Genet, *Bull. Soc. Fr. Mineral. Cristallogr.* **96**, 218 (1973).
- [91] S. Sun and Y. Dong, *Phys. Rev. B* **72**, 174101 (2005).
- [92] N. G. Wright, M. I. McMahon, R. J. Nelmes, and A. San-Miguel, *Phys. Rev. B* **48**, 13111 (1993).
- [93] R. G. Parr, *Electronic Structure of Solids* (Akademie Verlag, 1991).
- [94] M. S. Hybertsen and S. G. Louie, *Phys. Rev. B* **34**, 5390 (1986).
- [95] F. Bechstedt, *Adv. Solid State Phys.* **32**, 161 (1992).
- [96] P. E. Blöchl, O. Jepsen, and O. K. Andersen, *Phys. Rev. B* **49**, 16223 (1994).
- [97] C. H. Bates, W. B. White, and R. Roy, *Science* **137**, 993 (1962).
- [98] J. C. Jamieson, *Phys. Earth Plan. Inter.* **3**, 201 (1970).
- [99] F. Decremps, J. Zhang, and R. C. Liebermann, *Europhys. Lett.* **51**, 268 (2000).
- [100] F. Decremps, J. Zhang, B. Li, and R. C. Liebermann, *Phys. Rev. B* **63**, 224105 (2001).
- [101] S. C. Yu, I. L. Spain, and E. F. Skelton, *Solid State Commun.* **25**, 49 (1978).
- [102] H. Karzel, W. Potzel, M. Köfferlein, W. Schiessl, M. Steiner, U. Hiller, G. M. Kalvius, D. W. Mitchell, T. P. Das, P. Blaha, et al., *Phys. Rev. B* **53**, 11425 (1996).
- [103] J. M. Recio, M. A. Blanco, V. Luaña, R. Pandey, L. Gerward, and J. S. Olsen, *Phys. Rev. B* **58**, 8949 (1998).
- [104] J. Z. Jiang, J. S. Olsen, L. Gerward, D. Frost, D. Rubie, and J. Peyronneau, *Europhys. Lett.* **50**, 48 (2000).
- [105] L. Gerward and J. S. Olsen, *J. Synchrotron Rad.* **2**, 233 (1995).
- [106] S. Desgreniers, *Phys. Rev. B* **58**, 14102 (1998).
- [107] A. Qteish, *J. Phys.: Condens. Matter* **12**, 5639 (2000).

- [108] Y. Azzaz, S. Kacimi, A. Zaoui, and B. Bouhafs, *Phys. B: Cond. Mat.* **403**, 3154 (2008).
- [109] J. A. Majewski and P. Vogl, *Phys. Rev. B* **35**, 9666 (1987).
- [110] H. Liu, H. K. Mao, M. Somayazulu, Y. Ding, Y. Meng, and D. Häusermann, *Phys. Rev. B* **70**, 094114 (2004).
- [111] R. J. Guerrero-Moreno and N. Takeuchi, *Phys. Rev. B* **66**, 205205 (2002).
- [112] I. M. Tsidil'kovskii, V. V. Shchennikov, and N. G. Gluzman, *Sov. Phys. Semicond.* **19**, 901 (1985).
- [113] A. Schleife, F. Fuchs, J. Furthmüller, and F. Bechstedt, *Phys. Rev. B* **73**, 245212 (2006).
- [114] D. R. Lide, ed., *Handbook of Chemistry and Physics, 79th ed.* (CRC, 1998).
- [115] J. E. Jaffe, J. A. Snyder, Z. Lin, and A. C. Hess, *Phys. Rev. B* **62**, 1660 (2000).
- [116] J. Serrano, A. H. Romero, F. J. Manjón, R. Lauck, M. Cardona, and A. Rubio, *Phys. Rev. B* **69**, 094306 (2004).
- [117] F. Decremps, F. Datchi, A. M. Saitta, A. Polian, S. Pascarelli, A. DiCiccio, J. P. Itié, and F. Baudelet, *Phys. Rev. B* **68**, 104101 (2003).
- [118] J. Zhang, *Phys. Chem. Miner.* **26**, 644 (1999).
- [119] I. A. Ovsyannikova, E. M. Moroz, and A. I. Platkov, *Inzh.-Fiz. Zh.* **22**, 735 (1972).
- [120] O. Madelung, U. Rössler, and M. Schulz, eds., *II-VI and I-VII Compounds, Semimagnetic Compounds*, vol. 41B of *Landolt-Börnstein, New Series, Group III* (Springer Verlag, 1999).
- [121] J. C. Boettger, *Int. J. Quant. Chem.* **107**, 2988 (2007).
- [122] V. B. Singh, *Indian J. Pure Appl. Phys.* **9**, 367 (1971).
- [123] Z. M. Hanafi and F. M. Ismail, *Z. Phys. Chem. Neue Folge* **158**, 81 (1988).
- [124] S. Biering, A. Hermann, J. Furthmüller, and P. Schwerdtfeger, *J. Phys. Chem. A* **113**, 12427 (2009).

- [125] M. Cococcioni and S. de Gironcoli, *Phys. Rev. B* **71**, 035105 (2005).
- [126] J. Bouchet, B. Silberchicot, F. Jollet, and A. Pasturel, *J. Phys.: Condens. Matter* **12**, 1723 (2000).
- [127] V. I. Anisimov, J. Zaanen, and O. K. Andersen, *Phys. Rev. B* **44**, 943 (1991).
- [128] C. E. Moore, *Atomic Energy Levels*, vol. III (U.S. Government Printing Office, 1958).
- [129] L. von Szentpály, *J. Phys. Chem. A* **112**, 12695 (2008).
- [130] S. Desgreniers, L. Beaulieu, and I. Lepage, *Phys. Rev. B* **61**, 8726 (2000).
- [131] S. Minomura and H. G. Drickamer, *J. Phys. Chem. Solids* **23**, 451 (1962).
- [132] P. L. Smith and J. E. Martin, *Phys. Lett.* **19**, 541 (1965).
- [133] S. Ves, U. Schwarz, N. E. Christensen, K. Syassen, and M. Cardona, *Phys. Rev. B* **42**, 9113 (1990).
- [134] Y. Zhou, A. J. Campell, and D. L. Heinz, *J. Phys. Chem. Solids* **52**, 821 (1991).
- [135] A. Nazzal and A. Qteish, *Phys. Rev. B* **53**, 8262 (1996).
- [136] A. Qteish, M. Abu-Jafar, and A. Nazzal, *J. Phys.: Condens. Matter* **10**, 5069 (1998).
- [137] J. López-Solano, A. Mujica, P. Rodríguez-Hernández, and A. Muñoz, *Phys. Stat. Sol. (b)* **235**, 452 (2003).
- [138] A. Qteish and M. Parinello, *Phys. Rev. B* **61**, 6521 (2000).
- [139] R. Gangadharan, V. Jayalakmi, J. Kalaiselvi, S. Mohan, R. Murugan, and B. Palanivel, *J. Alloys Comp.* **359**, 22 (2003).
- [140] A. L. Edwards and H. G. Drickamer, *Phys. Rev.* **122**, 1149 (1961).
- [141] N. B. Owen, P. L. Smith, J. E. Martin, and A. J. Wright, *J. Phys. Chem. Solids* **24**, 1519 (1963).
- [142] G. A. Samara and H. G. Drickamer, *J. Phys. Chem. Solids* **23**, 457 (1962).

- [143] C. F. Cline and D. R. Stephens, *J. Appl. Phys.* **36**, 2869 (1965).
- [144] B. Batlogg, A. Jayaraman, J. E. van Cleve, and R. G. Maines, *Phys. Rev. B* **27**, 3920 (1983).
- [145] T. Suzuki, T. Yagi, S. Akimoto, T. Kawamura, S. Toyoda, and S. Endo, *J. Appl. Phys.* **54**, 748 (1983).
- [146] N. Benkhattou, D. Rached, and M. Rabah, *Czech. J. Phys.* **56**, 409 (2006).
- [147] D. Kirin and I. Lukačević, *Phys. Rev. B* **75**, 172103 (2007).
- [148] T. Huang and A. L. Ruoff, *J. Appl. Phys.* **54**, 5459 (1983).
- [149] A. Werner, H. D. Hochheimer, K. Strössner, and A. Jayaraman, *Phys. Rev. B* **28**, 3330 (1983).
- [150] M. Bilge, S. Özdemir Kart, H. H. Kart, and T. Cagin, *JAMMA* **31**, 29 (2008).
- [151] R. Chen, X. F. Li, L. C. Cai, and J. Zhu, *Solid State Commun.* **139**, 246 (2006).
- [152] J. E. Jaffe, R. Pandey, and M. J. Seel, *Phys. Rev. B* **47**, 6299 (1993).
- [153] O. Madelung, ed., *Numerical Data and Functional Relationship in Science and Technology*, vol. 17 of *Landolt-Börnstein, New Series, Group III* (Springer-Verlag, 1982).
- [154] C.-E. Hu, L.-L. Sun, Z.-Y. Zeng, and X.-R. Chen, *Chin. Phys. Lett.* **25**, 675 (2008).
- [155] E. H. Kisi and M. M. Elcombe, *Acta. Cryst.* **C45**, 1867 (1989).
- [156] M. Catti, Y. Noel, and R. Dovesi, *J. Phys. Chem. Solids* **64**, 2183 (2003).
- [157] F. Bechstedt and W. A. Harrison, *Phys. Rev. B* **39**, 5041 (1989).
- [158] C. Y. Yeh, Z. W. Lu, S. Froyen, and A. Zunger, *Phys. Rev. B* **46**, 10086 (1992).
- [159] N. Benkhattou, D. Rached, B. Soudini, and M. Driz, *Phys. Stat. Sol.* **241**, 101 (2004).
- [160] K. Wright and J. D. Gale, *Phys. Rev. B* **70**, 035211 (2004).

- [161] S.-H. Wei and S. B. Zhang, *Phys. Rev. B* **62**, 6944 (2000).
- [162] X. Chen, X. Hua, J. Hu, J.-M. Langlois, and W. A. Goddard III, *Phys. Rev. B* **53**, 1377 (1996).
- [163] F. Benkabou, H. Aourag, and M. Certier, *Mater. Chem. and Phys.* **66**, 10 (2000).
- [164] J. R. Chelikowsky, *Phys. Rev. B* **35**, 1174 (1987).
- [165] D.-W. Fan, W.-G. Zhou, C.-Q. Liu, F. Wang, Y.-S. Xing, J. Liu, Y.-C. Li, and H.-S. Xie, *Chin. Phys. Lett.* **26**, 046402 (2009).
- [166] K. L. Aurivillius, *Acta Chem. Scand.* **4**, 1423 (1950).
- [167] A. Hao, C. Gao, M. Li, C. He, X. Huang, D. Zhang, C. Yu, H. Liu, Y. Ma, Y. Tian, et al., *J. Phys.: Condens. Matter* **19**, 425222 (2007).
- [168] A. Delin and T. Klüner, *Phys. Rev. B* **66**, 035117 (2002).
- [169] P. W. Bridgeman, *Proc. Am. Acad. Sci.* **74**, 21 (1940).
- [170] A. Fleszar and W. Hanke, *Phys. Rev. B* **71**, 045207 (2005).
- [171] P. Schröer, P. Krüger, and J. Pollmann, *Phys. Rev. B* **47**, 6971 (1993).
- [172] K. Dybko, W. Szuszkiewicz, E. Dynowska, W. Paszkowicz, and B. Witkowska, *Physica B* **256**, 629 (1998).
- [173] S. Sun and Y. Dong, *Solid State Commun.* **138**, 476 (2006).
- [174] M. Cardona, R. K. Kremer, R. Lauck, G. Siegle, A. Muñoz, and A. H. Romero, *Phys. Rev. B* **80**, 195204 (2009).
- [175] G. J. Piermarini and S. Block, *Rev. Sci. Inst.* **46**, 973 (1975).
- [176] S. Ves, K. Strössner, N. E. Christensen, C. K. Kim, and M. Cardona, *Solid State Commun.* **56**, 479 (1985).
- [177] S. R. Tiong, M. Hiramatsu, Y. Matsushima, and E. Ito, *Jpn. J. Appl. Phys.* **28**, 291 (1989).
- [178] G. Itkin, G. R. Hearne, E. Sterer, M. P. Pasternak, and W. Potzel, *Phys. Rev. B* **51**, 3195 (1995).

- [179] M. I. McMahon and R. J. Nelmes, *Phys. Stat. Sol. (b)* **198**, 389 (1996).
- [180] M. Côté, O. Zakharov, A. Rubio, and M. L. Cohen, *Phys. Rev. B* **55**, 13025 (1997).
- [181] A. Qteish and A. Muñoz, *J. Phys.: Condens. Matter* **12**, 1705 (2000).
- [182] J. Pellicer-Porres, A. Segura, V. Muñoz, J. Zúñiga, J. P. Itié, A. Polian, and P. Munsch, *Phys. Rev. B* **65**, 012109 (2001).
- [183] S. Cuia, H. Hua, W. Fenga, X. Chenb, and Z. Fenga, *J. Alloys Comp.* **472**, 294 (2005).
- [184] C. J. M. Rooymans, *Phys. Lett.* **4**, 186 (1963).
- [185] A. N. Mariano and E. P. Warekois, *Science* **142**, 672 (1963).
- [186] P. Cervantes, Q. Williams, M. Côté, O. Zakharov, and M. L. Cohen, *Phys. Rev. B* **54**, 17585 (1996).
- [187] O. A. Ignatchenko and A. N. Babushkin, *Phys. Solid State* **35**, 1109 (1993).
- [188] O. Zakharov, A. Rubio, and M. L. Cohen, *Phys. Rev. B* **51**, 4926 (1995).
- [189] J. A. Kafalas, H. C. Gatos, M. C. Levine, and M. D. Banus, *J. Phys. Chem. Solids* **23**, 1541 (1962).
- [190] N. G. Gluzman and V. V. Shchennikov, *Sov. Phys. Solid State* **21**, 1844 (1979).
- [191] A. Ohtani, T. Seike, M. Motobayashi, and A. Onodera, *J. Phys. Chem. Solids* **43**, 627 (1982).
- [192] A. Onodera, A. Ohtani, M. Motobayashi, T. Seike, and O. Fukunaga, in *Proceedings of the 8th AIRAPT Conference*, edited by C. M. Backman, T. Johansson, and L. Tenger (World Scientific, 1982), vol. 1, p. 321.
- [193] A. Jayaraman, W. J. Klement, and G. C. Kennedy, *Phys. Rev.* **130**, 2277 (1963).
- [194] R. J. Nelmes, M. I. McMahon, and S. A. Belmonte, *Phys. Rev. Lett.* **79**, 3668 (1997).
- [195] M. I. McMahon, H. Liu, R. J. Nelmes, and S. A. Belmonte, *Phys. Rev. Lett.* **77**, 1781 (1996).

- [196] T. Huang and A. L. Ruoff, *Phys. Rev. B* **27**, 7811 (1983).
- [197] V. I. Smelyansky and J. S. Tse, *Phys. Rev. B* **52**, 4658 (1995).
- [198] B. H. Lee, *J. Appl. Phys.* **41**, 2988 (1970).
- [199] R. Khenata, A. Bouhemadou, M. Sahnoun, A. H. Reshak, H. Baltache, and M. Rabah, *Comp. Mat. Sci.* **38**, 29 (2006).
- [200] V. V. Shchennikov and S. V. Ovsyannikov, *Phys. Stat. Sol. (b)* **244**, 437 (2007).
- [201] K. K. Zhuravlev, *Physica B: Cond. Matter* **394**, 1 (2007).
- [202] E. Rabani, *J. Chem. Phys.* **116**, 258 (2002).
- [203] T. Huang and A. L. Ruoff, *Phys. Rev. B* **31**, 5976 (1985).
- [204] J. Gutowski, K. Sebald, and T. Voss, eds., *Semiconductors: New Data and Updates for II-VI Compounds*, vol. 44B of *Landolt-Börnstein, New Series, Group III* (Springer Verlag, 2009).
- [205] A. Oltani, M. Motobayashi, and A. Onodera, *Phys. Lett.* **75A**, 435 (1980).
- [206] K. Strössner, S. Ves, C. K. Kim, and M. Cardona, *Solid State Commun.* **61**, 275 (1987).
- [207] K. Strössner, S. Ves, W. Hönle, W. Gebhardt, and M. Cardona, in *Proceedings of the 18th International Conference on the Physics of Semiconductors*, edited by O. Engstrom (World Scientific, 1987), p. 1717.
- [208] M. I. McMahon, R. J. Nelmes, N. G. Wright, and D. R. Allan, in *High Pressure Science and Technology*, edited by S. C. Schmidt, J. W. Shaner, G. A. Samara, and M. Ross (AIP Press, 1994), vol. 309 of *AIP Conf. Proc.*, p. 633.
- [209] R. J. Nelmes, M. I. McMahon, N. G. Wright, and D. R. Allan, *J. Phys. Chem. Sol.* **56**, 545 (1995).
- [210] K. Kusaba and D. J. Weidner, in *High Pressure Science and Technology*, edited by S. C. Schmidt, J. W. Shaner, G. A. Samara, and M. Ross (AIP Press, 1994), vol. 309 of *AIP Conf. Proc.*, p. 553.

- [211] S. B. Qadri, E. F. Skelton, A. W. Webb, and J. Z. Hu, in *High Pressure Science and Technology*, edited by S. C. Schmidt, J. W. Shaner, G. A. Samara, and M. Ross (AIP Press, 1994), vol. 309 of *AIP Conf. Proc.*, p. 319.
- [212] A. San-Miguel, A. Polian, M. Gauthier, and J.-P. Itié, *Phys. Rev. B* **48**, 8683 (1993).
- [213] G.-D. Lee and J. Ihm, *Phys. Rev. B* **53**, R7622 (1996).
- [214] R. J. Nelmes, M. I. McMahon, N. G. Wright, and D. R. Allan, *Phys. Rev. Lett.* **73**, 1805 (1994).
- [215] J. Camacho, I. Loa, A. Cantarero, and K. Syassen, *J. Phys.: Condens. Matter* **14**, 739 (2002).
- [216] O. Shimomura, W. Utsumi, T. Urakawa, T. Kikegawa, K. Kusaba, and A. Onodera, *Rev. High Press. Sci. Tech.* **6**, 207 (1997).
- [217] I. Y. Borg and D. K. J. Smith, *J. Phys. Chem. Solids* **28**, 49 (1967).
- [218] J. González, F. V. Pérez, E. Moya, and J. C. Chervin, *J. Phys. Chem. Solids* **56**, 335 (1995).
- [219] R. J. Nelmes, M. I. McMahon, N. G. Wright, and D. R. Allan, *Phys. Rev. B* **48**, 1314 (1993).
- [220] R. Ahuja, P. James, O. Eriksson, J. M. Wills, and B. Johansson, *Phys. Stat. Sol. (b)* **199**, 75 (1997).
- [221] D. Martínez-García, Y. Le Godec, M. Mézouar, G. Syfosse, J.-P. Itié, and J. M. Besson, *Phys. Stat. Sol. (b)* **211**, 461 (1999).
- [222] M. I. McMahon, R. J. Nelmes, N. G. Wright, and D. R. Allan, *Phys. Rev. B* **48**, 16246 (1993).
- [223] R. J. Nelmes, M. I. McMahon, N. G. Wright, and D. R. Allan, *Phys. Rev. B* **51**, 15723 (1995).
- [224] J. Blair and A. C. Smith, *Phys. Rev. Lett.* **7**, 124 (1961).
- [225] A. San-Miguel, N. G. Wright, M. I. McMahon, and R. J. Nelmes, *Phys. Rev. B* **51**, 8731 (1995).

- [226] T. Huang and A. L. Ruoff, *Phys. Stat. Sol. (a)* **77**, K193 (1983).
- [227] M. I. McMahon, N. G. Wright, D. R. Allan, and R. J. Nelmes, *Phys. Rev. B* **53**, 2163 (1993).
- [228] V. Briois, C. Brouder, P. Sainctavit, A. San-Miguel, J.-P. Itié, and A. Po-
lian, *Phys. Rev. B* **56**, 5866 (1997).
- [229] N. E. Christensen and O. B. Christensen, *Phys. Rev. B* **33**, 4739 (1986).
- [230] R. Franco, P. Mori-Sánchez, J. M. Recio, and R. Pandey, *Phys. Rev. B* **68**,
195208 (2003).
- [231] M. B. Kanoun, W. Sekkal, H. Aourag, and G. Merad, *Phys. Lett. A* **272**,
113 (2000).
- [232] P. E. van Camp and V. E. van Doren, *Solid State Commun.* **91**, 607 (1994).
- [233] A. Hao, X. Yang, R. Yu, C. Gao, Y. Han, R. Liu, and Y. Tian, *J. Phys.*
Chem. Solids **70**, 433 (2009).
- [234] A. Onodera, A. Ohtania, S. Tsudukia, and O. Shimomurab, *Solid State*
Commun. **145**, 374 (2008).
- [235] B. Paulus, *Phys. Rep.* **428**, 1 (2006).